Kinetics of charge carriers in Si/SiN_x heterojunctions

im Fachbereich Physik
der Freien Universität Berlin
eingereichte Dissertation

von

Elías Martínez Moreno
aus Barcelona

angefertigt am
Helmholtz Zentrum Berlin für Materialien und Energie

November 2009

Erstgutachter:
Prof.a.D. William D. Brewer, PhD
FU Berlin

Zweitgutachter:
PD Dr. Thomas Dittrich
FU Berlin - Helmholtz Zentrum Berlin

Betreuung:
Dr. Marinus Kunst
Helmholtz Zentrum Berlin

Disputationsdatum: 14.12.09

Abstract

In the present work charge carrier kinetics at the Si/SiN_x interface are investigated. SiN_x films deposited on silicon wafers by plasma-enhanced chemical deposition (PECVD) act as antireflecting and surface recombination passivating layers in solar cells. PECVD SiN_x films are a low-temperature and cheap promising alternative to the standard silicon passivation method by thermal oxidation involving high temperatures.
The aim of this work is to characterize the Si/SiN_x interface by (photo)-conductance and impedance methods. Impedance (C-V) measurements have been performed on Si/SiN_x Metal-Insulator-Semiconductor structures and (photo)electrochemical cells. A positive fixed surface charge density over $10^{12}cm^{-2}$ and donor and acceptor-like gaussian distributions over $10^{11}cm^{-2}eV^{-1}$ around mid-gap have been found to characterize the Si/SiN_x interface. This fixed charge brings the $n-Si$ into strong accumulation regime and the $p-Si$ into strong inversion regime without the need of an applied external voltage. Potential-modulated microwave reflection measurements have been proved to be a compatible and valuable characterization technique at electrochemical cells, confirming and complementing the impedance characterization.
Cyclic voltammetry and photoelectrochemical measurements have shown that SiN_x is not an inert layer in Si/SiN_x devices. It has been proved that leakage currents change the Si/SiN_x electronic configuration and that charge carriers can be exchanged between the layers. SiN_x has proven to be not appropriate for (photo)catalytic applications in aqueous medias.
Time Resolved Microwave Conductivity measurements have been performed on electrochemical cells as a function of the applied potential. It has been found that the SiN_x passivation on Si wafers is induced by a field effect.
Dark conductivity microwave measurements on pSi/SiN_x samples suggest a strongly reduced mobility of electrons at the interface, probably due to the presence of a high density of interface states.
TRMC and Surface Photovoltage (SPV) measurements show a strongly non linear recombination behavior at low injection levels which is quenched with increasing injection level. This decay at low injection levels is not characteristic of pSi/SiO_2 and cannot be easily ascribed to a recombination over the potential barrier of the depletion layer.

Kurzzusammenfassung

Die vorliegende Arbeit beinhaltet die Untersuchung der Ladungsträgerkinetik an der Si/SiN_x Grenzfläche. SiN_x Schichten werden mittels Plasmaunterstützter chemischer Gasphasenabscheidung (PECVD) auf Silizium abgeschieden und dienen als Antireflektionsschicht sowie zur Oberflächenpassivierung in Form einer Reduktion der Rekombinationsprozesse bei Silizium-Solarzellen. Die durch PECVD hergestellten SiN_x Schichten bieten eine auf niedrigen Temperaturen basierende, günstige Alternative zu konventionellen Passivierungsmethoden von Silizium durch thermische Oxidation unter Einsatz hoher Temperaturen.
Ziel dieser Arbeit ist eine Charakterisierung der SiN_x Grenzfläche mit (Foto)-Leitfähigkeits und Impedanzmessungen. Impedanzmessungen (C-V) wurden an Si/SiN_x Metall-Isolator-Halbleiter Systemen und (Foto)elektrochemischen Zellen durchgeführt. Dabei wurde festgestellt, dass die Si/SiN_x Grenzfläche durch eine feste positive Oberflächenladung mit Werten über $10^{12}cm^{-2}$ und einer Donor- und Akzeptorzuständen ähnlichen gaußförmigen Verteilung mit Werten über $10^{11}cm^{-2}eV^{-1}$ nahe der Mitte der Bandlücke charakterisiert wird. Die feste Ladung bewirkt ohne äußeres angelegtes Potential eine starke Anreicherungszone im $n-Si$, sowie eine starke Inversionszone im $p-Si$. Potentialmodulierte Mikrowellenreflektionsmessungen haben sich als passende und wertvolle Untersuchungsmethode für elektrochemische Zellen erwiesen, welche die Charakterisierung durch Impedanzmessungen bestätigen und vervollständigen können.
Die Untersuchungen mittels zyklischer Voltametrie sowie fotoelektrochemische Messungen haben gezeigt, dass SiN_x keine inerte Schicht in Si/SiN_x Systemen ist. Es konnte gezeigt werden, dass Leckströme die elektronische Konfiguration des Si/SiN_x Systems dahingehend ändern, dass ein Ladungsträgeraustausch zwischen den Schichten möglich ist. SiN_x zeigte sich ungeeignet für die Anwendung in (foto)katalytischen Systemen in wässrigen Medien.
Zeitaufgelöste Mikrowellenleitfähigkeitsmessungen wurden an elektrochemischen Zellen durchgeführt unter Änderung des angelegten Potentials. Die Passivierung von Si Wafern durch SiN_x konnte als Folge eines Feldeffektes identifiziert werden.
Dunkel-Leitfähigkeit Mikrowellenmessungen an pSi/SiN_x Proben deuten auf eine stark eingeschränkte Beweglichkeit der Elektronen an der Grenzfläche hin, welche wahrscheinlich auf eine hohe Dichte von Grenzlächenzuständen zurückgeführt werden kann.

TRMC und Oberflächen-Fotospannungsmessungen (SPV) zeigten ein stark nicht-lineares Rekombinationsverhalten für niedrige Injektionsdichten, welches mit ansteigender Injektionsdichte unterdrückt wird. Dieses Abklingen bei niedriger Injektionsdichte ist nicht charakteristisch für pSi/SiO_2 und kann nicht (leicht) einer Rekombination über die Potentialbarriere der Verarmungsschicht zugeschrieben werden.

Contents

Chapter 1

Introduction

Charge carriers kinetics is essential for the functioning of semiconductor devices. In particular charge carrier kinetics in the space charge region is pertinent to their relevant properties as rectifying, charge storage and charge carrier separation for energy conversion.
In this work, charge carrier kinetics in space charge region is investigated in view of photovoltaic energy conversion.
Here it is appropriate to study excess charge carrier kinetics induced by light. Related fields as solar fuel production and photocatalysis are covered by the same kind of systems.
The system Si/SiN_x is the combination of a semiconductor with an insulator and as such a hetero junction. As for the previously investigated Si/SiO_2 heterojunction, a fixed charge in the isolator has been observed, compensated by a negative charge (mostly mobile electrons) in the semiconductor. For the Si/SiN_x hetero junction this fixed positive charge is even much higher and exceeds $10^{12}cm^{-2}$. So in the system Si/SiN_x, excess charge carrier kinetics can be studied in the depletion regime ($p - Si$) and in the accumulation regime ($n - Si$).

Some aspects of the Si/SiN_x heterojunctions make it very appropriate as a model system for charge carriers kinetics in space charge regions:

- An appreciable space charge region is already present without the application of an external field. This is important for contactless measurements. The space charge region can be modulated by bias light in this case.

- In principle there is no appreciable current through the SiN_x film. So

in the ideal case a direct current has not to be taken into account.

- There is no high conductivity component as a metal or highly doped semiconductor. So microwave methods, which are very cumbersome if high conductivity components are present, can be applied without great problems.

The system Si/SiN_x is very important for solar energy conversion. In this field the most useful applications are:

- SiN_x as antireflection coating for Si solar cells. The refractive index of SiN_x makes this material appropriate for an antireflection coating on silicon.

- Electrical passivation of the silicon surface. The deposition of SiN_x films on silicon leads to a drastic reduction of the surface recombination velocity, mainly due to field passivation.

It must be noted that most commercial (Si) photovoltaic solar cells contain nowadays SiN_x films as antireflection coating and electrical surface passivation.

- SiN_x offers also a chemical protection of the corrosive properties of Si. This material may be appropriate in photocatalysis and solar fuels production on base of Si-systems.

Beside these applications the Si/SiN_x system is on large scale applied in MOSFETS and non-volatile memories.
In all these applications, (excess)charge carrier kinetics plays the leading part. So the study on (excess)charge kinetics in the Si/SiN_x systems is important as well for the further development and examination of the system.
In this work a number of analytical techniques have been applied to the Si/SiN_x heterojunction. Some of them can be called more or less standardly as:

- (Photo)impedance measurements

- (Photo)electrochemical measurements

- Quasi Steady State Photoconductance (QSSPC) measurements

- Contactless microwave conductivity measurements

- Transient photoconductance measurements in the microwave frequency range by the Time Resolved Microwave Conductivity (TRMC) method

Other ones are relatively new or rarely used and this work will explore their possibilities. The following techniques can be mentioned:

- Microwave electrochemical measurements
- Microwave impedance measurements
- Small signal surface photovoltage measurements in combination with TRMC measurements
- TRMC measurements in photoelectrochemical cells as a function of the applied potential.

Chapter 2

Principles of semiconductor physics

2.1 Band structure and statistics in semiconductors

The specification "semiconductor" defines a material with respect to its electronic properties. These materials present resistivity (ρ) values between that of a conductor ($\rho < 10^{-3}\Omega cm$) and an insulator ($\rho > 10^{8}\Omega cm$). Experimentally a semiconductor is characterized by a weak conductivity ($\sigma = 1/\rho$ Scm^{-1}) at room temperature which is increasing with rising temperature, is sensitive to external electric forces [1] and increases under illumination. It was found that the addition of specific type of impurities leads to a strong increase of the conductivity [2].
The electron distribution in a semiconductor is given by the Fermi-Dirac distribution $f(E)$:

$$f(E) = \frac{1}{1 + e^{\frac{E-E_F}{kT}}} \tag{2.1}$$

with E_F the Fermi level, k the Boltzmann constant, T the temperature and E the energy.
The allowed energy levels for the electrons in a semiconductor form two bands: the valence band, lower in energy, and the conduction band, the upper one; separated by a forbidden energy region (the band gap).
These bands are constituted by a series of discrete energy levels so close to each other that formally, the band can be considered as a continuous distribution of allowed energy states for electrons. The top of the valence

band has an energy E_v and the bottom of the conduction band has an energy E_c. These energy bands are separated by an energy $E_g = E_c - E_v$ called the band gap.
The Fermi level of a semiconductor lies between these two permitted energy bands, within the band gap.
The high density of available energy levels in the conduction band allow the electrons in the conduction band to change easily from one energetic state to another by increasing or diminishing its kinetic energy under the effect of external forces. The electron vacancies in the valence band, "holes", show similar properties: electrons from a neighbor valence band energy level can easily occupy the vacancies leading to the transport of "holes" through the semiconductor under the effect of external forces. Thus, electrons in the conduction band and holes in the valence band contribute to the charge transport properties in a semiconductor.
The density of electron states in the conduction band ($N_c(E)$) and of the hole states in the valence band ($N_v(E)$) is given by [1]:

$$N_c(E) = 4\pi \left(\frac{2m_e^*}{h^2}\right)^{3/2} (E - E_c)^{1/2} \tag{2.2}$$

$$N_v(E) = 4\pi \left(\frac{2m_h^*}{h^2}\right)^{3/2} (E_v - E)^{1/2} \tag{2.3}$$

where m_e^* and m_h^* are the effective mass of an electron and an electron vacancy, respectively, and h the Planck constant.
In order to obtain the total density of free charge carriers in the semiconductor, the integration over all conduction levels for electrons and all valence levels for holes must be done:

$$n = \int_{E_c}^{\infty} N_c(E)\, f(E)\, dE \tag{2.4}$$

$$p = \int_{E_v}^{\infty} N_v(E)\, (1 - f(E))\, dE \tag{2.5}$$

where $(1 - f(E))$ is the distribution of holes in the semiconductor.

For the case in which the Fermi level satisfies the condition for non degenerated semiconductors:

$$2kT + E_v < E_F < E_c - 2kT \tag{2.6}$$

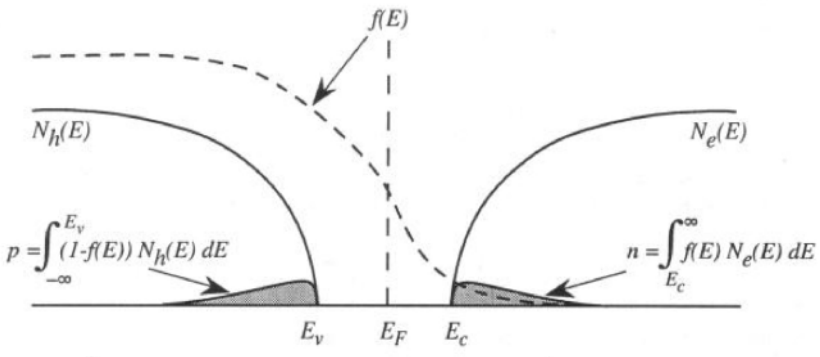

Figure 2.1: Illustration representing the density of electron and holes in the conduction and valence band.

the Fermi-Dirac distribution can be approximated by a Boltzmann distribution [3]:

$$f\left(E\right) \approx e^{-\left(\frac{E-E_F}{kT}\right)} \tag{2.7}$$

and the density of free charge carriers approximated by:

$$n = 2\left(\frac{2\pi m_e^* kT}{h^2}\right)^{3/2} e^{-\left(\frac{E_c-E_F}{kT}\right)} = N_c^* e^{-\left(\frac{E_c-E_F}{kT}\right)} \tag{2.8}$$

$$p = 2\left(\frac{2\pi m_p^* kT}{h^2}\right)^{3/2} e^{-\left(\frac{E_F-E_v}{kT}\right)} = N_v^* e^{-\left(\frac{E_F-E_v}{kT}\right)} \tag{2.9}$$

with

$$N_c^* = 2\left(\frac{2\pi m_e^* kT}{h^2}\right)^{3/2},\ N_v^* = 2\left(\frac{2\pi m_p^* kT}{h^2}\right)^{3/2} \tag{2.10}$$

the equivalent density of states in the conduction and valence band, respectively.
The product of the concentration of free electrons (n) and free holes (p) in a non degenerated semiconductor is given by:

$$np = N_c^* N_v^* e^{-\frac{E_c-E_v}{kT}} = N_c^* N_v^* e^{-\frac{E_g}{kT}} = {n_i}^2 \tag{2.11}$$

where n_i is defined as the intrinsic concentration and depends only on the temperature and the band gap of the semiconductor. A semiconductor is called intrinsic if the concentration of free electrons and holes are identical

in thermal equilibrium:

$$n = p = n_i = \sqrt{N_c^* N_v^*} e^{-\frac{E_g}{2kT}} \tag{2.12}$$

with the position of the Fermi level in an intrinsic semiconductor:

$$E_F = \frac{E_c + E_v}{2} + \frac{kT}{2} \ln \frac{N_v^*}{N_c^*} = \frac{E_c + E_v}{2} + \frac{3kT}{4} \ln \frac{m_p^*}{m_n^*} \tag{2.13}$$

A semiconductor is called extrinsic if the concentration of free electrons and holes is not the same in thermal equilibrium. Defects in the lattice, such as vacancies, or the presence of impurities, such as doping atoms, modify the population of mobile charge carriers. Impurities and defects introduce a permitted energy state within the band gap, which can emit and trap electrons from/to the conduction or valence band.

Donor impurities introduce an energetic state within the band gap close to the conduction band and provide extra electrons, which are emitted to the conduction band (electron injection) enhancing the density of mobile electrons. Acceptor impurities introduce an allowed energy level close to the valence band and take electrons from the valence band (hole injection) enhancing the density of mobile holes.
When ionized, impurities introduce extra charge in the semiconductor. Donor impurities are positively charged and acceptor negatively. The free charge carriers compensate these charges and the charge neutrality in a semiconductor is expressed by:

$$n + N_A^- = p + N_D^+ \tag{2.14}$$

where N_D^+ and N_A^- refers to the concentration of ionized donor and acceptor impurities, respectively.
In the low temperature regime, for extrinsic (doped) semiconductors the main part of the free charge carriers originate from the ionized impurities. At low temperatures the intrinsic contribution to free charge carriers is very small compared to the one from the doping atoms. An intrinsic (non doped) semiconductor would have the valence band completely filled with electrons and the conduction band practically empty. Thus, considering an extrinsic semiconductor only doped with donor impurities, the neutrality of charge can be expressed as:

$$n = N_D^+ \tag{2.15}$$

and the energy of the Fermi level will be:

$$E_F = kT \ln \left[\frac{1}{4} e^{\frac{E_D}{kT}} \left(\sqrt{1 + \frac{8N_D}{N_c^*} e^{\frac{E_c - E_D}{kT}}} - 1 \right) \right] \tag{2.16}$$

with E_D the energy level of the donor impurity. For the case of very low temperatures (under $150K$ for Si with $N_D = 10^{15} cm^{-3}$ [1]), the second term in the square root dominates over the other terms in the parenthesis $\left(\sqrt{1 + \frac{8N_D}{N_c^*} e^{\frac{E_c - E_D}{kT}}} - 1 \right) \approx \left(\sqrt{\frac{8N_D}{N_c^*} e^{\frac{E_C - E_D}{kT}}} \right)$ and the Fermi level and the density of electrons can be approximated as:

$$E_F = \frac{E_c + E_D}{2} + \frac{kT}{2} \ln \frac{N_D}{2N_c^*} \tag{2.17}$$

$$n = \sqrt{\frac{N_c^* N_D}{2}} e^{-\frac{E_c - E_D}{2kT}} \tag{2.18}$$

This is the regime called ionized impurity regime, due to the fact that the main contribution to the free charge carriers is from ionized donors. For medium temperatures (between $150K$ and $450K$ [1]), the dependence of the equivalent density of states in the conduction band, $N_c^* \propto T^{\frac{3}{2}}$, decreases the weight of the exponential term in the root. Approximating using Taylor's series until first order $\sqrt{1+x} \approx 1 + \frac{x}{2}$ taking $x = \frac{8N_D}{N_c^*} e^{\frac{E_c - E_D}{kT}}$

$$E_F = E_c - kT \ln \frac{N_c^*}{N_D} \tag{2.19}$$

$$n = N_D \tag{2.20}$$

This regime is called the impurity saturation; it is the situation that all donors are ionized and the number of free charge carriers corresponds to the density of donors. This regime is the one valid at room temperature and will be the regime suitable for the present work.

2.2 Charge carrier transport

Here will be considered the charge carrier transport leading to electrical current (j in A/cm^2) due to the action of an external force as an electric field or a concentration gradient.

2.2.1 Carrier drift

In a first approximation, the current due to a field E, the drift current, is described by the Drude model: an electron is accelerated by the electric field until part of the excess kinetic energy gained from the field is dissipated via collisions with defects in the lattice. This process of acceleration interrupted by collisions leads to a steady state where electrons are moving with a constant average velocity, the drift velocity v_d [4]. The lattice exerts a friction force on the electron which compensates the force of the electric field. The drift velocity is proportional to the electric field:

$$|v_d| = \mu_d |E| \tag{2.21}$$

The mobility, μ_d, is the proportionality factor between the field strength, E, and the drift velocity. The drift current is carried by electrons (j_n^d) with a mobility μ_n and by holes (j_p^d) with a mobility μ_p:

$$j_n^d = q\mu_n nE \tag{2.22}$$

$$j_p^d = q\mu_p pE \tag{2.23}$$

where q is the unity charge ($1.6 \cdot 10^{-19} C$).
Electrons and holes move in opposite directions under the influence of a field, but they contribute to the current (j^d) with the same sign:

$$j^d = j_n^d + j_p^d = q\left(\mu_n n + \mu_p p\right) E = \sigma E \tag{2.24}$$

$$\sigma = q\left(\mu_n n + \mu_p p\right) \tag{2.25}$$

where the conductivity σ is the proportionality factor between the electric field strength and the total current.

2.2.2 Carrier diffusion

The diffusion current is due to a gradient in concentration of charge carriers in the semiconductor. Mobile charge carriers can be seen as particles with an average kinetic energy, which move randomly in the absence of forces. An homogeneous distribution gives a zero contribution to the total particle displacement, but in the case of a concentration gradient, the net displacement of free charge carriers is not zero. There is a net displacement of charge carriers to regions with lower charge carriers' concentrations. This transport leads

to a diffusion current (j^{diff}) that in a linear (small perturbation) approximation is proportional to the gradient of the charge carrier concentration (Fick's law [5],[6]):

$$j_n^{diff} = qD_n\vec{\nabla}n \tag{2.26}$$

$$j_p^{diff} = -qD_p\vec{\nabla}p \tag{2.27}$$

with j_n^{diff} and j_p^{diff} the diffusion currents for electrons and holes and D_n and D_h, the diffusion constants of electrons and holes, respectively. For an identical gradient electrons and holes move together, from higher to lower concentration, but the electrical currents have opposite signs, thus:

$$j^{diff} = j_n^{diff} + j_p^{diff} = qD_n\vec{\nabla}n - qD_p\vec{\nabla}p \tag{2.28}$$

The total electrical current for electrons (j_n) and holes (j_p) considering only diffusion and drift is:

$$j_n = qD_n\vec{\nabla}n + q\mu_n nE \tag{2.29}$$

$$j_p = -qD_p\vec{\nabla}p + q\mu_p pE \tag{2.30}$$

and the total current (j):

$$j = j_n + j_p \tag{2.31}$$

2.3 Excess charge carrier kinetics

The distribution of charge carriers described above (2.1) is valid for thermal equilibrium. But the semiconductor can be submitted to the influence of external sources that can change the population of charge carriers due to the injection or extraction of them. In that situation, the distribution function changes. The total number of charge carriers for no equilibrium conditions can be expressed as:

$$n = n_0 + \Delta n\,, \qquad p = p_0 + \Delta p \tag{2.32}$$

Δn and Δp are the concentration of excess electrons and holes respectively. The introduction of quasi Fermi levels (E_{F_n} for electrons and E_{F_p} for holes) is convenient for the description of excess charge carrier kinetics [7]. For one dimensional dependence in the $x - direction$, E_{F_n} and E_{F_p} are defined by:

$$E_{F_n} = E_c\left(x\right) + kT\ln\left[\frac{n\left(x\right)}{N_c^*}\right] \tag{2.33}$$

$$E_{F_p} = E_v(x) - kT \ln\left[\frac{p(x)}{N_v^*}\right] \tag{2.34}$$

where $E_c(x)$ and $E_v(x)$ designate the position dependent energy of the bottom of the conduction band and the top of the valence band respectively. The quasi Fermi levels, different for electron and holes, replace the electro chemical potential for transport phenomena [6].

Under low injection level, after an external perturbation is switched off, the semiconductor will restore to thermal equilibrium and the distribution function relaxes again to the thermal equilibrium case with an unique Fermi level. This relaxation process induced by mechanisms which will be discussed in the next section (2.4) is described by the net recombination rate $U(n, p, n_0, p_0, t)$:

$$\frac{\partial \Delta n(t)}{\partial t} = -U(n, p, n_0, p_0, t) \tag{2.35}$$

and an effective relaxation time $\tau_{eff}(t)$:

$$U(n, p, n_0, p_0, t) = \frac{\Delta n(t)}{\tau_{eff}(t)} \tag{2.36}$$

If different relaxation mechanisms are active, the relaxation is described by the difference between the generation rates G_i and the recombination rates R_i for the different mechanisms:

$$U(n, p, n_0, p_0, t) = \frac{\Delta n(t)}{\tau_{eff}(t)} = \sum_i U_i(t) = \sum_i (G_i - R_i) \tag{2.37}$$

The summation is extended over all the possible mechanisms that lead to a generation-recombination process. A net-recombination rate U_i and a relaxation time τ_i can be attributed to every relevant mechanism:

$$U_i(t) = \frac{\Delta n(t)}{\tau_i(t)} \tag{2.38}$$

were τ_i denotes the characteristic time constant for the specific process i. For the total relaxation is valid:

$$\frac{\Delta n(t)}{\tau_{eff}(t)} = U(n, p, n_0, p_0, t) = \sum_i U_i(t) = \sum_i \frac{\Delta n(t)}{\tau_i(t)} \tag{2.39}$$

$$\frac{1}{\tau_{eff}(t)} = \sum_i \frac{1}{\tau_i(t)} \tag{2.40}$$

2.4 Charge carrier generation and recombination

A more detailed picture of excess charge carrier kinetics considers the specific generation and recombination processes. These processes are very important for the description of the behavior of a semiconductor out of thermal equilibrium because of an excitation by an external source and the relaxation processes which let it return to thermal equilibrium after the excitation.

2.4.1 Band-to-band generation-recombination

leading to a nett recombination expression:

$$U_{BB} = R_{BB} - G_{BB} = r_0 \left(np - n_i^2 \right) \tag{2.41}$$

It is called radiative or optical recombination (generation) when the energy emitted (absorbed) in the annihilation (formation) of an electron-hole pair is a photon.
It is called non-radiative or thermal recombination (generation) when the energy involved in the annihilation (formation) of an electron-hole pair is due the interaction with phonons, thermal vibration modes of the crystal.
In direct band gap semiconductor, the recombination does not implicate a change in momentum between the electron-hole in the excited state and the electron-hole in the relaxed state. Therefore, the energy emitted can present a minor momentum, that is a photon. Radiative recombination is the recombination mechanism used in devices such as LEDs, based on direct band gap semiconductor technology. For indirect band gap semiconductors, the recombination process implicates a change in momentum and the conservation laws needs the participation of an element which takes that momentum with; the phonon. The phonon is an harmonic expression for a vibrational mode of the crystal lattice.

2.4.2 Recombination through defects:

In most cases recombination takes place by defects. Defects act as effective trapping centers with an energy level within the band gap. In the simple case of a monoenergetic level excess electrons in the conduction band can, in

a first step, relax to that trapped energy-state and, secondly, to the valence band or in other words, a hole is trapped in the center, leading to a two step recombination process. In the same way, the first step can be hole trapping in a defect followed by electron trapping. In the most cases minority carrier trapping is the first step in an extrinsic semiconductor.
The formalism for defect recombination was developed by Shockley and Read [8] as well as by Hall [9] and is often referred to as Shockley-Read-Hall (SRH) recombination formalism.
Taking into account emission from the recombination center, the recombination rate U_{SRH} can be determined.

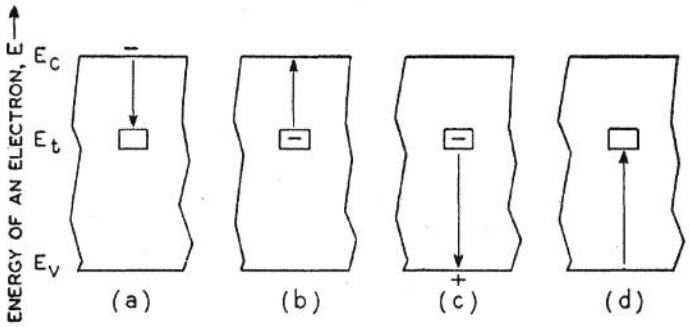

Figure 2.2: The basic processes involved in recombination by trapping: a) electron capture, b) electron emission, c) hole capture and d) hole emission (from [8]).

Following a statistical model, for a volume concentration of defects N_T with an energy level E_T, the net-recombination process U_{SRH} for a system out of thermal equilibrium has the expression in the steady state:

$$U_{SRH} = \frac{v_{th} N_T \left(np - n_i^2\right)}{\frac{1}{\sigma_p}\left(n + n_1\right) + \frac{1}{\sigma_n}\left(p + p_1\right)} \tag{2.42}$$

with

$$n_1 = n_i exp\left(\frac{E_T - E_i}{kT}\right), \qquad p_1 = n_i exp\left(\frac{E_i - E_T}{kT}\right) \tag{2.43}$$

where v_{th} is the average thermal velocity of electrons and σ_p and σ_n the capture cross sections of holes and electrons, respectively.

2.4.3 Surface recombination

Special attention has to be given to the surface characteristics of a semiconductor. On the surface, the crystal symmetries are broken and high densities of defects exist. The statistics of generation-recombination processes on surfaces can be described as an extension of the SRH formalism, but instead of using a monoenergetic intra-band level, a continuous distribution of trapping levels $D_{it}(E)$ is used [10, 11]. Moreover, generation-recombination rates depend on the local concentration of free charge carriers, therefore, surface generation-recombination processes depend on the surface concentration of electron and holes. In order to calculate the net-recombination rate, the contribution due to each surface state must be taken into account and an integration between the valence and conduction band must be carried out:

$$U_S = \left(n_s p_s - n_i^2\right) \int_{E_v}^{E_c} \frac{v_{th} D_{it}(E)\, dE}{\frac{1}{\sigma_p(E)}\left(n_s + n_1(E)\right) + \frac{1}{\sigma_n(E)}\left(p_s + p_1(E)\right)} \tag{2.44}$$

with n_s and p_s being the surface concentration of electron and holes, respectively.

2.4.4 Auger recombination

Auger generation is better called impact ionization for the case of semiconductors. Impact ionization implies a high energetic free charge carrier, an electron or a hole with a high kinetic energy, which gives part of that energy to the lattice generating an electron-hole pair, decreasing its kinetic energy but without recombining. Inversely, Auger recombination occurs when an electron-hole pair recombines and the energy loss is given to another free charge carrier in the form of kinetic energy. Auger processes require the presence of a third particle and the nett-recombination rate has the expression:

$$U_A = C_n\left(n^2 p - {n_i}^2 n\right) + C_p\left(n p^2 - {n_i}^2 p\right) \tag{2.45}$$

where C_n and C_p are the Auger recombination coefficients for the two-electrons/one-hole and two-holes/one-electron processes respectively.

2.5 Continuity equation

A continuity equation describes the conservation of a parameter [6]. For our purpose, the conservation of charge carriers is important:

$$\frac{\partial p}{\partial t} = -\frac{1}{q}\vec{\nabla}\vec{j_p} - R_p + G_p \tag{2.46}$$

$$\frac{\partial n}{\partial t} = \frac{1}{q}\vec{\nabla}\vec{j_n} - R_n + G_n \tag{2.47}$$

where R_p (R_n) represents the decay rate of holes (electrons), G_p (G_n) the generation rate of holes (electrons) (Eq. 2.37) and j_p (j_n) is the total electrical current of holes (electrons) due to diffusion and drift (Eq. 2.31). Because electrons and holes are charged particles, every movement of these particles is accompanied by a field change and so the Poisson equation must be taken into account [3]:

$$\frac{\partial p}{\partial t} = -p\mu_p\vec{\nabla}\vec{E} - \mu_p\vec{E}\vec{\nabla}p + D_p\vec{\nabla}\left(\vec{\nabla}p\right) - R_p + G_p \tag{2.48}$$

$$\frac{\partial n}{\partial t} = n\mu_n\vec{\nabla}\vec{E} + \mu_n\vec{E}\vec{\nabla}n + D_n\vec{\nabla}\left(\vec{\nabla}n\right) - R_n + G_n \tag{2.49}$$

$$\vec{\nabla}\vec{E} = \frac{\rho}{\epsilon} = \frac{q}{\epsilon}\left(p + N_D - n - N_A\right) \tag{2.50}$$

being ρ the charge density and ϵ the permitivity of the material. The field E in these equations refers to the total field, sum of a uniform external field and the internal field induced by charge carrier movements.
Solving this equation requires numerical calculation, but it can be simplified by some simple boundary conditions and an analytical solution can be found.

2.5.1 Continuity equation in a (quasi)-neutral region and ambipolar diffusion transport

Electrons and holes move with different velocities under drift or diffusive transport. The difference in the effective masses between electrons and holes leads to different mobilities and diffusion coefficients [1]. Thus, electrons and holes under diffusive transport present different distribution profiles in space and being charged particles, an internal field E_i between electrons and holes is built. This field, on the other hand, accelerates the particles which diffuse slower (usually the holes) and slows down the particles that diffuse faster

(the electrons).
Ambipolar diffusion is a macroscopic simplification for the electron-hole pair diffusion. It considers that both kinds of particles diffuse together with an equivalent diffusion coefficient D_{ap} [3]. The simplifications assumed in the ambipolar diffusion model are:

1. it will be restricted to one dimension dependence, $x - direction$ and it will assumed to be homogeneous in the z/y-directions.

2. low injection level $\Delta n, \Delta p << n_0 + p_0$ and a homogeneous distribution of charge carriers in thermal equilibrium $n_0 \neq n_0(x), p_0 \neq p_0(x)$.

3. Quasi neutrality is assumed. This implies that the local electric current is zero.

The third condition is the most important. If no external field is applied, electrons and holes move together, $\Delta n(x,t) = \Delta p(x,t)$, in fact by diffusion and drift (from the internal field) but their transport can be described by diffusion alone in a (quasi)neutral region characterized by a modified diffusion constant, the ambipolar diffusion constant D_{ap}:

$$j_p = j_n = \approx qD_{ap}\frac{\partial \Delta n}{\partial x} = qD_{ap}\frac{\partial \Delta p}{\partial x} \tag{2.51}$$

Being $D_{ap} = \frac{(p+n)D_nD_p}{pD_p+nD_n}$ the ambipolar diffusion constant which is the equivalent diffusion constant from a macroscopical point of view for electrons and holes diffusing as pairs [3].

It must be noted that the microscopic internal field due to electrons and holes is not zero. The corresponding voltage, the Dember voltage [12], can be measured by Surface Photo Voltage Measurements [13].

In this model, recombination and generation mechanisms are considered the same for holes and electrons, they are generated together and recombine together $R_n = R_p$ and $G_n = G_p$. Under these conditions, the continuity equation will be reduced to a unique form for both types of excess charge carriers:

$$\frac{\partial \Delta n}{\partial t} = \frac{\partial \Delta p}{\partial t} = D_{ap}\frac{\partial^2 \Delta n}{\partial x^2} - R + G \tag{2.52}$$

It is now considered the specific case of a semiconductor of a thickness d in the $x-direction$, perpendicular to the $zy-plane$. The boundary conditions at both surfaces are given by the surface recombination rates assumed to be proportional to the surface charge carrier concentration:

$$R_s^0 = S_0 \Delta n\,(x=0,t) \tag{2.53}$$

$$R_s^d = S_d \Delta n\,(x=d,t) \tag{2.54}$$

where S_0, S_d are the surface recombination velocities of front and back side respectively. In the case of the volume, the recombination rate is described by:

$$R_v\,(x,t) = \frac{\Delta n\,(x,t)}{\tau_v} \tag{2.55}$$

with τ_v the volume recombination time. The effective lifetime τ_{eff} of charge carriers can be considered as the parallel combination of the recombination processes in the volume and on the surface:

$$\frac{1}{\tau_{eff}} = \frac{1}{\tau_s^0} + \frac{1}{\tau_s^d} + \frac{1}{\tau_v} \tag{2.56}$$

The generation rate for the case of optical excitation is given by the Lambert-Beer law:

$$G\,(x,t) = \alpha F_0\,(t)\, e^{-\alpha x} \tag{2.57}$$

This general expression with a time dependent intensity amplitude $F_0\,(t)$ can describe different types of optical excitation as:

- **Stationary excitation.** The excitation source is not turned off and the system reaches a stationary regime under constant external excitation.

- **Pulsed excitation.** The excitation has a very short duration, in the limiting case a delta function $\delta\,(t)$ which generates excess charge carriers during a short time. It is used to study the relaxation processes in a time-resolved way.

- **Quasi-Steady-State excitation.** The system is excited by an intensive light pulse with a duration long compared to the relaxation times of the system. Knowing the time profile of the excitation pulse, the effective (quasi)-stationary life time is determined for a large range of excitation levels (QSSPC with determination of the photoconductance in the radio-frequency range).

- **Harmonic excitation.** The system is excited by an harmonically modulated source and its harmonic response is studied. The modulation frequency of the excitation is changed over a range of frequencies and the phase and amplitude of the response are studied.

2.5.2 Charge carrier profile under stationary conditions and illumination

The continuity equation for ambipolar diffusion under stationary conditions is reduced to:

$$0 = D_{ap}\frac{\partial^2 \Delta n}{\partial x^2} - \frac{\Delta n}{\tau} + \alpha F_0 e^{-\alpha x} \tag{2.58}$$

and the solution for the excess charge carriers has the form:

$$\Delta n\,(x) = Ae^{-\frac{x}{L}} + Be^{\frac{x}{L}} + \frac{F_0 \alpha \tau}{1-\alpha^2 L^2} e^{-\alpha x} \tag{2.59}$$

with $L = \sqrt{D_{ap}\tau}$ the diffusion length of excess charge carriers. The values A and B are constants depending on the boundary conditions:

1. **Case for a semiconductor with a thickness** $d >> L, \frac{1}{\alpha}$

   For illumination at $x = 0$, the boundary conditions can be defined as:

   $$\Delta n\,(x \to \infty) = 0 \qquad D_{ap}\left|\frac{\partial \Delta n}{\partial x}\right|_{x=0} = S\Delta n\,(x=0) \tag{2.60}$$

   and the charge carrier profile is given by:

   $$\Delta n\,(x) = \frac{F_0 \alpha \tau}{1-\alpha^2 L^2}\left(e^{-\alpha x} - \frac{\frac{s}{D_{ap}} + \alpha}{\frac{s}{D_{ap}} + \frac{1}{L}} e^{-\frac{x}{L}}\right) \tag{2.61}$$

2. **General case**

   The boundary conditions are given by the recombination rates on the surfaces:

   $$D_{ap}\left|\frac{\partial \Delta n}{\partial x}\right|_{x=0} = S_0 \Delta n\,(x=0) \qquad D_{ap}\left|\frac{\partial \Delta n}{\partial x}\right|_{x=d} = S_d \Delta n\,(x=d) \tag{2.62}$$

and the value of the B and A constants are:

$$B = \frac{F_0\alpha\tau}{1-\alpha^2L^2} \times \left[\frac{\left(\frac{D_{ap}}{L}+S_0\right)\left[e^{-\alpha d}\left(D_{ap}\alpha+1\right)-e^{-\frac{d}{L}}\left(\frac{D_{ap}}{L}+S_d\right)\right]}{\left[e^{\frac{d}{L}}\left(\frac{D_{ap}}{L}-S_d\right)\left(\frac{D_{ap}}{L}+S_0\right)-e^{-\frac{d}{L}}\left(\frac{D_{ap}}{L}-S_0\right)\left(\frac{D_{ap}}{L}+S_d\right)\right]}\right] \tag{2.63}$$

$$A = \frac{B\left(\frac{D_{ap}}{L}-S_0\right)}{\left(\frac{D_{ap}}{L}+S_0\right)} - \frac{F_0\alpha\tau}{1-\alpha^2L^2} \tag{2.64}$$

2.5.3 Time dependent solution after optical pulsed excitation

A time dependent solution of the continuity equation for a pulse generation function can be found by the use of Fourier analysis [14], [15].
This yields that the time and position dependent density of excess charge carriers can be described by an infinite superposition of harmonic (cos and sin) modes that independently exponentially decay with time:

$$\Delta n\left(x,t\right) = \sum_{m=1}^{\infty} A_m \cos\left(k_m x\right) e^{-\left(\frac{t}{\tau_m}\right)} + \sum_{n=1}^{\infty} B_n \sin\left(k_n x\right) e^{-\left(\frac{t}{\tau_n}\right)} \tag{2.65}$$

with A_m and B_n being the amplitudes of the m and n mode, respectively and τ_m and τ_n the characteristic decay time constant of the m and n mode, given by:

$$\frac{1}{\tau_m} = \left(D_{ap}k_m^2 + \frac{1}{\tau_v}\right) \tag{2.66}$$

and

$$\frac{1}{\tau_n} = \left(D_{ap}k_n^2 + \frac{1}{\tau_v}\right) \tag{2.67}$$

Imposing the boundary conditions (Eq. 2.62) on the surface and considering $m = n$, the following equation for k_m must be satisfied:

$$\tan\left(k_m d\right) = \frac{k_m D_{ap}\left(S_1+S_2\right)}{k_m^2 D_{ap}^2 - S_1 S_2} \tag{2.68}$$

$$k_m d = \arctan\left(\frac{S_1}{k_m D_{ap}}\right) + \arctan\left(\frac{S_2}{k_m D_{ap}}\right) + k_m \pi \tag{2.69}$$

with d being the thickness of the wafer and S_1 and S_2 the surface recombination velocities at the surfaces.
For long enough times, the prevailing mode is the mode with the longest time constant and corresponds to the first mode (the fundamental mode with $m = 1$) and the effective decay time is:

$$\frac{1}{\tau_{eff}} = D_{ap} k_1^2 + \frac{1}{\tau_v} = \frac{1}{\tau_{S_1}} + \frac{1}{\tau_{S_2}} + \frac{1}{\tau_v} \tag{2.70}$$

and thus:

$$D_{ap} k_1^2 = \frac{1}{\tau_{S_1}} + \frac{1}{\tau_{S_2}} = \frac{1}{\tau_s} \tag{2.71}$$

being $\tau_s = D_{ap}^{-1} k_1^{-2}$ the effective surface decay constant. Considering simple boundary conditions, the relation can be simplified:

- Symmetry: $S_1 = S_2 = S$

  $$\tan(k_1 d) = \frac{k_1 D_{ap} 2S}{\left(k_1^2 D_{ap}^2 - S^2\right)} \tag{2.72}$$

  and by use of eq. 2.69

  $$\tan\left(\frac{k_1 d}{2}\right) = \frac{S}{k_1 D_{ap}} \tag{2.73}$$

  For the case that the surface recombination is very small, $\tan\left(\frac{k_1 d}{2}\right) \approx \left(\frac{k_1 d}{2}\right)$ and thus:

  $$\frac{1}{\tau_s} = \frac{2S}{d} \tag{2.74}$$

  For the case that both surfaces are a sink for excess charge carriers ($S \to \infty$) and $\tan\left(\frac{k_1 d}{2}\right) \to \infty$, thus:

  $$\frac{1}{\tau_s} = \frac{D_{ap} \pi^2}{d^2} \tag{2.75}$$

- One of the surfaces has surface recombination S ($S_1 = S$) and the other is a sink ($S_2 = S \to \infty$)

  $$\tan(k_1 d) = -\frac{k_1 D_{ap}}{S} \tag{2.76}$$

for the case that the surface recombination is very small at the first (illuminated) surface ($S \to 0$), $(k_1 d) \to -\pi/2$ and thus:

$$\frac{1}{\tau_s} = \frac{D_{ap}\pi^2}{4d^2} \tag{2.77}$$

From an experimental point of view it is important to note that the final decay after pulsed excitation is due to decay from the fundamental mode and characterized by τ_{eff} from Eq. 2.70

2.6 Space charge capacity and space charge capacity regimes

A Metal-Insulator-Semiconductor device, MIS-device, consists of an insulator with a defined thickness and dielectric constant in close contact with a semiconductor. The Semiconductor-Insulator structure is contacted on both extreme surfaces by a metal contact to polarize it. The metal-semiconductor contact is supposed to be ideally ohmic and current can easily flow through it, injecting or extracting free charge carriers, while the insulator-metal interface is supposed to be blocking and no faradaic current can flow through it. These structures have been extremely important for the development of electronic devices and also, for the study the surface characteristics of semiconductors.
The capacity C is a magnitude which evaluates the charge accumulated on the surface of a material under polarization and is defined by:

$$C = \left|\frac{dQ}{dV}\right|_s \tag{2.78}$$

where Q is the charge in the semiconductor and V the surface potential.
This section will focus on the calculation of the semiconductor capacity in contact with an insulator. In order to simplify the problem a series of assumptions are taken:

1. The interface semiconductor-insulator is ideally flat, infinite in the lateral (YZ plane) and homogeneous. The properties of the system will only depend on the $x - direction$, perpendicular to the semiconductor-insulator (YZ) plane.end on the $x - direction$, perpendicular to the semiconductor-insulator (YZ) plane.

2. All impurities present in the semiconductor are homogeneously distributed.

3. In a first approximation, the influence of the surface states will be neglected.

4. The study will be developed for an extrinsic semiconductor in the ionized impurities regime.

5. The field in the bulk of the semiconductor ($x = \infty$) will be zero, the (quasi)-neutral region, and it is taken as reference for the potentials and energies. The influence of an applied voltage and the band bending of the energy bands is restricted to in a region adjacent to the semiconductor-insulator interface called the space charge region with a thickness W_{sc}.

For $\Psi(x)$, the potential in the semiconductor at position x, the following equations and boundary conditions are assumed:

$$\psi(x) = -\frac{E_i(x) - E_i(\infty)}{q} = -\frac{E_c(x) - E_c(\infty)}{q} = -\frac{E_v(x) - E_v(\infty)}{q} \tag{2.79}$$

$$\Psi(x = \infty) = 0 \tag{2.80}$$

$$\Psi(x = 0) = \Psi_s \tag{2.81}$$

being Ψ_s the potential at the interface insulator-semiconductor. Ψ_s is the potential at the interface semiconductor-insulator, E_i, E_c and E_v are the intrinsic, conduction and valence energies of the semiconductor. The potential is conventionally chosen as positive if the energy of the conduction band is below the value in the bulk (that is far away enough from the surface) and negative the other way around. A field in the space-charge zone will modify the density of free charge carriers. Electrons and holes will drift until the field is compensated by the new distribution of charge carriers. This can be expressed as a bending in the conduction and valence band energies which describes the new density profile of charge carriers:

$$E_c(x) = E_c(\infty) - q\psi(x), \qquad E_v(x) = E_v(\infty) - q\psi(x) \tag{2.82}$$

for an extrinsic semiconductor under stationary conditions:

$$n(x) = N_C^* \, e^{\frac{E_F - (E_C - q\psi(x))}{kT}} = n_0 e^{\frac{q\psi(x)}{kT}} \tag{2.83}$$

$$p(x) = N_V^* \, e^{-\frac{E_F - (E_V - q\psi(x))}{kT}} = p_0 e^{-\frac{q\psi(x)}{kT}} \tag{2.84}$$

being n_0 and p_0 the density of electrons and holes in the quasi neutral region ($x = \infty$). The charge present in a material can be calculated using the Poisson equation:

$$\vec{\nabla}\vec{E} = \frac{\rho}{\epsilon} \tag{2.85}$$

being ϵ the permittivity of the semiconductor. In one dimension this yields:

$$\frac{d^2\psi(x)}{dx^2} = -\frac{\rho(x)}{\varepsilon} \tag{2.86}$$

The density of charge present in a semiconductor will be given by:

$$\rho(x) = q(N_D - N_A + p(x) - n(x)) \tag{2.87}$$

N_D and N_A are the density of donors and acceptors, respectively, and $n\,(x)$ and $p\,(x)$ are position dependent. In the (quasi)-neutral region (volume), the total charge is zero, thus:

$$\rho(\infty) = 0 = q(N_D - N_A + p(\infty) - n(\infty)) = q(N_D - N_A + p_0 - n_0) \tag{2.88}$$

$$N_D - N_A = n_0 - p_0 \tag{2.89}$$

Consequently in the (quasi)neutral region, volumes charge of the ionized impurities is totally compensated by electrons and holes in the conduction and valence bands ($N_D = n_0$ and $N_A = p_0$). Introducing these relations into the Poisson equation the following differential equation is found:

$$\frac{d^2\psi(x)}{dx^2} = -\frac{q}{\varepsilon}\left(n_0 - p_0 + p(x) - n(x)\right) = -\frac{q}{\varepsilon}\left[p_0(e^{-\frac{q\psi(x)}{kT}} - 1) - n_0(e^{\frac{q\psi(x)}{kT}} - 1)\right] \tag{2.90}$$

Using the differential relation $\frac{d^2\psi(x)}{dx^2} = \frac{1}{2}\frac{d}{dx}\left(\frac{d\psi(x)}{dx}\right)^2 \cdot \frac{dx}{d\psi}$ and introducing the reduced potential $\psi^*(x) = \frac{q\psi(x)}{kT}$, the Poisson equation simplifies to:

$$\frac{d}{dx}\left(\frac{d\psi^*}{dx}\right)^2 \cdot dx = -2 \cdot \frac{q^2}{kT\varepsilon}\left[p_0(e^{-\psi^*} - 1) - n_0(e^{\psi^*} - 1)\right] \cdot d\psi^* \tag{2.91}$$

Integrating the equation from the bulk position to the position x:

$$\int_\infty^x \frac{d}{dx}\left(\frac{d\psi^*}{dx}\right)^2 \cdot dx = -2 \cdot \frac{q^2}{kT\varepsilon}\int_0^{\psi^*}\left[p_0(e^{-\psi^*} - 1) - n_0(e^{\psi^*} - 1)\right] \cdot d\psi^* \tag{2.92}$$

$$\left(\frac{d\psi^*}{dx}\right)^2 |_x - \left(\frac{d\psi^*}{dx}\right)^2 |_\infty = -2 \cdot \frac{q^2}{kT\varepsilon} \left[p_0(-e^{-\psi^*} - \psi^*) - n_0(e^{\psi^*} - \psi^*)\right]_0^{\psi^*} \tag{2.93}$$

Using the relation between electrical field and potential:

$$E(x) = -\frac{d\psi(x)}{dx}, \;\; E(x)^2 = \left(\frac{d\psi(x)}{dx}\right)^2 = \left(\frac{kT}{q}\right)^2 \left(\frac{d\psi^*(x)}{dx}\right)^2 \tag{2.94}$$

introducing the boundary conditions (Eq. 2.80) and combining Eqs. 2.93 and 2.94, an expression for the field can be obtained:

$$\left(\frac{d\psi^*}{dx}\right)^2 |_x = \left(\frac{q}{kT}\right)^2 E(x)^2 = 2 \cdot \frac{q^2}{kT\varepsilon} \left[p_0(e^{-\psi^*} + \psi^* - 1) + n_0(e^{\psi^*} - \psi^* - 1)\right] \tag{2.95}$$

$$E\,(x) = \pm \sqrt{2 \cdot \frac{kT}{\varepsilon} \left[p_0(e^{-\psi^*} + \psi^* - 1) + n_0(e^{\psi^*} - \psi^* - 1)\right]} \tag{2.96}$$

The positive sign is taken for $\Psi^* > 0$ and the negative sign for $\Psi^* < 0$. Introducing the bulk Debye Length defined as:

$$L_B = \sqrt{\frac{\varepsilon kT}{q^2(n_0 + p_0)}} \tag{2.97}$$

and evaluating the equation on the surface, the field on the surface has the value:

$$E_s = \pm \frac{kT}{q} \frac{1}{L_B} \sqrt{\frac{2}{(n_0 + p_0)} \left[p_0(e^{-\psi_s^*} + \psi_s^* - 1) + n_0(e^{\psi_s *} - \psi_s^* - 1)\right]} \tag{2.98}$$

The total charge existing in the semiconductor can be calculated integrating the density of charge through the semiconductor volume and using the Gauss relation:

$$Q_{sc} = \int_0^\infty \rho(x) \cdot dx = \int_0^\infty \left(\frac{d}{dx}\left(\varepsilon E\right)\right) \cdot dx = \varepsilon E(\infty) - \varepsilon E(0) = -\varepsilon E_s \tag{2.99}$$

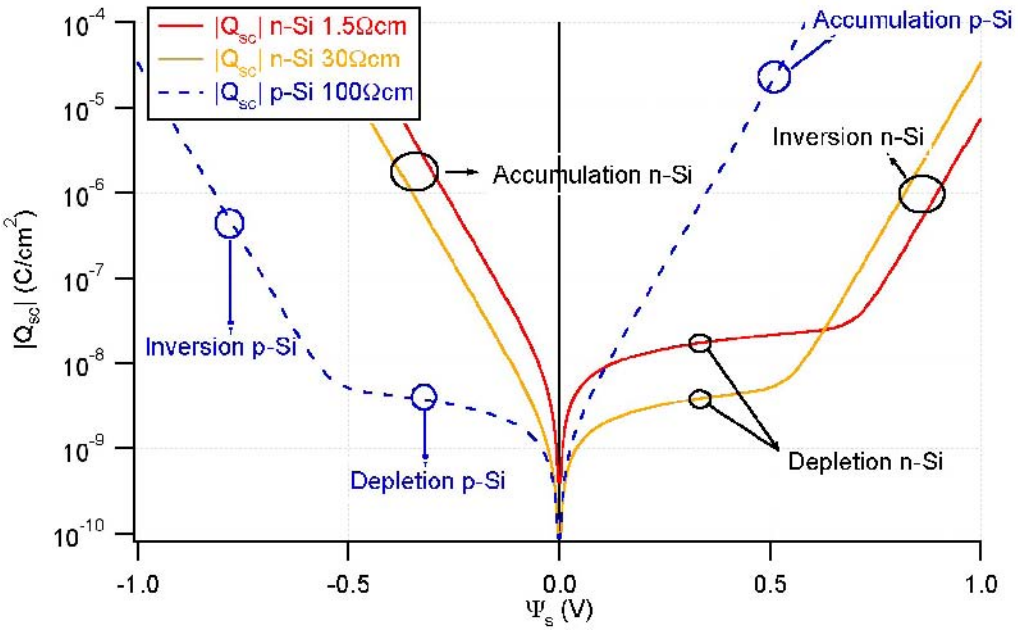

Figure 2.3: Logarithmic plot of the modulus of Q_{sc} as function of the surface potential. Q_{sc} is simulated for three different semiconductors: $nSi-1.5\Omega cm$, $nSi-30\Omega cm$ and $pSi-100\Omega cm$. The ranges indicated (inversion, depletion, accumulation) are mentioned at the end of this section. The sign of the surface potential has been taking following the electrochemical convention.

$$Q_{sc} = \mp \frac{kT}{q}\frac{\varepsilon}{L_B}\sqrt{\frac{2}{(n_0+p_0)}\left[p_0(e^{-\psi_s^*}+\psi_s^*-1)+n_0(e^{\psi_s*}-\psi_s^*-1)\right]} \quad (2.100)$$

Note that the charge calculated is the result of an integration over the semiconductor length, normalized to the surface on the $ZY-plane$ (in C/cm^2). The charge for $\Psi_s^* > 0$ will be negative and for $\Psi_s^* < 0$ will be positive. In Fig.2.3 modulus of Q_{sc} against surface potential is calculated for semiconductors with different doping characteristics. The different charge regimes described in section 2.6 are indicated.

Now C_{sc} can be calculated:

$$C_{sc} = \mid \frac{dQ_s}{d\psi_s} \mid = \frac{\varepsilon}{2L_B}\sqrt{\frac{2}{(n_0+p_0)}} \left| \frac{\left[p_0(-e^{-\psi_s^*}+1)+n_0(e^{\psi_s*}-1)\right]}{\left[p_0(e^{-\psi_s^*}+\psi_s^*-1)+n_0(e^{\psi_s*}-\psi_s^*-1)\right]^2} \right| \tag{2.101}$$

The space charge capacity can be simplified for specific potential regimes [16]. Defining the potential difference between the intrinsic energy level in the semiconductor and the Fermi level:

$$u_b = \frac{E_F - E_i}{kT} \tag{2.102}$$

1. **Strong accumulation:** $|\psi_s^*| > 4$. The accumulation regime is characterized by the accumulation of majority charge carriers on the surface, responsible for the uncompensated charge present in the semiconductor. It must be distinguished between n and p type semiconductor:

   - n-type ($\psi_s^* > 0$)

   $$C_{sc} = \frac{\varepsilon}{2L_B}\sqrt{\frac{2}{(n_0+p_0)}} \cdot n_0 e^{\frac{\psi_s*}{2}} \tag{2.103}$$

   - p-type ($\psi_s^* < 0$)

   $$C_{sc} = \frac{\varepsilon}{2L_B}\sqrt{\frac{2}{(n_0+p_0)}} \cdot p_0 e^{-\frac{\psi_s*}{2}} \tag{2.104}$$

2. **Flat band:** $|\psi_s^*| = 0$. This regime occurs when no band bending is present in the semiconductor, the concentration of charge carriers is the same in the bulk as on the surface and the total charge within the semiconductor is zero.

   $$C_{sc} = \frac{\varepsilon}{L_B} = C_{FB} \tag{2.105}$$

3. **Depletion:** $|u_b| > 2$, $2 < |\psi_s^*| < 2\,|u_b| - 2$. This regime corresponds to those potentials in which majority charge carriers are swept away from the surface and only a small concentration of minority charge

carriers accumulate on the surface (n-type ($\psi_s^* < 0$), p-type ($\psi_s^* > 0$)). The main contribution to the charge is due the uncompensated ionized impurities present in the semiconductor.

$$C_{sc} = \mid \frac{dQ_s}{d\psi_s} \mid \approx \frac{\varepsilon}{L_B} \sqrt{\frac{1}{2 \cdot (|\psi_s^*| - 1)}} \tag{2.106}$$

The Mott-Schottky relation uses this approximation for the calculation of the doping density in a semiconductor:

$$\left(\frac{1}{C_{sc}}\right)^2 = 2\left(\frac{L_B}{\varepsilon}\right)^2 (|\psi_s^*| - 1) = \frac{2}{q\varepsilon\,(n_0 + p_0)} \left(|\psi_s^*| - \frac{kT}{q}\right) \tag{2.107}$$

4. **Inversion:** $|\psi_s^*| > 2\,|u_b| + \log|u_b| + 3$. Minority charge carriers accumulate on the surface and are mainly responsible for the charge in the semiconductor.

   - n-type ($\psi_s^* < 0$)

   $$C_{sc} = \frac{\varepsilon}{2L_B} \sqrt{\frac{2}{(n_0 + p_0)}} \cdot p_0 e^{-\frac{\psi_s^*}{2}} \tag{2.108}$$

   - p-type ($\psi_s^* > 0$)

   $$C_{sc} = \frac{\varepsilon}{2L_B} \sqrt{\frac{2}{(n_0 + p_0)}} \cdot n_0 e^{\frac{\psi_s^*}{2}} \tag{2.109}$$

In Fig.2.4 C_{sc} is calculated as function of the surface potential for semiconductors with different doping characteristics. The different capacity regimes here described are indicated.

It is important to note that for accumulation, flat band and depletion the response of the semiconductor to an applied voltage is only determined by the majority carriers and for the experiments treated in this work infinitely fast. However, in inversion this response is also (and in strong inversion exclusively) determined by the minority carriers. The corresponding response is not infinitely fast and must be taken into account.

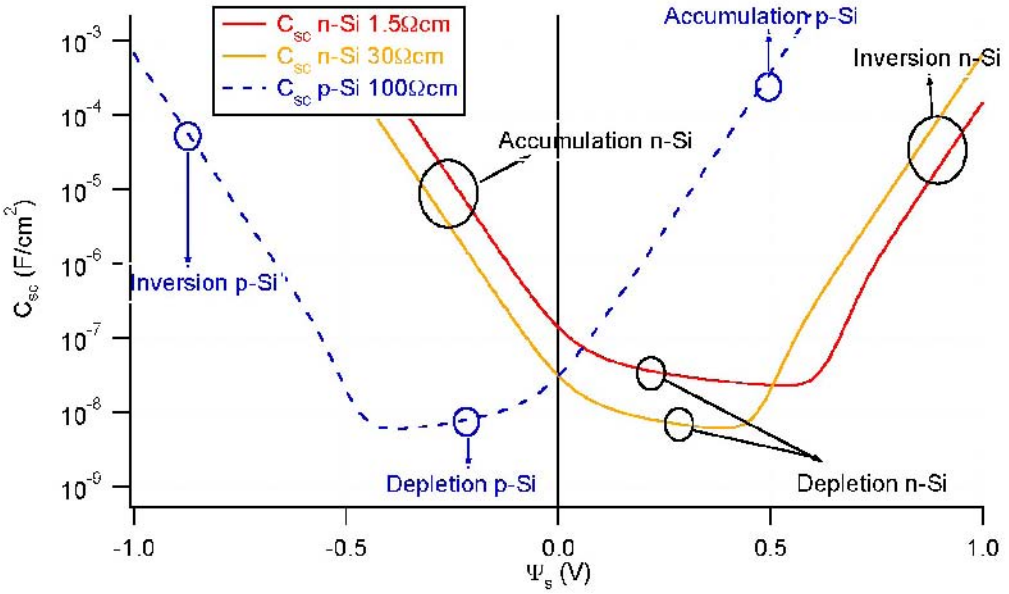

Figure 2.4: Logarithmic plot of C_{sc} as function of the surface potential. C_{sc} is simulated for three different semiconductors: $nSi - 1.5\Omega cm$, $nSi - 30\Omega cm$ and $pSi - 100\Omega cm$. The capacity ranges mentioned in this section are indicated. The sign of the surface potential is taken following the electrochemical convention.

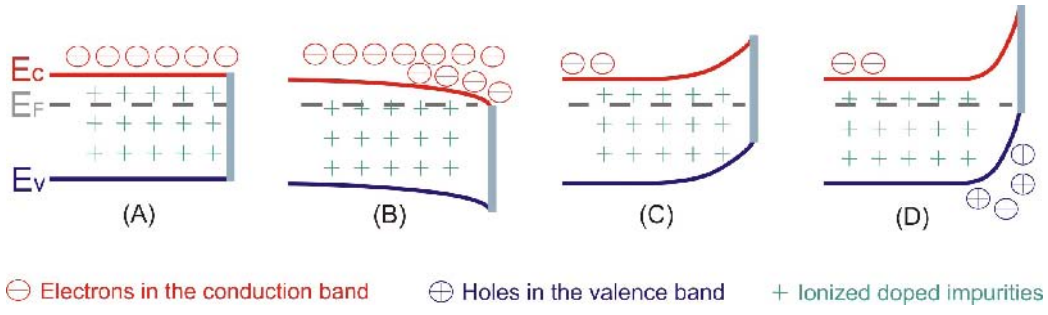

Figure 2.5: Energy band diagram for an n-type doped semiconductor at the different regimes: (A) Flat band, (B) Strong accumulation, (C) Depletion and (D) Inversion. The conduction band is plotted in red line, the valence band in blue line and the Fermi energy level in dashed gray line.

Chapter 3

MIS devices and semiconductor-liquid junction

Real MIS devices present a density of defect states D_{it} due to non-saturated bonds on the interfacial region semiconductor/insulator. These defect states can be positively or negatively charged depending on their nature and they present a total interfacial charge density Q_{it} which depend on the Fermi energy level. Moreover, the insulator layer can posses a fixed charge, Q_f or a mobile ionic charge within its volume. These extra charges modify the characteristics of an ideal MIS device.

In the last section a brief description of the semiconductor/electrolyte junction is given.

3.1 Real MIS devices and Interface Traps

Interface defect states are of different nature, donor or acceptor, according to its charge contribution. Donor interface states contribute with a positive charge when not occupied by an electron and neutral when an electron is trapped. Acceptor interface states are neutral when empty and negative while filled by an electron. The number of defects on the interface is very high and their energy levels are so closely spaced in energy over the semiconductor bandgap that their distribution can be approximated with a continuous profile. $D_{it}^{d}(E)$ and $D_{it}^{a}(E)$ are the distributions of donor-like and acceptor-like interface states with respect to their energy.
The total charge due to interface states Q_{it} is calculated by integrating the product of the interface states density with its occupation level distribution

over the bandgap:

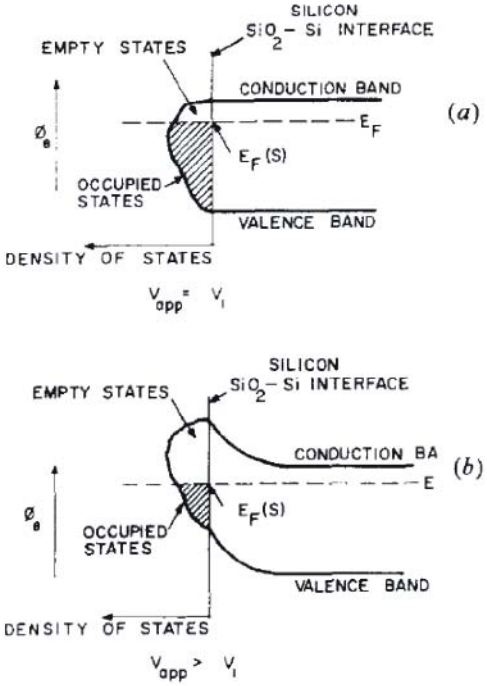

Figure 3.1: Illustration of the energy distribution of interface states of a MOS device. The change in the occupancy level under stationary conditions due to a stationary polarization: a) flatband potential, b) depletion regime (from [17]).

$$Q_{it} = q \int_{E_v}^{E_c} \left[D_{it}^{d}(E) \cdot (1 - f_d(E)) - D_{it}^{a}(E) \cdot f_a(E) \right] dE \tag{3.1}$$

where f_d and f_a is the occupancy levels for donor and acceptor like interface states in non thermal equilibrium:

$$f_d(E) = \frac{\sigma_{cd}(E) \cdot n_s + \sigma_{nd}(E) \cdot p_1}{\sigma_{cd}(E)(n_s + n_1) + \sigma_{nd}(E)(p_s + p_1)} \tag{3.2}$$

$$f_a(E) = \frac{\sigma_{na}(E) \cdot n_s + \sigma_{ca}(E) \cdot p_1}{\sigma_{na}(E)(n_s + n_1) + \sigma_{ca}(E)(p_s + p_1)} \tag{3.3}$$

where n_s and p_s are the density of electrons and holes at the semiconduc-

tor/insulator interface, respectively. n_1, p_1 are given by:

$$n_1(E) = n_i e^{\frac{(E-E_i)}{kT}}, \quad p_1(E) = n_i e^{\frac{(E_i-E)}{kT}} \tag{3.4}$$

$\sigma_{ni}(E)$ and $\sigma_{ci}(E)$ are the capture cross sections for electrons and holes, respectively. The second sub index ($i = a, d$) distinguishes between donor and acceptor like trapping states. There are two capture cross-sections for each type of defects (donor and acceptor-like) which distinguish the capture by a neutral charged state and the capture by a charged state which includes a Coulomb interaction. The Coulomb cross section is some orders of magnitude greater than the neutral case, enhancing the probability of capture when a defect is charged.

The concentrations n_s and p_s do not correspond to the thermal equilibrium case. As indicated in the previous chapter (section 2.3), excitation of a semiconductor (by light) induces a splitting of the Fermi level in two (quasi)Fermi-levels and $(np - n_i^2) \neq 0$. This fact happens as well in steady state situations, where the semiconductor is brought to a new equilibrium by an external perturbation (such as a temperature change or voltage polarization change) as in transient situation by a pulsed perturbation. For these cases the occupancy levels of the interface states must be described by f_a and f_d.

In thermal equilibrium, (as shown in Fig.3.1) with $(np - n_i^2) = 0$, the occupancy of the interface states is given by the Fermi distribution [7],[16], thus:

$$f_a = f_d = f \tag{3.5}$$

As simplification, averaged values and non-energy dependent cross sections, σ_n and σ_c, can be taken for an evaluation of Q_{it}.
Q_{it} is dependent on the surface potential (implying the dependence on n_s and p_s). The capacity due to interface states is given by:

$$C_{it}(\psi_s) = \frac{dQ_{it}(\psi_s)}{d\psi_s} = q \int_{E_v}^{E_c} \left[D_{it}^d(E) \cdot \left(1 - \frac{df_d}{d\psi_s}\right) - D_{it}^a(E) \cdot \frac{df_a}{d\psi_s} \right] dE \tag{3.6}$$

This capacitance is parallel combined (see section 4.1.2) with the semiconductor capacitance, C_{sc}; both are polarized under the same surface potential. The surface potential determines the semiconductor space charge capacity and the occupation levels for the interface states. The interface states and

semiconductor share the same Fermi level under stationary conditions. Thus, the total capacity at the interface C_s is:

$$C_s(\psi_s) = C_{sc}(\psi_s) + C_{it}(\psi_s) \tag{3.7}$$

and the charge density at the interface Q_s is the total charge contribution from both parallel elements:

$$Q_s(\psi_s) = Q_{it}(\psi_s) + Q_{sc}(\psi_s) \tag{3.8}$$

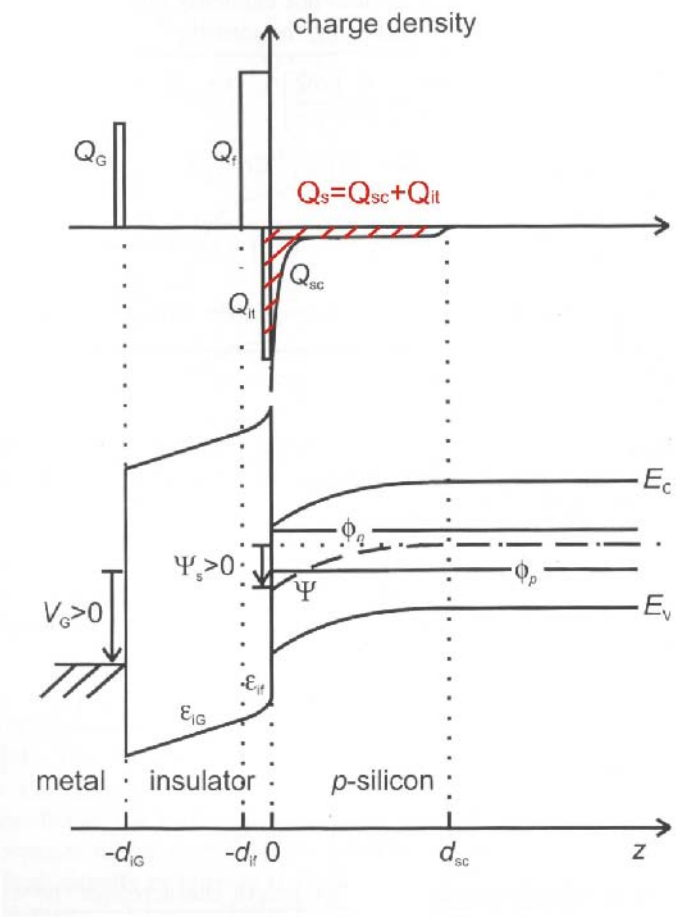

Figure 3.2: Charge density distribution and energy band diagram of a MIS device based on a p-type semiconductor (from [18]).

Q_s is potential dependent and must be actively compensated by the charge present at the gate electrode Q_G. Q_G is a direct accessible parameter

and can be modified by the variation of the gate potential V_G. The neutrality of charge in the MIS system leads to:

$$Q_G(V_G) + Q_f + Q_{it}(\psi_s) + Q_{sc}(\psi_s) = 0 \tag{3.9}$$

where Q_f is the fixed charge present in the insulator, it is not voltage dependent and as simplification is considered uniformly distributed at the edge of the insulator/semiconductor interface. This fixed charge is of great importance for the field effect passivation on semiconductor surfaces. What remains is the relation between V_G (the experimentally controllable parameter) and ψ_s, which is the induced surface potential at the insulator/semiconductor interface. The potential drop in an ideal plane-parallel capacitor is:

$$\Delta V_i = \frac{Q}{C_i} \tag{3.10}$$

being Q the "mirror" charge accumulated on both extremes of the insulator. Thus, the gate potential V_G is related to the surface potential ψ_s:

$$V_G = \psi_s + \Delta V_i + \phi_{ms} = \psi_s + \frac{Q_f + Q_{it}(\psi_s) + Q_{sc}(\psi_s)}{C_i} + \phi_{ms} \tag{3.11}$$

with ϕ_{ms} the potential difference between the metal gate work function and the electron affinity of the semiconductor.

In contrast to the interface charge density that depends on the Fermi level position, the fixed charge in the insulator shows no voltage dependence. The determination of the flatband potential can lead to an estimation of the fixed charge present in the insulating layer. Considering that at the flat band potential the density of charge due to interface states is negligible compared to the fixed charge in the insulator ($Q_{it}(\psi_s = 0) << Q_f$).

$$V_{fb} = \phi_{ms} + \frac{Q_{sc}(\psi_s = 0) + Q_{it}(\psi_s = 0) + Q_f}{C_i} \approx \phi_{ms} + \frac{Q_f}{C_i} \tag{3.12}$$

3.2 The Si/SiN_x and Si/SiO_2 interface

In MIS devices, the transition from the semiconductor to the insulator leads to a discontinuity in the material characteristics, located at the interface between them. Different structural defects are present at this interface. The crystal periodicity of the silicon wafer is abruptly broken. Stretched and

dangling silicon bonds are present at the semiconductor surface. The atoms of the insulating layer interact chemically with the silicon dangling bonds leading sometimes to its passivation [19]. After the successful passivation of the silicon surface by the growth of SiO_2, silicon could be stabilized and used as a transistor [20].
The electrical characteristics of an insulator/semiconductor interface like in a MIS structure are mainly determined by the interface state density D_{it}. The presence of dangling bonds of different nature introduce permitted energy levels in the bandgap of the semiconductor. These permitted states are located at the interface or in the near region to the interface (depending on its quality).
The Si/SiN_x and Si/SiO_2 interface are different, even when sharing the same silicon characteristics (silicon dangling and stretched bonds). The chemical bonds of the silicon atoms with the atoms of the insulating layer differ for O and N. This leads to different interface state density characteristics.

A brief description of the models existing for the distribution of interface states proposed for Si/SiO_2 and Si/SiN_x interfaces is given.

3.2.1 The Si/SiO_2 interface

Füssel et al. have proposed a distribution of interface states D_{it} as function of the energy position for the Si/SiO_2 interface [21], [22], [23]. The defects present at the interface are of different chemical nature and contribute independently to the D_{it} as illustrated in the scheme in Fig. 3.3.

There are mainly two types of defects that contribute to the D_{it}, the intrinsic and the extrinsic ones.
The $(Si_3) \equiv Si - Si \equiv (Si_3)$ stretched bonds and the $(Si_3) \equiv Si^0$ dangling bonds are called the intrinsic defects since they are caused only by imperfections of the silicon lattice. These defects can be donor or acceptor like and the literature suggests that only the silicon dangling bonds act as recombination center [21]. The surface states which originate from the stretched bonds contribute to D_{it} in a Boltzmann-like distribution (exponential-U_T) with the maximum values at the edges of the band gap. The intrinsic silicon dangling bonds induce a broad double peaked distribution with the maximum at the band gap edges and a valley between them (with minimum around the middle of the band gap, U_M). This U_M-distribution has been approximated by a constant D_{it} value in several publications [7], [18].

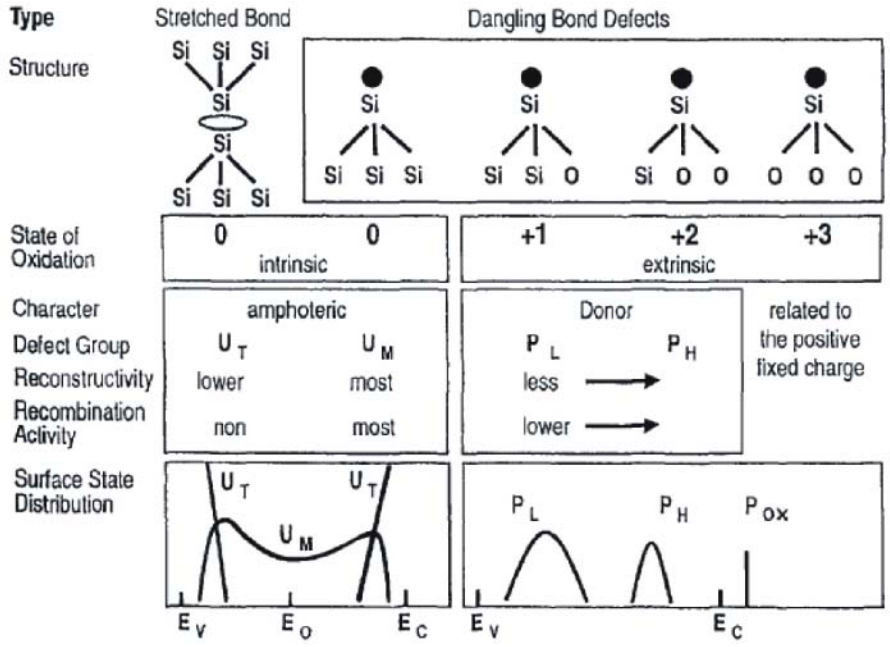

Figure 3.3: Proposed defect model for the Si/SiO_2 interface from [21]

The dangling bonds coming from the partially oxidized silicon are called extrinsic dangling bonds. There are three types of extrinsic dangling bonds: $Si_2O \equiv Si^0$ and $SiO_2 \equiv Si^0$, which lay in the Si band gap, and $O_3 \equiv Si^0$, which is situated energetically above the conduction band. The energetic distribution of these defects becomes narrower with the number of Oxygen atoms bond to the silicon. This is due to from the higher electronegativity of the Oxygen atom.
The intra band defects can be approximated by two donor-like gaussian D_{it} distributions (P_L and P_H). The gaussian distribution due to the $Si_2O \equiv Si-$ defect (P_L) is energetically located in the lower part of band gap. The $SiO_2 \equiv Si-$ one (P_H) is located slightly above the middle of the energy gap [23], [24].

The $O_3 \equiv Si-$ dangling bond, above the conduction band, is under thermal equilibrium conditions unoccupied and contributes with a positive charge. This dangling bond is related to the fixed charge Q_f at the Si/SiO_2 interface.

3.2.2 The Si/SiN_x interface

The Si/SiN_x interface is expected to show the same intrinsic silicon defects as the Si/SiO_2 interface. The extrinsic defects originate this time from the presence of $Si-N$ bonds.

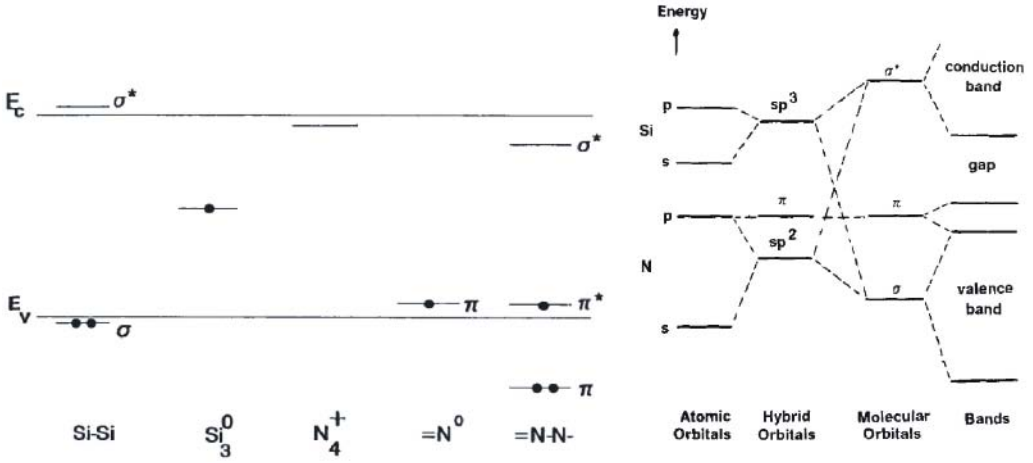

Figure 3.4: On the left side, an scheme for the energy levels and occupancies for the $Si-Si$ bond, the neutral Si and N dangling bonds, the $=N-N-$ and the N_4^+ groups (from [25]) present in Si_3N_4. On the right side, an scheme of the development of the orbitals and bands in Si_3N_4 (from [26]).

The SiN_x layer, deposited by PECVD, is an amorphous material with a high density of dangling bonds even in the bulk structure. During the SiN_x deposition by PECVD, Hydrogen from the precursors (SiH_4 and NH_3) is incorporated in the layer. Depending on the deposition conditions the content of Hydrogen can be up to 40mol % [27]. The SiN_x layers deposited in the present work have about 20% content of H [28].
Defects due to Hydrogen are present at the interface even though it is known that Hydrogen also plays an important role for the passivation of defects by saturating the free dangling bonds. This Hydrogen passivation is weak and unstable [25], [22].

The energy levels and possible dangling bonds in non-hydrogenated amorphous (stoichiometric) Si_3N_4 are mainly Si and N dangling bonds as illustrated in Fig. 3.4. Their energetic position is plotted in relation to the valence and conduction bands of the insulating material [25]. The orbitals in

the Si_3N_4 volume originate from the combination of the sp^3 hybrid orbitals of the Si atoms with the sp^2 hybrid orbitals of the N atoms forming the $Si-N$ bondings (σ) and antibondings (σ^*) orbitals. When extending the orbitals from a single molecule to a periodic structure the molecular σ orbital form the valence band and σ^* the conduction band. The Si_3N_4 band gap is estimated to be about $5.3eV$.

The incorporation of hydrogen into the amorphous material passivates the $Si-$ and $N-$ related dangling bonds forming the ($\equiv Si-H$), ($=N-H$) and ($=N-N-H$) compounds with binding energies outside the Si_3N_4 band gap. The energy characteristics of the dangling bonds have been calculated by the tight-binding method [26], [25].

At the Si/SiN_x interface the silicon related dangling bonds play a major role in the formation of the interface states. Three kinds of extrinsic defects from the combination of Si and N atoms can provide a $Si-$ dangling bond: $SiN_2 \equiv Si-$, $Si_2N \equiv Si-$ and $N_3 \equiv Si-$. In contrast to the Si/SiO_2 interface, the energetic position of these extrinsic dangling bonds with respect to the Si (semiconductor) conduction and valence band is not well clarified in the literature.

The most extended studies involving amorphous hydrogenated SiN_x are related to the metal-nitride-oxide-semiconductor structures (MNOS) which are extensively used in electronic charge storage devices and thin film transistors [29].

The microscopical view of the memory effect in the SiN_x layer is still not perfectly understood. It is well known that the charge fixed in the SiN_x can be modified by the injection or emission of charge carriers from the Si to the SiN_x volume, tunneling through the thin SiO_2 layer. This can be controlled by polarizing the Si into strong accumulation or strong inversion regime as illustrated in Fig. 3.5. In the absence of external polarization, the charge configuration within the SiN_x remains stable for long enough times and can be used as a "memory". SiN_x presents different dangling bonds which are candidates to be responsible of this charge (memory) trapping.

One model suggests from the study of SiN_x by electron spin resonance (ESR) measurements that the $N_3 \equiv Si^0$ group is responsible for the charge storage characteristics in the MNOS structures. This group has been named

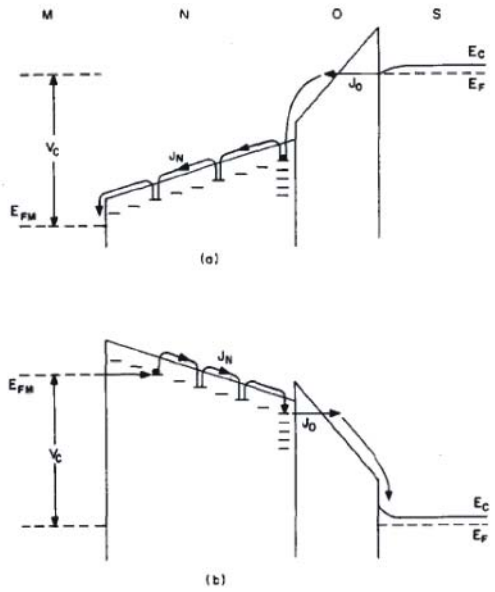

Figure 3.5: Energy band diagram of a MNOS structure under (a) positive bias and (b) negative bias, from [29].

in the literature the K-center [30] or the T-center [31] and would explain the absence of a paramagnetic signal in SiN_x with injected carriers [32]. The K-center can have three different electronic configurations as schematized in Fig. 3.6: it can be negatively charged if the orbital is occupied by two electrons, neutrally charged if occupied by one electron and positively charged if not occupied. This K-center can trap electrons as well as holes.

Another model suggests that the $Si - Si$ bond is responsible for the charge trapping. Experiments in amorphous SiN_x with a high content of silicon present an enhancement of electron and hole trapping [33]. In SiO_2 the traps are mainly present by oxygen vacancies as $Si - Si$ bonds. Amorphous Si_3N_4 has a similar electronic structure and in a similar way, nitrogen vacancies would favor the $Si - Si$ bond formation responsible of the memory effect as shown in Fig. 3.7. This bond has been found by XPS measurements [34] at the SiN_x/SiO_2 interface in MNOS and ONO structures. This bond is proposed to be formed by the incorporation of oxygen in the SiN_x as follows [35]:

$$2 \equiv Si_3N + 2O \rightarrow 2 \equiv Si_2O + 2 \equiv Si^0 + 2N \tag{3.13}$$

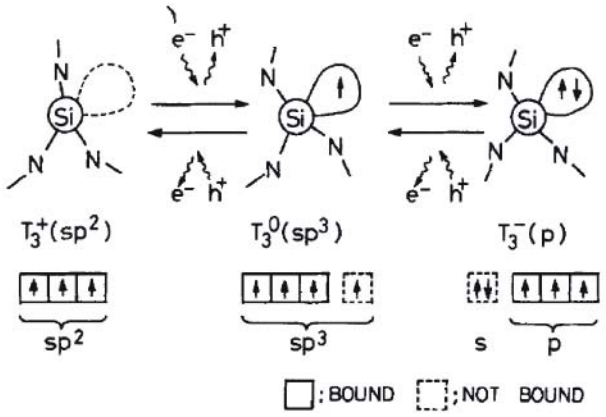

Figure 3.6: Model for transition of the dangling bonds among three charged states: positive, neutral and negative, symbolized by T_3^+, T_3^0, T_3^-, respectively, after [31].

where the $2 \equiv Si^0$ is a bond with three possible electronic configurations depending on the electronic occupation as indicated in Fig. 3.7.

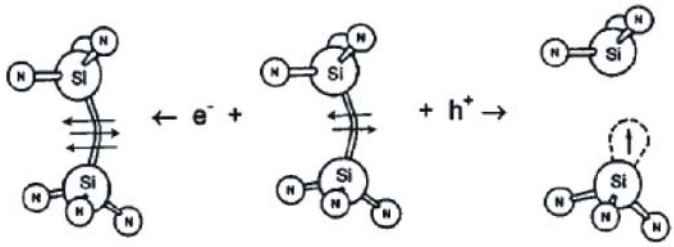

Figure 3.7: Atomic model of amphoteric neutral diamagnetic $Si - Si$ defect with electron and hole capturing in SiN_x from [35].

This bond can trap electrons and holes and is not in disagreement with the one proposed in [31].

3.3 Semiconductor-liquid junctions

In the MIS model, the insulator/semiconductor heterojunction is contacted by an ohmic contact at the rear side of the device, at the semiconductor,

and a metallic contact at the front side on top of the insulating layer, the gate electrode. The gate electrode can be substituted by an aqueous or aprotic electrolyte in which a counter electrode (Platinum, Carbon, Gold) is submerged to close the circuit. In this type of device, in principle an electrochemical cell, charge transfer through the semiconductor/liquid junction takes place in form of an oxidation or reduction reaction with chemical species in the electrolyte or the solvent itself [36], [37].
This does not mean that chemical reactions could not take place at solid state devices but this is usually an unwanted side or degradation process. The strong leakage currents in dielectrics for example lead to such changes in its chemical composition that modify its useful properties.
In an electrochemical system the only way to transport an electron or hole to the counter electrode is by the change of the oxidation state of a molecule in the liquid by a transferred charge from the semiconductor.

Electrochemical devices are of high interest in several fields like electrochemical sensor applications, high power batteries [38], transformation of solar energy into electricity (as solar cells) [39], store solar energy in the form of chemical fuels [38] (as hydrogen formation [40]), purification of waste water or micromachining semiconductor surfaces [18].
There have to be differentiated between an reduction or oxidation process, depending on the type of charge carrier present at the semiconductor surface. A reductive reaction will take place when the semiconductor transfers an electron into the electrolyte and an oxidative reaction will take place when a hole is transferred. Being the electrolyte composed by different chemical species, there are several possibilities for the charge carriers from the semiconductor to be transfered. Depending on the redox potential of all chemical species and the Fermi level position in the system one chemical reaction is more probable than other. In Fig. 3.8 the redox energy levels of different chemical species is represented together with the energy position of the conduction and valence bands of different semiconductors.

Chemical redox energy levels are usually referred with respect to the standard hydrogen electrode which is taken as origin of the electrochemical scale. The potential of this reaction is determined to be $-4.44V$ at $298K$ with respect to the absolute scale (an electron at rest in vacuum) [41].

Next to the classical reversible redox systems like I^-/I_3^-, $Fe(CN)_6^{3-}/Fe(CN)_6^{4-}$ or Fe^{2+}/Fe^{3+} which can accept charges without corroding the

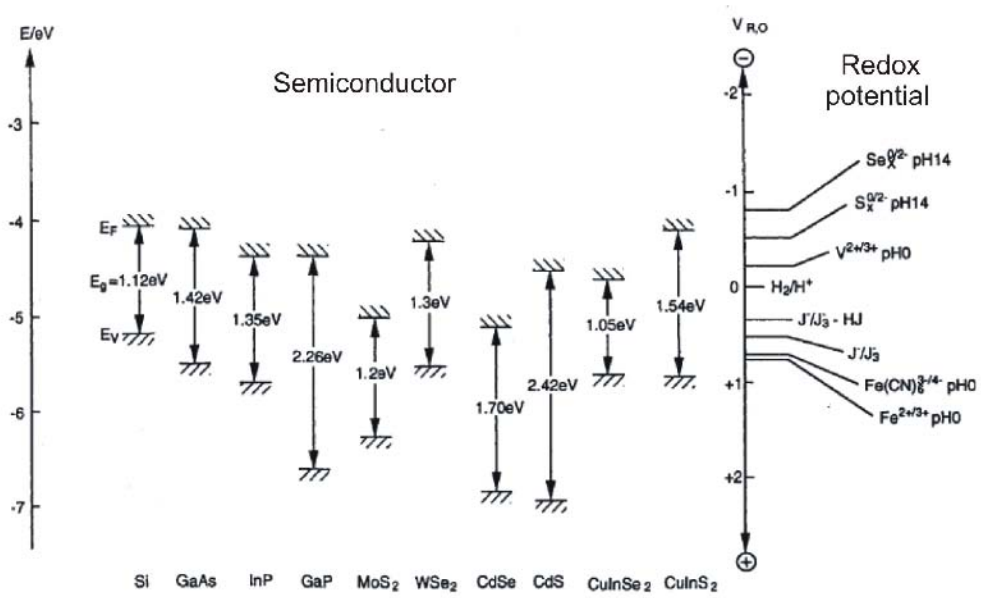

Figure 3.8: Redox energy levels for different chemical species represented in reference to the NHE potential (right axis). Conduction and valence bands energy positions of different semiconductors are given referred to the absolute scale (left axis). Both scales are graphically coordinated being the NHE potential $-4.44V$ respect the absolute scale.

semiconductor, also the water solvent itself can be oxidized or reduced forming oxygen or hydrogen respectively [42].
The conduction and valence band of the semiconductor and the redox potentials of the electrolyte and ions have to be chosen carefully due to the amount of possible side reactions in an electrochemical cell e.g. the semiconductor itself can be attacked by chemical species (as when water oxidation leads to oxygen formation that rapidly reacts corroding the semiconductor surface [43]).
Another possibility to avoid semiconductor corrosion would be to protect it by a thin insulating layer which would still enable the charge transfer through it (electrons or holes) but not the attacking chemical species [40].

A semiconductor/electrolyte redox reaction for an electron can be formulated as a transfer between an occupied energy level in the semiconductor and a vacant one of a chemical species present in the electrolyte. An electron

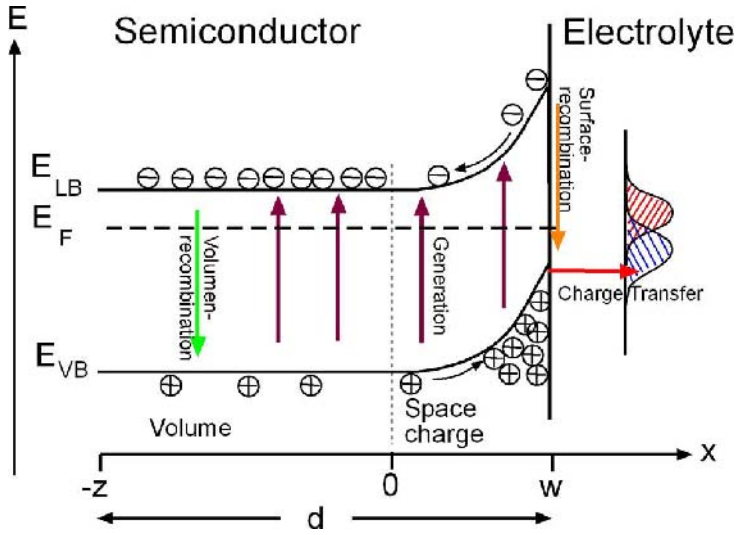

Figure 3.9: Energy band diagram for a semiconductor in contact with an electrolyte. E_{LB} and E_{VB} refers to conduction and valence band of the semiconductor respectively. At the electrolyte side the energy distribution for a redox species is represented. The colored arrows represent possible charge carriers transfer.

in the semiconductor conduction band relaxes into a lower unoccupied energy level from the chemical species. The electronic energy levels of isolated ions or molecules are localized but in an electrolyte have a broad Gaussian shaped energetic distribution which finds its origin in the different energetic interactions with other species in the electrolyte. These Gaussian energetic distributions are centered on the most probable energy level in the reduced (E^0_{red}) and oxidate (E^0_{ox}) state of the species as shown in Fig. 3.10. An species is in its reduced state when an electron occupies its reduced energy level and in its oxidized if an electron occupies its oxidation state [41].

The E^0_R value is the average electron energy for a given species. Under thermal equilibrium, the standard redox Fermi level $E_{F,redox}$ of an electrolyte (equivalent to the Fermi level in the semiconductor) depends on the concentration of reduced and oxidized species in the electrolyte:

$$E_{F,redox} = E^0_{F,redox} - kT \ln\left(\frac{c_{ox}}{c_{red}}\right) \tag{3.14}$$

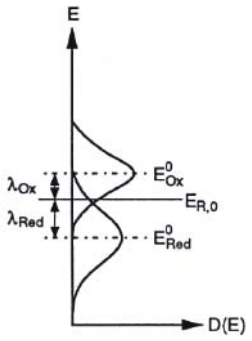

Figure 3.10: Density distribution of oxidation and reduction energetic states for a chemical specie in an electrolyte. The standard redox Fermi level lies between the energy with the maximum density of oxidation states and the energy with the maximum reduction states.

with c_{ox} and c_{red} the concentration in the electrolyte of oxidized and reduced species in the electrolyte respectively.

When a semiconductor is put in contact with an electrolyte, electrons are exchanged between the semiconductor and the electrolyte until the equilibrium is reached where the Fermi level of the semiconductor is equal to the standard redox Fermi level of the electrolyte. This usually induces a certain surface potential at the semiconductor surface.

Chapter 4

Methods and instrumentation

4.1 Impedance analysis

4.1.1 Linear circuit and linear elements

An electrical circuit is a closed path in which current can flow. It is called linear circuit if it can be described by a linear differential equation . Very often, real electronic systems are not linear and in order to study them, small signal perturbation techniques are useful to approximate its behavior by a linear system for specific working conditions.

Linearization for a real system: Real systems do not usually present a linear relation between current and voltage; however, the system can be linearized around a working voltage V_0 for a small perturbation voltage v_p

$$V = V_0 + v_p \tag{4.1}$$

$$I(V) = I(V_0 + v_p) \simeq I(V_0) + \frac{dI(V)}{dV}|_{V_0} \cdot v_p \tag{4.2}$$

with

$$\frac{dI(V)}{dV}|_{V_0} \simeq \frac{I(V_0 + v_p) - I(V_0)}{v_p} \tag{4.3}$$

Truncating the Taylor series after the first order power yields the linearization of a function. Thus, for a small voltage range around V_0, the current can be approximated by an expression linearly dependent on the perturbation voltage.

Linear elements of a circuit: The elements present in a linear electronic circuit are called linear elements and can be active or passive. Active elements are the voltage and current sources, elements that give energy to the system. The potentiostat is the main energy source, able to apply voltages or currents through the circuit of study. The passive elements present in the circuit are the ones that consume or store the energy applied by the sources. In a linear circuit these are simplified to resistors, inductors, and capacitors:

- **Resistor, R:** This element is related to the loss of energy due to the opposition of a material to a current flow. The characteristic parameter the resistance R is given by Ohm's law:

$$R \equiv \frac{V_1 - V_2}{j} = \frac{v\,(t)}{j\,(t)} = R_{cte} \tag{4.4}$$

  with $j\,(t)$ the current through the resistor and $v\,(t)$, the voltage drop between the two extremes of the resistor. An ideal resistor does not introduce any temporal dependence between voltage and current, it is the proportionality factor between them.

- **Capacitor, C:** This element represents the charge that can be stored by a material when voltage is applied between its extremes. The current in a capacitor is due to the movement of bound charges and is called a displacement current. It is a charging/discharging current, which in contrast to a faradaic current, does not involve a charge crossing through the capacitor material. The charge accumulated in a capacitor due to a displacement current is defined by:

$$q_c\,(t) = \int_{-\infty}^{t} i_c\left(t^{'}\right) dt^{'} \tag{4.5}$$

  being $i_c\left(t^{'}\right)$ the displacement current at a certain time $t^{'}$. The characteristic parameter the capacity C is the proportionality factor between the accumulated charge and the voltage applied between the extremes of the capacitor:

$$q_c\,(t) = C \cdot v\,(t) \tag{4.6}$$

  the change in accumulated charge $q_c\,(t)$ is modified due to a displacement current.

$$\frac{dq_c\,(t)}{dt} = C\frac{dv\,(t)}{dt} = i_c\,(t) \tag{4.7}$$

  if the applied voltage is constant, the (stationary) displacement current $i_c\,(t)$ is zero.

- **Inductor, L:** An inductor is a circuit element that represents the magnetic effects of a current. A linear approximation of Faraday's induction law determines the inductance L:

$$v(t) = L\frac{di_L(t)}{dt} \tag{4.8}$$

The electro-magnetic characteristics of a material (in a linear approximation regime) can be characterized by the combination of these three elements (R, C and L).

4.1.2 Complex notation and combination of impedances

If a sinusoidal voltage, $V(t) = v_t \cos \omega t$, is applied to the linear circuit elements defined above, the following relations are found:

- Resistor, R: $i(t) = \frac{1}{R} v_t \cos(\omega t)$
- Capacitor, C: $i(t) = \omega C v_t \cos\left(\omega t - \frac{\pi}{2}\right)$
- Inductor, L: $i(t) = \frac{\omega}{L} v_t \cos\left(\omega t + \frac{\pi}{2}\right)$

The current that flows through a resistor is completely in phase with the voltage perturbation applied, while the current that flows through a capacitor is $-\frac{\pi}{2}$ shifted respect to the potential perturbation and for an inductor the phase shift is $\frac{\pi}{2}$. Under sinusoidal polarization, capacitor and inductors elements do induce a voltage drop between their extremes, analogous to a resistor, but moreover, do shift the phase of the current response flowing through them.
The Euler notation, in the complex plane, simplifies these trigonometric relations:

$$\cos(\varphi) = \frac{e^{i\varphi} + e^{-i\varphi}}{2} \tag{4.9}$$

$$\sin(\varphi) = \frac{e^{i\varphi} - e^{-i\varphi}}{2i} \tag{4.10}$$

$$i = \sqrt{-1} = e^{i\frac{\pi}{2}} \tag{4.11}$$

The impedance ($Z \in \mathbb{C}$) is defined as the quotient $Z = \frac{v(t)}{i(t)}$. Therefore, the impedance of the linear elements is

- Resistor, R: $Z_R = \frac{v(t)}{i(t)} = R$

- Capacitor, C: $Z_C = \frac{v(t)}{i(t)} = \frac{i}{\omega C}$
- Inductor, L: $Z_L = \frac{v(t)}{i(t)} = i\omega L$

This notation can simplify the calculation of problems related to linear circuits but in order to find the physical meaning, magnitude and time dependence, of voltage and current must be projected in the real part again

$$i\left(t\right) = Re\left[\frac{v\left(t\right)}{Z}\right] \tag{4.12}$$

$$v\left(t\right) = Re\left[i\left(t\right)Z\right] \tag{4.13}$$

Combination of impedances For the combination of impedances ($Z \in \mathbb{C}$) series and parallel configuration can be distinguished:

- **Series configuration:** the current that flows through each single element i is the same; in this case, the potential drop due to each of the impedances is given by:

$$v_i\left(t\right) = Re\left[i\left(t\right)Z_i\right] \tag{4.14}$$

$$v_t\left(t\right) = \sum_i v_i\left(t\right) = Re\left[i\left(t\right)\sum_i\left(Z_i\right)\right] = Re\left[i\left(t\right)Z_t\right] \tag{4.15}$$

$$Z_t = \sum_i Z_i \tag{4.16}$$

- **Parallel configuration:** the potential drop over each single element i is the same; in this case, the current that flows through each single element is given by:

$$i_i\left(t\right) = Re\left[\frac{v\left(t\right)}{Z_i}\right] \tag{4.17}$$

$$i_t\left(t\right) = \sum_i i_i\left(t\right) = Re\left[v\left(t\right)\sum_i\left(\frac{1}{Z_i}\right)\right] = Re\left[v\left(t\right)\left(\frac{1}{Z_t}\right)\right] \tag{4.18}$$

$$\frac{1}{Z_t} = \sum_i \frac{1}{Z_i} \tag{4.19}$$

4.2 Modulation frequency dependence of the MIS capacitance

The emission and capture of electrons and holes by interface states has a characteristic time constant. This implies that the whole system needs a certain time period to reach the stationary equilibrium after a change in the energy position of the Fermi level.
For harmonic voltage perturbation of a fixed frequency, MIS $C_T - V_G$ measurements can fall into the two extreme cases of high (C^{hf}) and low (C^{lf}) frequency behavior:

4.2.1 High frequency perturbation

For the case that the frequency is faster than the characteristic capture-emission time of a trapping level, there is no C_{it} contribution to the total measured capacity. Even though the direct polarization (DC), for a slow enough scanning sweep velocity, does reach the stationary case for the interface states charge contribution, the AC modulation does not. The gate electrode compensates the DC charge coming from the interface states, leading to a stretch-out of the ideal MIS device C-V characteristics against gate potential but with no C_{it} contribution. Time response of trapping levels is much slower than the characteristic time of the thermal generation of minority charge carriers. It is understood that for sufficiently high modulation frequencies where C_{it} can not be directly measured, neither it can the inversion capacity contribution be determined experimentally.

$$C_T^{hf} = \frac{C_i C_{sc}^{hf}}{C_i + C_{sc}^{hf}} \tag{4.20}$$

$$Q_G = -\left(Qsc + Qit + Q_f\right) \tag{4.21}$$

$$V_G = \psi_s + \frac{Qsc + Qit + Q_f}{C_i} \tag{4.22}$$

therefore, deriving by ψ_s

$$C_{it}\left(\psi_s\right) = C_i \left[\left(\frac{d\psi_s}{dV_G}\right)^{-1} - 1\right] - C_{sc}^{hf}\left(\psi_s\right) \tag{4.23}$$

This method needs to determine $V_G\left(\psi_s\right)$. A numerical comparison between an ideal MIS device curve and the real MIS sample measurement must be

done. From the ideal MIS device the relation between capacity and surface potential can be calculated. Relating the gate voltages with the surface potentials for the same capacity values (ideal and the measured), the displacement in gate voltage due to the charge of the interface states can be estimated.

4.2.2 Low frequency perturbation

In this case, the modulation frequency is sufficiently slow to modify the Fermi level energy position under stationary conditions. This time the contribution to the total capacity due to the interface states is measurable. Thus:

$$C_T^{lf} = \frac{C_i \left(C_{sc}^{lf} + C_{it}\right)}{C_i + C_{sc}^{lf} + C_{it}} \tag{4.24}$$

The expressions for Q_G and V_G remain the same as in the high frequency case (Eqs.4.21,4.22) since they are referred as DC variables.

4.2.3 Intermediate frequency perturbation

This situation takes place for the frequency range between the low and high frequency extremal cases. It exhibits a partial interface states capacity contribution. Only those interface states which have an emission/capture characteristic time smaller than the modulation period, contribute to the C_{it}. This range of frequencies can help to distinguish "'faster"' from "slower" energy level traps. Impedance-spectroscopy is a useful measuring technique to identify the characteristic time constant of a specific energy interface state.

4.2.4 Extraction of Interface Trap Properties by the high-low frequency capacitance method

Interface state capacity can be calculated experimentally if two $C-V$ measurements are performed at the same MIS device, one at high frequency modulation and the second one at low frequency modulation. For C_{it} extraction, only the C_i value is needed and that can be experimentally determined by measuring the total capacity under strong accumulation conditions. By

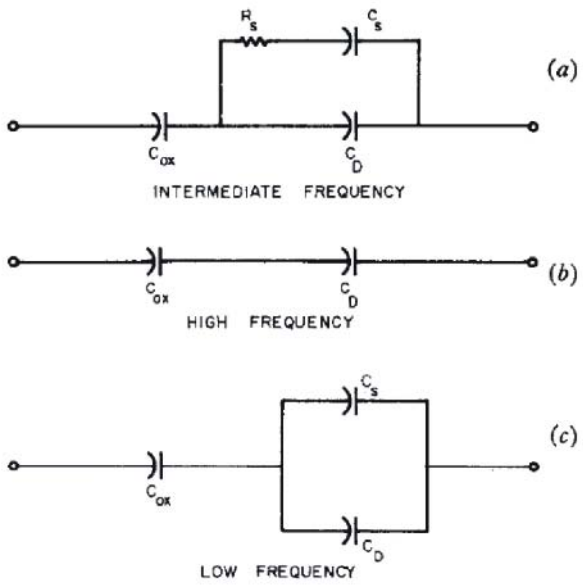

Figure 4.1: Equivalent circuits for MIS devices with interface states for a) intermediate frequency and partial AC contribution from the interface states, b) high frequency and no contribution from interface states and c) low frequency and total contribution from interface states. Illustration taken from [17]

combination of Eq. 4.24 and 4.20 and considering that under accumulation/depletion regimes $C_{sc}^{hf} = C_{sc}^{lf}$, C_{it} can be extracted by the use of:

$$C_{it} = \left(\frac{1}{C_T^{lf}} - \frac{1}{C_i}\right)^{-1} - \left(\frac{1}{C_T^{hf}} - \frac{1}{C_i}\right)^{-1} \tag{4.25}$$

This C_{it} evaluation is only valid for accumulation/depletion regime and the C_{it} obtained is in reference to that gate potential. It is not necessary to calculate the relation between V_G and ψ_s by the use of a simulation. But, in order to obtain $D_{it}(E)$, the $V_G(\psi_s)$ dependence must be known as well as $\psi_s(E_c)$.

As mentioned previously, another uncertainty is introduced in inversion regime due to the characteristic generation lifetime of minority charge carriers. For the measured C_T^{hf} there is no AC evidence of minority charge carrier contribution to the space charge capacity and no evidence for interface states

capacity whereas for the C_T^{lf} both contribute to the total capacity and can not be distinguished experimentally.

In Fig. 4.2 it is given an example of the high and low capacity curves as function of the applied potential for a MIS device with a random distribution of interface states. The calculation by the high-low capacitance method gives an interface state density as a function of the potential at the gate electrode which is not that easily related to the energy position.

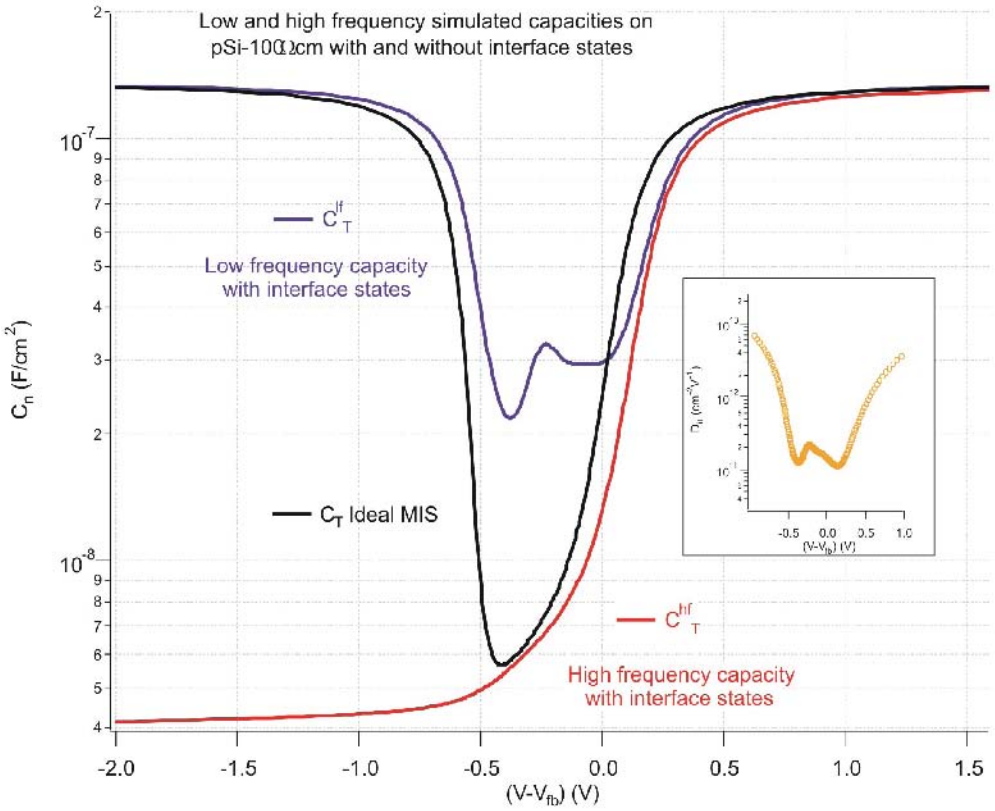

Figure 4.2: High (red line) and low (purple line) capacity curves as function of the applied potential for a simulated $pSi - 100\Omega cm$ with a series capacitor $C_i = 140nF/cm^2$ and a random distribution of interface traps. The black line is the capacity for the ideal case without the presence of interface states. In the insert is given the D_{it} curve extracted by use of Eq. 4.25

4.3 Microwave conductance methods

Although electrical impedance measurements yield information directly related to the functioning of MIS devices, it is important to determine separately, by complementary measuring techniques, the relevant processes in the semiconductor part of these devices such as charge carrier transport. The study of charge carrier transport under the influence of an applied potential or excess charge carrier kinetics induced by optical excitation is essential for optoelectronic devices.
An adequate tool to study such characteristics is offered by (photo)-conductivity measurements. Moreover, non-invasive, contactless measurements are advantageous because the influences of contacts are discarded. This can be achieved by the measurement of the absorbed power of an electromagnetic wave by the media under investigation as illustrated in Fig. 4.3.

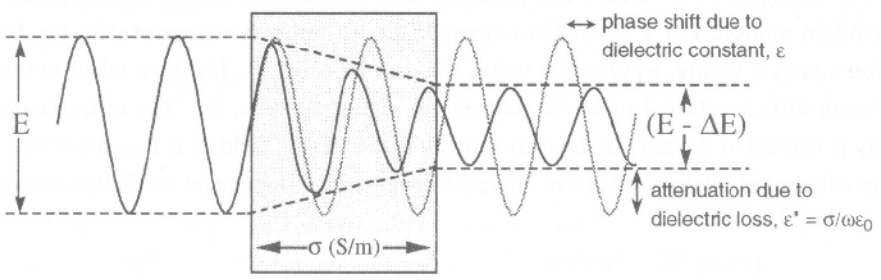

Figure 4.3: Schematic representation of the attenuation (and phase shift) of the microwaves when propagating through a (weakly) conducting dielectric medium.

The free charge carrier absorption is given by the product of the conductivity and the square of the electric field strength. This absorption and so the conductivity can be determined from reflection or from transmission measurements. It must be noted that at high frequencies (at room temperature) above 100GHz the conductivity becomes frequency dependent. This can be described by a frequency dependent mobility. In the most simple model (the Drude model) this frequency dependence is characterized by the momentum exchange time τ_m which is in the order of $10^{-11}s$ or less in semiconductors at room temperature [44]. This implies that conductivities measurements i.e. lower than $100GHz$ (or still lower frequencies) yield a conductivity independent of the frequency. Besides, the mobilities obtained for some species from

these measurements are equal to the DC mobilities of this species.
These qualitative remarks are valid for band transport in semiconductors and certainly in silicon. For semiconductors with more complicated transport mechanisms (organic, amorphous, polymer semiconductors) a more detailed consideration of charge carrier transport is required.

Measuring techniques are available in different frequency ranges from radiofrequency up to the optical range. Most useful of them are the radiofrequency, microwave and terahertz (far infra red) frequency ranges. In these frequency ranges, the conductivity is measured via the free charge carrier absorption.

- Radiofrequency $(10 - 500\ MHz)$
- Microwave $(5 - 100\ GHz)$
- Teraherz-farIR $(0.1 - 10\ GHz)$

The advantages of the microwave measurements are based on the independence of the conductivity σ on the frequency ω of the electromagnetic field, so that the microwave (photo)conductivity is equal to the DC (photo)conductivity.

4.3.1 Theory and experimental considerations

Microwave reflection conductivity measurements are contactless conductivity measurements. The microwave radiation is absorbed, transmitted and reflected by materials. Its frequency range makes it ideal for the study of semiconductor materials due to its low energy because it does not produce a band to band excitation but interacts with the mobile charge carriers present in a continuous density of states in the conduction and valence bands.
Being $P(\sigma)$ the microwave power reflected by a measuring cell containing a material with a conductivity σ, the change in power reflection due to a small conductivity change $\Delta\sigma$ can be approximated by a linear relation

$$P(\sigma + \Delta\sigma) \approx P(\sigma) + \frac{dP(\sigma)}{d\sigma}\Delta\sigma \tag{4.26}$$

therefore the change induced in the reflected power is represented by:

$$\Delta P(\Delta\sigma) = P(\sigma + \Delta\sigma) - P(\sigma) \approx \frac{dP(\sigma)}{d\sigma}\Delta\sigma \tag{4.27}$$

Normalization to $P(\sigma)$, the unperturbed microwave reflected power, yields

$$\frac{\Delta P(\Delta\sigma)}{P(\sigma)} \approx \frac{dP(\sigma)}{d\sigma}\frac{\Delta\sigma}{P(\sigma)} \tag{4.28}$$

The sensitivity factor S is defined as

$$S = \frac{dP(\sigma)}{d\sigma}\frac{1}{P(\sigma)} = \frac{dR(\sigma)}{d\sigma}\frac{1}{R(\sigma)} \tag{4.29}$$

and is the proportionality factor between the conductivity change $\Delta\sigma$ and the signal measured, the change in microwave reflected power $\Delta P(\Delta\sigma)$. This magnitude is normalized to the unperturbed microwave reflected power $P(\sigma)$ and can be related to the reflection coefficient $R(\sigma)$ by $P(\sigma) = P_{in}R(\sigma)$ with P_{in} the incident microwave power to the sample. Experimentally it is easier to measure $P(\sigma)$ in situ than P_{in}. $\Delta P(\Delta\sigma)/P(\sigma)$ is the signal acquired by the microwave excess conductance.
The sensitivity factor, in linear approximation, does only depend on the unperturbed characteristics of the media, and can be calculated from the reflection coefficient $R(\sigma)$. It is easier for the calculation of S to consider an ideal closed microwave system or short-circuit configuration for a sample of thickness d in the z direction, the propagation direction of the microwave wave. Short-circuit configuration implies that the cell containing the sample is closed by a metal plate totally reflecting the microwave. Therefore, the reflected microwave power is the difference between the incident one and the power dissipated by the medium:

$$P(\sigma) = P_{in} - A(\sigma) \tag{4.30}$$

being $A(\sigma)$ the absorbed microwave power. The absorption of an electromagnetic wave by a conductive media is given by:

$$A(\sigma) = \frac{1}{2}\int_0^d \sigma |E(\sigma, z)|^2 dz \tag{4.31}$$

In a first simplified case it will be considered that the conductivity σ is homogeneous for the whole media. The modulus of an electromagnetic wave propagating within a conductive media, presents an exponential decay with the form:

$$E(z) = E_0 e^{-\gamma z} \tag{4.32}$$

where E_0 is the electrical field at position $z = 0$ and γ the complex propagation constant for a conductive media [45]. In a rectangular wave guide with

inner dimensions Wx$(W/2)$ (suitable for the methods used at the present work), the complex propagation constant γ for the principal transverse electric mode is given by [46], [47]:

$$\gamma = \left[\left(\frac{\pi}{W} \right)^2 - \omega^2 \mu_0 \epsilon_0 \epsilon_r + i\omega\mu_0\sigma \right]^{\frac{1}{2}} \tag{4.33}$$

being ϵ_r the relative permittivity of the material, ϵ_0 (μ_0) the permittivity (permeability) of the free space and ω the angular frequency of the propagating electromagnetic wave.
If there is a change in the conductivity $\Delta\sigma$, the absorbed power changes to

$$A(\sigma + \Delta\sigma) = \frac{1}{2} \int_0^d (\sigma + \Delta\sigma) \left| E(\sigma + \Delta\sigma, z) \right|^2 dz \tag{4.34}$$

for a small conductivity change, the field term in the integral can be simplified to

$$\left| E(\sigma + \Delta\sigma, z) \right|^2 \approx \left| E(\sigma, z) \right|^2 + \frac{d \left| E(\sigma, z) \right|^2}{d\sigma} \Delta\sigma \tag{4.35}$$

The change in the absorbed power can be approximated, ignoring the term weighted in $\Delta\sigma^2$, to:

$$A(\sigma + \Delta\sigma) \approx \frac{1}{2} \int_0^d \left((\sigma + \Delta\sigma) \left| E(\sigma, z) \right|^2 + \sigma\Delta\sigma \frac{d \left| E(\sigma, z) \right|^2}{d\sigma} \right) dz \tag{4.36}$$

considering that the change in conductivity $\Delta\sigma$ is homogeneous in the volume (no z dependence), the change in reflected microwave power ΔP can be simplified to:

$$\begin{aligned} \Delta P(\Delta\sigma) &= P(\sigma + \Delta\sigma) - P(\sigma) = -A(\sigma + \Delta\sigma) + A(\sigma) \qquad (4.37) \\ &\approx -\frac{1}{2}\Delta\sigma \int_0^d \left| E(\sigma, z) \right|^2 dz - \frac{1}{2}\Delta\sigma\sigma \int_0^d \left(\frac{d \left| E(\sigma, z) \right|^2}{d\sigma} \right) dz \end{aligned}$$

leading to a sensitivity factor:

$$S = -\frac{1}{2P(\sigma)} \left[\int_0^d \left| E(\sigma, z) \right|^2 dz + \sigma \int_0^d \left(\frac{d \left| E(\sigma, z) \right|^2}{d\sigma} \right) dz \right] \tag{4.38}$$

Eq.4.38 shows that the sensitivity factor is composed of two contributions:

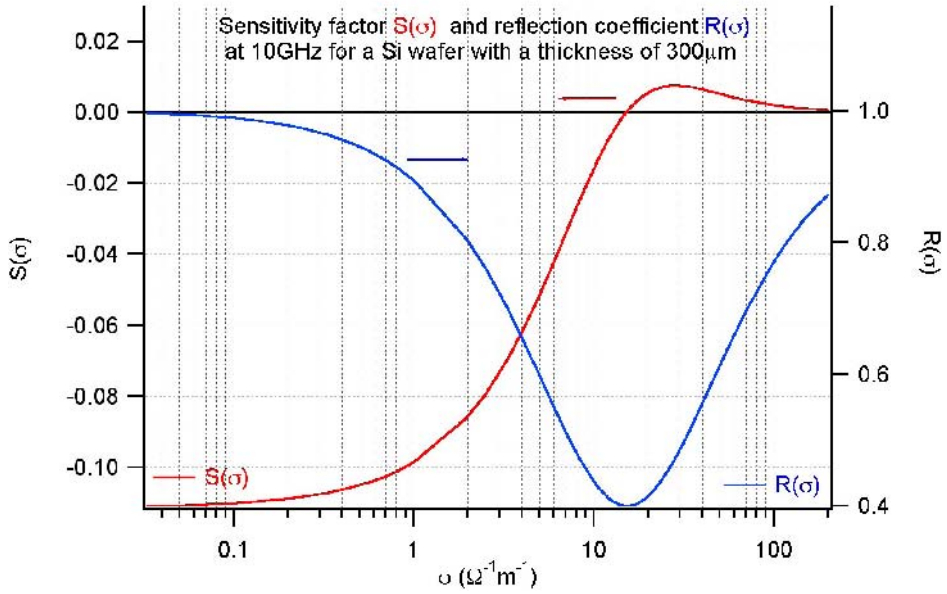

Figure 4.4: Power reflection coefficient $R(\sigma)$ and sensitivity factor $S(\sigma)$ calculated at $10GHz$ as a function of the dark conductivity σ for a sample of thickness $d = 300\mu m$ and $\epsilon_r = 12$.

- The first one (first term) due to the absorption of microwave energy by the excess charge carriers. This contribution is positive.
- The second one (second term) reflects the decrease of the microwave field absorption of the dark charge carriers (σ) by the influence of the excess charge carriers ($\Delta\sigma$). In fact, $\Delta\sigma$ induces a change in the reflection/absorption characteristics of the sample. This contribution is negative.

The first contribution is preponderant at low dark conductivities whereas the second contribution increases with increasing conductivity. So the sensitivity factor is negative at low dark conductivity becoming positive at high dark conductivity.
This can be seen for the simple case of a Si-sample directly adjacent to a short circuit (an ideal reflector) as shown in Fig.4.4: as long as the reflection coefficient decreases with increasing conductivity, the sensitivity factor is negative. As the reflection coefficient increases with the conductivity, the sensitivity factor becomes positive.

The penetration depth of the microwave field into the semiconductor sample is a characteristic parameter for the sensitivity as well and is related with the absorption/reflection characteristics. If the microwave field is totally extinguished after a certain penetration distance δ, it will not interact with a conductivity change at deeper regions than δ, given by [27]:

$$\delta = \frac{c}{2\pi f}\left[\frac{\epsilon_{sc}}{2}\left(\sqrt{1+\left(\frac{\sigma_0}{2\pi f \epsilon_0 \epsilon_{sc}}\right)^2}-1\right)\right]^{-\frac{1}{2}} \tag{4.39}$$

being σ_0 the dark conductivity of the semiconductor, f the frequency of the microwave harmonic field, ϵ_{sc} the relative permittivity of the semiconductor and c the light propagation velocity in the vacuum.
Penetration depths for the samples measured lie above the Si-wafer thickness. Thus microwave radiation is sensitive to any local conduction change within the sample.

For determination of Eqs.4.37-4.38 it was assumed that $\Delta\sigma$ is uniform. Unfortunately, this is relatively rare in a real system and therefore a more detailed discussion is required. Generalizing, the change in microwave excess conductance can be expressed by a position dependent sensitivity factor $S(z)$:

$$\frac{\Delta P}{P} = \int_0^d S(z)\,\Delta\sigma(z)\,dz \tag{4.40}$$

A quantitative description is possible for a multilayer system in the z direction and homogeneous in the x/y plane:

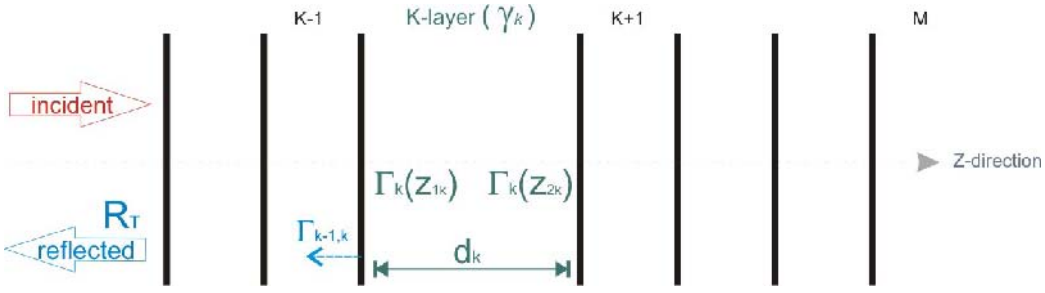

Figure 4.5: Scheme of a multilayer system of m layers, upon which a uniform plane wave is normally incident from the left.

The k-layer in a multilayer system is characterized by an homogeneous complex propagation constant γ_k and a thickness $d_k = (z_{1_k} - z_{2_k})$. The electrical field reflection coefficient changes with position z due to phase and modulus change of the propagating field. That change between the z_1 and z_2 positions (limits of the k-layer) is

$$\Gamma_k\left(z_{1_k}\right) = \Gamma_k\left(z_{2_k}\right) e^{-2\gamma_k}\left(z_{1_k} - z_{2_k}\right) \tag{4.41}$$

the relation between the reflection coefficient of the medium $k-1$ and k is given, at an infinitesimal distance from the interface, by

$$\Gamma_{k-1} = \frac{\left(\Gamma_{k-1,k} + \Gamma_k\right)}{\left(1 + \Gamma_{k-1,k}\Gamma_k\right)} \tag{4.42}$$

were $\Gamma_{k-1,k}$ is the Fresnel reflection coefficient between mediums $k-1$ and k:

$$\Gamma_{k-1,k} = \frac{\left(\gamma_{k-1} - \gamma_k\right)}{\left(\gamma_{k-1} + \gamma_k\right)} \tag{4.43}$$

using these relations recursively the field reflection coefficient just before the sample, Γ_T, can be calculated for a multilayer system if the field reflection coefficient at the last interface Γ_m is known.
The energy (or power) reflected by the system R_T can be calculated by:

$$R_T = \Gamma_T {\Gamma_T}^* \tag{4.44}$$

being ${\Gamma_T}^*$ the conjugated reflection coefficient.

The position dependence of E^2 (until now neglect) depends for low conductivity samples on the wavelength of the microwaves in the sample and for high conductivity samples on the microwave penetration depth. An extended discussion in the literature is given in literature [47], [48].

Useful is the observation that if S is independent of z, always that the dependence of E^2 on z can be neglected. If this is the case:

$$\frac{\Delta P}{P} = S \int_0^d \Delta\sigma\left(z\right) dz \tag{4.45}$$

and the microwave signal is proportional to the excess conductance, or in other words, the contribution of excess charge carriers to the signal does not depend on their position. This assures that a decay in the microwave signal is due to the decay of mobile excess charge carriers (trapping, recombination, charge transfer or decrease of mobility). The measurements reported in this work are performed under conditions where Eq.4.45 is valid.

4.3.2 Dark conductivity measurements

The use of a variable short circuit (Fig. 4.6) enables the variation of the distance l between the short circuit and the sample. This allows to change the position of the sample in the microwave field.

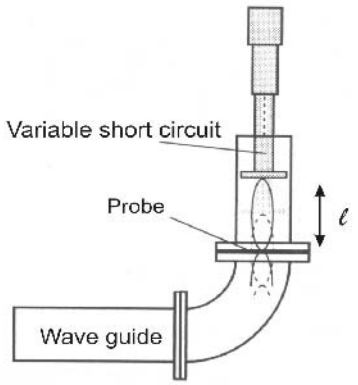

Figure 4.6: Scheme for dark conductivity measurements. The distance l between sample and short circuit is variable.

In principle, the conductivity can be determined from the reflection coefficient $R_T = \Gamma_T \Gamma_T^*$ at one fixed distance l; but the dependence of R_T on l enables a larger accuracy and the verification of the theory given above (section 4.3.1).
As indicated above, the system can be stratified as $air/sample/air/shortcircuit$ where the short circuit has a reflection coefficient $\Gamma_m = -1$.
A program based on the Eqs. 4.41-4.44 is used to calculate $R_T(\sigma)$ for different values of σ. The value of σ yielding the best fit to the experimental data is the conductivity of the sample.

4.3.3 Time Resolved Microwave Conductivity (TRMC) measurements

For TRMC measurements the sample is excited by a short pulse ($10ns$ FWHM) and $\Delta P(\Delta\sigma)/P(\sigma)$ is the signal acquired and is called the TRMC

signal.
The position and time dependent excess conductivity $\Delta\sigma(z,t)$ is:

$$\Delta\sigma(z,t) = q\left[\mu_n \Delta n(z,t) + \mu_p \Delta p(z,t)\right] \tag{4.46}$$

After the pulse excitation, excess charge carriers redistribute through the volume until for long enough times, the fundamental mode prevails (section 2.5.3). Then, $\Delta\sigma$ can be described as:

$$\Delta\sigma(z,t) = \Delta\sigma_1(z) f(t) \tag{4.47}$$

where $\Delta\sigma_1(z)$ refers to the principal mode distribution.
Even if the sensitivity factor is position dependent, the TRMC signal presents the same decay characteristics as the excess charge carriers decay:

$$\frac{\Delta P(t)}{P} = f(t) \int_0^d S(z)\,\Delta\sigma_1(z)\,dz \tag{4.48}$$

As in most cases in single crystalline silicon $\Delta n(x,t) = \Delta p(x,t)$, the decay of the TRMC signal represents the decay of excess minority carriers, therefore:

$$\frac{1}{\Delta n^*(t)}\frac{d\Delta n^*(t)}{dt} = \left(\frac{\Delta P}{P}\right)^{-1}\frac{d}{dt}\left(\frac{\Delta P(t)}{P}\right) = \frac{1}{\tau_{eff}(t)} = \frac{1}{\tau_{vol}(t)} + \frac{1}{\tau_s(t)} \tag{4.49}$$

being $\Delta n^*(t) = \int_0^d \Delta n(z,t)\,dz$; τ_s is the characteristic lifetime of recombination on the surfaces and τ_{vol} the characteristic volume recombination lifetime. The physical meaning of $\tau_{eff}(t)$ is the decay time (at time t) of the actual excess charge carriers distribution (at time t). If τ_{eff} is determined by fitting a part of an experimental decay curve to an exponential behavior, τ_{eff} is the average decay time of the time range covered (as mentioned in section)

4.3.4 Stationary photoconductivity measurements

Stationary conditions mean that there is no time dependence of the conductivity. Therefore, the microwave signal would be proportional to the conductivity integrated over the thickness of the sample.

4.3.5 Potential modulated conductivity measurements

The microwave power reflection induced by a small perturbation of the potential can be described as

$$\begin{aligned}\frac{\Delta P}{P} &= S\int_0^d \Delta\sigma dz = qS\int_0^d (\mu_n\Delta n + \mu_p\Delta p)\,dz \\ &\approx qS\int_0^d \left(\mu_n\frac{dn}{d\psi}\Delta\psi + \mu_p\frac{dp}{d\psi}\Delta\psi\right)dz \\ &= qS\Delta\psi\mu_n\int_0^d \left(\frac{dn}{d\psi} + \frac{\mu_p}{\mu_n}\frac{dp}{d\psi}\right)dz = qS\Delta\psi\mu_p\int_0^d \left(\frac{\mu_n}{\mu_p}\frac{dn}{d\psi} + \frac{dp}{d\psi}\right)dz\end{aligned} \tag{4.50}$$

The total charge in the volume of a semiconductor is given by:

$$Q_{sc}(\psi) = q\left[\int_0^d (-n(\psi) + N_D + p(\psi) - N_A)\,dz\right] \tag{4.51}$$

considering the doping densities N_D and N_A uniform in the whole volume, the space charge capacity can be calculated as

$$C_{sc} = \frac{dQ_{sc}}{d\psi} = q\left[\int_0^d \left(-\frac{dn}{d\psi} + \frac{dp}{d\psi}\right)dz\right] \tag{4.52}$$

Under small perturbation conditions and for the depletion regime, majority charge carriers are the only contribution to a change in conductivity:

- p-semiconductor under depletion regime: $\Delta p >> \Delta n \approx 0$

$$\frac{\Delta P}{P} \approx qS\mu_p\Delta\psi\int_0^d \frac{dp}{d\psi}dz = S\mu_p\Delta\psi C_{sc} \tag{4.53}$$

- n-semiconductor under depletion regime: $\Delta n >> \Delta p \approx 0$

$$\frac{\Delta P}{P} \approx qS\mu_n\Delta\psi\int_0^d \frac{dn}{d\psi}dz = S\mu_n\Delta\psi C_{sc} \tag{4.54}$$

Under depletion conditions the potential modulation changes the population of majority charge carriers which are injected or collected by the ohmic back contact. In such conditions, the conductance change induced in the semiconductor is proportional to the space charge capacity. The *DC* polarization from flatband regime to depletion and deep-depletion conditions

(reverse polarization) decreases the total number of majority charge carriers within the semiconductor:

$$\int_0^d \sigma(\psi_1) - \int_0^d \sigma(\psi_2) > 0 \tag{4.55}$$

For inversion conditions the approximation given above is not valid because minority charge carriers start to contribute to the space charge capacity. For slow enough DC and AC polarizations, the contribution to the C_{sc} is measurable. The number of charge carriers is not decreasing with the DC reverse polarization, it increases while minority charge carriers start to compensate the polarization. The total number of free charge carriers in the semiconductor is higher than before:

$$\int_0^d \sigma(\psi_1) - \int_0^d \sigma(\psi_2) < 0 \tag{4.56}$$

therefore, $\Delta P/P$ experiments show a change of sign by AC modulation techniques when the inversion regime is acquired.

4.3.6 Instrumentation

For all microwave measurements the microwave source is a Gunn diode with a maximum emitting power of about $200mW$. The microwaves are guided via a rectangular waveguide system to a circulator and then to a cell containing the sample as shown in Fig. 4.7 and 4.8. The reflected microwaves pass via the circulator, which separates the incoming from the reflected microwaves, to a detector that measures the intensity of the reflected waves.

- a) **Dark conductivity and TRMC contactless measurements:**

  A microwave Gunn Diode with a variable frequency oscillator cavity in the $X-band$ frequency range, between $8GHz$ and $12.4GHz$, was used as the microwave radiation source. For dark conductivity and TRMC measurements, the sample is placed between a variable short circuit and the waveguide system (Fig.4.7). This enables the variation of the distance between the sample and the short circuit. Thus the microwave field in the sample can be varied.

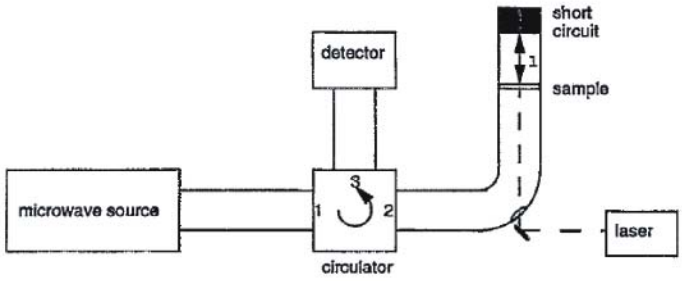

Figure 4.7: Scheme of the set up used for TRMC measurements and for dark conductivity measurements from [49].

The light pulse excitation of the samples was produced by $10ns$ FWHM pulses of a Nd:YAG laser at $532nm$ and $1064nm$ wavelength with $3mm$ diameter spot.

- b) **Potential modulated and light modulated electrochemical measurements:**

The microwave radiation source is a Gunn Diode with a variable frequency oscillator cavity in the $Ka - band$ frequency range, between $28GHz$ and $40GHz$.

The cell is polarized by use of a computer-controlled potentiostat (Gamry 600) with different software to perform cyclic voltammetry and impedance measurements. Microwave detector signal and potentiostat signal are plugged to lock-in amplifiers triggered by the cell perturbation. In case of impedance measurements, the voltage perturbation of the potentiostat is used as the reference frequency for the lock-ins and in case of light modulated measurements, the light modulation frequency is taken as the reference. In the later measurements, illumination took place by laser light diodes with $635nm$ and $875nm$ wavelengths.
Lock-in signals were stored on a computer using a $GPIB$ interface and potentiostat signals by an USB port. Calculation of photocurrent, current and capacity measurements were done by use of the software controlling the stations.

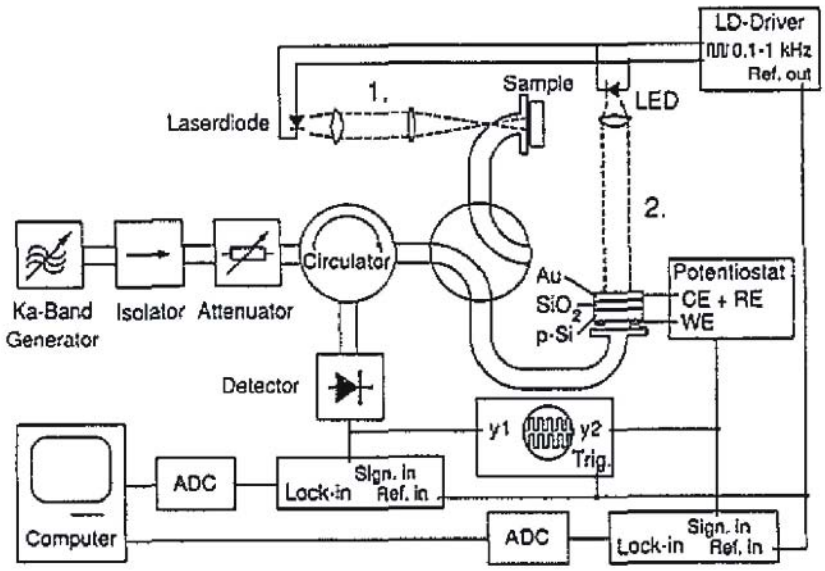

Figure 4.8: Scheme of the set up used for potential modulated and light modulated electrochemical measurements from [49]

TRMC measurements as function of the applied potential were done too on electrochemical cells by instrumentation similar to the one in Fig. 4.8. The sample was positioned at the end of the open $Ka-band$ waveguide; no mirror to short circuit the wave path was used. Illumination took place at the free side of the sample, on the upper sample surface, by a laser pulse with $10ns$ FWHM of a Nd:YAG laser at $532nm$ and $1064nm$ wavelength with $3mm$ diameter spot. Microwave radiation was incident on the bottom side. The cell was polarized by use of an external potential source.

4.4 Transient Surface Photo-Voltage methods

The surface photovoltage (SPV) is defined as the change in surface potential as a result of illumination [13], [50]. The virtue of this technique is its direct measurement of surface potential (or surface potential changes) without involving any impedance measurements where the surface potential is induced and calculated from capacitance measurements (sections 4.1 and 3.1).
SPV is a measurement with contacts which can be performed noninvasively by the use of high impedance coupled electrodes (see 4.4.3).

Illumination leads to electron-hole generation. In general there is a redistribution of excess electrons and holes, in particular in a region of the semiconductor close to the illuminated surface. This process leads to a decrease in the semiconductor band bending. This decrease is termed the surface photovoltage. Increasing light intensity increases the SPV signal until the extreme case, under very strong illumination, where the bands become completely flattened and the SPV signal saturates. This saturation SPV signal is equal in magnitude and opposite to the total band-bending or surface potential.

4.4.1 Description and theory

The photovoltage measured in MIS devices is the difference between the gate voltage V_G under illumination and dark conditions. As described in section 3.1 (eq. 4.22) V_G depends on the surface potential ψ_s and the charge accumulated on the *isolator/semiconductor* interface. Optical excitation modifies the concentration of charge carriers on the semiconductor surface and that can be described with a new equivalent surface potential ψ_s^{il}.
The difference in gate potential due to illumination is:

$$\Delta V_G = V_G^{il} - V_G = \psi_s^{il} - \psi_s + \frac{Q_{sc}\left(\psi_s^{il}\right) - Q_{sc}\left(\psi_s\right)}{C_i} + \frac{Q_{it}\left(\psi_s^{it}\right) - Q_{it}\left(\psi_s\right)}{C_i} \quad (4.57)$$

But the surface potential change is not the only contribution to the SPV signal.
A more general definition of the SPV signal is that its signal reflects the position shift of the center of gravity of the positive charge relative to that of the negative charge induced by light stimulation.
In addition, if illumination leads to the diffusion of electron-hole pairs, there is a voltage contribution from the bulk of the semiconductor due to the Dember potential V_D. The difference between hole and electron mobility leads to the presence of an internal field E_i between electron and hole whereas charge carrier diffuse "together" as treated in section 2.5.1 and in [51]. The contribution to the SPV signal due to the Dember potential is given by [52]:

$$V_D = \frac{b-1}{b+1}\frac{kT}{q}\ln\left(\frac{\rho_0}{\rho_I}\right) \quad (4.58)$$

where b is the ratio of electron to hole mobility and ρ_0 and ρ_I the resistivity of the semiconductor in the dark and under illumination respectively.

Moreover, for semiconductors with large charge carriers mobilities, which is the case for silicon, the diffused excess charge carriers can reach the rear surface (non illuminated). Once more the SPV signal is sensitive to the processes (recombination, trapping, storage) which take place on the rear side.
Thus, SPV signal is not only sensitive to the photovoltage change on the illuminated sample surface but also to other magnitudes such as Dember potential and surface photovoltage on the back surface.
In order to compare quantitatively SPV signals with $TRMC$ signals on the same samples, linearity between signal and intensity of illumination must be followed by SPV signals. For the present work, the recombination processes in silicon under depletion conditions is of special interest. Under depletion conditions, considering a $p-doped$ semiconductor, Q_{sc} can be expressed by:

$$Q_{sc}\left(\psi_s\right) = -\sqrt{2q\epsilon kTN_A\left(\psi_s - \frac{kT}{q}\right)} \tag{4.59}$$

Considering that the illumination does not change the regime of the semiconductor (the bands are not totally flattened), the difference in surface potential is:

$$\psi_s^{il} - \psi_s = \frac{Q_{sc}\left(\psi_s^{il}\right)^2 - Q_{sc}\left(\psi_s\right)^2}{2q\epsilon kTN_A} \tag{4.60}$$

where $Q_{sc}\left(\psi_s^{il}\right)$ can be rewritten as:

$$Q_{sc}\left(\psi_s^{il}\right) = Q_{sc}\left(\psi_s\right) + \Delta Q_{sc} \tag{4.61}$$

Considering only small values of ΔQ_{sc}, the surface potential change is simplified to a linear relation with ΔQ_{sc}:

$$\psi_s^{il} - \psi_s \approx \frac{Q_{sc}\left(\psi_s\right)}{q\epsilon kTN_A}\Delta Q_{sc} \tag{4.62}$$

For low illumination intensities and strongly absorbed light, it can be assumed that all excess charge carriers are generated in the space charge region and immediately separated by the present field. As a result, minority charge carriers accumulate on the semiconductor surface diminishing the total field in the semiconductor. Thus, the space charge region narrows with a new surface potential ψ_s^{il}.
The gate potential difference, neglecting the Dember potential and the change

of interface charge ($\Delta Q_{it} = Q_{it}\left(\psi_s^{il}\right) - Q_{it}\left(\psi_s\right) << \Delta Q_{sc}$) is simplified to:

$$\Delta V_G \approx \left(\frac{Q_{sc}\left(\psi_s\right)}{q\epsilon kTN_A} + \frac{1}{C_i}\right)\Delta Q_{sc} \tag{4.63}$$

Under these simplifications; considering illumination only in the space charge region, no diffusion of excess charge carriers and no contribution from Q_{it}, the SPV signal is proportional to the illumination intensity.

4.4.2 Applications

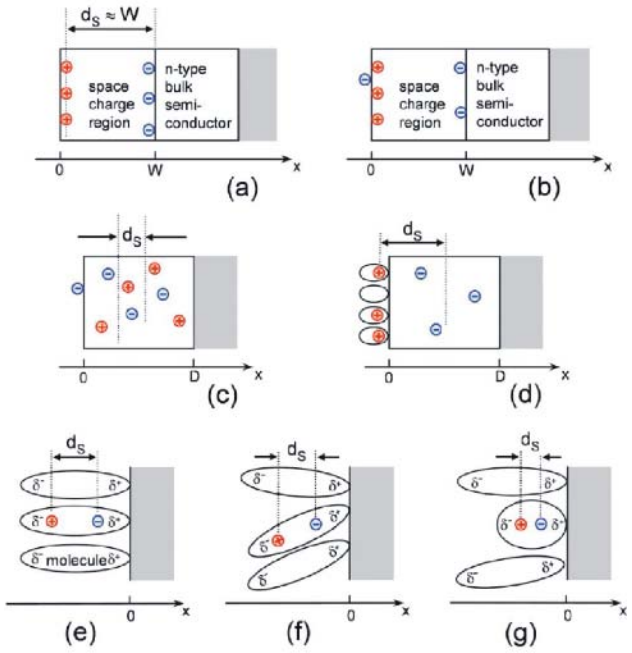

Figure 4.9: The figure illustrates, taken from ([53]) different mechanisms of charge separation. a) space charge charge separation, b)trapping in the space charge region, c)diffusion transport, d)charge injection into a semiconductor, such as sensitization of semiconductors and e), f), g) represent dipole and molecular reorganization under light stimulation.

Depending on the excitation source, relaxation response (after pulsed excitation), harmonic response (under harmonic excitation) and stationary

response (under stationary illumination) can be investigated by SPV measurements.
For example, a detailed analysis of the SPV signals under strong pulsed stimulation as a function of the gate voltage on MIS devices can lead to the extraction of interface states $D_{it}(E)$ [13],[50].
But as mentioned previously, a more generalized description includes all phenomena where charge distribution changes under illumination conditions. The SPV signal can be interpreted as the potential difference in a plane-parallel capacitor:

$$SPV = Q\frac{d_s}{\epsilon_r \epsilon_0} \tag{4.64}$$

being Q the equivalent charge with a gravity center separated at distance d_s under illumination conditions.
With this general definition, other systems than MIS devices can be investigated. In Fig. 4.9 examples of different mechanisms which contribute to SPV signal such as: orientation of dipoles due to light interaction, injection of charge carriers into the semiconductor from an external source or charge carrier trapping are shown.

4.4.3 Instrumentation

The SPV signal is measured via a high-impedance transparent buffer amplifier as illustrated in Fig. 4.10. The sample is back contacted by a grounded

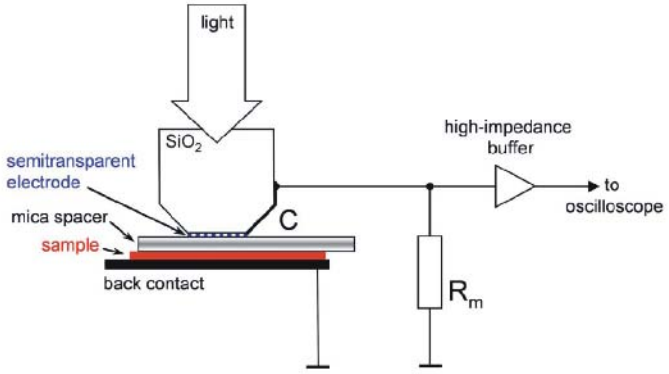

Figure 4.10: Principal configuration for SPV in the capacitor arrangement (by [53]).

TCO or metal on the rear (non illuminated) side and front contacted (illuminated side) by a semitransparent $SnO_2 : F$ electrode. A mica spacer of about 40 μm was placed between front side and the $SnO_2 : F$ electrode which can be gently pressed via a cardanic spring. On the front electrode a quartz lens is used to collimate the light.
Parallel to the capacity measured between front and back contact, assigned by the capacitor C in Fig. 4.10, a R_m resistor (variable) is connected. The long time resolution of the SPV signal is limited by the R_mC time constant with C being the measured capacity and the shorter time resolution depends on the length of the laser pulse (for transient measurements).
The SPV signal is amplified by a high-impedance ($10G\Omega$ input shunt resistor) buffer amplified with a 50Ω output (OPA656 from Texas Instruments) configured as unity-gain voltage followers.

Chapter 5

Capacitance characteristics of Si/SiN_x based MIS devices

5.1 Introduction

In this chapter Metal-Isolator-Semiconductor (MIS) diodes are investigated. Different from the metal-semiconductor junction (Schottky diodes) [1], [3] the MIS devices present an insulating layer between the metal contact (called the gate electrode) and the semiconductor. In the ideal case, the insulator blocks any faradaic current (except for very thin insulating layers where the tunneling effect may occur [54]). However, real MIS devices present leakage currents under high polarization and temperatures [1]. The insulator presents structural defects and impurities which make possible the transport of charge through it.

The current as function of the applied potential (I-V curves) has been measured on Si/SiN_x MIS devices. The doping density (N_D), flatband potential (V_{fb}), fixed charge (Q_f) and interface state density (D_{it}) have been determined from impedance measurements as function of the applied voltage (C-V measurements). Impedance spectroscopy analysis has also been used to characterize the rear cell contact.

5.2 Experimental

Two different $n-Si$ (phosphorous doped) wafers were used for MIS devices:

- Mitsubishi $1.5\Omega cm$, $< 111 >$ oriented and $245\mu m$-thick

- Wacker $30\Omega cm$, $< 100 >$ oriented and $530\mu m$-thick.

Amorphous hydrogenated SiN_x layers of different thicknesses were deposited by PECVD on the nSi wafers as described in [28]. Aluminum gate electrodes were deposited on top of the SiN_x layers and contacted with a wire using silver epoxy. As back contact $In : Ga$ eutectic paint was applied on the rear silicon surface and glued to a copper foil as shown in Fig. 5.1.

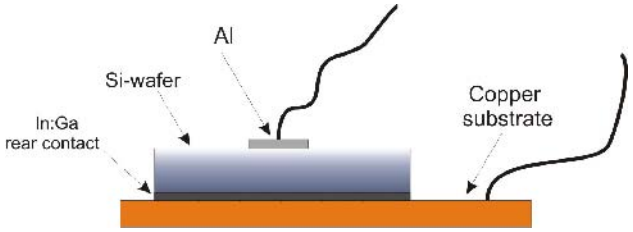

Figure 5.1: Schema of the built MIS devices.

A potentiostat as described in section 4.3.6 was used to polarize and perform impedance measurements on the MIS devices. The counter electrode was plugged together with the reference electrode in order to use the three electrode configuration as a two electrode set-up. Using the electrochemistry convention, the working-electrode has been connected to the semiconductor rear contact and the $reference/counter$ electrode has been connected to the gate aluminum electrode on the isolator.
These MIS devices were built in order to complement information on electrochemical cells based on the same $semiconductor/isolator$ working electrodes (chapter 6).

5.3 Results

5.3.1 I-V characteristics

I-V measurements of the MIS devices with $nSi - 1.5\Omega cm$ with different SiN_x thicknesses ($70nm$, $50nm$ and $30nm$) are shown in Fig. 5.2 and for the MIS devices with $nSi - 30\Omega cm$ with different SiN_x thicknesses ($75nm$, $50nm$, $30nm$ and $15nm$) in Fig. 5.3.

All MIS devices present similar I-V characteristics: at negative potentials a high negative leakage current is measured. At high positive voltages (over $5V$ or $6V$) some samples present high positive leakage currents. Between

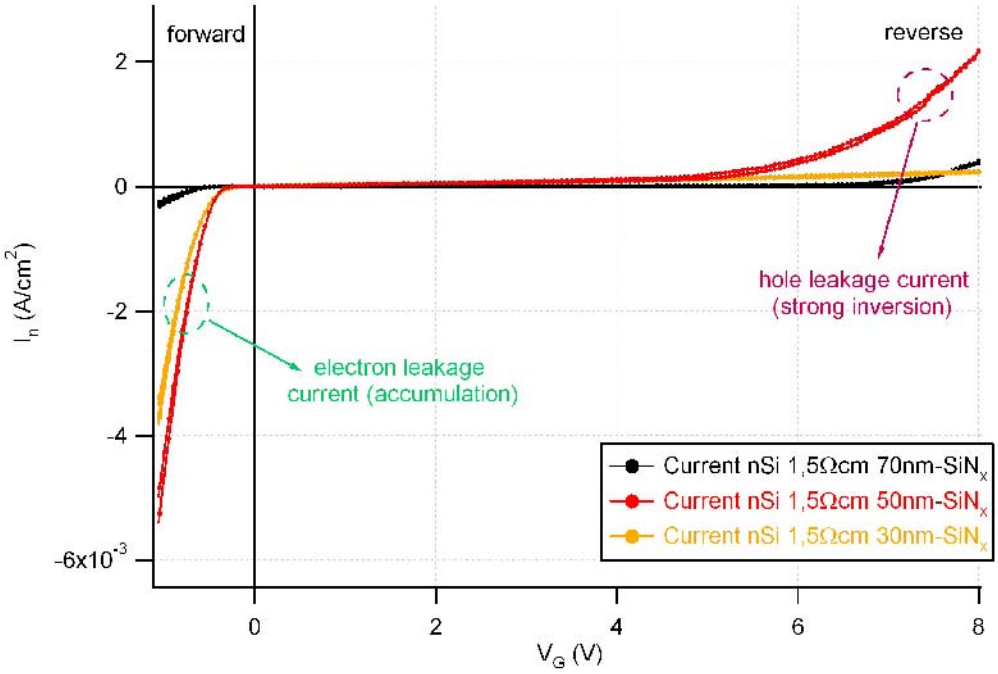

Figure 5.2: Current as function of the applied potential measurement of MIS devices composed by $nSi - 1.5\Omega cm$ semiconductor and $70nm$, $50nm$ and $30nm - SiN_x$ thick insulating layer. The scanning velocity was $100mV/s$.

these two ranges with leaking current, there is a voltage regime (between $0V$ and $5V$) where the leakage currents measured are small.
Negative currents corresponds to electrons flowing from the semiconductor to the gate electrode while positive currents to holes flowing in the same direction (or electrons in the opposite direction). Under negative polarization leakage currents are much higher than the currents measured under positive polarization; currents up to$-4mA/cm^2$ at $-1V$ measured while this magnitude is not attained even at $8V$ positive polarization. This behavior can be explained by the different concentration of charge carriers at the Si/SiN_x interface or a different current mechanism for holes and electrons.

SiN_x contains a positive fixed charge Q_f which bends the nSi into accumulation regime in the absence of applied potential. This Q_f can be evaluated by the determination of the flat band potential as is done in section 5.3.2. At $0V$ the concentration of electrons at the Si/SiN_x interface compensates the Q_f present in the insulating layer leading to an electron concentration

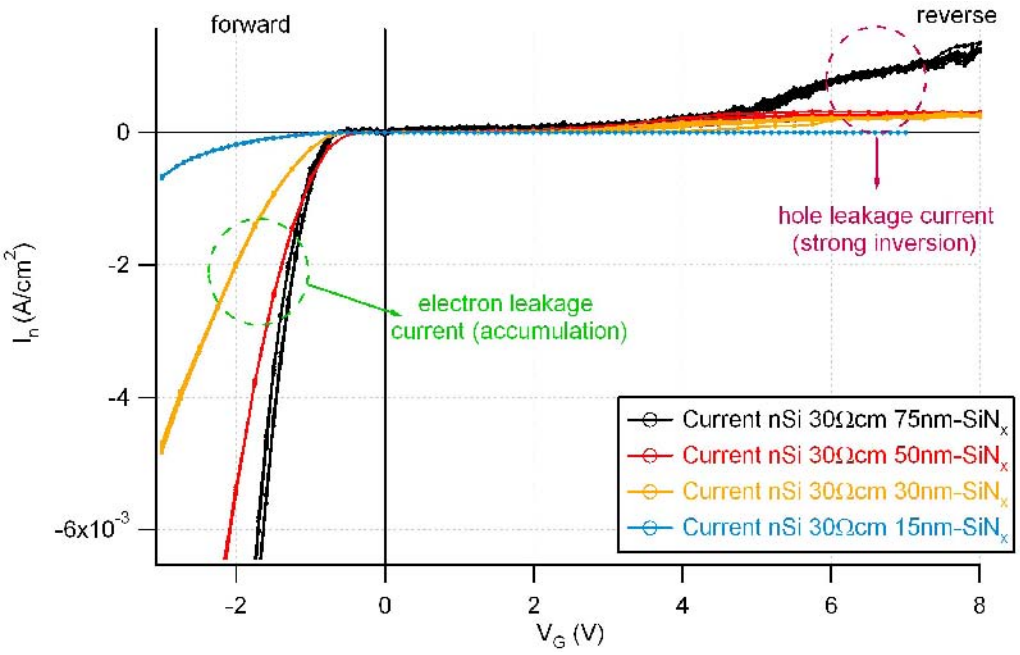

Figure 5.3: Current as function of the applied potential of MIS devices composed by $nSi - 30\Omega cm$ semiconductor and $75nm$, $50nm$, $30nm$ and $15nm - SiN_x$ isolator thickness. The scanning velocity was $100mV/s$.

at the Si surface around $10^{12}cm^{-2}$ (see Tab. 5.2). Small negative polarization enhances the concentration of electrons at the Si surface and this excess negative charge must be compensated by the positive charge present at the gate electrode (Q_G). Under this regime (concentration of electrons higher than the Q_f), electrons flow from the Si/SiN_x interface to the gate electrode through the SiN_x insulating layer.
For strong positive polarizations (exceeding $5V$), for most of the samples the external potential is larger than flat band potential (given in Tab. 5.2) and the nSi is in inversion or strong inversion regime. In this case holes are present at the Si/SiN_x interface and a positive current is measured. This current may reflect holes flowing from the semiconductor to the gate electrode through the SiN_x insulating layer or electrons from the gate electrode to the semiconductor.
The current may pass via defects in the SiN_x, different for electrons from that from holes. The different defect properties may lead to different current transport and magnitudes for electrons and holes. The literature suggests that the current through the SiN_x at high potentials and at room tempera-

ture is due to the Poole-Frenkel effect [55] and via different defects for holes and electrons [56].

Between these two leakage currents regimes (related to the strong accumulation and inversion regimes) the currents measured are in the μA range and related to the "weak" accumulation and depletion regime. For positive potentials under flat band, the concentration of electrons at the Si surface is smaller than Q_f and the gate charge Q_G is negative to satisfy the charge neutrality (Eq. 3.9). Under these conditions the electrons from the interface do not flow to the gate electrode, but in the other direction: electrons are extracted out of the semiconductor by the rear contact ($In : Ga$), reducing its concentration at the Si/SiN_x interface and driving the semiconductor to flat band regime.
An influence of the SiN_x thickness in the current characteristics is not clearly observed. The devices which present higher leakage currents are not the ones with the thinner insulator as in principle is expected. However, it is observed that the samples characterized by higher currents in negative polarization, present, generally, also higher currents in positive polarization. This suggests that the current mechanism through the SiN_x is field dependent [1].

In Fig. 5.4 the semilogarithmic plot of the current as function of the squared root of the applied field, ($E = V/d$), is shown for the $nSi - 1.5\Omega cm$ with $50nm - SiN_x$. A linear relation between the $\ln(I_n)$ and $\sqrt{E}$ is satisfied for values of $\sqrt{E}$ exceeding $10(V/m)^{1/2}$. This field domain corresponds to the inversion regime where the MIS devices is polarized in reverse direction and the leakege current is ascribed to holes (Fig. 5.2). This suggests the Poole-Frenkel mechanism plausible for charge transport in SiN_x because it leads to the following relation for the current j_n as function of the applied field E [55], [57]:

$$j_n = C_1 E exp\left\{ -\frac{q\left[\phi_{pf} - (\frac{qE}{\pi\epsilon_i\epsilon_0})^{\frac{1}{2}}\right]}{kT} \right\} \tag{5.1}$$

being ϵ_i the relative permittivity of the material (as well called the dielectric constant) and ϕ_{pf} the potential barrier high for an electron to move between defects (C_1 is a proportionality constant, q the electronic charge, ϵ_0 the permittivitty of the free space and k and T the Boltzmann constant and temperature respectively).

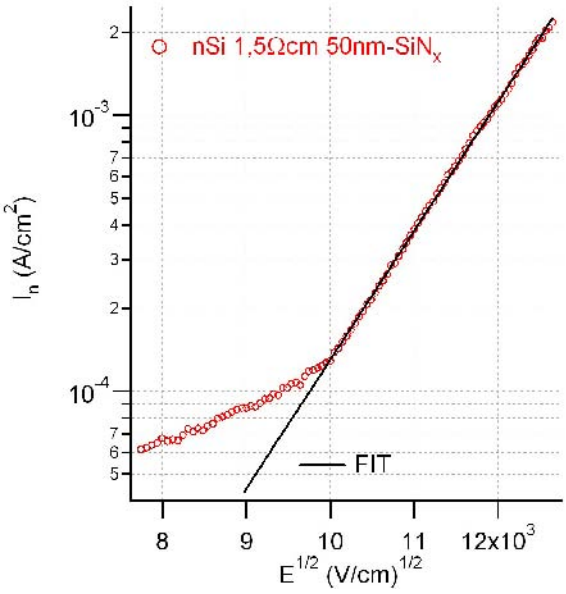

Figure 5.4: The current as a function of the square root of the field for the $nSi - 1.5\Omega cm$ with $50nm - SiN_x$ shown in Fig. 5.2 in the inversion regime.

The linear fit shown Fig.5.4 (black line) leads to a dielectric constant $\epsilon_i = 7.6$ and a potential barrier $\phi_{pf} = 0.5V$. These results are in agreement with [55] although with a higher value for the dielectric constant (also reported in other works [58]). This value for ϵ_i derived from I-V measurements, is about a factor two higher than the one found by ellipsometric methods where $\epsilon_i = 3.6$ [28]. This difference has been previously found [59] and attributed to dynamic processes active between DC and the ellipsometric range [55].

The results presented in Fig.5.4 have not been observed in all the MIS devices shown in Figs. 5.2 and 5.3. The Poole-Frenkel relation is only satisfied for those samples with higher direct currents in inversion regime, ascribed to hole leakage current. Electron leakage current, measured at negative potentials (inverse polarization), did not satisfy the relation in the potential range presented here. This indicates that Poole-Frenkel effect may not be the single transport mechanism active in SiN_x.
A model for the trapping characteristics and charge transport in SiN_x layers is still being discussed in the literature [56], [60] but nowadays it is generally accepted that the transport in SiN_x at room temperatures is trap assisted

transport involving the Poole-Frenkel effect.

5.3.2 C-V characteristics

5.3.2.1 High frequency characteristics: V_{fb}, N_D and Q_f determination

In the present section, the doping density (N_D), flatband potential (V_{fb}) and an estimation of the fixed charge Q_f within the SiN_x of the MIS devices already characterized by I-V measurements (Figs. 5.2 , 5.3) are investigated by capacity measurements as a function of the applied potential (C-V). Potential modulation of frequencies between $10kHz$ and $1MHz$ with a $20mV$ amplitude was used to extract the doping and flat band characteristics. This range of modulation frequencies can be considered in the high frequency range for silicon MIS devices: no AC capacity contribution from minority charge carriers or interface states is expected 4.2. Therefore, the Mott-Schottky relation (Eq. 2.107) will give a good estimation for N_D and V_{fb}.

The C-V measurements yield the total capacity of the device (C_T) as a function of the gate electrode potential (V_G). The Mott-Schottky relation (Eq. 2.107) is given for space charge capacity (C_{sc}) values against surface potential (ψ_s). This can lead to an error in the estimation of doping and flat band potential by the effect of the insulating capacitor C_i .

However, regarding the doping extraction, under depletion conditions the $(1/C_T)^2$ against V_G relation presents the same slope as $(1/C_{sc})^2$ against ψ_s as it is proved below:

$$\frac{1}{N_D} \propto \frac{d}{d\psi_s}\left(\frac{1}{C_{sc}}\right)^2 \tag{5.2}$$

so the doping density N_D is proportional to the slope of $(1/C_{sc})^2$ against the surface potential ψ_s. The differential relation between V_G and ψ_s (neglecting the charge contribution from the interface states) yields:

$$dV_G = d\psi_s + \frac{dQ_{sc}}{C_i} = d\psi_s + \frac{C_{sc}d\psi_s}{C_i} = \frac{C_i + C_{sc}}{C_i}d\psi_s \tag{5.3}$$

the slope of $(1/C_T)^2$ with respect to V_G leads to:

$$\frac{d}{dV_G}\left(\frac{1}{C_T}\right)^2 = \frac{C_i}{C_i + C_{sc}}\frac{d}{d\psi_s}\left(\frac{1}{C_i} + \frac{1}{C_{sc}}\right)^2 = \frac{2}{C_{sc}}\frac{d}{d\psi_s}\left(\frac{1}{C_{sc}}\right) = \frac{d}{d\psi_s}\left(\frac{1}{C_{sc}}\right)^2 \tag{5.4}$$

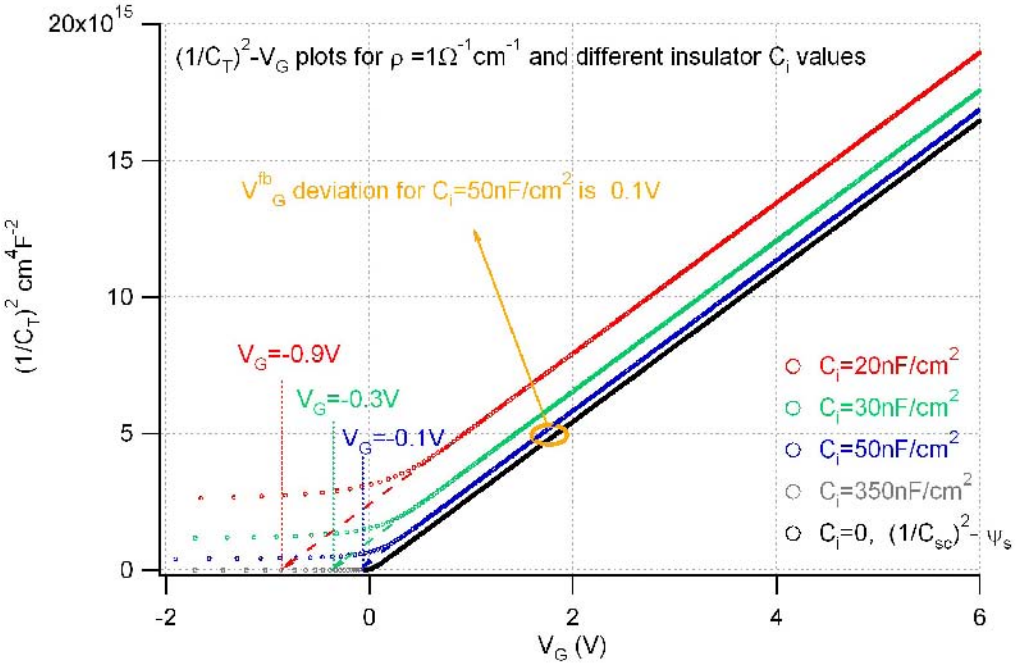

Figure 5.5: Simulation of $(1/C_T)^2 - V_G$ plots for ideal MIS devices with different series capacitors.

Therefore, N_D can be correctly determined from the $(1/C_T)^2$ against V_G plot. In Fig. 5.5 the Mott-Schottky relation for a MIS device with $1\Omega cm$ semiconductor and different C_i values is simulated. It is seen that the slope of the different curves is independent of C_i. However, it is not the same thing for the flat band determination. The flat band potential in the absence of insulating layer (black dots Fig. 5.5) corresponds to the origin $V_G = \psi_s = 0$. The presence of the insulating layer shifts the flatband (gate)-potential (V_G^{fb} in Fig. 5.5) to more negative potentials. This effect is negligible for big capacity values but it introduces an error for small capacity values. Experimentally, the minimum capacitor value found was over $C_i = 50nF/cm^2$ which introduces approximately a shift of $0.1V$. This deviation is not significant for the comparison of flat band potentials between the different MIS samples

presented in the following.

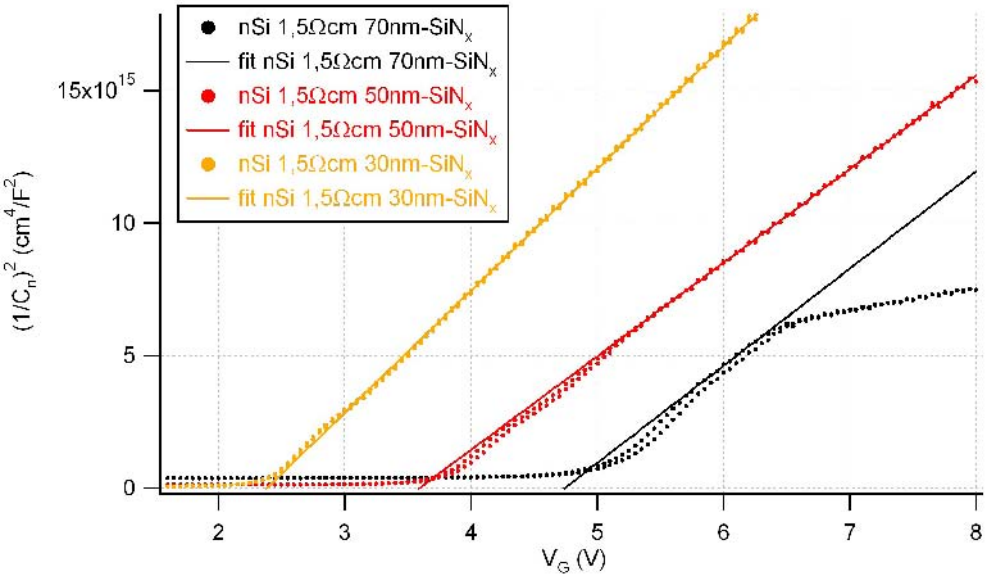

Figure 5.6: $(1/C_T)^2$ plots against V_G for MIS devices composed by $nSi - 1.5\Omega cm$ and $70nm$, $50nm$ and $30nm$ SiN_x isolator thickness.

In Figs. 5.6 and 5.7 experimental values for $(1/C_T)^2$ as function of the applied potential are plotted for the MIS devices previously measured (Figs. 5.2, 5.3). It is observed that the flat band potential increases in value with increasing SiN_x thickness (see Tab. 5.2).

First of all, in order to calculate the Q_f present in the SiN_x, the C_i values are required. These values were experimentally determined by the C_T-V_G curves under strong accumulation conditions (at $0V$). Several errors are involved in the C_i determination. The effect of high leakage currents observed in some samples introduces an inaccuracy in the displacement current measured. Moreover, the impedance of the rear contact may introduce a frequency dependence (discussed in next section 5.3.3) which complicates an accurate determination of C_i, especially for the highest modulation frequencies. Finally, errors related to the area determination of the gate electrode can contribute to the error in C_i. In Tab. 5.1 the C_i values experimentally determined for the different samples have been used to calculate the dielectric constant ϵ_i of the SiN_x. ϵ_i has been calculated using the theoretical

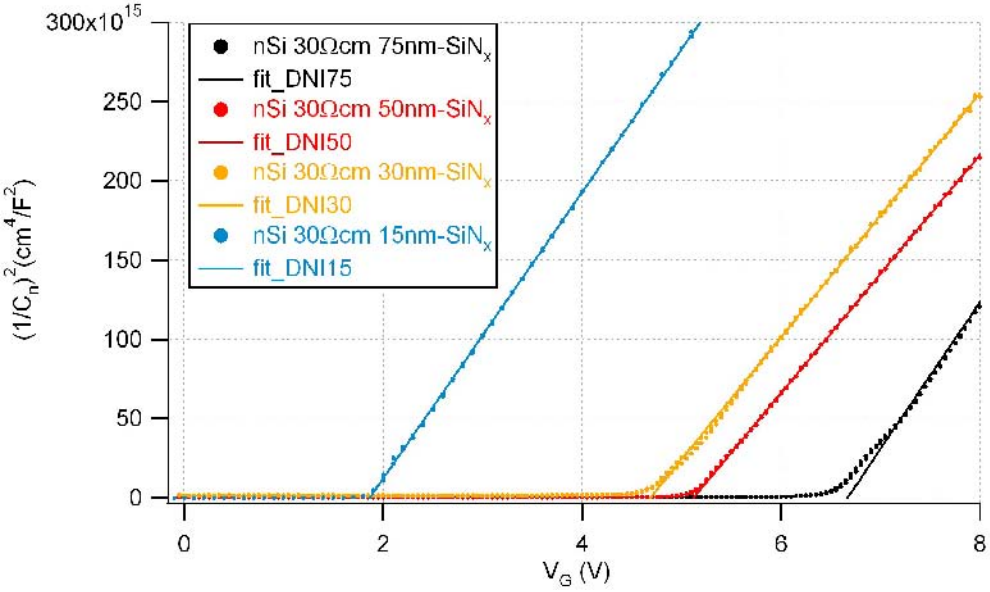

Figure 5.7: $(1/C_T)^2$ plots against V_G for MIS devices composed of $nSi - 30\Omega cm$ and $70nm$, $50nm$, $30nm$ and $15nm$ SiN_x isolator thickness.

plane-parallel capacity value for a capacitor of thickness d [44]:

$$C_i^t = \frac{\epsilon_0 \epsilon_i}{d} \tag{5.5}$$

$\rho(\Omega cm)$	30	1.5	30	1.5	30	30	1.5
$d(nm)$	15	30	30	50	50	75	70
$C_i(nF/cm^2)$	320	160	120	105	92	65	60
ϵ_i	5.4	5.4	4.1	5.9	5.2	5.5	4.7

Table 5.1: Calculation of the dielectric constant ϵ_i of SiN_x from the experimental data by use of Eq. 5.5.

The thickness of the isolating layer d was taken from the deposition rate of the SiN_x by PECVD as described in [28] where the thickness and refractive index characteristics of SiN_x were determined by ellipsometric methods. The ϵ_i values found in Tab. 5.1 lay between 4.5 and 6 and are slight smaller

than the value found for the Poole-Frenkel mechanism.

Q_f was calculated by Eq. 3.12 taken $\phi_{ms} = 0.21V$ for the $nSi - 30\Omega cm$ samples and $\phi_{ms} = 0.13V$ for the $nSi - 1.5\Omega cm$ samples and the experimental C_i values given in Tab. 5.1. The Q_f values obtained for all samples lie between $3,5 \cdot 10^{12} cm^{-2}$ and $1.5 \cdot 10^{12} cm^{-2}$ (given in Tab. 5.2).
The data suggests a decrease in Q_f by increasing the insulator thickness. Q_f values obtained for the $nSi - 30\Omega cm$ samples are slightly higher than the ones for the $nSi - 1.5\Omega cm$ samples.
Thicker SiN_x-layers need of longer deposition times at chamber temperatures of $350C$ [28]. Remaining longer times at this temperature can lead to an stabilization (passivation) of the defects responsible of the positive charge in the layer and so a decrease in Q_f with increasing thickness.

$\rho\Omega cm$ $n - Si$	$d - SiN_x$ (nm)	N_d (cm^{-3})	V_{fb} (V)	C_i (nF/cm^2)	Q_f (cm^{-2})
$1.5\Omega cm$	30	$3.0 \cdot 10^{15}$	2.36	160	$2.2 \cdot 10^{12}$
$1.5\Omega cm$	50	$3.1 \cdot 10^{15}$	3.57	105	$2.2 \cdot 10^{12}$
$1.5\Omega cm$	70	$2.4 \cdot 10^{15}$	4.72	65	$1.8 \cdot 10^{12}$
$30\Omega cm$	15	$1.2 \cdot 10^{14}$	1.84	320	$3.3 \cdot 10^{12}$
$30\Omega cm$	30	$1.4 \cdot 10^{14}$	4.66	120	$3.3 \cdot 10^{12}$
$30\Omega cm$	50	$1.4 \cdot 10^{14}$	5.10	92	$2.8 \cdot 10^{12}$
$30\Omega cm$	75	$1.2 \cdot 10^{14}$	6.64	60	$2.4 \cdot 10^{12}$

Table 5.2: Parameters obtained from C_T and $1/C_T^2$ plots against the gate potential applied for the MIS devices composed of $nSi - 30\Omega cm$ and $nSi - 1.5\Omega cm$ and different SiN_x layer thickness.

Experimental doping densities were calculated using the Mott-Schottky relation and are in agreement with the doping density values calculated from the resistivity of the wafers provided by the manufacturers ($1.5\Omega cm$ and $30\Omega cm$ with a 10% of deviation). The nominal doping densities for $1.5\Omega cm$ and $30\Omega cm$ nSi are $N_d = 2.7 \cdot 10^{15} cm^{-3}$ and $N_d = 1.2 \cdot 10^{14} cm^{-3}$, respectively. For the $nSi - 1.5\Omega cm$ samples, the values obtained experimentally using the Mott-Schottky relation have a maximal deviation of 15% from the theoretical value. For the $30\Omega cm$ devices, a deviation up to 20% is found for the $50nm - SiN_x$ sample. These errors greater than the 10% guaranteed

by the manufacturers can be related to the effect of leakage currents (which introduce an uncertainty in the voltage which actually decays within the semiconductor) and area determination of the gate electrode. It is curious that the range of potentials in which the Mott-Schottky relation is valid is so extended. The capacity value seems to decrease continuously with increasing the gate potential without reaching a minimum value related to the maximum width of the space charge region [7]. This is a clue to identify the deep depletion as explained in the following section 5.3.2.2.

Experimentally it has been determined that:

- The fixed charge concentration in SiN_x grown by PECVD on nSi wafers exceeds $10^{12}cm^{-2}$ and is positive.

5.3.2.2 Deep-depletion regime

In Fig. 5.8 $(1/C_T)^2$ as a function of $(V_G - V_{fb})$ for the device $nSi - 1.5\Omega cm$ with $50nm - SiN_x$ is plotted together with the simulation of a a MIS device ($nSi - 1.5\Omega cm$ and $C_i = 93nF/cm^2$) for two different MIS regimes: the depletion/inversion case (dotted gray line) and the deep-depletion case (black line). It is clearly seen that the experimental data of this sample follows the deep-depletion case.

MIS devices in the absence of leakage current present a saturation of the capacity measured at high modulation frequencies corresponding to the inversion regime of the semiconductor as indicated in Fig. 5.8. The inversion regime, characterized by the presence of minority charge carriers at the semiconductor surface, presents two regimes: weak inversion and strong inversion. In the weak inversion regime the density of minority charge carriers at the semiconductor surface is smaller than the number of majority charge carriers in the bulk. In this regime the main contribution to the semiconductor charge is still from the ionized impurities in the space charge region. In the strong inversion regime, the number of minority charge carriers at the surface is greater than majority charge carriers in the bulk and they constitute the main contribution to the semiconductor charge [61]. This last regime is characterized by (minority)charge carriers with a reduced mobility [62]. In Fig. 5.9 the inversion charge (red markers) and depletion charge (blue markers) contributions to the total semiconductor space charge (black line) are plotted as function of the Q_{sc} for an $nSi - 30\Omega cm$ silicon wafer.

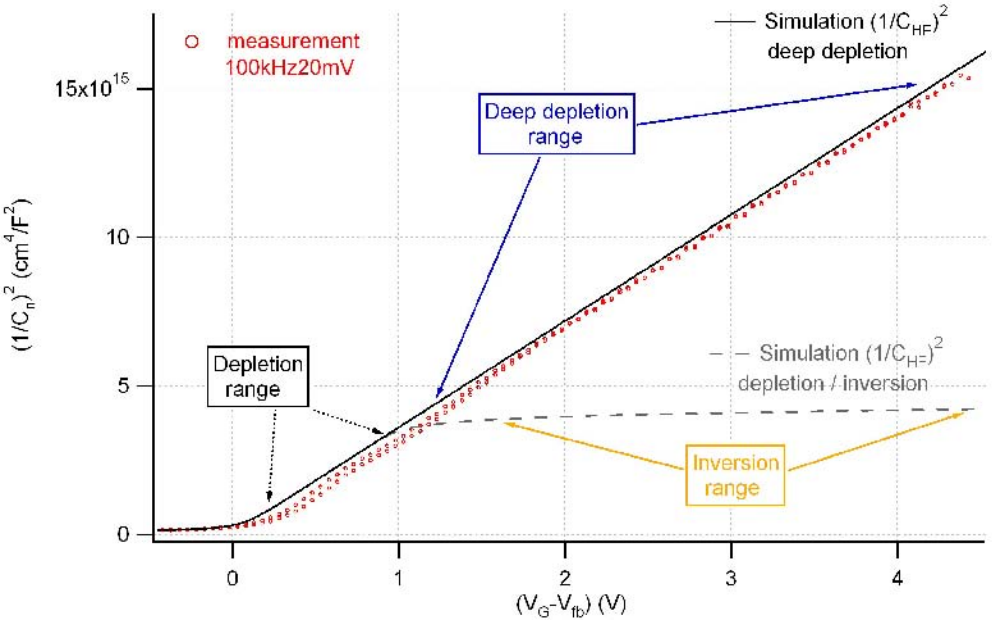

Figure 5.8: $(1/C_T)^2$ plot as function of the applied potential for MIS device $nSi - 1.5\Omega cm$ with $50nm\text{-}SiN_x$. The applied potential is expressed as $(V_G - V_{fb})$. The experimental data is compared to two simulated high frequency capacity curves: the *depletion/inversion* case (gray dotted line) and *deep − depletion* case (black line). The values used for the simulation are for an $nSi - 1.5\Omega cm$ wafer in series with $C_i = 93nF/cm^2$ insulator.

This behavior of the C_T-V_G or $(1/C_T)^2$ curves occurs when the strong inversion regime is reached. Minority charge carriers, even without contributing to the total capacity measured at high frequencies, accumulate at the Si/SiN_x interface compensating the DC (stationary) gate charge. With the presence of minority charge carriers at the interface, the charge is not only compensated by the ionized impurity (doping) atoms in the semiconductor. Thus, the Mott-Schottky relation is not valid in this regime and the $(1/C_T)^2$ curve, deviates from the linear V_G dependence.

The deep-depletion regime occurs when no minority charge carriers accumulate at the Si/SiN_x interface and so, the stationary gate charge must be compensated by the ionized doping atoms in the semiconductor [7]. In this situation, the inversion layer is not built and the width of the space charge increases with increasing the gate polarization. Thus, the Mott-Schottky re-

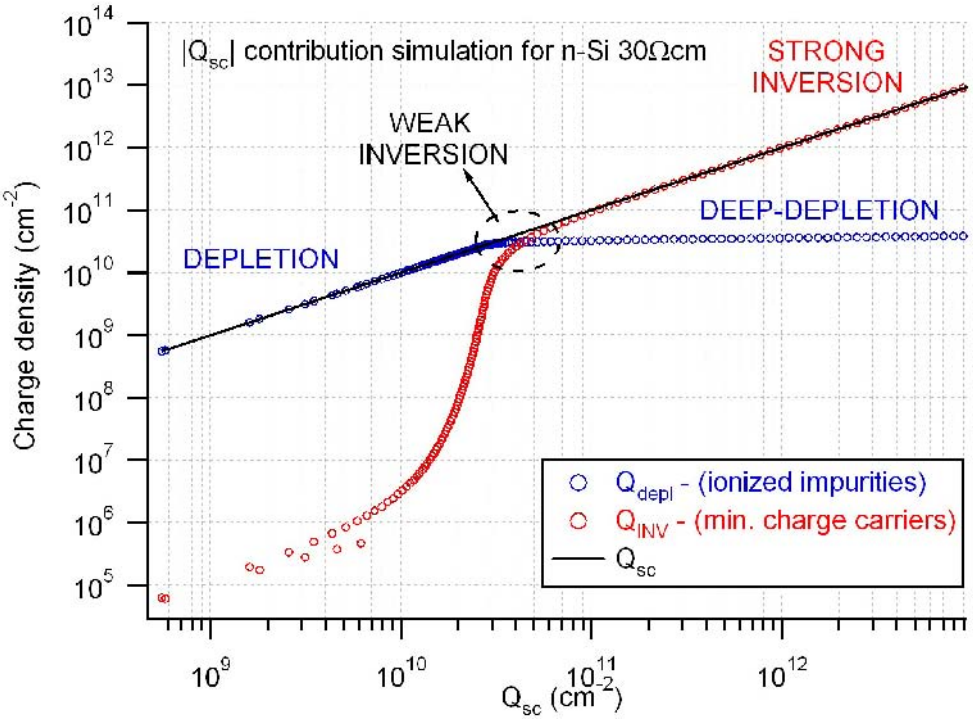

Figure 5.9: Simulation of the inversion layer charge Q_{INV} density (due to minority charge carriers) and the depletion charge (due to ionized doping impurities) as function of the the total semiconductor charge Q_{sc}.

lation is satisfied for a larger voltage range. This is exactly what occurs for the measured MIS device in Fig. 5.8 (and in Figs. 5.6 , 5.7). The measured MIS device (red markers) keeps on satisfying the Mott-Schottky relation for potentials exceeding $1V$ (with respect to flat band) and fits properly with the simulated deep-depletion regime. The dotted gray line shows the high frequency measurement if the MIS device shows the inversion regime.

Mainly two cases drive a MIS device into the deep-depletion regime: non steady state measurement and fast extinction of minority charge carriers. The first case is not applicable for the measuring conditions presented here. Non steady state response from the MIS device is achieved when a very fast voltage scan (or a voltage pulse) is applied to the sample and the displacement current is measured [63]. Being the ramp-voltage pulse shorter than the generation life time of the minority charge carriers, the unique displacement current is due to the majority charge carriers which react instantaneously

to the potential perturbation. In the present measurements, the DC polarization of the sample was done point per point (about $20s$ at every voltage point), letting the sample to reach the stationary state. Thus, the deep depletion regime must occur because of the extinction of minority charge carriers.

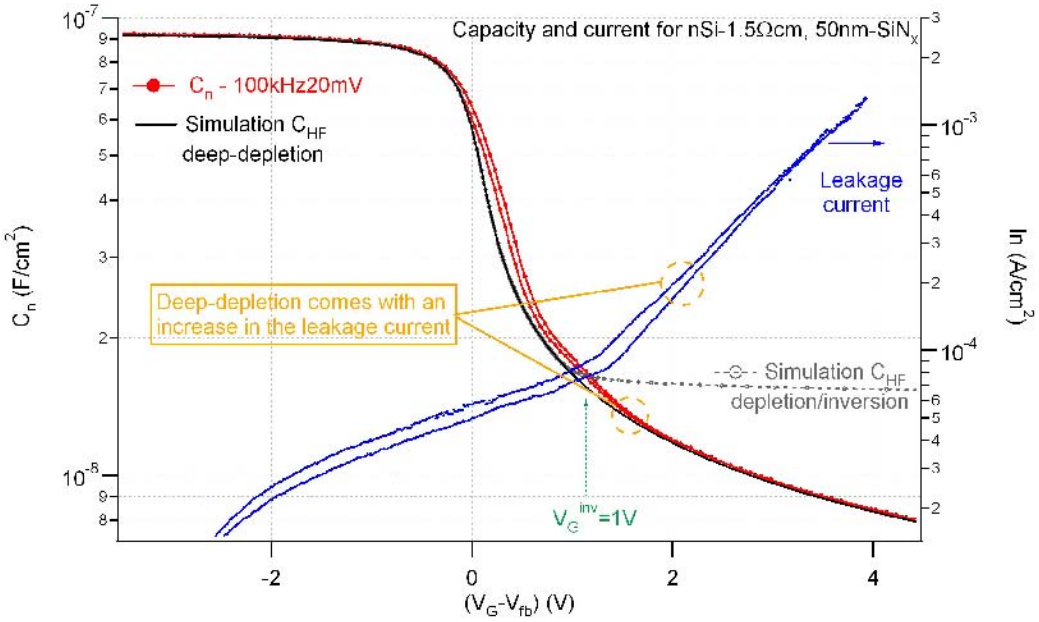

Figure 5.10: C_T-V_G measurement for $nSi - 1.5\Omega cm$ and $50nm - SiN_x$ MIS device (left axis) compared to its I-V characteristics (right axis). Simulation of an ideal C-V curve for high frequency modulation in the deep-depletion case for an ideal MIS device (using $1.5\Omega cm$ and series capacitor of $93nF/cm^2$ simulation values) is shown.

It has been shown that the MIS devices present positive leaking currents under strong positive polarization (Figs. 5.2 , 5.3). At these potentials, the nSi is in the inversion or deep-depletion regime. In Fig. 5.10 the high frequency capacity (left axis) and the current measurements (right axis) are plotted together as function of the applied potential. The high frequency capacity simulations for the inversion case (gray dotted line) and deep-depletion case (black solid line) are as well represented. As before, the experimental curve follows the deep-depletion case, clearly seen for potentials over $2V$. The interesting thing to observe is the rise of the current when the MIS device falls into deep-depletion regime (for potentials over $1V$). The inversion

regime is expected to start at $V_G^{inv} \approx 1V$ where the simulation curve for the inversion case (gray line) begins to saturate and tends to a constant value. At this potential the current shows a change: a strong increase with increasing potential. This current corresponds to holes leaking from the semiconductor to the gate electrode through the SiN_x layer (or electrons flowing in the opposite direction) and might be the reason for the deep-depletion characteristics observed in the MIS devices.

Fig. 5.11 shows that the high frequency capacity curves for the MIS devices as function of the applied potential follow the deep-depletion case in good agreement with the deep-depletion theoretical simulations.

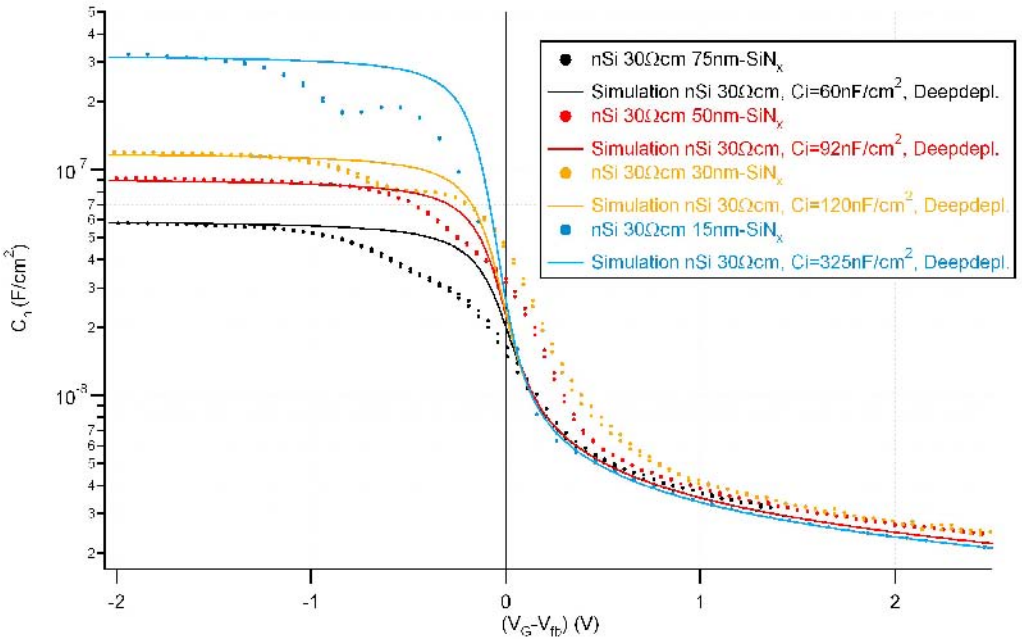

Figure 5.11: High frequency C_T measurements as function of the applied potential for MIS samples with $nSi - 30\Omega cm$ with $70nm$, $50nm$ and $30nm$ and $15nm - SiN_x$ insulator. The voltage is expressed as $(V_G - V_{fb})$ in order to compare them with the simulated curves (solid lines) for the deep-depletion case.

The experimental curves differ from the simulated curves at potentials around flat band $(V_G - V_{fb}) \approx 0$. This is ascribed to charge trapping at the nSi/SiN_x interface. In MIS devices a high density of traps is found at the heterojunction between the semiconductor (Si) and the insulator (SiN_x)

(section 3.1). These traps capture electrons or holes from the semiconductor when these are in a near position (that is at the Si/SiN_x interface) and retain them for a certain time. Traps present a charge depending on their nature and its electronic state (occupied or not by an electron). Under thermal equilibrium conditions, traps contribute with a charge Q_{it} to the total surface charge which is located at the interface. So the gate charge Q_G must compensate the total charge at the Si/SiN_x interface and that is not only the Q_{sc} but $(Q_{sc} + Q_{it})$ (Eq. 3.9). With this, the high frequency capacity from a MIS device as function of the gate potential V_G seems stretched out (see Eq. 4.22), compared to the theoretical (ideal) value (shown by the simulated curves in Fig. 5.11).

In section 5.3.4 the extraction and analysis of the interface state density (the density of trapping states and its energy position) is treated.

5.3.3 The frequency dependence of C_i and the effect of a non ohmic rear contact

In ideal MIS devices the C_i value can be experimentally determined by measuring the total capacity under strong accumulation conditions. In the accumulation regime the semiconductor capacity is much higher than the insulating one. The series configuration of both makes that the main potential drop is in the insulating layer. Under strong accumulation conditions, the semiconductor acts practically as a metal plate due to the high density of charge carriers that accumulate at the semiconductor/insulator interface and the high velocity of injection and extraction of majority charge carriers by the rear contact.

With this, the capacity measured in accumulation regime is C_i which is not potential dependent and its value is determined by the dielectric constant of the insulating media ϵ_i and its width d (approximation of the plane-parallel capacitor). The characteristic relaxation time of dielectrics is in the $ns - ps$ ranges. It is expected that the ϵ_i value does not present a frequency dependence up to the GHz range and thus,is constant and with its stationary characteristics when voltage perturbations up to $1MHz$ are used to measure its capacity. In Fig. 5.12 the total capacity as function of the applied potential is shown for the MIS device $nSi - 30\Omega cm$ with $50nm - SiN_x$. The different curves correspond to different modulation frequencies. It is observed

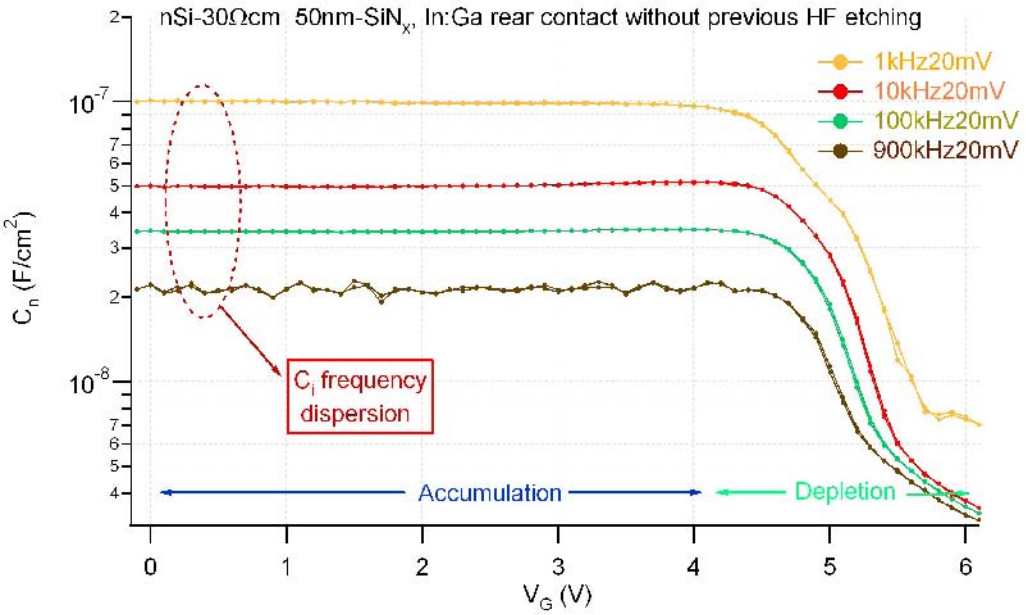

Figure 5.12: C_T against V_G for different modulation frequencies for the MIS device $nSi - 30\Omega cm$ with $50nm - SiN_x$.

that the C_T under accumulation conditions (between $0V$ and $4V$) is constant as function of the applied potential (as expected) but its value depends on the modulation frequency, decreasing with increasing frequency. This characteristic does not fit with the MIS model. At these potentials the total capacity should be the insulator one C_i and its value does not vary with the modulation frequency until the GHz range.
At more positive potentials (between $5V$ and $6V$) the C_T-V_G curves converge into a frequency independent value corresponding to potentials in the depletion regime.

This characteristic has been observed for almost all the MIS devices measured and affects the calculation and interpretation of the MIS structure characteristic parameters (C_i, V_{fb}, N_D, D_{it}). What can be the reason of the deviating behavior of a MIS device under accumulation conditions?
In order to have a better view of the frequency dependence of the MIS device under accumulation conditions, impedance spectroscopy measurements have been done on the sample. In impedance spectroscopy measurements the frequency of the voltage perturbation is swept and the real and imaginary components of the current are registered as function of the modulation

frequency. The analysis of the impedance spectra can lead to information about the different kinetics involved when the system is perturbed by a voltage change. Fast electronic processes can react (and follow) high frequency perturbations while slow processes only react to those modulation frequencies which are slow enough for their kinetics. So, the impedance of the system changes as a function of the modulation frequency and the analysis of its spectra can lead to the identification of different electronic processes, with characteristic time responses.
It is useful to compare the experimental results of real systems to those calculated for the so called "equivalent circuits". The equivalent circuit consists of linear electronic elements (resistors, capacitors and inductors) combined in a certain configuration that can simulate the spectra measured (section 4.1.1). Usually more than one equivalent circuit can fit the impedance spectra but only those circuits which have a certain physical meaning are of interest [36].

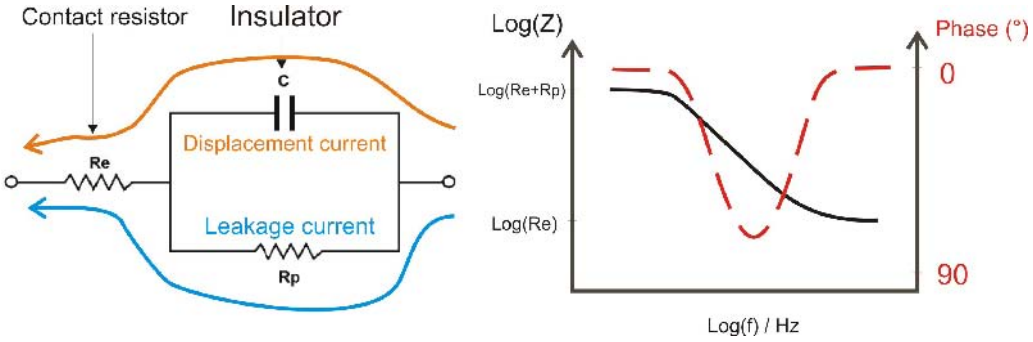

Figure 5.13: On the left side, the equivalent circuit for a MIS device under accumulation conditions. Ideally, only the processes occurring in the insulating layer as storage and leakage of charge carriers contribute to the impedance. The series resistor reflects the contacting of the insulating layer. On the right side the impedance modulus and phase spectra of the circuit is schematically displayed.

Under accumulation conditions the main potential drop is in the insulating layer and thus, only the insulator properties are expected to be present in the impedance spectra. The simplest equivalent circuit for an insulating layer is a capacitor. If the insulating layer presents a leakage current, then the simplest equivalent circuit will be the parallel combination of a resistor (due to the leaking current) and a capacitor (due to the charge carriers storage at the limits of the dielectric). This circuit is called *RC*-circuit and is

represented in Fig. 5.13. The extra series resistor represents the contacting elements to the insulating layer (the $In : Ga$ rear contact, the Si wafer resistivity and the aluminum gate electrode and cables).

In Fig. 5.14 the modulus and phase of the impedance is plotted as function of the modulation frequency between $1Hz$ and $1MHz$ for three different DC potential polarizations: $0V$, $2V$ and $4V$.

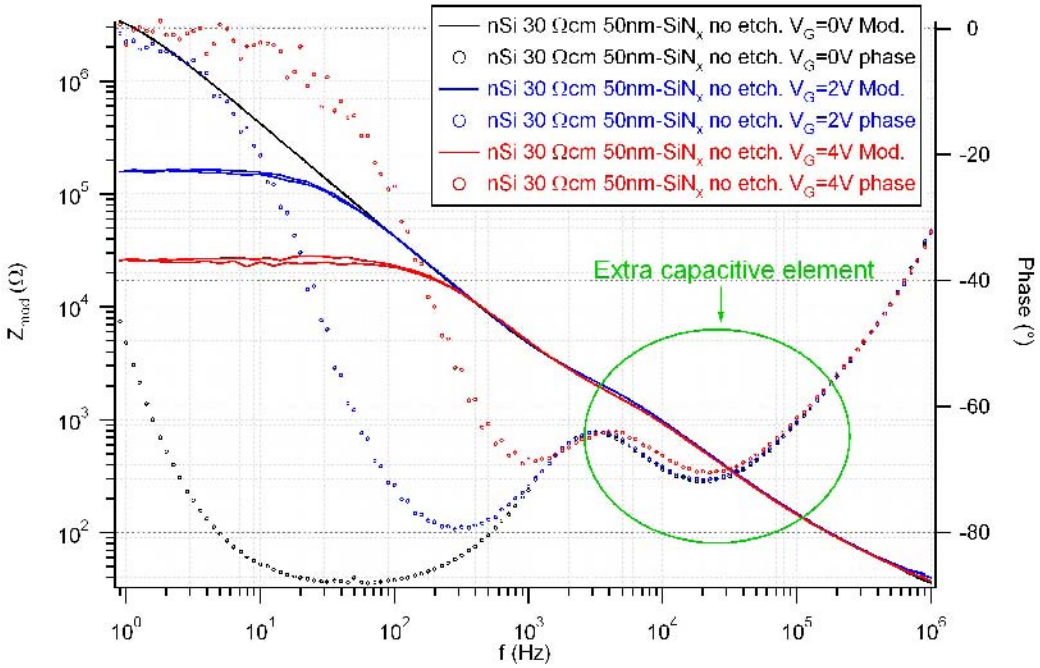

Figure 5.14: Modulus (solid lines, left axis) and phase (dotted lines, right axis) as function of the modulation frequency for the $nSi - 30\Omega cm$ with $50nm - SiN_x$ MIS device. The spectra are taken for three different DC polarizations: $0V$ (black lines), $2V$ (blue lines) and $4V$ (red lines).

The impedance response measured in Fig. 5.14 cannot be simulated with the simple circuit defined before (Fig. 5.13). All spectra present two capacitive elements: the phase of the impedance presents two minimums; one at low frequencies (between $1Hz$ and $1kHz$) and a second one at high frequencies (between $1kHz$ and $1MHz$). The RC-circuit (Fig. 5.13) can only represent one of these capacitive behaviors, not both. Another, more complicated equivalent circuit is required to simulate the spectra. The most simple one containing two capacitive elements is the series combination of two RC-

circuits as indicated in Fig.5.15.
The phase minimum at low frequencies shows a voltage dependence. It is less pronounced when the DC polarization increases: the device becomes more "conductive" with higher faradaic current and a decrease in its impedance (see that the impedance modulus diminishes too in Fig. 5.14). This is in agreement with the experimental I-V curves measured in Fig. 5.3 where the current slightly increases with increasing potential.
The phase component at high frequencies does not show any potential dependence. A new equivalent circuit is needed in order to simulate the spectra. The most simple one containing two capacitive elements is the series combination of two circuits as the one presented in Fig. 5.15.

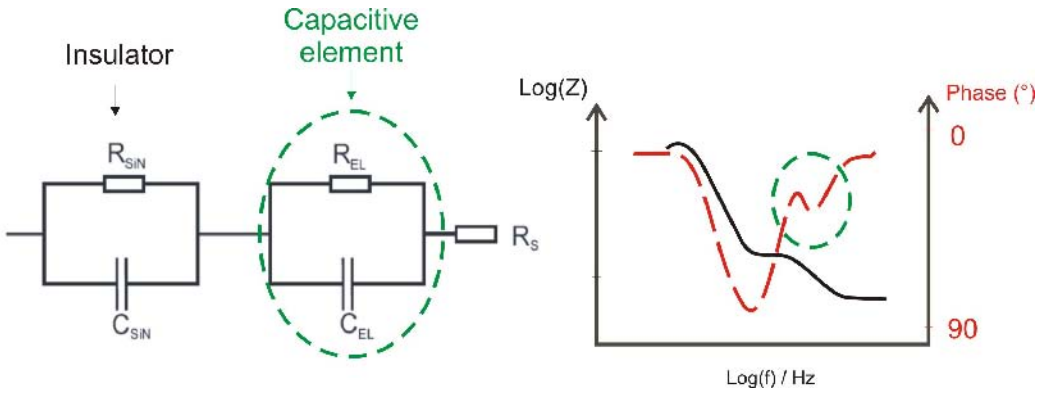

Figure 5.15: On the left side, the equivalent circuit used to fit the measured spectra (Fig. 5.14). Two capacitors are needed to fit the two phase minimums. C_{SiN} and R_{SiN} are the elements referring to SiN_x while C_{EL} and R_{EL} are the elements which lead to the extra capacitive behavior. R_s is the series ohmic contact of the cell.

The equivalent circuit in Fig. 5.15 was used successfully to fit the impedance spectra at $0V$ by use of the $Zview$ program. The results obtained are presented in Tab. 5.3 and plotted in Fig. 5.16.

The $50nm - SiN_x$ insulating layer is characterized in the equivalent circuit of Fig. 5.15 by a capacitor of $106nF/cm^2$ and a parallel resistor of $4.5M\Omega$. The capacity has the same value as the capacity measured at $1kHz$ perturbation frequency in Fig. 5.12. $1kHz$ is about the highest frequency which falls into the slow response regime of the MIS device (see in Fig. 5.14 that $1kHz$ lies in the frequency range of the phase minimum at low fre-

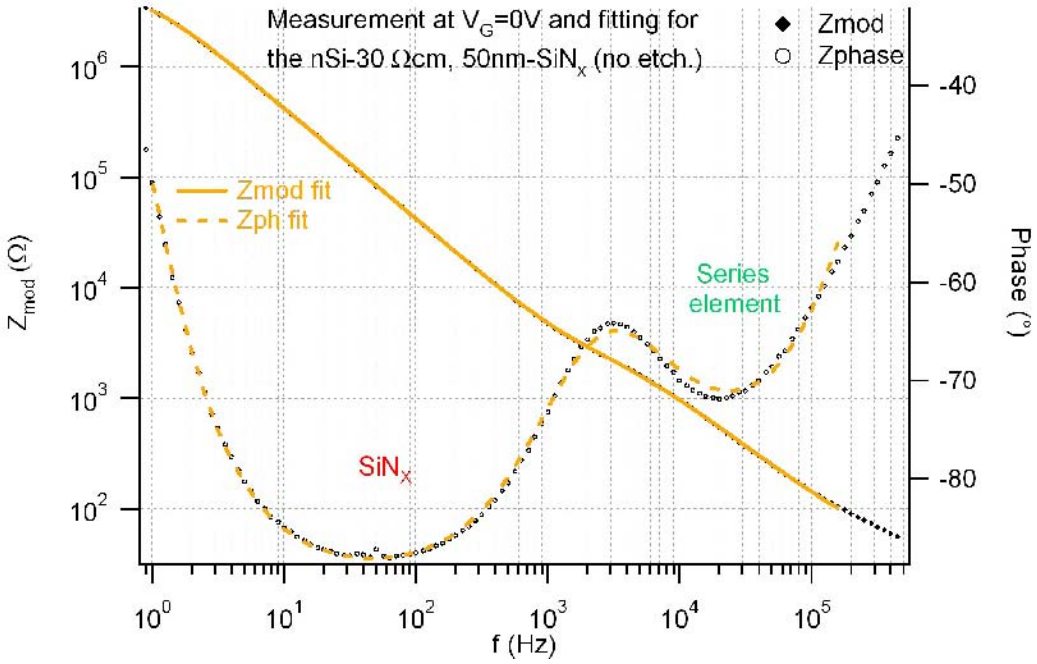

Figure 5.16: Modulus and phase of the impedance as function of the modulation frequency for the $30\Omega cm$, $50nm - SiN_x$ MIS device, measured at $0V$ DC polarization (black lines). The spectra resulting from the equivalent circuit given in Tab. 5.3 is plotted in orange lines.

$R_S\,(\Omega)$	$R_{EL}\,(\Omega)$	$C_{EL}\,(nF/cm^2)$	$R_{SiN_x}\,(M\Omega)$	$C_{SiN_x}\,(nF/cm^2)$
42 ± 1	1608 ± 27	288 ± 15	4.5 ± 0.1	106 ± 1

Table 5.3: Values obtained for the equivalent (Fig.5.15) circuit by "$Zview$" fitting program of the experimental data of Fig. 5.14 at $0V$. The capacity values were normalized to the gate electrode surface.

quencies). The resistor is related to the leakage current through the SiN_x. This resistor value is small for an insulator material (usually characterized by $\rho_{ins} \geq 10^{12}\Omega cm$ [1]). This small resistance might be a consequence of the high density of defects in the SiN_x volume which allow the charge transport under the presence of a field (section 5.3.1). The $RC = \tau$ product has time units and is related to the time needed for a charge, initially accumulated at the capacitor, to be transfered through the resistor [64], [36] (as leakage current) and for the SiN_x is $\tau_{SiN_x} = 0.5s$.

The extra series RC-circuit presents a higher capacitor value ($288nF/cm^2$) with a parallel resistor three orders of magnitude smaller ($1.6k\Omega$) giving a characteristic time about $\tau_{el} = 0.5ms$. The electrical response of this circuit is three orders of magnitude faster than the one of the SiN_x. It is for the range of frequencies where this element is active that the capacity under accumulation conditions differs from the C_i value of $106nF/cm^2$ (see Fig. 5.12).

The equivalent circuit suggest that there is another element that stores charge carriers for short times. The electrodes at the MIS extremes can introduce this effect. During processing the contacts an undesired lossy layer can be formed between materials [65]. The aluminum contact on SiN_x can change the dielectric properties of the insulator at the surface. Silicon wafer surface cleaning and processing previous to the SiN_x deposition or the $In : Ga$ contacting can lead to the same effect.

$In : Ga$ eutectic paint is commonly used as the rear contact in silicon based electrochemical cells [66], [67], [68]. It is easy to apply and does not need a tempering step which may modify the electrode characteristics. $In : Ga$ contact paint is active through the dangling Si bonds, charge carriers are exchanged by interface states. The paint is applied after scratching gently the rear Si surface in order to enhance the number of dangling bonds in contact with the $In : Ga$. Si wafers have a native SiO_2 thin layer at the surface which must be removed to make a better contact with the Si crystal. The contacts of the samples presented above were prepared under the assumption that the scratching step removes this native oxide. In order to be sure that the native oxide is really removed the rear Si surface can be additionally etched before deposition of the $In : Ga$ paint with a HF solution. This was tested for the MIS device presented in Fig. 5.12. The rear contact of the MIS device was removed, the wafer was cleaned with alcohol and milli-Q water, scratched again and etched with $20\% HF$ solution previous to the application of the $In : Ga$. The MIS device with this improved back contact was measured by impedance spectrocopy under accumulation conditions.

Fig. 5.17 shows the modulus and phase of the impedance as function of the modulation frequency at $0V$, $2V$ and $4V$ DC polarization for the MIS device with the improved rear contact. This time only the phase minimum at low modulation frequency is found. The impedance spectra shows again a dependence of the DC polarization. The spectra can be fitted by a single

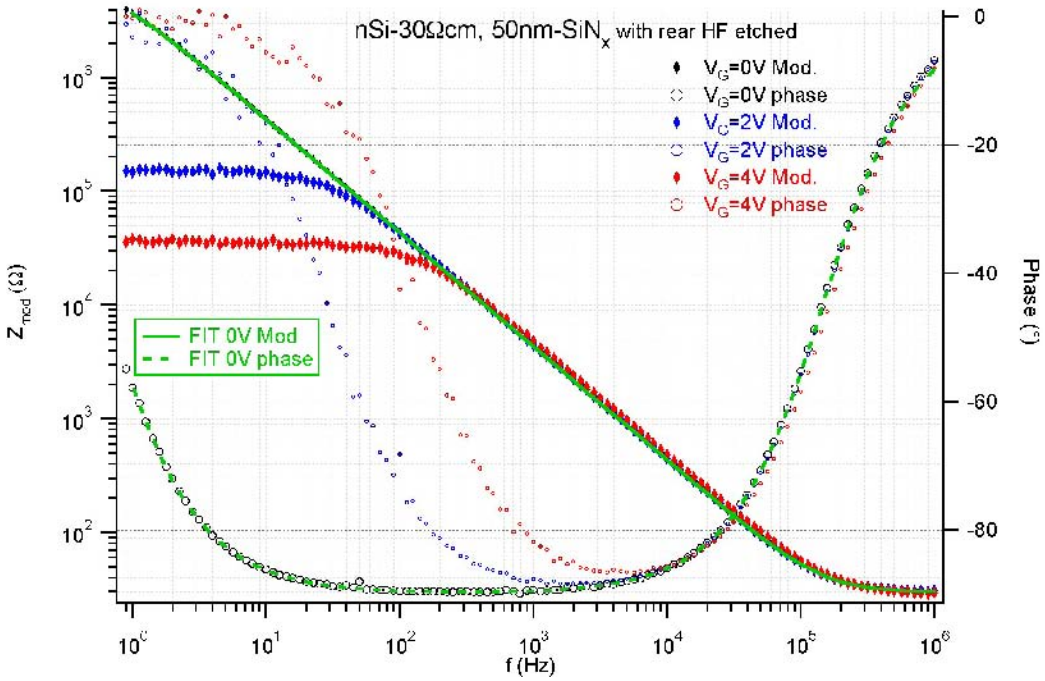

Figure 5.17: Impedance spectra for $nSi - 30\Omega cm$ with $50nm - SiN_x$ MIS device with improved rear contact at three stationary voltage polarizations under accumulation condition.

RC-circuit as given in Fig.5.13. The results of the fittings with the equivalent circuit of Fig. 5.13 at $0V$ polarization are given in Tab. 5.4 and are shown by green lines in Fig. 5.17 fitting properly with the measured impedance (black markers).

$R_S\,(\Omega)$	$R_{SiN_x}\,(M\Omega)$	$C_{SiN_x}\,(nF/cm^2)$
30 ± 0.1	6 ± 0.1	105 ± 1

Table 5.4: Values obtained for the equivalent circuit (Fig.5.13) by fitting with "$Zview$" fitting program of the MIS device with improved rear contact of Fig. 5.17 at $0V$. The capacitor values were normalized to the gate electrode surface.

After the modification of the rear contact the faster RC-circuit is not needed to fit the spectra. Only the SiN_x insulating layer characteristics are

the ones measured, as expected for a MIS device under accumulation conditions. The SiN_x is characterized again approximately by the same capacity ($C_{SiN_x} = 105nF/cm^2$) and resistance ($R_{SiN_x} = 6M\Omega$) values indicating that its storage and transport of charge carriers has not varied.

In Fig. 5.18 the total capacity of the MIS device with the improved rear contact as function of the applied potential is given. Now, the frequency dependence of the total capacity under strong accumulation conditions has disappeared converging approximately to the same capacity value of the SiN_x layer (about $100nF/cm^2$). For the device with improved rear contact the contribution to the total capacity due to the interface states for potentials around flat band is clearer. The capacity curves differ from the fastest frequency curve ($900kHz$), showing a deviation increasing with decreasing modulation frequency. Interface states contribute to the total capacity by trapping and emission of charge carriers at the Si/SiN_x interface. This process has characteristic times given by the capture and emission time of charge carriers (which depends on the nature of the interface state). At $900kHz$ modulation frequency, the perturbation is too fast to let the trapping/emission of charge carriers to happen and no contribution to the capacity is measured. At lower modulation frequencies, the faster interface states are able to follow the modulation and thus, contributing to the capacity. Unfortunately, the MIS devices could only be measured at high modulation frequencies under depletion/deep-depletion conditions. The leakage current in deep-depletion regime is high (compared to the displacement current magnitude) and a higher current range had to be used to measure the C_T-V_G curves when measuring at low frequencies. This excludes accurate measurements at low frequencies. This is already seen for the $1kHz$ curve in Fig. 5.18 at deep-depletion potentials (over $6V$). The measurement is not accurate enough to measure capacities under $40nF/cm^2$.

- In this section the origin of the complicated behavior of the capacity of the MIS devices under accumulation conditions was found. Impedance spectroscopy methods were used to characterize the sample under accumulation conditions and find the origin of the non ideal behavior. It has been concluded that for the use of $In : Ga$ as rear Ohmic contact for Si based devices an etching step during the manufacture of the rear contact is necessary. Etching the rear surface with $20\%HF$ solution after the scratching step and previously to the $In : Ga$ application removes the capacitive behavior of the rear contact.

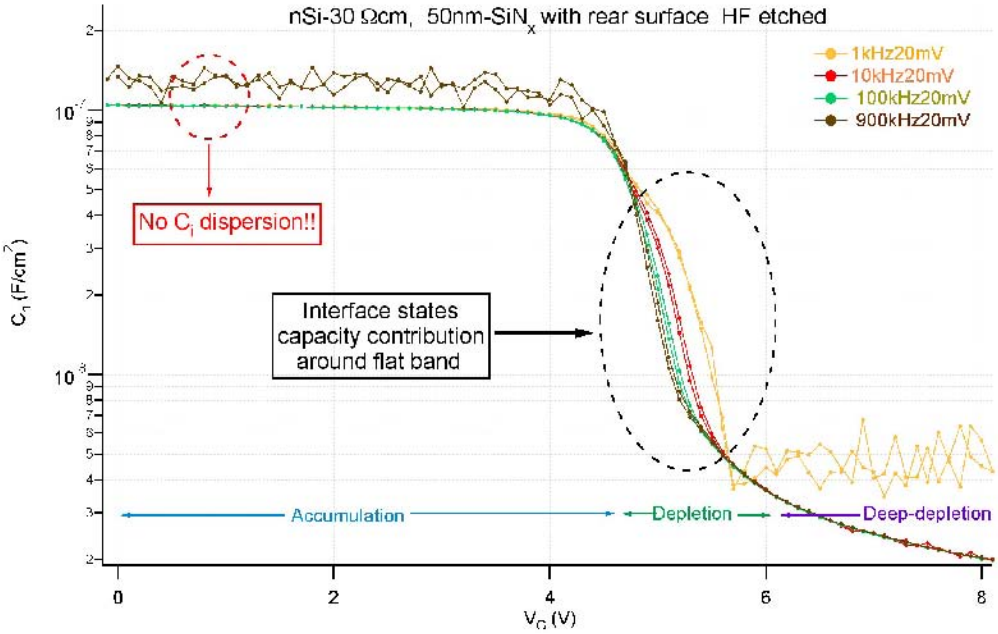

Figure 5.18: C_T against V_G for different modulation frequencies for the MIS device $nSi - 30\Omega cm$ with $50nm - SiN_x$ with improved rear contact.

5.3.4 D_{it} extraction by low-high modulation frequency capacity measurements

In Fig. 5.19, the interface density experimentally obtained from the extraction of the interface state capacity by use of the high and low frequency curves is given (section 4.2.4). Unfortunately the lowest useful modulation frequency was $1kHz$. This frequency is still too high to contain the total capacity contribution due to the interface states and the minority charge carriers.

A simulation program was used to find a distribution of interface states (the calculation done by the program is briefly explained in section 6.3.2.5). The curve given by the simulation is the red line in Fig. 5.19. For the simulation a constant value, an exponential distribution (with maximum at the bottom of conduction band) and a Gaussian distribution of acceptor-like states to simulate the experimental value found:

$$D_{it}^{a}(E) = 3 \cdot 10^{10} + 6 \cdot 10^{14} e^{-\frac{(E_c - E)}{0.03}} + 2.9 \cdot 10^{11} e^{-\left(\frac{E-0.85}{0.25}\right)^2} \qquad (5.6)$$

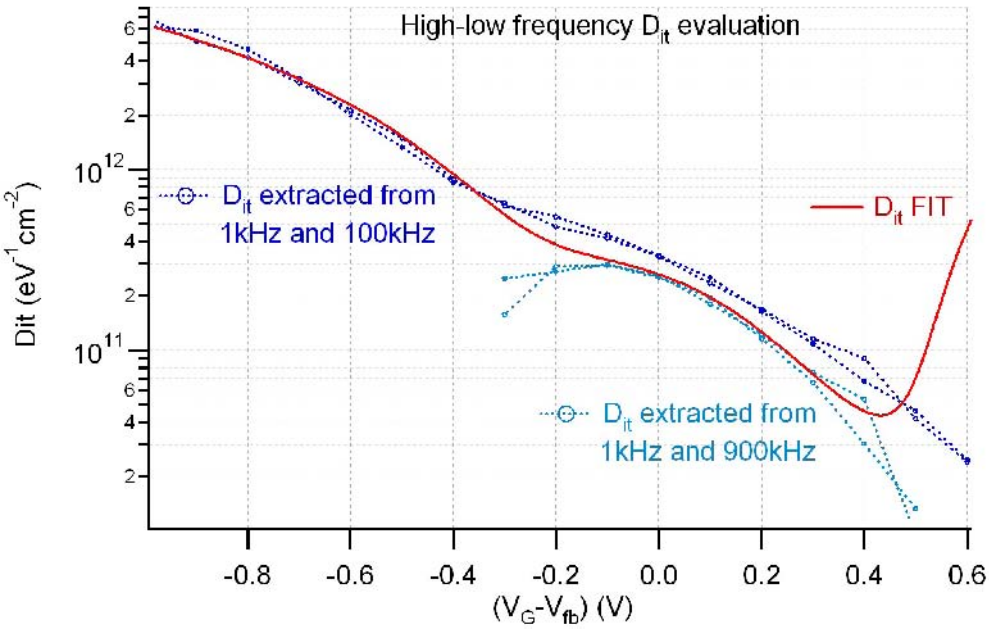

Figure 5.19: D_{it} as function of the applied potential $(V_G - V_{fb})$ obtained by the high-low frequency method. The use of two different curves ($900kHz$ and $100kHz$) was necessary to extract the exponential-like interface distribution.

In Fig. 5.20 are shown the high frequency ideal curve for the device (black line), the low frequency total capacity curve (green line) and the high frequency total capacity curve (red line). The stretching of the high frequency curve is indicated by the red arrows. This is an effect of the stationary equilibrium between the charge at the gate electrode and the total charge at the Si/SiN_x interface (involving Q_{it}). The capacity contribution due to the interface states is indicated by the green arrows. Only those states fast enough to follow the $1kHz$ modulation contribute to the measurement. This complicates the proper fitting of the curves because the slower states are not able to be extracted from the high-low capacity measurements but they contribute to the stretching of the C_T-V_G curve at high frequencies.

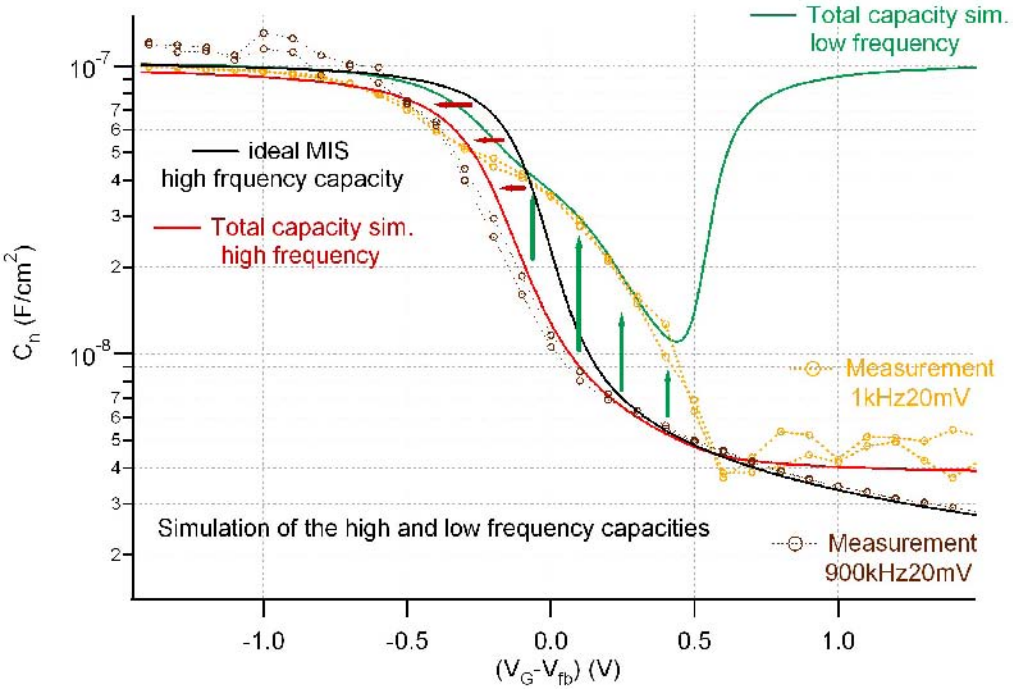

Figure 5.20: The high (red line) and low (green line) simulated capacity curves with the interface states effect are plotted as function of the applied potential $(V_G - V_{fb})$. The measured curves at $900kHz$ (brown) and $1kHz$ are as well plotted. The capacity contribution due to the gaussian distribution of interface states (green arrows) and the stretching of the ideal curve (red arrows) is indicated.

Chapter 6

Capacitance and conductance characterization of Si/SiN_x based electrochemical cells

6.1 Introduction

In this chapter, cyclic voltammetry and impedance measurements as function of the applied potential in combination with microwave reflection conductivity measurements (MWR) are presented for Si/SiN_x based electrochemical cells.
In cyclic voltammetry, current as a function of the applied potential is registered. The total capacity of the cells as a function of the applied potential (C_T-V) is used to extract doping level of the Si-wafers, flat band potential of the cells and interface state density at the Si/SiN_x interface. MWR in combination with C_T-V measurements gave complementary information about the cell working regime.
In contrast to MIS structures where the Si/SiN_x heterojunction is front contacted by an aluminum gate electrode on top of the SiN_x and an Ohmic contact on the rear Si surface (section 5.3.3), in the Si/SiN_x electrochemical cells the SiN_x is front contacted by an electrolyte.
This cell configuration, with the absence of a metallic front contact, allowed successfully the application of MWR at the cells under external polarization.

Contacting the front SiN_x with an electrolyte introduces possible electrochemical reactions at the electrode/electrolyte interface. This can effect the Si/SiN_x interface but it is of special interest when considering the Si/SiN_x

heterojunction as a candidate for photo-catalytic applications [40], [69].

6.2 Experimental

The working electrodes were Si/SiN_x heterojunctions. Two different nSi wafers were used (as for the MIS devices):

- Mitsubishi $1.5\Omega cm$, $< 111 >$ oriented and $245\mu m$-thick
- Wacker $30\Omega cm$, $< 100 >$ oriented and $530\mu m$-thick.

and a $p - Si$ wafer was used:

- Wacker $100\Omega cm$, $< 100 >$ oriented and $504\mu m$-thick

Different thicknesses of SiN_x layer were grown by the PECVD method as described in [28].

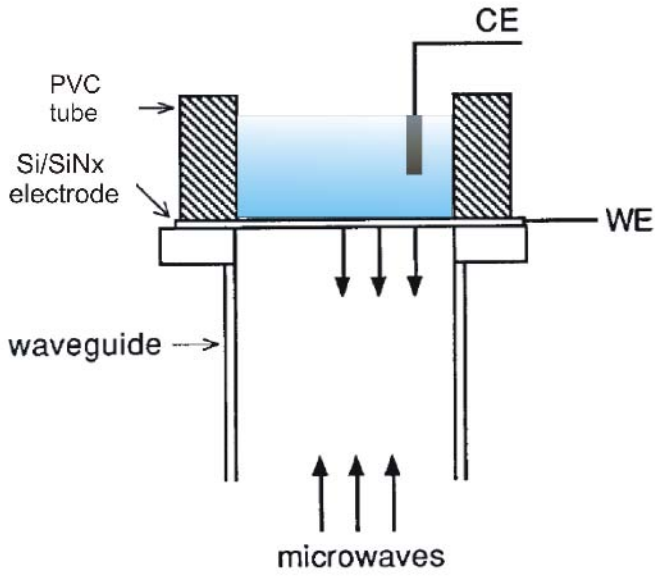

Figure 6.1: Schema of nSi/SiN_x electrochemical cell built on the Ka-band microwave guide used for MWR measurements (illustration from [70]).

The electrochemical cells were constructed as indicated in Fig. 6.1. The rear silicon face of the Si/SiN_x heterojunction (bare Si side) was contacted with $In : Ga$ eutectic paint and glued with epoxy to a special copper Ka-band substrate. A PVC tube was glued at the opposite side onto the SiN_x as a container for the electrolyte and a platin wire was used as counter electrodes. The rear $In : Ga/Si$ contact was properly manufactured with the HF etching step needed to accomplish its ohmic function.

All MWR measurements were done in a Ka-band microwave system.
The electrolytes were composed of Milli-Q water ($18,2M\Omega$) with KCl (from $1M$ to $4M$) in order to enhance the electrolyte conductivity (conducting salt).
All measurements were performed in a three electrode setup. A saturated calomel electrode (SCE) was used as reference electrode (241mV v.s. NHE) and a platinum wire as counter electrode. All potentials in the figures refer to the SCE (if not otherwise indicated).
For the cyclic voltammetry measurements the scanning velocities ranged between $10mV/s$ and $1V/s$. For the impedance measurements, the DC (bias) potential polarization was applied point per point. The AC potential was modulated with frequencies between $1MHz$ and $1Hz$ and an amplitude of normally $20mV$ and occasionally $100mV$ was applied.

6.3 Results

6.3.1 I-V characteristics

Two different kinds of current contribute to the current measured in cyclic voltammetry: the faradaic currents (I_f) and the displacement currents (I_d). The total current (I_T) is expressed as follows when the potential uniformly changes with a constant scan velocity v_{scan} ([64]):

$$I_T = I_f + I_d = I_f + \frac{dQ_c}{dt} = I_f + \frac{dQ_c}{dV}\frac{dV}{dt} = I_f + C \cdot v_{scan} \qquad (6.1)$$

The displacement current is related to the capacity C of the cell: it is the charging current due to the change of the potential. This term is important when faradaic currents are small and the scanning velocity is high.
The total capacity of an electrochemical cell can be described by two capacitors in series connected. One capacitor refers to the total capacity of

the electrode and the second one is the capacity of the electrolyte. The distribution of the ions in the electrolyte can be considered homogeneous and macroscopically neutral in the absence of external electric fields. Only in the region adjacent to the electrode the ion distribution is not homogeneous [36], [64]: under electrode polarization, positive or negative charges from the electrolyte (ions or dipolar molecules) are adsorbed at the electrode forming a non-neutral diffuse layer screening the electrode charge. There are different models that describe this electrolyte charge distribution adjacent to the electrode. Experimentally, the double layer capacity C_{dl}, formed by the charges at the electrode at one side and the charges in the electrolyte layer at the other side, lies usually between $20\mu F/cm^2$ and $40\mu F/cm^2$ [64]. This capacity is about two orders of magnitude higher than the capacity of the Si/SiN_x electrode. So, the total capacity measured in the cell will be mainly determined by the capacity of the electrode.
A capacitive current is expected to be proportional to the Si/SiN_x capacity. Using ramp-like voltage scanning profiles, it will present a clear symmetry with respect to the (potential) axis: the capacitive current will be positive for positive scan velocities and negative for negative scan velocities.

A faradaic current, in terms of electrochemistry, requires charge transfer by the reduction or oxidation of chemical species [64], [41]. In the electrochemical cell, it is the charge transfer from the electrode to chemical species present in the electrolyte.
In contrast to the capacitive currents, faradaic currents do not present this symmetry with respect to the (potential) axis: the charge transfer direction does not depend on the sign of the scanning velocity.

Faradaic and capacitive currents are characteristic in different voltage ranges for the Si/SiN_x electrodes in contact with aqueous electrolytes:

6.3.1.1 Faradaic current regimes

A faradaic current was found in two potential regimes: at potential more negative than $-1V$, a negative faradaic current related to the proton reduction was observed (shown in Fig. 6.2); at positive potentials exceeding the flat band regime a positive faradaic current related to the oxygen formation and SiO_2 formation was observed (shown in Fig. 6.3).

In Fig. 6.2 the cyclic voltammetry measurements at negative potentials

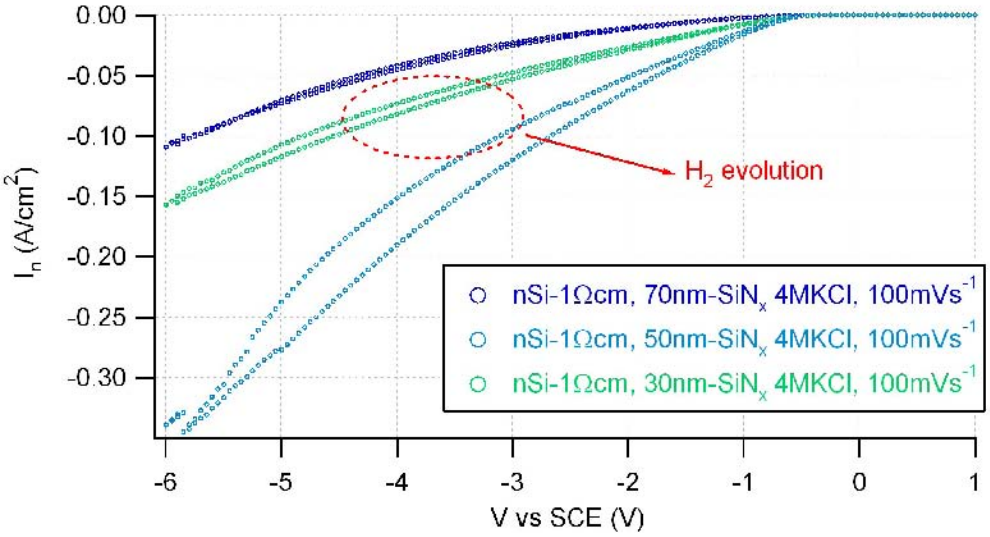

Figure 6.2: The current measured at negative potentials (cathodic regime) for a $nSi-1.5\Omega cm$ sample with different SiN_x thicknesses in $4MKCl$ electrolyte at a $100mVs^{-1}$ sweep rate. The current measured at negative potentials is accompanied by H_2 gas evolution.

for three different Si/SiN_x electrodes in contact with a $4MKCl$ aqueous electrolyte are shown. All electrodes were $nSi-1.5\Omega cm$-wafer but with different SiN_x thickness ($70nm$, $50nm$ and $30nm$). The SiN_x thickness does not seem to be determining for the current magnitude. This result was already found for MIS devices (5.3.1).
The current is negative and high (up to $0.3A/cm^2$ at $-6V$). Negative currents indicate electrons flowing from the electrode to the platin wire. The current was followed by gas evolution. Considering that in cathodic regime positively charged species are attracted to the electrode and that K^+ ions reduction does not produce a gas evolution, the most probable gas observed is H_2 due to the reduction of the protons present in the aqueous electrolyte.

With this, the SiN_x layer seems to be suitable for catalytic applications allowing the electron transfer to reduce species (H^+) in the electrolyte. The main reason to use an insulating layer on top of a semiconductor in photo catalytic applications is to protect the semiconductor for direct corrosion by the electrolyte. The conditions for a suitable insulating layer are on the one hand to permit the charge transfer to reduce/oxidize species and on the other

hand to be chemically stable in contact with the electrolyte, protecting the semiconductor from corrosion.
Non-reproducible I-V curves point out that the Si/SiN_x is not chemical stable.
In Fig. 6.3 are given the consecutive cycles between $-2V$ and $8V$ for a $nSi - 30\Omega cm$ with $70nm - SiN_x$ electrode in an aqueous electrolyte. Two cases are shown: the first I-V curves (red markers) were measured before hydrogen evolution at negative potentials took place at the electrode and the second I-V curves were measured after the electrode showed hydrogen evolution at negative potentials (blue markers).
A change in the I-V characteristics is observed before and after hydrogen evolution at the electrode. Before hydrogen evolution (red markers) the current presents only a capacitive component while after hydrogen evolution a faradaic component is observed at potentials over $6V$ (blue markers). This faradaic current is decreasing for every consecutive cycle and presents very similar I-V characteristics observed when SiO_2 is chemically grown at bare Si electrodes in contact with aqueous electrolytes [71].
The SiO_2 formation occurs when holes from the Si come in contact with water molecules [18]:

$$Si + 2H_2O + 4h^+ \longrightarrow SiO_2 + 4H^+ \tag{6.2}$$

This chemical reaction is simplified, usually the electrochemical oxidation of Si involves the incorporation of the hydroxide group (OH^-) into the Si dangling bonds with the form $Si\,(OH)_4$ which later is oxidized in a second step. Partly oxidation of Si is also possible (leading to SiO^{2-}). For nSi based electrodes, these reactions take place for potentials over flat band when the inversion regime is attained (over $6V$ in Fig. 6.3).
The current decreases at every new cycle due to the increase in thickness of the SiO_2 layer. As it grows (in the inversion regime) it is more difficult for the water molecules to reach Si dangling bonds [18], [71], [43].

How can that reaction take place if the Si wafer is covered by a SiN_x film protecting layer?
Considering that the SiN_x material is rather non reactive in aqueous media, the oxidation might take place at the Si surface. The hypothesis is that H_2 evolution modifies the SiN_x layer characteristics and destroys it by the effect of the gas evolution.

In Fig. 6.4 are shown two pictures of the electrode surface (measured

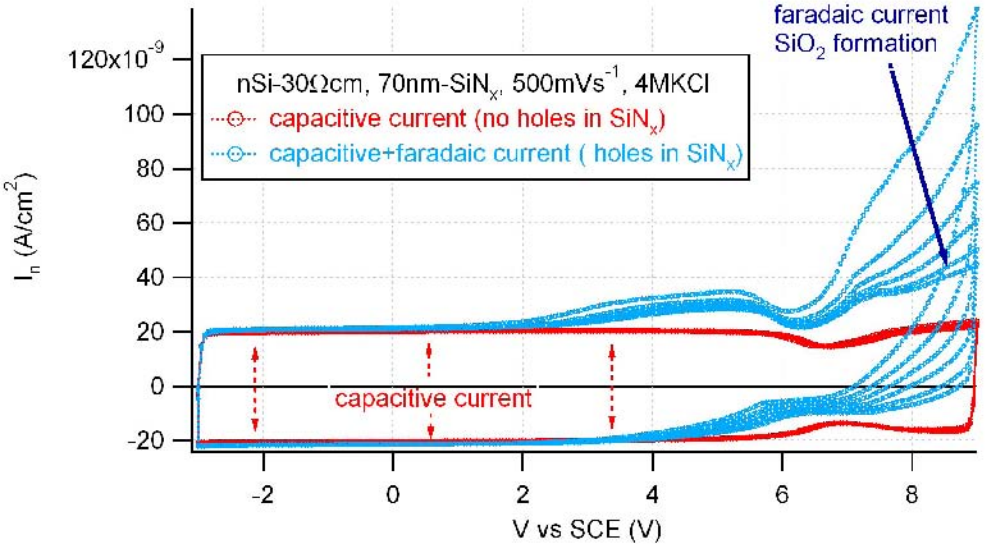

Figure 6.3: Current as function of the applied potential for an $nSi - 30\Omega cm$ with $70nm - SiN_x$ electrode in $4MKCl$. The voltage range is between $-2V$ and $8V$ without involving H_2 evolution. Two groups of curves are shown: the first group of cycles (red markers) were done before any cathodic polarization involving H_2 evolution; the second cycles group of (blue markers) were measured after driving the electrode into H_2 evolution at negative potentials.

in Fig. 6.3) after the measurements of the I-V signals at negative and positive potentials. The pictures were taken with an optical microscope Leica $DFC320$ with magnification between $2x$ and $100x$.

The pictures show two different regions on the electrode surface: an extended dark area corresponding to the $70nm - SiN_x$ layer onto the nSi (characterized by a dark color under visible light illumination) and little gold-yellow spots which correspond to the "bare" Si substrate reflecting the illuminating light. So the SiN_x layer contains pores down to the Si wafer.

The insert in Fig. 6.4 shows one of the SiN_x pores in the electrode. The SiN_x pore is about $20\mu m$ in diameter and shows a specific geometry. This geometrical structure is related to the anisotropic etching of silicon in alkaline solutions [72]. The presence of a fixed positive charge Q_f in the SiN_x layer in the $10^{12}cm^{-2}$ range makes that high positive potentials are needed in order to bring holes to the Si surface. Under high positive potentials, the

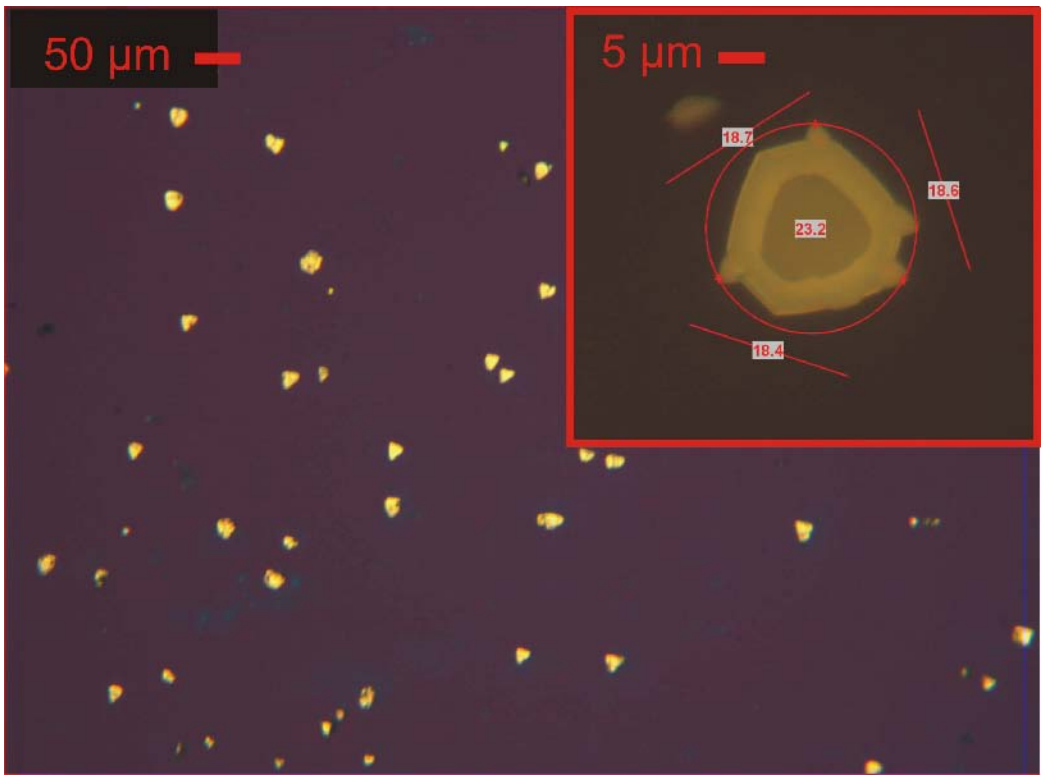

Figure 6.4: Microscope image of SiN_x surface of a $nSi-30\Omega cm$ with $70nm-SiN_x$ electrode after several cyclic voltammograms performed between $-6V$ and $8V$. Dark region corresponds to SiN_x whereas yellow dots to bare Si.

concentration of OH^- groups in the electrolyte adjacent to the silicon surface is very elevated and the solution can be considered alkaline. Thus, the etching mechanism in alkaline electrolytes is possible. That may explain the geometry found at pores. Even though this etching process may dominate at some voltage, the oxide formation is more probable when a high density of holes is present at the Si/electrolyte interface. Evidence of oxide formation is given by I-V characteristics with a current decrease at every consecutive cycle [71].

The pore formation in the SiN_x layer might happen at negative potentials due to H_2 evolution. In section 5.3.1, it has been shown that MIS devices present high leakage currents. It has been concluded that electrons (and holes) can be transported through defects in the SiN_x. Thus, electrons may reach the electrolyte in the electrochemical cell configuration. However, in

this case there is no aluminum gate electrode that collects the electrons but H^+ species waiting to be reduced. H^+ is a very small species which can easily intercalate in materials. The SiN_x deposited on silicon by PECVD methods already presents a high content of H in its volume (up to 20%) [28]. When electrons reach the required energy to reduce the H^+ species, H_2 molecules are formed in the SiN_x volume leading to "microcavities" filled with hydrogen gas. The high pressure inside the microcavity stresses mechanically the insulating layer and expands until the SiN_x breaks. This cleavage of the insulating layer is enhanced at negative potentials when H_2 evolution takes place. The fact that the observed SiN_x pores reach the Si wafer surface suggests that H_2 formation takes place at the Si/SiN_x interface as indicated by Fig. 6.5.

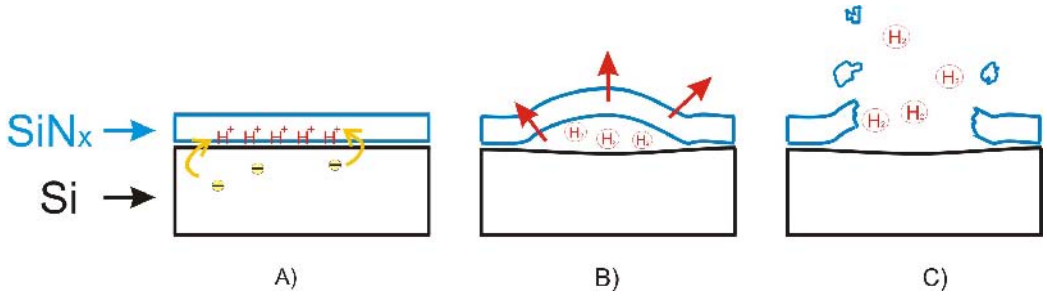

Figure 6.5: Illustration showing the SiN_x layer cleavage due to H_2 formation at the Si/SiN_x interface: A) H^+ species are reduced by electrons from the Si wafer, B) H_2 gas microcavites are formed at the interface stressing the SiN_x layer due to the gas pressure and C) the insulating layer breaks in those structural weak points leading to the pores formation.

This phenomenon has been observed previously in Si semiconductors where H was implanted at the wafer surface [73], [74] and is extensively used by the industry for low power, voltage and high speed electronic devices based on the silicon-on-insulator (SOI) technology [75].

- These results suggest that SiN_x insulating layers on Si wafers are not suitable for catalytic purposes, at least in aqueous electrolytes due to the destruction of the SiN_x insulating layer by H_2 gas formation.

- However, SiN_x (in the absence of pores) is a good corrosion protection. It protects the silicon wafer from the contact with the electrolyte and shifts the corrosion reactions to high positive potentials. The last fact

is a consequence of the fixed charge present in the SiN_x which pushes the holes away from the silicon surface.

6.3.1.2 Capacitive current

A capacitive current is observed in the potential range where no H_2 evolution takes place (below $-2V$) and no corrosion at positive potentials happens (expected in inversion regime). This last process depends on the onset potential of the inversion regime (related to the Q_f magnitude) and the quality of the SiN_x insulating layer (density of pores). In Fig. 6.6 the I-V characteristics between $3V$ and $8V$ for different scanning velocities have been measured for an $nSi - 1.5\Omega cm$ with $50nm - SiN_x$ electrode in $4MKCl$ electrolyte.

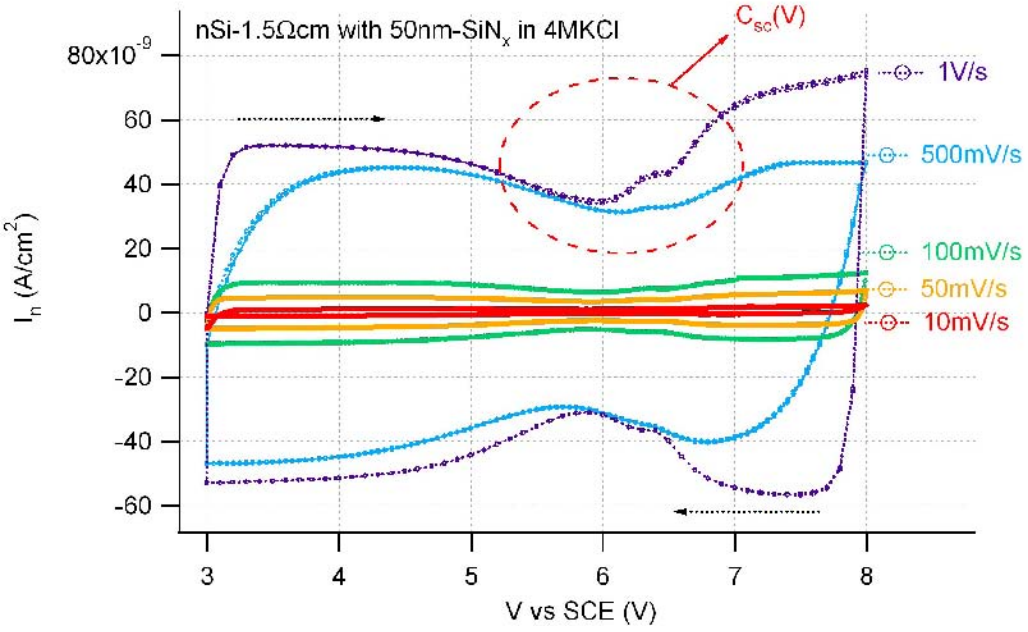

Figure 6.6: The current as a function of the applied potential for a $nSi - 1.5\Omega cm$ with $50nm - SiN_x$ electrode in $4MKCl$ aqueous electrolyte. Every color curve correspond to a different scanning velocity. The scanning velocities used were varied between $10mVs^{-1}$ and $1Vs^{-1}$.

Two characteristics helped to identify the current as a charging (capacitive) one: the current magnitude depends strongly on the scanning velocity

and two: the sign of the current has the same sign as the scanning direction. When the potential is swept from $3V$ to $8V$ (positive scanning velocity) the current is positive and when is swept from $8V$ to $3V$ (negative scanning velocity) it is negative.
The capacitive current must be equal to the product of the electrode capacity with the scanning velocity. In Fig. 6.7, the magnitude of the current at $7.5V$ as function of the scanning velocity has been plotted. All points fit a linear dependence excepting the point at $1V/s$ scanning velocity. The curve measured at $1V/s$ (Fig 6.6) was in the limit of the range specified for the potentiostat, thus the inaccuracy of the measurement is large. This point has not been taken for the calculation of the slope for the current as function of the scanning velocity. The capacity found (equal to the slope) is of $90nF/cm^2$ which is close to the insulator capacity, estimated about $100nF/cm^2$ by impedance analysis (not shown). At $7.5V$ the nSi is in strong inversion and the total electrode capacity tends to the insulator capacity.

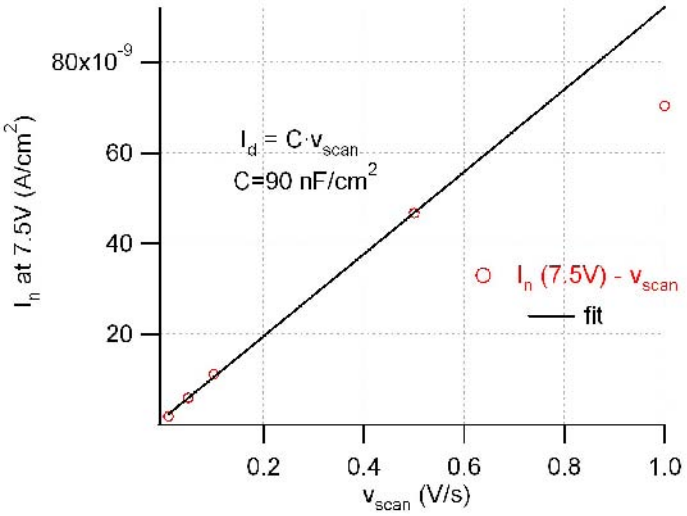

Figure 6.7: . Magnitude of the current at $7.5V$ (from Fig. 6.6) as function of the scan velocity. The linear fit gives an slope equivalent to a capacity $C = 90nF/cm^2$. The current point at $1V/s$ is not taken into account for the linear fit.

The I-V curves of the electrochemical cells remind the C-V characteristics of a MIS device. In Fig. 6.6, the current has a constant value between $3V$ and $4.5V$, between $4.5V$ and $7V$ presents a voltage dependence and over

$7V$ it seems to reach again a constant value. Between $4.5V$ and $7V$ there is probably a transition from the weak accumulation regime to the weak inversion regime. In this situation, the total capacity of the electrode tends to be the space charge capacitance of the semiconductor one (C_{sc}) which is voltage dependent. This can explain the voltage characteristics of the capacitive current.

In order to analyze the capacity characteristics of the electrodes, impedance measurements as function of the applied potential have been done for several cells.

6.3.2 C-V and MWR-V measurements

The total capacity of the cells (C_T) has been measured as a function of the applied potential (V). Electrodes with different SiN_x thickness have been measured in aqueous electrolytes. The insulator capacity (C_i) has been determined by measuring C_T under strong accumulation conditions. Doping level (N_D), flat band potential (V_{fb}), and SiN_x fixed charge (Q_f) have been extracted from the analysis of the data measured at high modulation frequencies.
Contacting the Si/SiN_x electrodes by an electrolyte permitted to combine impedance (C-V) measurements with microwave conductance reflection (MWR) measurements. Under the experimental conditions given, the MWR signal is proportional to the change in conductance induced by the voltage modulation (section 4.3.5).

In the electrochemical cells the inversion regime was observed in contrast to the MIS devices (section 5.3.2.2). The absence of high leakage currents between $0V$ and $8V$ is responsible for this characteristic. Low modulation frequencies (as $1Hz$) were successfully used to measure the capacity contribution of slow interface states and minority charge carriers. This allowed a better determination of the interface state density (D_{it}) by the high-low modulation frequency method (section 6.3.2.5).

6.3.2.1 Low frequency characteristics and C_i capacity

In Fig. 6.8 the total cell capacity (C_T) as function of the applied potential (V) is shown from four different electrodes. All electrodes were $nSi - 30\Omega cm$ wafer but with different SiN_x thicknesses between $15nm$ and $70nm$. The

electrodes were front contacted by $1MKCl$ aqueous electrolyte and $1Hz$ modulation frequency was used for the measurements shown in Fig. 6.8.

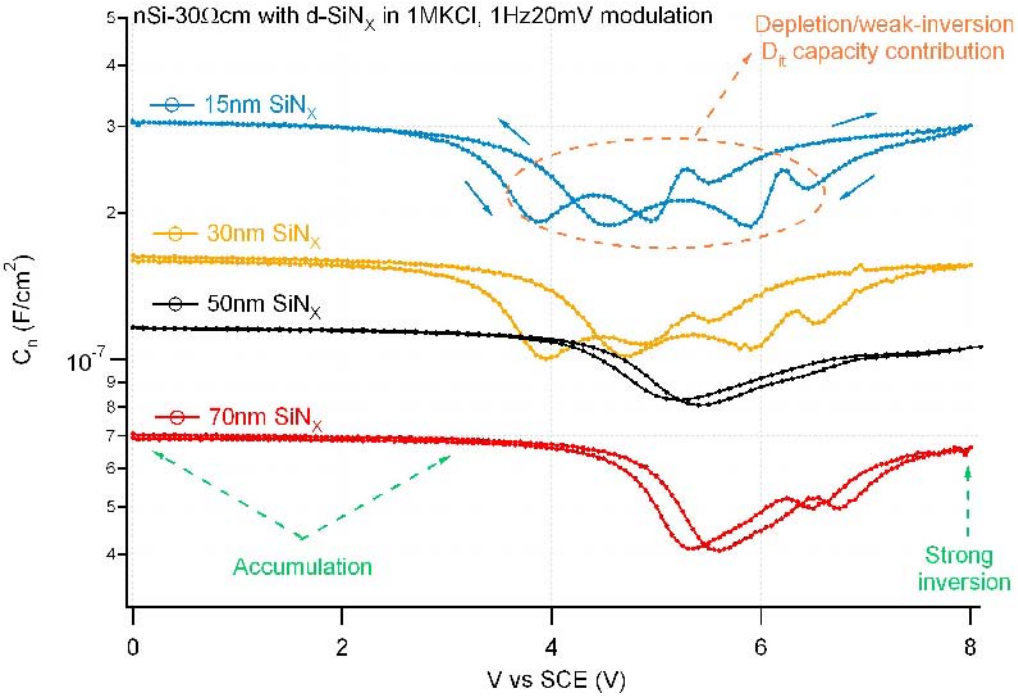

Figure 6.8: C_T as a function of V at $1Hz$ modulation frequency for four $nSi-30\Omega cm$ samples with $15nm$ (blue markers), $30nm$ (yellow), $50nm$ (black) and $70nm$ (red) thick layers. All Si/SiN_x electrodes were contacted by $1MKCl$ electrolyte.

At $1Hz$ modulation frequency, C_T presents the contribution due to the slow interface states and the minority charge carriers. This makes the measurements not useful for the doping and flat band determination by the Mott-Schottky relation, but the insulator capacity C_i can better be evaluated. All samples are under strong accumulation conditions at $0V$ and under strong inversion conditions at $8V$. This corroborates the conjecture at the end of section 6.3.1 that the transition between $4.5V$ and $7V$ corresponds to the transition from weak accumulation to weak inversion. In both extreme cases, the semiconductor capacity is much larger than the insulator one and so, the total capacity value is the C_i value. That is seen for all samples for potentials between $0V$ and $3V$ (accumulation) where C_T does not present any potential dependence. It is seen as well how the total capacity approaches the same C_i

value for potentials higher than $7V$ and this is a clear sign that the inversion regime is attained. Between $3V$ and $7V$ C_T presents a voltage dependence. This corresponds to depletion and weak inversion regimes where the semiconductor capacity is smaller than the insulator one. In this potential range (depletion and weak inversion) at low frequencies the capacity of interface states can be observed and extracted as deviations from the ideal MIS device C_T-V characteristics. Little hysteresis is observed between the forward (from $0V$ to $8V$) and backward (from $8V$ to $0V$) scan.

In Tab. 6.1 the dielectric constant ϵ_i is calculated from the measured C_i values at $0V$ by use of Eq. 5.5. The thickness of the sample d were taken from the SiN_x deposition time as indicated in [28].

$C_i(nF/cm^2)$	307	165	117	71
$d(nm)$	15	30	50	70
ϵ_i	5.2	5.6	6.6	5.6

Table 6.1: Calculation of the dielectric constant ϵ_i of SiN_x from the experimental data by use of Eq. 5.5.

It is found that the dielectric constant of SiN_x lays between 5 and 7 being in agreement with the results previously found for the MIS devices (Tab. 5.1) and corroborated in the literature [76], [77].

6.3.2.2 High frequency characteristics: V_{fb}, N_D and Q_f determination

High modulation frequency measurements were done to extract doping density (N_D) and flat band potential (V_{fb}) with the Mott-Schottky relation. High frequency measurements do not present the capacity contribution from the minority charge carriers (inversion) or the interface states, because the kinetics of these phenomenas is too slow to follow the perturbation due to the fast modulation. However, the effect of the interface states can be observed by the stretched form of the C_T curves when plotted as a function of the applied potential V (equivalent to the gate potential V_G). The DC polarization was applied point by point allowing the system to reach the stationary equilibrium at every V point. In this situation, the gate charge (Q_G) compensates the sum of the semiconductor charge (Q_{sc}) and interface

states charge (Q_{it}) and thus, the applied potential V differs from the ideal case where only Q_{sc} is compensated by Q_G and the case at high scanning velocities.

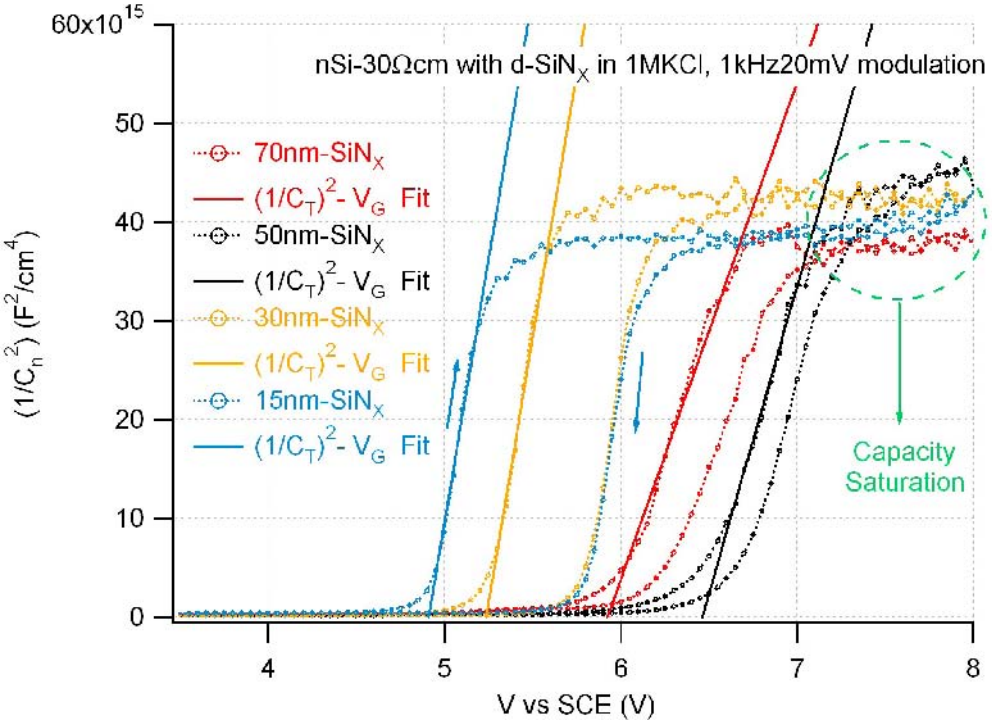

Figure 6.9: $(1/C_T)^2$ as function of the applied potential V for the $nSi - 30\Omega cm$ samples with different SiN_x thickness (shown in Fig. 6.8) contacted by $1MKCl$ electrolyte. $1kHz$ modulation frequency was used to register the capacity.

In Fig.6.9 are shown the high frequency $(1/C_T)^2 - V$ plots for the $nSi - 30\Omega cm$ electrodes where their low frequency data is represented in Fig. 6.8. Doping density (N_D) and flat band potential (V_{fb}) were extracted by the Mott-Schottky relation and are given in Tab. 6.2, together with the insulator capacity C_i and the fixed charge in the SiN_x (Q_f).
The capacity measured at high modulation frequency shows a saturation value at sufficiently high potentials. For nSi this corresponds to the inversion regime characteristics; even though the modulation is too fast to monitor the inversion capacity contribution, the inversion layer exists and follows the stationary (DC) polarization. In other words: the minority carriers follow

the gate (DC) bias but do not follow the AC modulation. In inversion, the negative charge in the gate electrode is compensated by holes at the nSi/SiN_x interface and is not further compensated by the ionized positive impurities in the depletion region. So, the depletion capacity (what is measured at high frequencies) tends to an stationary value.

The Si/SiN_X electrodes present a (substantial) difference when contacted by a metal (MIS devices) or by an electrolyte (electrochemical cells): MIS devices show deep-depletion whereas the electrochemical cells show an inversion regime. This can be related to the absence of strong leakage currents when the electrodes are contacted by an electrolyte.

$\rho\ \Omega cm$ $n-Si$	$d-SiN_x$ (nm)	N_d (cm^{-3})	V_{fb} (V)	C_i (nF/cm^2)	Q_f (cm^{-2})
$30\Omega cm$	15	$1.0 \cdot 10^{14}$	4.8	307	$8.9 \cdot 10^{12}$
$30\Omega cm$	30	$1.0 \cdot 10^{14}$	5.2	165	$5.1 \cdot 10^{12}$
$30\Omega cm$	50	$1.7 \cdot 10^{14}$	6.4	117	$4.5 \cdot 10^{12}$
$30\Omega cm$	70	$2.2 \cdot 10^{14}$	5.9	71	$2.5 \cdot 10^{12}$

Table 6.2: Doping level (N_D), flatband (V_{fb}) and SiN_x fixed charge (Q_f) estimation. N_D and V_{fb} were calculated by the fitting of the Mott-Schottky relation to the experimental data. C_i and $\phi_{ms} = 0.21V$ were used in the calculation of Q_f by Eq. 3.12.

The doping density for an $30\Omega cm$ Si wafer is $1.2 \cdot 10^{14} cm^{-3}$. The results found are within the accuracy of the approximation that no influence of the interface states has been taken into account. For the electrochemical cell configuration, the region where the Mott-Schottky relation is valid is only in depletion. However, this is the regime where the effect of the interface states is present.
The Q_f value lays between $2 \cdot 10^{12}$ and $9 \cdot 10^{12}$. It increases with decreasing the SiN_x thickness and the values are higher than the ones obtained for the MIS devices (in Tab. 5.2). This difference may be related to the absence of the high leakage currents or an influence of the electrolyte contact.

The electrodes in Fig. 6.9 show hysteresis. The flat band potentials given in Tab. 6.2 are taken for the forward scan (from $4V$ to $8V$) and are different from the ones obtained in the backward scan. This strong hysteresis was not observed in MIS devices.

In Fig. 6.10 are compared the $(1/C_T)^2$-V plots from the $15nm - SiN_x$ (blue markers) with the $50nm - SiN_x$ (black markers) already given in Fig. 6.9. The $15nm$ electrode has the maximum hysteresis measured and the $50nm$ the minimum one. The change in flat band ΔV_{fb} and in fixed charge ΔQ_f found for all samples (in Fig. 6.9) are given in Tab. 6.3.

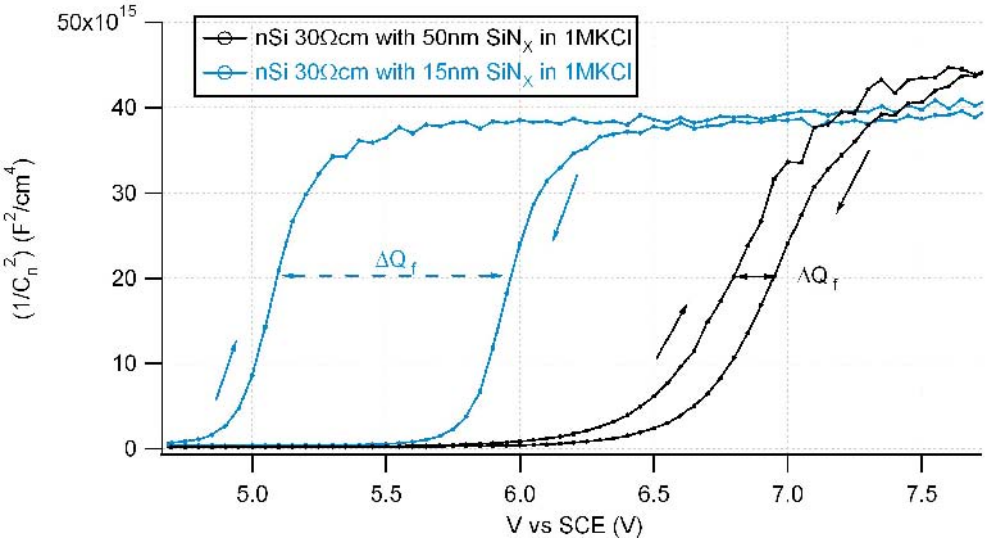

Figure 6.10: $(1/C_T)^2 - V$ plots for $nSi - 30\Omega cm$ with $15nm - SiN_x$ and a second sample with $50nm - SiN_x$, the extreme cases in hysteresis observed in Fig.6.9.

Hysteresis implies a change in the electrode properties such as a change in the fixed charge in the insulating layer, the reduction/oxidation of species or a destruction of the electrode. The hysteresis measured is reproducible thus, it is discarded to be due to an irreversible change in the electrode (as chemical corrosion). The most probable hypothesis is that the hysteresis is due to a change in charge in the SiN_x. SiN_x is used in memory device technology. The high density of traps present in its volume can be used to store charge carriers which are injected from the Si wafer. In the present case this could be a change in the fixed charge due to hole injection from the nSi wafer (or electron injection from the SiN_x into the Si). The experiments (Fig. 6.10) show that the "fixed" charge has changed to a higher positive value $(Q_f + \Delta Q_f)$ after the forward scanning and the change is greater for those electrodes which present a smaller flat band potential in the forward scan. This suggests that the injection of holes into the SiN_x would happen only in inversion regime when holes accumulate at the nSi/SiN_x interface.

All samples have been scanned in potentials between $3.5V$ and $8V$. Those electrodes with smaller flat band potential are driven more into inversion regime when reach the $8V$ return point (being all scanned in the same conditions). Therefore they are longer under inversion conditions and the number of holes accumulated at the nSi/SiN_x is higher. Thus the maximal hysteresis is expected for the $15nm$ electrode and the minimal for the $50nm$ one.The phenomenon can also be due to an interior quality of very thin SiN_x films characterized by a higher defect density.

Concerning the absence of hysteresis in the measured MIS devices, it might be related to the aluminum gate contact. The MIS devices presented a deep-depletion regime, so no holes are accumulated at the nSi/SiN_x interface (section 5.3.2.2). This was attributed to a leakage holes current from the Si to the gate electrode (or electrons from the gate to the Si). In that case the number of holes trapped in the SiN_x did not change. The aluminum contact can easily collect holes or inject electrons into the SiN_x. With an electrolyte contact that is not that simple. A chemical species must be oxidized to permit this process (losing its electron and taking the hole).

Semiconductor	$d - SiN_x(nm)$	$\Delta V_{fb}(V)$	$\Delta Q_f\ (cm^{-2})$
nSi $30\Omega cm$	15	0.9	$1.73 \cdot 10^{12}$
nSi $30\Omega cm$	30	0.55	$5.67 \cdot 10^{11}$
nSi $30\Omega cm$	50	$0,17$	$1.24 \cdot 10^{11}$
nSi $30\Omega cm$	70	0.3	$1.33 \cdot 10^{12}$

Table 6.3: Change in flatband and Q_f

Another possible explanation is that electrolyte ions intercalate into the SiN_x changing the volume charge but at positive polarization, negative ions are attracted to the electrode and a possible ion intercalation would provide a decrease in Q_f and this is not observed. In any case, the role of the electroctrolyte contact is obvious for hole trapping into the SiN_x due to the absence of a fast charge exchange between SiN_x and electrolyte or due to more subtle chemical changes within the insulating layer which enhances its trapping properties.

Some samples, specially the ones with very thin insulating layer presented higher leakage currents related to SiO_2 formation and O_2 evolution. This samples present other C_T-V characteristics which remember the ones

observed for MIS devices.

6.3.2.3 Leakage current and deep-depletion regime in electrochemical cells

In Fig. 6.11 are shown the capacity (blue markers, left axis) and current (green markers, right axis) as function of the applied voltage for an $nSi - 30\Omega cm$ with a thin $5nm - SiN_x$ insulating layer. The electrode was contacted by $1MKCl$ and the modulation frequency was of $10kHz$. This electrode presents a faradaic current at potentials higher than $2V$ (this is concluded from the positive sign of the current independent of the sign of the scanning velocity) and reaches the value of $1.3\mu A/cm^2$ at $8V$. Between $0V$ and $4V$ the C_T-V curve presents the same behavior observed for the samples with thicker SiN_x; the electrode presents the inversion regime characteristics with a saturation in the capacity value at potentials between $2V$ and $4V$ (in the forward scan). Hysteresis is also observed. But at potentials higher than $4V$, the capacity starts to decrease again. This decrease in capacity coincides with the onset of a leakage current.

In Fig.6.12 the capacity (yellow markers, left axis) and current (orange markers, right axis) as a function of the applied potential for an electrode with $30nm - SiN_x$ are shown. This sample presents a very low leakage current but mainly a capacitive current. At $8V$ the maximum current value is $3nA/cm^2$, that is almost three orders of magnitude smaller than for the sample with $5nm - SiN_x$ (Fig. 6.11). The electrode presents a constant value for the capacity at potentials higher than $6V$ in inversion regime. This indicates that the presence of a high leakage current is correlated with the deep-depletion regime (Fig. 6.12) and a low leakage currents coincides with the inversion regime (Fig. 6.12).

In Fig. 6.13 the $(1/C_T)^2$-V plot (dark-blue markers, left axis) for the measurements already shown in Fig. 6.11 is given. This plot shows also $(1/MWR)^2$ measurements as function of the applied potential (light-blue markers, right axis). The MWR signal is proportional to the space charge capacity in impedance measurements (Eqs. 4.53, 4.54). Consequently, where the Mott-Schottky relation (Eq. 2.107) is valid for C-V plots (depletion and deep-depletion), it is as well applicable for the MWR signal and $(1/MWR)^2$ signal must be proportional with the applied potential.

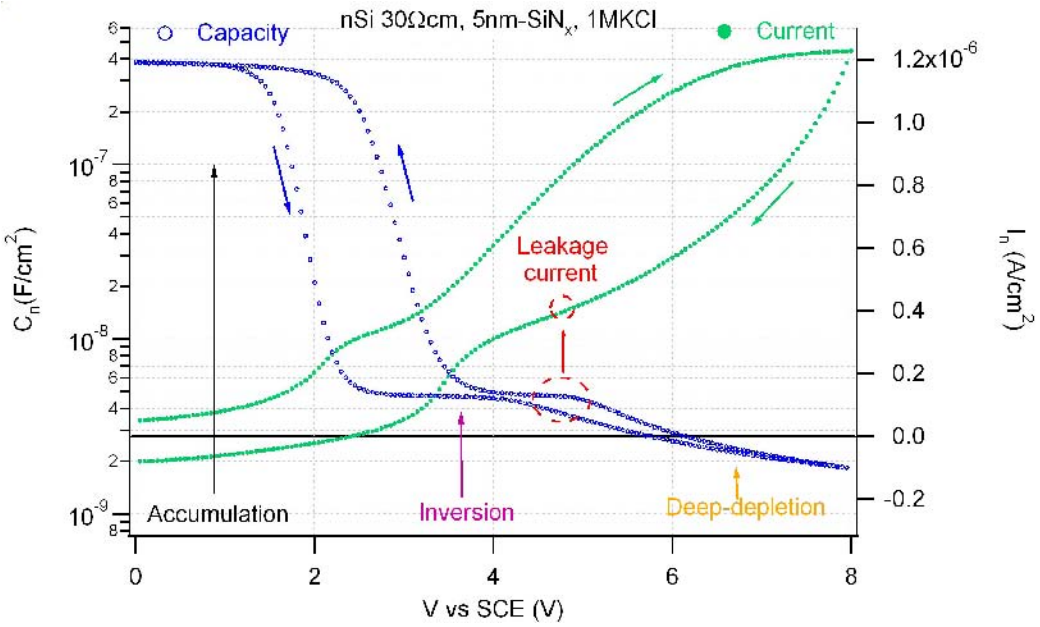

Figure 6.11: Capacity (blue markers, left axis) and current (green markers, right axis) measurements as a function of the applied potential for a $nSi{-}30\Omega$ with $5nm - SiN_x$ in $1MKCl$. Modulation frequency was $10kHz$.

Analyzing first the $(1/C_T)^2$-V: there are two regimes where the Mott-Schottky relation can be satisfactory applied (in the forward scan): between $2V$ and $2.5V$ (corresponding to depletion regime) and between $5V$ and $8V$. The linear fit (Fig. 6.13 dark solid line) for this last potential range is displayed. The doping density extracted is about $1.5 \cdot 10^{14} cm^{-3}$ (given in Tab. 6.4) in agreement with the calculated doping density for a $30\Omega cm$ Si wafer ($1.2 \cdot 10^{14} cm^{-3}$). This is a clue to identify this potential range as the deep-depletion regime. The doping density determined between $2V$ and $2.5V$ gave a similar result (see Tab. 6.4).
The $(1/MWR)^2$ presents also a dependence on the applied potential. The measurement is not so accurate as the impedance measured but it shows too how the nSi is driven into deep-depletion regime. The MWR measurement indicates that the change in capacity between $5V$ and $8V$ occurs in the semiconductor volume.

The sample shows hysteresis too. The hysteresis between the forward and backward scan is larger in the depletion regime than in deep-depletion regime. Considering that the hysteresis due to a change in Q_f is related to

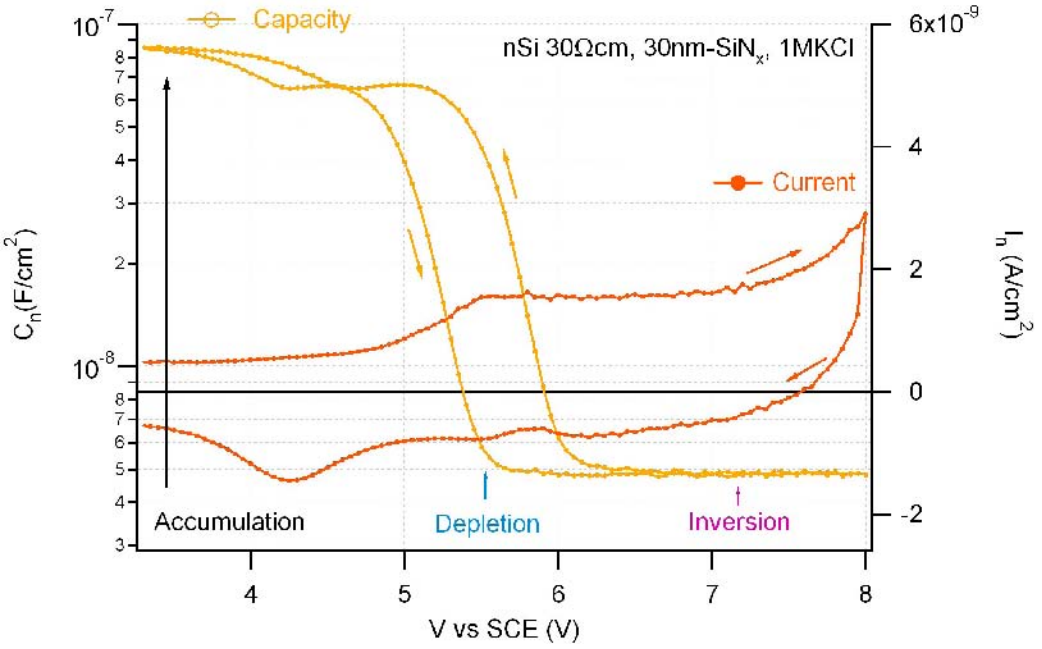

Figure 6.12: Capacity (yellow markers, left axis) and current (orange markers, right axis) measurements as function of the applied potential for an $nSi - 30\Omega$ with $30nm - SiN_x$ in $1MKCl$. Modulation frequency was $1kHz$.

Voltage range (V)	N_d (cm^{-3})	V_{fb} (V)	Q_f (cm^{-2})
$2 \rightarrow 2.5$	$1.3 \cdot 10^{14}$	2.0	$4.2 \cdot 10^{12}$
$5 \rightarrow 8$	$1.5 \cdot 10^{14}$	4.0	$9.0 \cdot 10^{12}$
MWR	-	3.9	$8.9 \cdot 10^{12}$

Table 6.4: Doping (N_D), flatband (V_{fb}) and fixed charge (Q_f) calculated from the capacity measurements for the forward scan of the $nSi - 30\Omega cm$ with $5nm - SiN_x$ electrode in $1MKCl$ (Fig. 6.13). An insulator capacity of $C_i = 382nF/cm^2$ was used in the calculation of Q_f. Additionally the flat band potential obtained from the MWR measurement is given.

the trapping of holes into the SiN_x volume, trapping may not be active in deep depletion regime. The existence of a leakage current is an evidence of charge flowing rather than being trapped. Above a certain potential, the insulating layer allows the transport of holes from the semiconductor to the

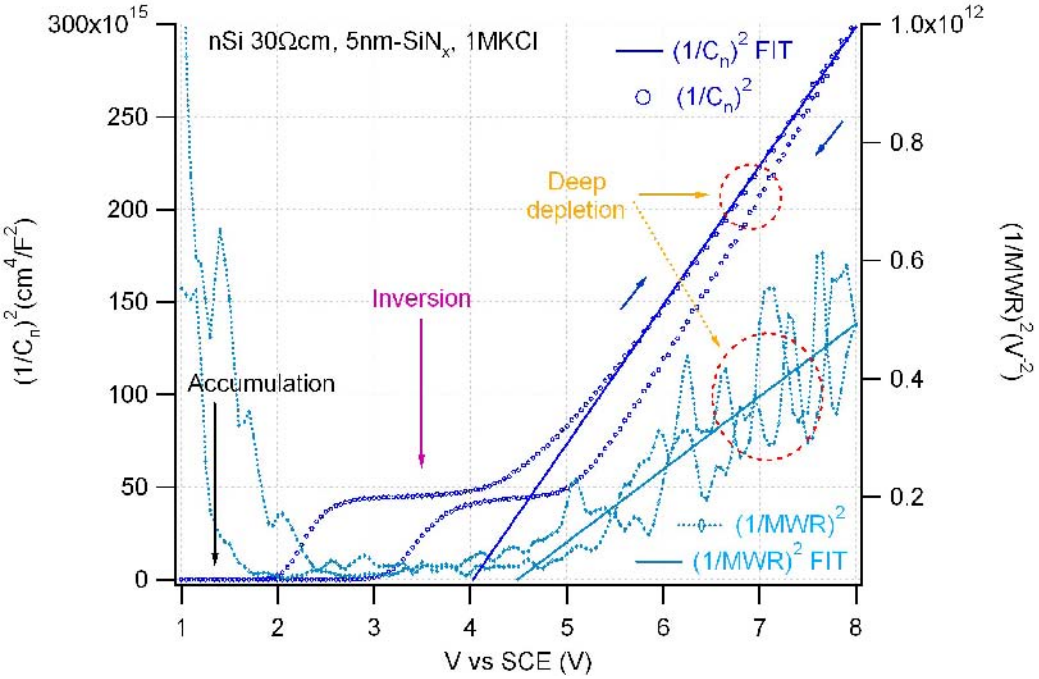

Figure 6.13: $(1/C_T)^2 - V$ and $(1/MWR)^2\, V$ plots for a $nSi - 30\Omega cm$ sample with $5nm - SiN_x$ in a $1MKCl$ electrolyte. Modulation frequency was $10kHz$ with voltage modulation of $20mV$.

electrolyte (or electrons from the electrolyte to the semiconductor). This leakage current has been related to the SiO_2 formation through the pores present in the SiN_x layer (after H_2 evolution at negative potentials). This $5nm - SiN_x$ sample presents the highest leakage current measured and so it may have the highest density of pores in the SiN_x where SiO_2 has been grown. This suggests that the stable charge trapping (the memory charge responsible for the hysteresis) occurs at the SiN_x/SiO_2 interface. Charges trapped in the SiN_x surrounded by SiO_2, must overcome an energy barrier due to the presence of SiO_2 (about $1.5eV$ [78], [60]) in order to be transferred. This is the working principle in MNOS devices where charge is trapped near the SiN_x/SiO_2 interface and remains there, in the absence of high electric fields [79].

Another explanation supposes the generation/annihilation of traps by the effect of electrochemical reactions in the SiN_x. Some role must play the electrolyte in the hysteresis observed because this effect is not observed in MIS

devices when the SiN_x is gate contacted by aluminum. It could be that the metal contact is able to provide always an electron to the SiN_x when a hole from the nSi is injected, or it could be that in MIS devices no SiO_2 is formed and so the trapped charge does not remain in the SiN_x after stress polarization. An energetic barrier must be present when the Si/SiN_x electrode is contacted by the electrolyte that stabilizes the trapped charges in the insulating layer.

The same behavior observed as for the $5nm - SiN_x$ electrode is observed for an electrode with a thicker SiN_x layer if higher positive potentials are applied. This is shown in Fig.6.14 where the $(1/C_T)^2 - V$ plot for a $nSi - 1.5\Omega cm$ with a $30nm - SiN_x$ electrode in $1MKCl$ is given.
In order to apply such high potentials to the cell, another potentiostat was used. Unfortunately, this was not able to perform cyclic voltammetry (uninterrupted forward and backward scanning) neither the I-V characteristics could satisfactorily been recorded. Consequently, the analysis of the hysteresis and the leakage current could not be done.

Fig. 6.14 presents two potential ranges where the Mott-Schottky relation seems valid. Between $15V$ and $17V$ the sample is in depletion regime and between $30V$ $40V$ in deep-depletion regime. In this last regime gas evolution was observed at the electrode. This might be due to O_2 formation and is a clue to say that there is a leakage current.

The capacity presents a constant value between $17V$ and $30V$ corresponding to the inversion regime at high frequency modulation measurement. Doping densities (N_D), flat band potentials (V_{fb}) and related fixed charge (Q_f) are given in Tab. 6.5.

The nominal doping level for a $1.5\Omega cm$ wafer is $N_D = 2.7 \cdot 10^{15} cm^{-3}$. Both doping levels found are in the same order of magnitude but closer to the theoretical value is the one extracted in the deep-depletion regime where the effects of the interface states is less relevant. The Q_f found is one order of magnitude greater than the one found for other electrodes. This can be explained by previous non-cyclic measurements performed on the cell, all from $0V$ to $40V$. In this polarization direction holes are trapped in the SiN_x probably leading to an increment in the Q_f.

Thus, a further polarization into positive potentials would imply injection

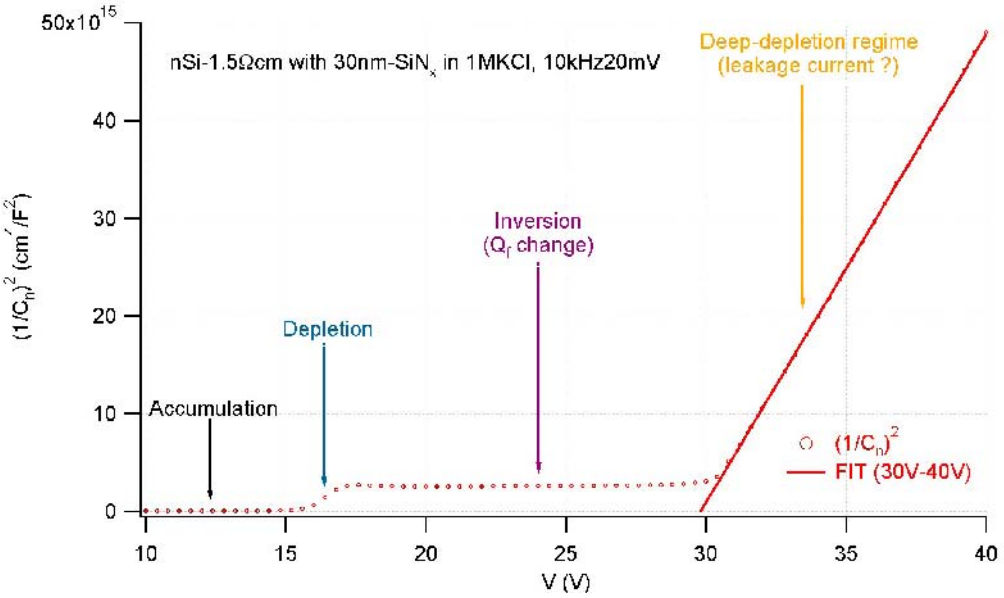

Figure 6.14: $(1/C_T)^2$ as a function of the applied potential for a $nSi - 1.5\Omega cm$ with $30nm - SiN_x$ electrode in $1MKCl$ electrolyte. The modulation frequency was $10kHz$.

$nSi - 1.5\Omega cm$ Voltage range (V)	$d - SiN_x$ (nm)	N_d (cm^{-3})	V_{fb} (V)	C_i (nF/cm^2)	Q_f (cm^{-2})
$15 \rightarrow 17$	30	$5.6 \cdot 10^{15}$	15.7	130	$1.2 \cdot 10^{13}$
$30 \rightarrow 40$	30	$2.3 \cdot 10^{15}$	29.8	130	$2.4 \cdot 10^{13}$

Table 6.5: Doping density (N_D), flat band potential (V_{fb}) and related fixed charge (Q_f) are given for the two voltage regimes where the Mott-Schottky relation seems valid for the $nSi - 1.5\Omega cm$ with $30nm - SiN_x$ electrode in $1MKCl$ shown in Fig. 6.14.

of holes from the silicon wafer into the SiN_x instead of a true change in the surface potential ψ_s and the pertinent increase of holes in the inversion layer. In the MIS model here used, both processes cannot be distinguished by the gate charge which compensates the total charge at the Si/SiN_x interface being at the insulator side and at the semiconductor one.

As conclusions:

- SiN_x presents the capability to trap charges (holes) in its volume. This has been concluded from the hysteresis observed in the C_T-V measurements.

- The presence of high leakage currents drive the Si into deep depletion regime as it was observed for the MIS devices.

- The hysteresis observed is an influence of contacting the electrodes with an electrolyte. Electrochemistry must play a role in this charge storage being responsible for the formation of new stable trap-levels or the generation of new structures (such as SiO_2 or SiN_xO_y) that present an energy barrier to overcome for the injection/emission of charges into/from the trapping levels (taking the MNOS model as example).

So far, the effects due to the SiN_x volume properties and contacting the Si/SiN_x structure by an electrolyte have been discussed for inversion and deep-depletion regimes. In continuation the Si/SiN_x characteristics in the depletion regime will be discussed. This is the range where solar cells usually work and is fundamental to the understanding of surface recombination phenomena to identify the density of interface states D_{it} characteristics present in the Si band gap. To study the D_{it}, high and low capacity measurements have been done for different cells in the depletion regime.

6.3.2.4 High and low modulation frequencies capacity and MWR signal characteristics

The inversion regime can be studied at low modulation frequencies in the electrochemical cell configuration. In Fig. 6.15 is shown the total capacity as function of the applied potential for a $nSi - 1.5\Omega cm$ with $40nm - SiN_x$ electrode in $4MKCl$ aqueous electrolyte. The sample was measured using different modulation frequencies (between $100kHz$ and $1Hz$) and the capacity contribution due to the minority charge carriers (inversion regime) and the interface states trapped charge are seen. This charge is at the Si/SiN_x interface and not in the SiN_x volume. By decreasing the modulation frequency, the capacity contribution due to the slower effects is observed.

For all experiments the electrode (Si/SiN_x) follows the DC bias (the constant gate potential) and so the system goes from accumulation via depletion to inversion. However, the AC capacity reflects the kinetics of the

charge carriers in the inversion layer and the interface states which only contribute to the capacity if they can follow the modulation.

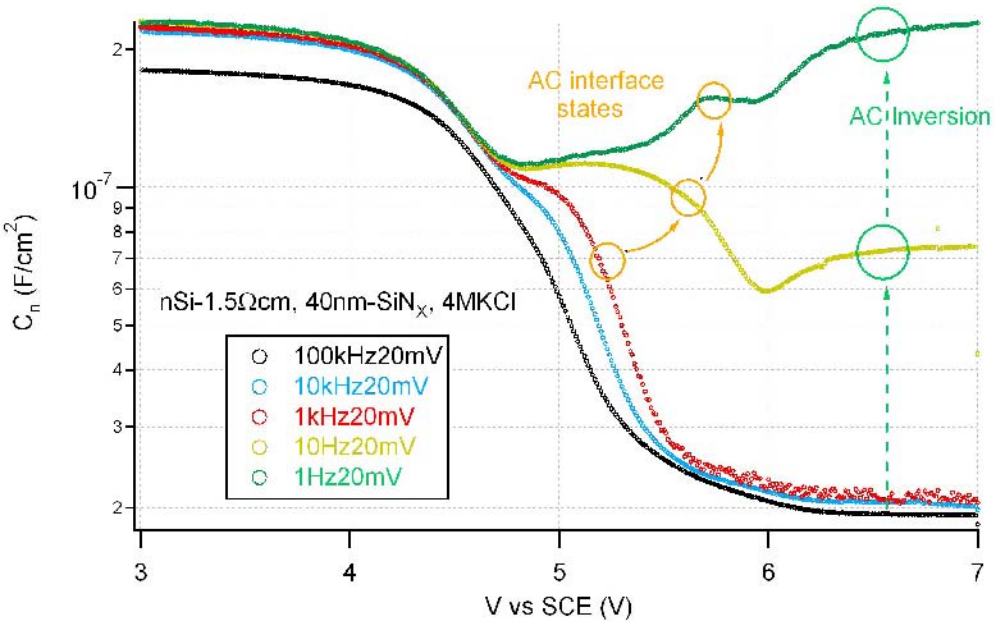

Figure 6.15: C_T as function of the applied potential for $nSi - 1.5\Omega cm$ with a $40nm - SiN_x$ layer in contact with a $4MKCl$ electrolyte. The sample was measured with different modulation frequencies between $1Hz$ and $100kHz$.

At high modulation frequencies ($100kHz$-$1kHz$), the capacity presents a saturation value (at potentials higher than $6V$) due to the onset of the inversion regime. The inversion capacity is directly measured at low modulation frequencies. At the $1Hz$ frequency measurement (green markers) the total capacity tends again to the insulator capacity value. This corresponds to strong inversion where the Si capacity is much higher than the insulator capacity and the total capacity falls again (as in accumulation) into the capacitor value.

In the depletion regime, between $4.5V$ and $6V$, the capacity contribution due to the interface states is observable too. At fast modulation frequencies ($100kHz$-$1kHz$) only the fast interface states contribute to the capacity (blue and red markers around $5V$). By decreasing the modulation frequency the capacity contribution from the slower interface states is as well measured

(yellow and green markers).

In Fig.6.16 the MWR signals as function of the applied potential are shown for the electrode in Fig. 6.15. The MWR signals could be better measured at fast modulation frequencies (between $100kHz$ and $1kHz$) and are compared to the capacity measurements. In principle, the MWR signal is proportional only to the semiconductor capacity 4.3.5. The capacity due to interface traps does not change the conductivity of the sample because charge in the trapped state is not mobile [70]. The MWR signal does not show differences between the different modulation frequencies in the depletion regime (between $4.5V$ and $7V$). Under accumulation conditions the $100kHz$ measurement yields a smaller signal than the lower frequencies. This might be still an effect of the rear $In:Ga$ contact.

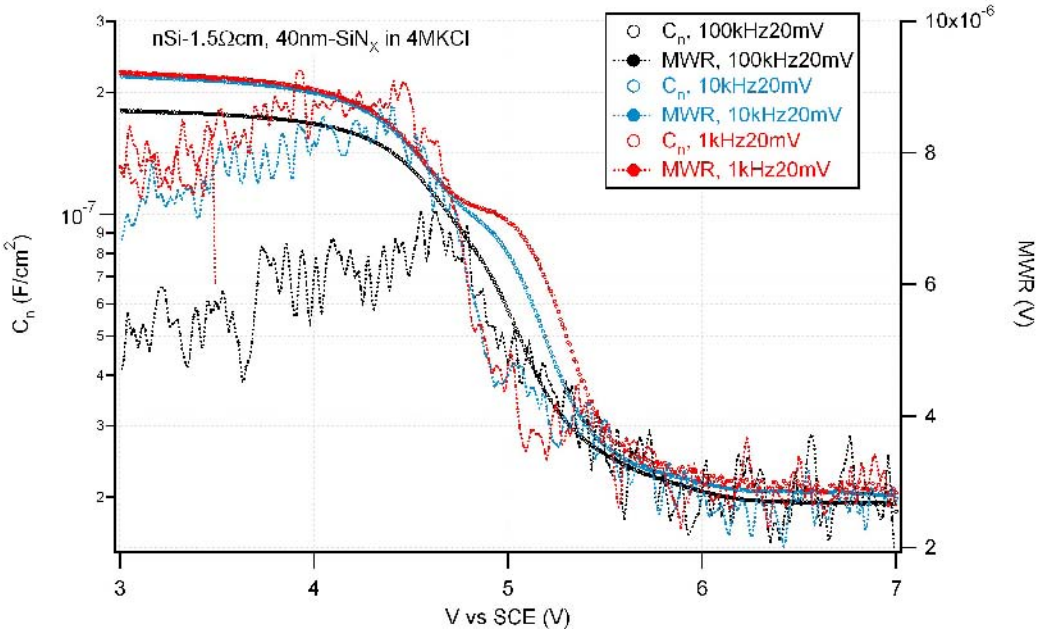

Figure 6.16: Total capacity and MWR signal as function of the applied potential for $nSi-1.5\Omega cm$ with $40nm-SiN_x$ in $4MKCl$ aqueous electrolyte. The modulation frequencies used were $100kHz$ (black markers), $10kHz$ (blue markers) and $1kHz$ (red markers).

In Fig.6.17 $(1/C_T)^2$ and $(1/MWR)^2$ signals are displayed as function of the applied potential. The MWR signal presents a satisfactory Mott-

Schottky behavior for potentials between $5V$ and $6V$. In spite of the noise, the validity of the Mott-Schottky relation is clearer for the MWR than for the C_T signal. The Mott-Schottky plots based on the capacity data do not yield an unambiguous slope between $5V$ and $6V$ even at $100kHz$. It is seen between $6.5V$ and $7V$ that the MWR signal tends to a constant value as expected for a inversion regime for high modulation frequencies.

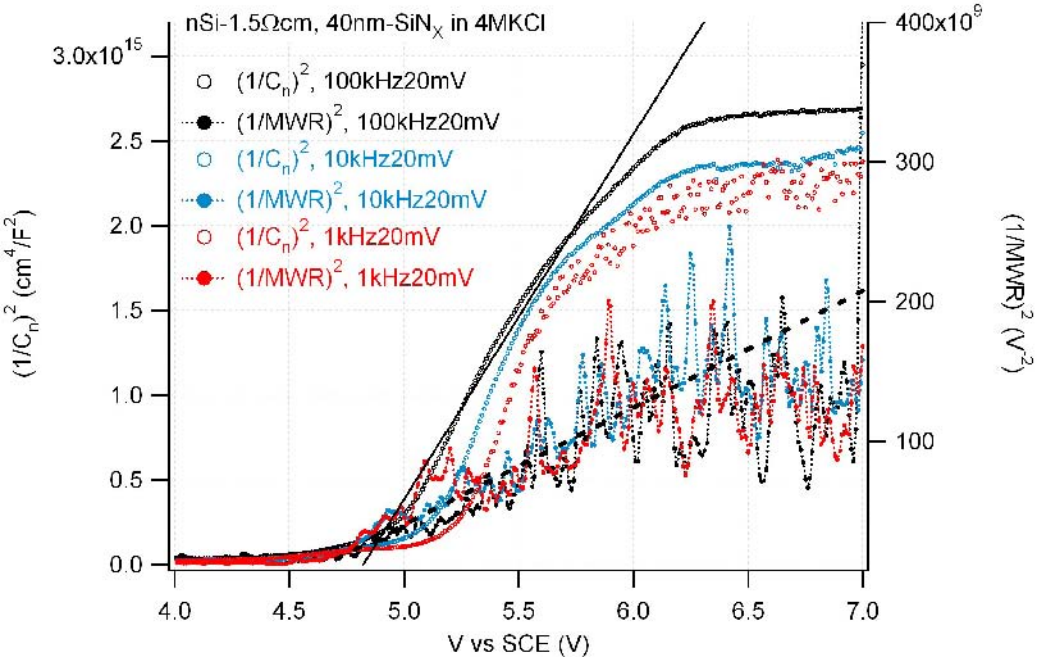

Figure 6.17: High frequency $(1/C_T)^2$ and $(1/MWR)^2$ measurements as function of the applied potential for an $nSi-1.5\Omega cm$ with $40nm-SiN_x$ electrode in $4MKCl$.

The flatband value found by the MWR analysis was $4.5V$ and the one from the capacity at $100kHz$ modulation of $4.8V$. The fixed charge of the electrode is about $Q_f = 6.8 \cdot 10^{12} cm^{-2}$. The doping density (averaged) found is $N_D = 4 \cdot 10^{15} cm^{-3}$. It is clear that the capacity data contains a contribution due to the capacity of interface states, a contribution decreasing with increasing modulation frequency.

In order to get a better MWR signal, a $100mV$ voltage perturbation was used in the measurements shown in Figs. 6.18, 6.19. MWR signal is proportional to the voltage perturbation in impedance measurements (Eqs. 4.53, 4.54). As the system is still in linear response using a $100mV$ voltage

modulation, this modulation depth can be used with the benefit of reducing considerably the MWR noise. The linearity was checked by comparison the $100mV$ modulation capacity measurement to the $20mV$ perturbation measurement (normally used) and no significant difference was found between the capacity curves.

In Fig.6.18 are shown the high frequency ($10kHz$, blue markers) and low frequency ($1Hz$, red markers) capacity and MWR signals as function of the applied potential for an $nSi - 1.5\Omega cm$ with $70nm - SiN_x$ electrode in $4MKCl$.
Under depletion conditions, between $4V$ and $5.5V$, the MWR signal (at both frequencies) is positive and decreases in magnitude with increasing potential. This is explained by the decrease of the number of charge carriers modulated by the potential modulation with increasing potential under depletion conditions (in fact this is the Mott-Schottky range).

For measurements under potential modulation the MWR signal is conventionally taken positive as a potential change in the sense of increasing depletion leads to a decrease of the number of mobile charge carriers.

The $10kHz$ frequency measurement (blue markers) shows that the MWR tends to an stationary value at potentials between $5.5V$ and $8V$. This is due to inversion in the high frequency modulation case. Only the majority charge carriers are able to follow the fast voltage modulation.
This leads to an approximately constant capacity value [7] as also shown in the high frequency measurement (blue markers) in Fig. 6.18. This implies also that the number of charge carriers modulated by the voltage modulation is constant in this range and consequently the MWR signal is constant.

The measurement at $1Hz$ (red markers) presents a completely different behavior at potentials between $5V$ and $8V$. Under depletion conditions, the MWR signal is positive and decreases with increasing potential as expected and measured at $10kHz$. Once the inversion regime is attained, at $1Hz$ modulation frequency the minority charge carriers can follow the perturbation and so the MWR signal is sensitive to their contribution. The perturbation induces an enhancement in conductivity increasing the microwave absorption and so the MWR signal changes sign showing the transition from decreasing the conductivity to increasing it in the inversion regime.

This can also be as well observed in Fig. 6.19 for a $pSi - 100\Omega cm$ with $50nm - SiN_x$ electrode in $4MKCl$. Capacity and MWR signals as function

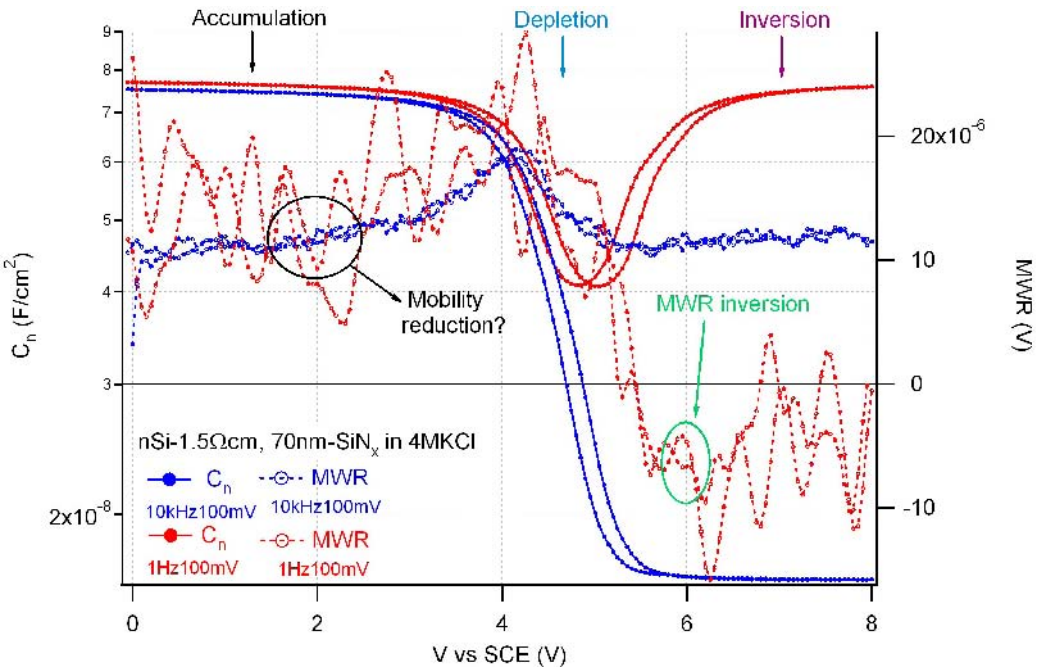

Figure 6.18: Capacity and MWR signal as function of the applied potential for a $nSi - 1.5\Omega cm$ with $70nm - SiN_x$ electrode in $4MKCl$ with the modulation frequencies $1Hz$ and $10kHz$ and a modulation depth of $100mV$.

of the applied potentials are given for different modulation frequencies between $10kHz$ and $1Hz$ with a $100mV$ voltage perturbation. From the fast frequency measurements a flatband potential of $4.52V$ and a doping density of $N_D = 1,45 \cdot 10^{14} cm^{-3}$, in agreement with the theoretical of $1.3 \cdot 10^{14} cm^{-3}$ for a $100\Omega cm$ wafer, were extracted by use of the Mott-Schottky relation. An insulator capacity of $C_i = 138nF/cm^2$ was extracted from the capacity measurement under strong accumulation conditions and a fixed charge concentration of $Q_f = 3.1 \cdot 10^{12} cm^{-2}$ was calculated taking $\phi_{ms} = 0.83V$ in Eq. 3.12.

In Fig.6.19 is seen again the effect of the inversion regime in the MWR signal for the $100Hz$ (yellow markers) and $1Hz$ (purple markers) frequency measurements. For both frequencies the MWR signal changes in sign becoming negative if $(V - V_{fb})$ is smaller than $-0.5V$. Because Fig. 6.19 reflects an electrode of a pSi wafer the transition from accumulation to inversion occurs in the reverse direction of that for the electrode shown in Fig. 6.18: by shifting potentials to more negative values. The existence of inversion

is corroborated by the capacity measurement at $1Hz$ (purple markers) that increases again between $-0.5V$ and $-1.5V$ until the insulator capacity value is reached.
At fast modulation frequencies ($10kHz$ and $1kHz$) the MWR signal presents an approximately constant positive value for potentials between $0V$ and $-1.5V$. This represents the high frequency inversion as discussed above for the nSi in Fig. 6.18

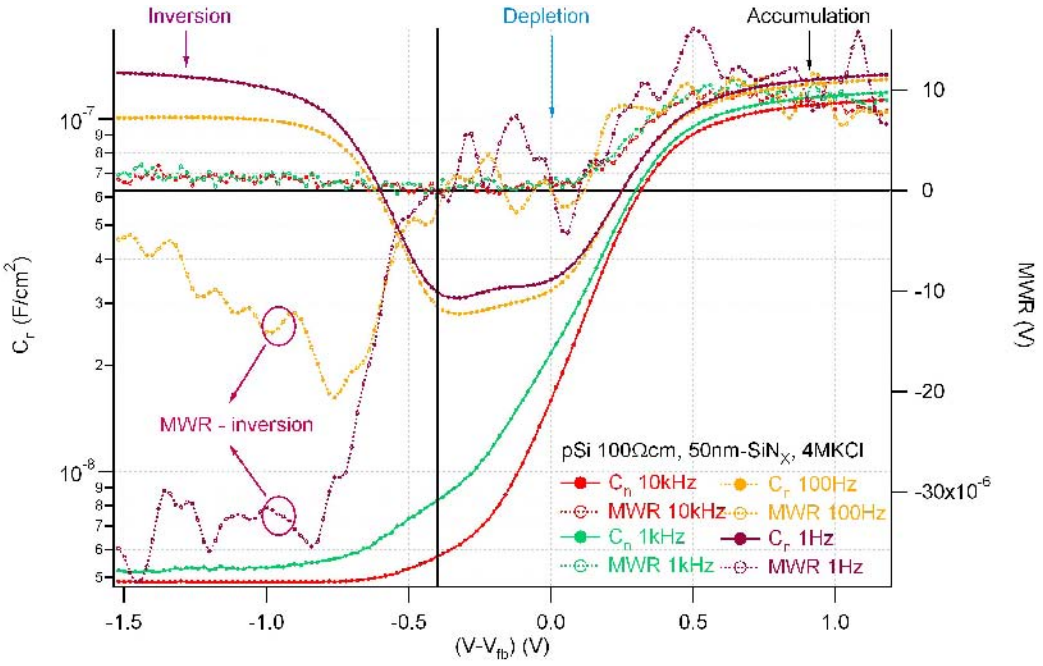

Figure 6.19: Capacity and MWR signal as function of the applied potential for a $pSi - 100\Omega cm$ with $50nm - SiN_x$ electrode in $4MKCl$ for different modulation frequencies between $10kHz$ and $1Hz$ with $100mV$ voltage perturbation. The applied potential V is given with respect to the flat band potential V_{fb}.

There is one interesting point observed in MWR measurements shown in Figs. 6.18 and 6.19: the change in magnitude of the MWR signal at low frequency between weak accumulation (the maximum of the MWR signal) and weak inversion (the minimum of the MWR signal) is about a factor 3 where the MWR changes sign because of the transition between a majority carrier controlled to a minority carrier controlled signal.

For the nSi sample (Fig. 6.18), the magnitude of the MWR signal in weak accumulation conditions (at $4V$) is a factor 2.7 higher than under weak inversion (at $6V$). For the pSi sample (Fig. 6.19) the MWR magnitude under accumulation conditions (at $0.5V$) is a factor of about 3 smaller than under weak inversion (at $-0.8V$). This can be related to the different mobilities that the charge carriers contribute to the conductivity. Electrons contribute to the conductivity with a mobility of $1450cm^2V^{-1}s{-}1$ and holes with a mobility of $450cm^2V^{-1}s{-}1$ being a factor of about 3 smaller than the electron mobility.
This effect is observed as well for the pSi (Fig. 6.19) sample where holes are the active charge carriers under accumulation (and depletion) regime and electrons at weak inversion (and strong inversion) regime. Unambiguous conclusions can not be drawn because the mobilities given above refer to charge carriers in the bulk of the material and a mobility reduction in accumulation or inversion is probable [16].

In the strong accumulation and strong inversion regime, the potential modulation induces a higher modulation of the number of charge carriers than under depletion and weak inversion conditions. So a decrease of the MWR signal magnitude is expected from $0V$ to $4V$ for the nSi wafer in Fig. 6.18. However, it is observed that the magnitude of the MWR signal increases with increasing potential between $0V$ and $4V$ (clearly seen at the $10kHz$ measurement). This could be interpreted as an effect of a reduced mobility under strong accumulation conditions.

6.3.2.5 Si/SiN_x interface characteristics: D_{it} extraction by the high-low modulation frequency capacity measurements

The interface state density characteristics are investigated in the present section. The capacity contribution from the interface states is measured, together with the space charge capacity at low modulation frequencies. Above a certain modulation frequency the interaction between charge carriers and interface states can no more follow the modulation and consequently do more contribution to the capacity so the contribution of the interface states to the capacity can be obtained by subtraction of the high frequency measurement from a low frequency one (see section 4.2.4). In this way the interface state density can be obtained as function of the applied potential V. A simulation program in Igor has been used to calculate the interface state density as

function of the energy position and the averaged density of interface states will be calculated for measurements of 6 different samples.

First of all two identical Si/SiN_x heterojunctions will be compared but one of them with a thin $3nm - SiO_2$ layer between the Si wafer and the SiN_x layer. The reproducibility of the Si/SiN_x samples is an issue. It has been observed that the passivation characteristics of the Si/SiN_x interface, as expressed in the excess charge carriers life time, although satisfying the minimum required for solar cell applications, present a range of life time values [28]. This is not exclusive for Si/SiN_x interfaces, differences between a "good" and a "bad" Si/SiO_2 interface have been as well an issue in the development of silicon based transistors [7] and it will be shown in section 9.3.5 that the charge carrier kinetics of a "good" and a "bad" oxide are not the same.

In the calculation of the fixed charge Q_f value, it has been taken as simplification that the interface states charge Q_{it} is much smaller than Q_f. Here the validity of this approximation will be discussed.

In Fig.6.20 the high ($10kHz$) and low ($1Hz$) frequency capacity measurements are shown as function of the applied potential for two $nSi - 1.5\Omega cm$ wafers covered by $45nm - SiN_x$ electrodes. One of them, but, has a $3nm - SiO_2$ thin layer between the Si and the $45nm - SiN_x$ (yellow markers). This thin oxide layer was chemically grown in order to have a more chemically stable Si surface previous to the SiN_x deposition. It has been observed that this pretreatment enhances the reproducibility of the passivating properties of Si wafers with SiN_x layers [28]. The samples were compared to identify if the SiO_2 pretreatment brings a considerable change of the interface states characteristics.

Fig.6.21 presents the density of interface states D_{it} as function of the applied potential for the samples measured in Fig. 6.20. The experimentally extracted $D_{it}(V)$ curves (by use of Eq. 4.25) are represented by markers while the simulated curves by solid lines. The program calculates Q_{it} and the high and low capacity curves from a given distribution of interface states as function of the energy position ($D_{it}(E)$) and its (donor-acceptor) nature. The distributions used for donor and acceptor states are defined by the sum of three terms:

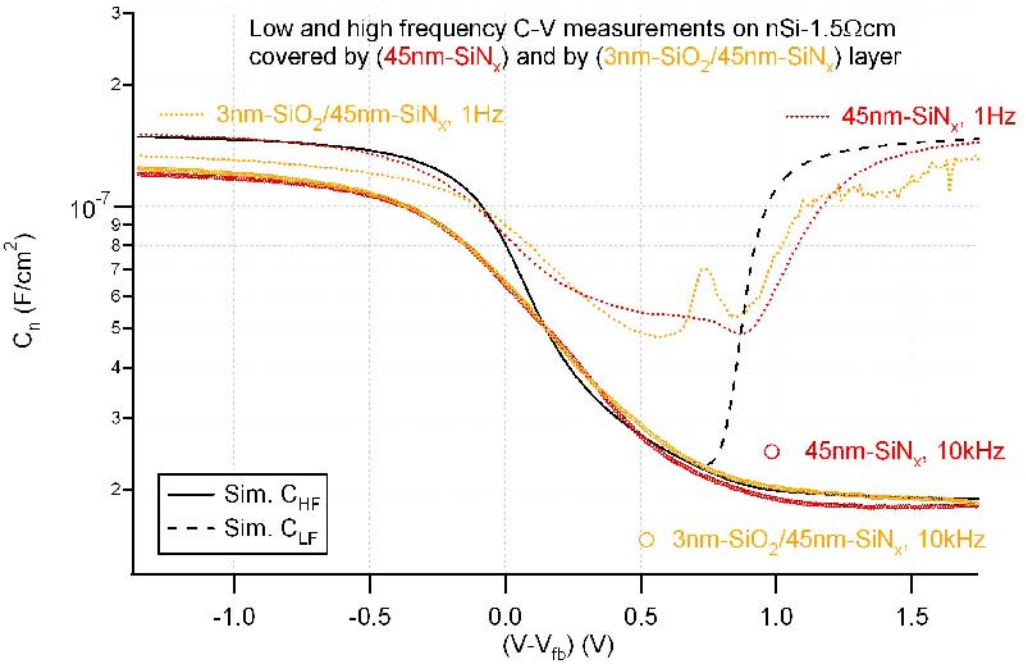

Figure 6.20: High and low capacity measurements as function of the applied potential for two $nSi-1.5\Omega cm$ wafers covered with $45nm-SiN_x$; one of them (yellow markers) presents a $3nm-SiO_2$ layer between the Si and the SiN_x layer which was chemically grown previously to SiN_x deposition [28]. The applied potential is given with respect to the flat band potential. Theoretical high and low frequency curves for an ideal MIS device are plotted in black lines.

$$D_{it}^{a}(E) = Ae^{-\left(\frac{E-E_c}{D_a}\right)} + Be^{-\left(\frac{E-V_a}{W_a}\right)^2} + cta \tag{6.3}$$

for the acceptor like, which contribute with a negative elementary charge when occupied by an electron and the donor like:

$$D_{it}^{d}(E) = Ce^{-\left(\frac{E_v-E}{D_b}\right)} + De^{-\left(\frac{E-V_b}{W_b}\right)^2} + ctb \tag{6.4}$$

which contribute with a positive elementary charge when unoccupied by an electron.

The acceptor (donor) distribution of interface states presents three contributions: an exponential term with its maximum A (C) at the band edge of the conduction band E_c (valence band E_v), a gaussian distribution with

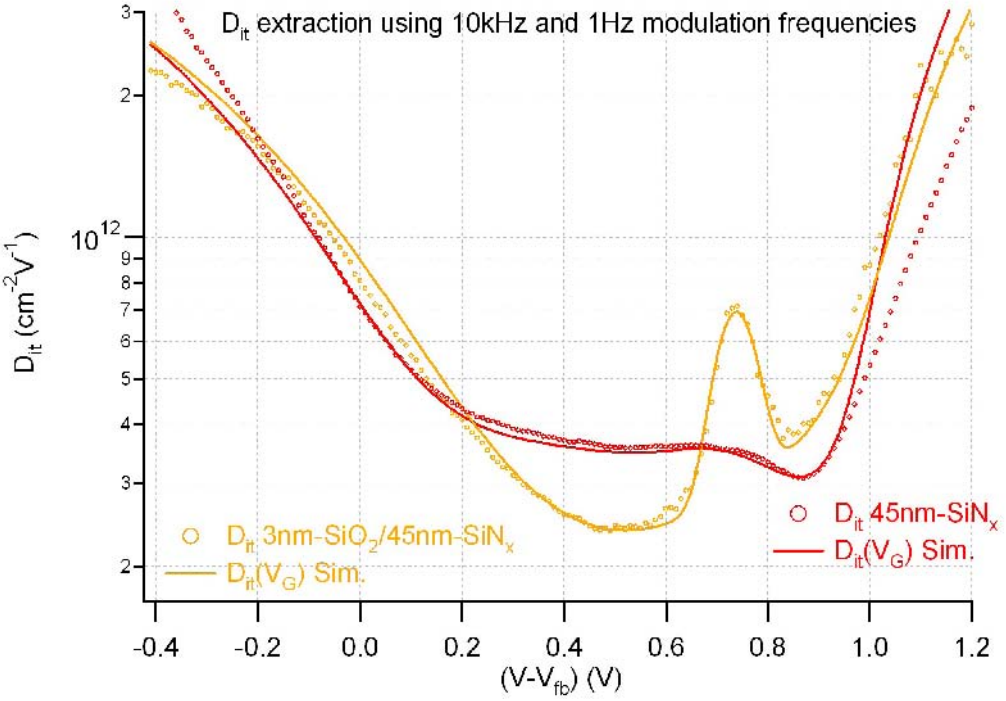

Figure 6.21: Interface state density as function of the applied potential for the two $nSi - 1.5\Omega cm$ wafers covered with $45nm - SiN_x$ shown in Fig.6.20. The applied potential is given with respect to the flat band potential. The solid lines correspond to the interface state density simulated by the program. The parameters used for the simulation can be found in Tab. 6.8 (see appendix in section 6.3.2.6).

amplitude B (D) centered in the energy position V_a (V_b) and a constant term cta (ctb) through the whole band gap.

The occupation level of the interface states was taken for the quasi-static case where the Fermi distribution can be used. The energy position of the conduction and valence band changes linearly with the surface potential ψ_s respect to the Fermi level [16], [7]. In the calculation of Q_{it} it is assumed that all the interface states with an energy above the Fermi level are not occupied and the ones with an energy below the Fermi level are occupied [17],[16], [7]. So given a $D_{it}(E)$ distribution Q_{it} can be calculated as function of ψ_s. Once the total charge at the semiconductor/insulator interface is calculated as function of ψ_s, the gate potential V_G (equivalent to the experi-

mental applied potential V) can also be calculated if the insulator capacity C_i is known. Finally, the high and low frequency capacity curves can be represented as function of the gate potential V_G and D_{it} as function of V_G can be extracted and compared to the experimental data. This has been the calculation proceeding used to simulate the curves here given. The simulation does not take into account the voltage shift due to the fixed charge Q_f but this is not relevant if the experimental curves are represented as function of $(V - V_{fb})$. Simulated plots and experimental curves were compared in the same graph and the parameters of $D^a_{it}(E)$ and $D^d_{it}(E)$ (in Eqs.6.3, 6.4) were changed until a reasonable assemblance was found for the low capacity and D_{it} as function of the applied (gate) potential between the simulated and experimental curves.

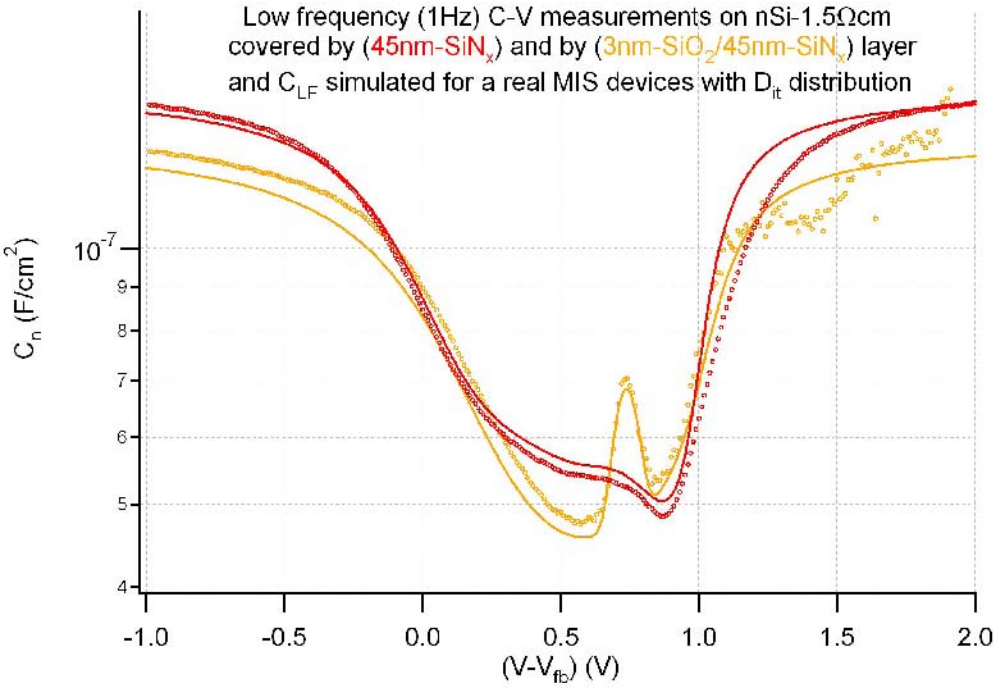

Figure 6.22: Low frequency capacity measurements (markers) and simulation (solid lines) as function of the applied potential for the samples shown in Figs. 6.20 and 6.21. The parameters used in the simulation are given in Tab. 6.8 (see appendix in section 6.3.2.6) where the electrodes are indicated as $EIS45$ the one without the $3nm - SiO_2$ layer and as $EIS45ox$ the one with the $3nm - SiO_2$.

In Fig. 6.22 is plotted the simulation of the slow capacity as function of the applied potential for the samples measured in Fig. 6.20. The main difference between both samples lays in the amplitude of the donor-like gauss distribution (given in Tab. 6.8 where the $EIS45$ and $EIS45ox$ samples correspond to the Si/SiN_x and $Si/SiO_2/SiN_x$ electrodes, respectively, shown in Fig. 6.21) but it is not particular due to the $3nm - SiO_2$ layer. Other samples without a SiO_2 layer grown previous to SiN_x deposition present higher and broader donor-like gauss distribution (see Fig 6.23). It is possible that all samples present SiO_2 interface characteristics due to corrosion of the electrode by the electrolyte, but high leakage currents were not observed for the cells measured here if not polarized at negative potentials (where the SiN_x. layer is destroyed).

In Tab. 6.8 (see appendix in section 6.3.2.6)the $D_{it}(E)$ parameters used in the capacity and the interface state density simulation as function of the applied potential from different measured cells are given. All cells except the one named "pSi50" were $nSi - 1.5\Omega cm$ electrode with SiN_x layers between $40nm$ and $50nm$. The "pSi50" cell had a $pSi - 100\Omega cm$ electrode covered by $50nm - SiN_x$ layer.
Experimentally, the D_{it} characteristics can not be extracted under inversion conditions. The high frequency capacity curve presents no contribution due to the inversion layer and the low frequency capacity curve presents the inversion layer and the interface states capacity contribution so the inversion layer effect cannot be subtracted using the high frequency curve. That is why pSi and nSi wafers are needed to be measured, to complement information.

In order to identify the capacity due to the interface states it is better to abandon the representation as function of the gate potential where the effect from the different insulator capacity C_i and the different interface state charge Q_{it} gives different stretching to the $C_T - V$ curves.
In Fig. 6.23 are shown the simulated space charge capacity C_{sc} (black line) and the parallel configuration of the C_{sc} and the interface state capacity C_{it} as a function of the surface potential ψ_s for the different $nSi - 1.5\Omega cm$ samples given in Tab. 6.8.

All nSi based electrodes show a capacity contribution due to the donor gaussian distribution of interface states and the exponential acceptor distribution.

In Tab. 6.6 are compared the values of the experimental fixed charge Q_f

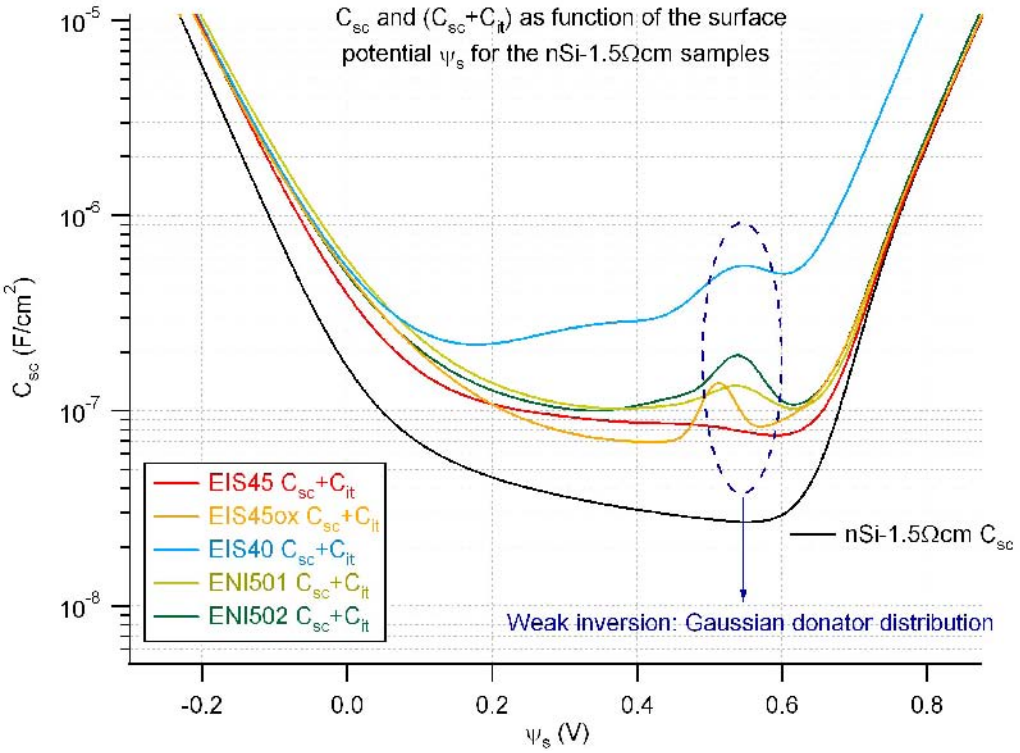

Figure 6.23: C_{sc} and $(C_{sc} + C_{it})$ as function of the surface potential ψ_s for the samples $nSi - 1.5\Omega cm$ in Tab. 6.8.

calculated from the V_{fb} position (extracted by from Mott-Schottky relation) and the simulated surface charge ($Q_s = Q_{sc}+Q_{it}$) when the applied potential is $V = -V_{fb}$. The model says that Q_s (charge at the Si/SiN_x interface) totally compensates the fixed charge in the isolator Q_f in the absence of external applied voltage. In order to test this, the simulation must calculate Q_s when the simulated applied potential V has the magnitude of the flat band potential but in opposite sign (remember that the simulation does not take into account the Q_f potential shift). The simulation is in very good agreement with the experimentally found Q_f so this test confirms that the simulation yields realistic parameters.

In the calculation of Q_f using the V_{fb} value, it assumed that $Q_{it} << Q_f$. The simulation of Q_{it} as function of the gate potential for the different samples presented in Tab. 6.8 is shown in Fig. 6.24 around the origin. Q_{it} can be considered one order of magnitude smaller than Q_f in the range of interest. This implies that the simplification considered above ($Q_{it} << Q_f$) gives

Sample	EIS45	EIS45ox	EIS40	ENI501	ENI502	pSi50
Q_f $(10^{12}cm^{-2})$	4.3	5.2	7	3	3	3.1
Q_s $(10^{12}cm^{-2})$	-4	-5	-6.5	-3	-3	-3.3

Table 6.6: Comparison of the values found for the fixed insulator charge Q_f to the semiconductor surface density of charge $Q_s = Q_{it} + Q_{sc}$ calculated for an applied (gate) potential $V = -V_{fb}$ by the simulation program.

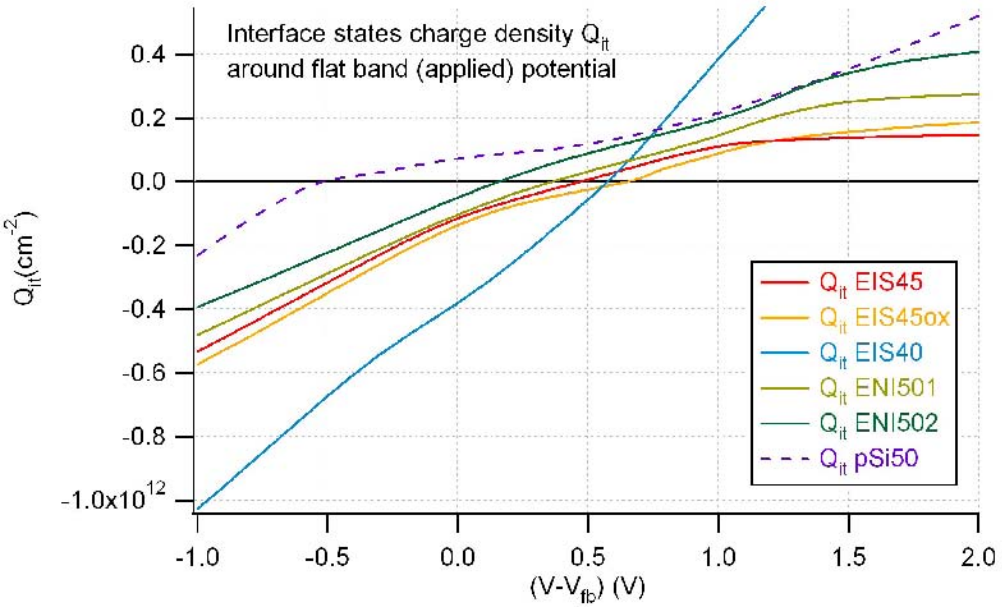

Figure 6.24: Total charge in interface states (normalized by the elemental charge) Q_{it} as function of the surface potential. Q_{it} has been calculated under thermal equilibrium with the simulation program for the D_{it} values given in Tab. 6.8.

about 10% error in the Q_f determination.

In Fig. 6.25 the averaged value for the interface state density found for all the samples presented in Tab. 6.8 is displayed. The donor and acceptor like gauss distributions are centered slightly below the intrinsic energy level, that is closer to the valence band. The valence band E_v has $2.93eV$ and conduction band E_c is positioned at $1.12eV$ higher in energy in the simulation.

Each type of these interface states present different trapping/emission ki-

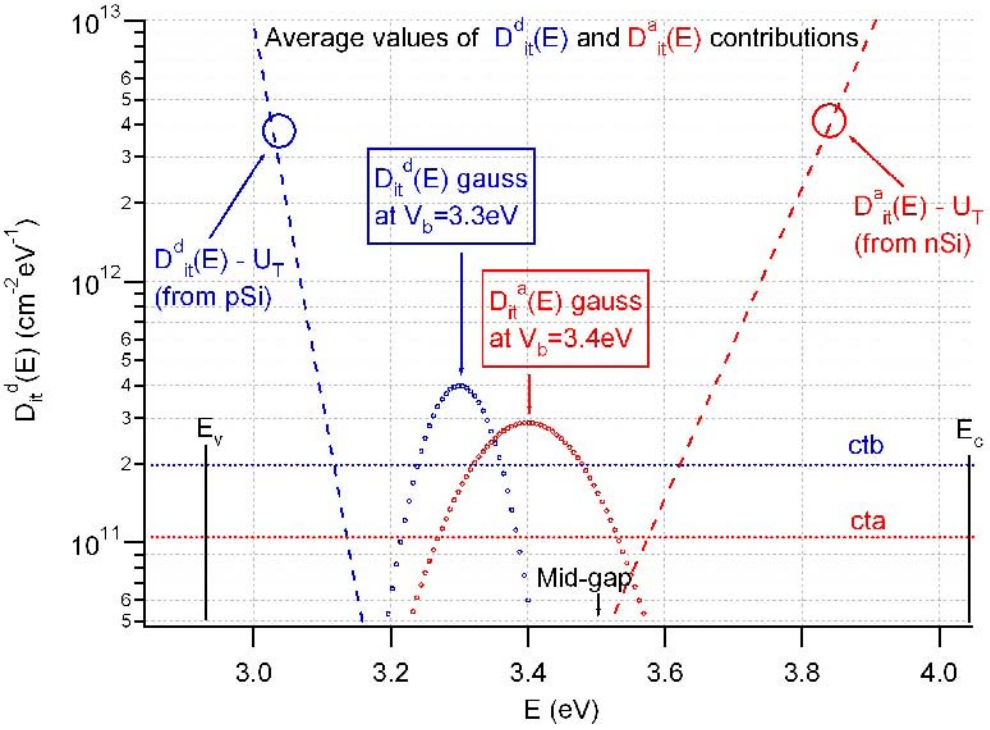

Figure 6.25: Average D_{it} distribution represented as function of the energy position. The valence band E_v is positioned at $2.93eV$ and conduction band E_c at $4.05eV$. The graph shows the independent contribution due to the different interface states contribution. Acceptor-like components are represented with red colored lines and the donor-like are blue.

netics with different characteristic times. This characteristic time is directly related to the frequency modulation range where the corresponding interface states contribute to the capacity.
This can be observed in Fig. 6.15 where the total capacity shows the frequency dependent capacity contribution from the interface states at potentials around V_{fb}.
The capacity contribution from the gaussian acceptor distribution (D^a_{it}-Gauss red markers in Fig. 6.25) is already observed at $10kHz$ modulation frequency (increasing with decreasing modulation frequency) whereas the contribution due to the donor gaussian distribution (D^d_{it}-Gauss blue markers in Fig. 6.25) is observed at $1Hz$ modulation frequency.

Comparing the Si/SiN_x interface state density here found to the Si/SiO_2

one given by the literature [23], [21] it is remarkable that Si/SiN_x interfaces present an acceptor-like gaussian distribution non existing at Si/SiO_2 interfaces.

In this section:

- Interface state density as a function of the energy position has been found and averaged for 6 Si/SiN_x electrodes contacted by an electrolyte and the frequency range and potentials where they are active are indicated.
- An acceptor-like gaussian distribution of interface states has been identified as characteristic of the Si/SiN_x interfaces.
- The MIS model and the validity of the experimentally found parameters (Q_f, V_{fb}, D_{it}) has been has been discussed.

6.3.2.6 Appendix

Sample characteristics:

Sample	ρ (Ωcm)	d (nm)	C_i (nF/cm^2)	N_d (cm^{-3})	V_{fb} (V)	Q_f $(10^{-12}cm^{-2})$	ϵ_i
EIS45	1.5	45	155	$3.5 \cdot 10^{15}$	4.5	4.3	7.8
EIS45ox	1.5	45	140	$3.6 \cdot 10^{15}$	6.2	5.2	7.1
EIS40	1.5	40	235	$4 \cdot 10^{15}$	4.9	7	10
ENI501	1.5	50	100	$4.3 \cdot 10^{15}$	5	3	5.6
ENI502	1.5	50	100	$4.5 \cdot 10^{15}$	5	3	5.6
pSi50	100	50	135	$1.5 \cdot 10^{14}$	4.5	3.1	7.6

Table 6.7: Resistivity ρ, SiN_x-thickness, measured capacity C_i, doping N_D and flatband V_{fb} found, calculated SiN_x fixed charge Q_f and calculated dielectric constant ϵ_i for the cells measured in section 6.3.2.5.

Simulation parameters:

Sample	cta $(cm^{-2}eV^{-1})$	A $(cm^{-2}eV^{-1})$	D_a (eV)	B $(cm^{-2}eV^{-1})$	V_a (eV)	W_a (eV)
EIS45	$1.2 \cdot 10^{11}$	$3 \cdot 10^{13}$	0.07	$8 \cdot 10^{10}$	3.53	0.2
EIS45ox	$1.1 \cdot 10^{11}$	$2.5 \cdot 10^{13}$	0.09	-	-	-
EIS40	$2.5 \cdot 10^{11}$	$3 \cdot 10^{14}$	0.08	$1 \cdot 10^{12}$	3.43	0.2
ENI501	$1.2 \cdot 10^{11}$	$3.9 \cdot 10^{13}$	0.08	$9 \cdot 10^{10}$	$3,33$	0.1
ENI502	$2 \cdot 10^{10}$	$3 \cdot 10^{13}$	0.08	$2 \cdot 10^{11}$	3.33	0.1
pSi50	$1.2 \cdot 10^{10}$	$8 \cdot 10^{14}$	0.04	$7 \cdot 10^{10}$	3.51	0.05
	ctb $(cm^{-2}eV^{-1})$	C $(cm^{-2}eV^{-1})$	D_b (eV)	D $(cm^{-2}eV^{-1})$	V_b (eV)	W_b (eV)
EIS45	$1.4 \cdot 10^{11}$	$1 \cdot 10^{11}$	0.05	$6 \cdot 10^{10}$	3.33	0.1
EIS45ox	$5 \cdot 10^{10}$	$1.2 \cdot 10^{12}$	0.15	$4.1 \cdot 10^{11}$	3.31	0.03
EIS40	$3 \cdot 10^{11}$	$4 \cdot 10^{14}$	0.05	$1.2 \cdot 10^{12}$	3.28	0.07
ENI501	$2.7 \cdot 10^{11}$	$1 \cdot 10^{11}$	0.08	$2 \cdot 10^{11}$	3.28	0.05
ENI502	$3.5 \cdot 10^{11}$	$1 \cdot 10^{13}$	0.05	$5 \cdot 10^{11}$	3.28	0.04
pSi50	$8.1 \cdot 10^{10}$	$1 \cdot 10^{14}$	0.03	$8.1 \cdot 10^{10}$	3.42	0.15

Table 6.8: Parameters used for the acceptor like interface states D_{it}^a in the simulation program to reproduce the experimental D_{it} extracted by high-low frequency modulation comparison. All the samples were covered by a SiN_x layer with a thickness between $40nm$ and $50nm$. The samples named "ENI" or "EIS" were nSi wafer with $\rho = 1.5\Omega cm$; the sample named "pSi50" was made by a pSi wafer with $\rho = 100\Omega cm$.

Chapter 7

Microwave photoelectrochemical measurements on Si/SiN_x based electrochemical cells

7.1 Introduction

In this chapter, steady state potential dependent photocurrent measurements of Si/SiN_x based electrochemical cells are presented.
As described in section 6.3.1, photocurrent measurements are performed by cycling of the applied potential while the electrochemical cell is illuminated by modulated light.
In an electrochemical cell the electrolyte takes the role of the gate electrode in a solid state device. In this case, a faradaic photocurrent will be always associated with the oxidation or reduction of chemical species from the electrode or from the electrolyte.
In the previous section 6.3.2, impedance measurements in electrochemical cells were performed in combination with microwave dark-conductance measurements. In this section photo-electrochemical measurements, are combined with microwave photoconductance measurements (MWR).
The combination of photocurrent and microwave photoconductance signals lead to complementary information: while a (faradaic) photocurrent indicates the number of photo-induced charge carriers that reach the external circuit of the electrochemical cell, the microwave signal indicates the number of (mobile) excess charge carriers present within the semiconductor [80], [81],

[82].
Of special interest is the study of the photo-catalytic properties of the Si/SiN_x electrodes. Bare Si electrodes are instable in aqueous electrolytes [83], [71] and that discards them as reliable candidates for photocatalytic applications in aqueous medias as e.g. water splitting.

In order to avoid the direct corrosion of the semiconductor, Si electrodes can be covered by a thin protecting layer which enables corrosion but enables charge transfer. SiN_x seems to be a candidate material to do this task [40], [69]. In this chapter the investigations aim to obtain information on the photocatalytic characteristics of Si/SiN_x electrodes for future (photo)electrocatalytic applications.

7.2 Experimental

Description of the cells measured is given in the previous chapter 6 (Fig. 6.1). In this section $pSi - 8\Omega cm$, $pSi - 100\Omega cm$ and $nSi - 1.5\Omega cm$ wafers covered by SiN_x of different thicknesses were used for the photoelectrochemical cells. The cells were illuminated by laser diodes at $635nm$ and $875nm$. Laser diode illumination was modulated by use of a function generator and the photocurrent and the MWR (a Ka-band system) signals were extracted by the lock-in measurement technique. Modulation frequencies between $500Hz$ and $10Hz$ were used in order to measure the cell photoresponse over wide modulation frequency range.
The electrochemical cells were polarized by use of a three electrode potentiostat as described in section 4.3.6. SCE was used as reference electrode. $4MKCl$ (aqueous), $1MHF$ (in $4MKCl$) and $0.5MLiCl$ in propylene carbonate (aprotic solvent) electrolytes were used to contact the Si/SiN_x electrodes.

7.3 Results

7.3.1 Non steady-state photocurrent around flatband

Illumination in the depletion regime enhances the concentration of minority charge carriers at the semiconductor surface.

- A fast electrode/electrolyte charge transfer diminishes the photoconductance in the semiconductor, leading to a small MWR signal com-

bined with a (faradaic) photocurrent: excess charge carriers are transfered from the semiconductor reaching fast the external circuit.

- Strong recombination processes can be identified by a low MWR signal and the absence of photocurrent. Excess charge carriers are annihilated.
- Accumulation of excess charge carriers on a passivated (non-recombinative) surface would lead to a high MWR signal where there is no photocurrent. The electrode/electrolyte charge transfer is very unprovable.

In Figs.7.1 and 7.2 the modulus of the photocurrent and MWR signals for $nSi-1.5\Omega cm$ and $pSi-8\Omega cm$ are presented. Both electrodes are covered by a $70nm-SiN_x$ isolating layer and in contact with $4MKCl$ aqueous electrolyte. The measurements are done at potentials around flatband potential.

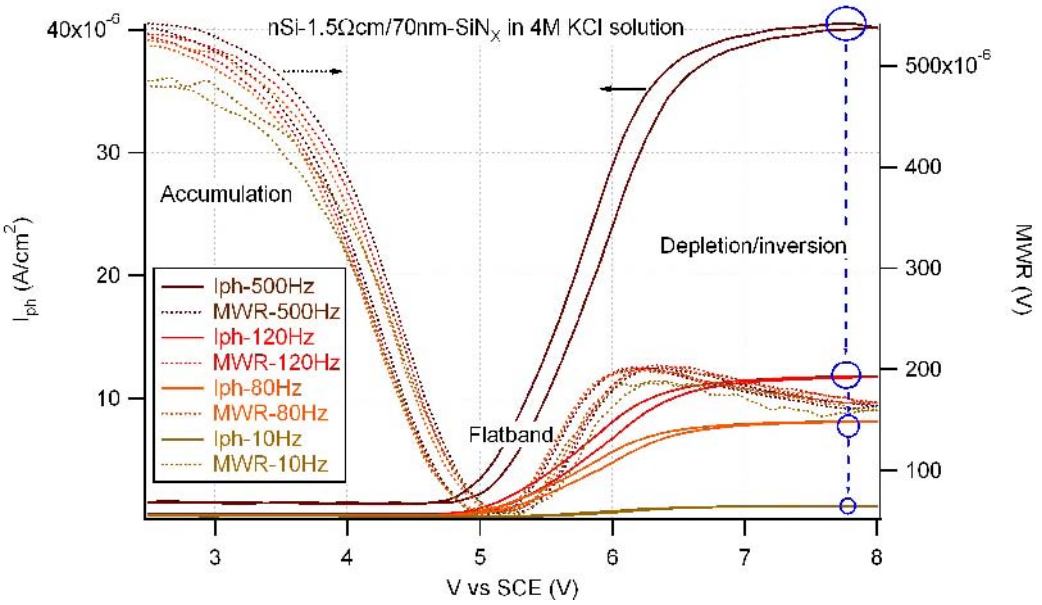

Figure 7.1: I_{ph} modulus and MWR signal for $nSi-1.5\Omega cm$ and $70nm-SiN_x$ electrode in $4MKCl$ aqueous electrolyte for different light modulation frequencies as a function of the applied voltage. Illumination was done by $635nm$ light with $\phi = 7 \cdot 10^{16} cm^{-2} s^{-1}$.

As seen in section 6.3.1 capacitive (dark)currents (in the absence of pores in the SiN_x layer) have been measured in aqueous electrolytes for potentials between $3V$ and $8V$ *vs SCE* (Fig. 6.6). Thus, only a small or no

charge transfer between *electrode/electrolyte* is expected. Light excitation, however, increases the density of minority charge carriers under depletion conditions at the *electrode/electrolyte* interface and charge transfer may increase since it may depend strongly on the concentration of minority charge carriers at the Si surface.
In both cells, a maximum saturation photocurrent (higher than $40\mu A/cm^2$) is measured at the $500Hz$ light modulation frequency. This saturation photocurrent is measured for potentials higher than $6.5V$ in the nSi/SiN_x cell (Fig.7.1) and for potentials below than $5V$ at the pSi/SiN_x cell (Fig.7.2). These potential ranges correspond to depletion/inversion regimes of the cells. The saturation value of the photocurrent shows a dependence on the modulation light frequency. By decreasing the modulation frequency, the photocurrent decreases dramatically. This indicates that the photocurrent measured at $500Hz$ is not stationary. Actually stationary photocurrent must be measured at lower modulation frequencies such as $10Hz$ or $1Hz$, allowing the system to reach stationary equilibrium. Photocurrent values at $10Hz$ are below $5\mu A/cm^2$, nearly one order of magnitude lower, and this occurs for both cells. This shows that there is practically no stationary photocurrent, in other words, that the charge transfer between *electrode/electrolyte* is very unprovable.

In Fig. 7.1 the MWR signal does not show a modulation frequency dependence. The MWR signal has a maximum in accumulation regime (between $2.5V$ and $4V$) and presents a relative maximum value at $6V$ (in depletion conditions). The MWR minimum observed at $5V$ corresponds to potentials near flatband potential where the recombination at Si/SiN_x is maximal and the onset of the photocurrent takes place.

Similar MWR and photocurrent characteristics are observed in the pSi/SiN_x cell (Fig.7.2); accumulation occurs for potentials higher than $8V$, depletion/inversion for potentials below $6V$ and flatband around $6.5V$. The MWR signal in depletion regime shows a frequency dependence: the MWR signal increases with increasing light modulation frequency and it is also observed an hysteresis between forward and backward scan. The hysteresis might be related to hole trapping in the accumulation regime and the change of the interface (passivating) properties.

It is observable for both samples a decrease in the MWR signal when increasing polarization from depletion to inversion regime, although the num-

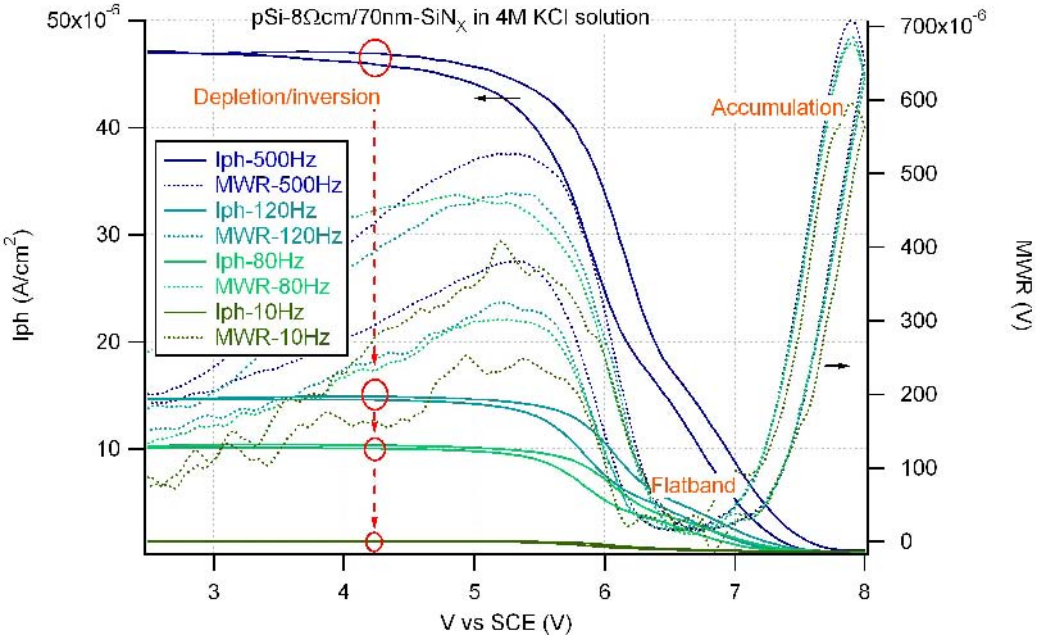

Figure 7.2: I_{ph} modulus and MWR for $pSi - 8\Omega cm$ and $70nm - SiN_x$ electrode in $4MKCl$ aqueous electrolyte for different light modulation frequencies as a function of the applied voltage. Illumination was done by $635nm$ light with $\phi = 7 \cdot 10^{16} cm^{-2} s{-}1$ incident photon flux.

ber of photo-induced minority charge carriers at the surface increases with increasing polarization into inversion. This can be interpreted as reduction in the charge carrier mobility at the surface. Realize that the change in the MWR signal is reduced to 15% for the pSi sample (comparing $5.5V$ to $3V$ in Fig.7.2) and to 75% for the nSi (comparing $6V$ to $8V$ in Fig.7.1). A mobility reduction (due to trapping or charge carrier injection in the inversion region) has a higher contribution to the silicon (photo)conductivity when electrons are involved due to their higher (bulk)mobility characteristics.

The two cases described above (Figs.7.1 and 7.2) show the enhancement of the concentration of excess charge carriers at the passivated Si/SiN_x interface (in accumulation and depletion regimes). In the flat band regime strong recombination of the excess charge carriers is observed. This shows again the field effect passivation of SiN_x on Si wafers under "stationary" conditions, also shown by the TRMC measurements in section 8.2.

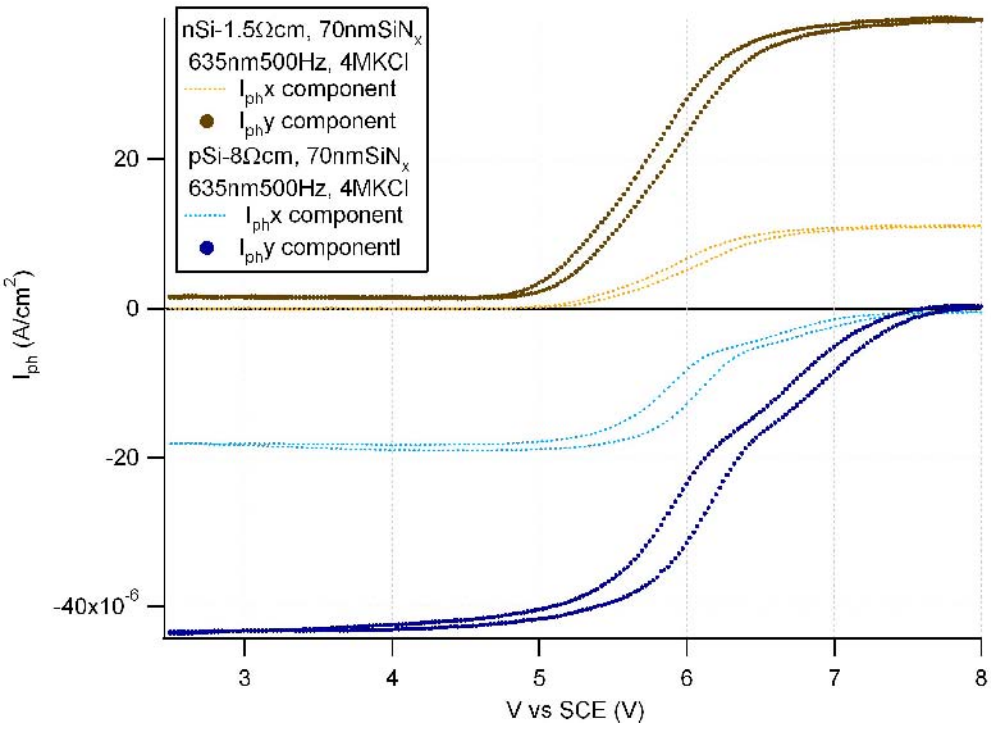

Figure 7.3: X and Y photocurrent components for a light modulation frequency of $500Hz$ at the pSi and nSi based samples shown above (Figs.7.1 and 7.2)as a function of the applied voltage. Illumination was done by $635nm$ light with $\phi = 7 \cdot 10^{16} cm^{-2} s{-}1$ incident photon flux.

If instead of the photocurrent modulus, the X (in phase) and the Y ($\pi/2$ out of phase) components of the photocurrent are measured, it can be observed that the highest contribution to the photocurrent modulus is due to the Y component as shown in Fig.7.3 for $500Hz$ modulation frequency. The photocurrent signs for the pSi sample are negative and for the nSi positive. Following the electrochemical configuration, negative current corresponds to negative charges flowing from working electrode to counter electrode and a positive current the other way around. In analogy to impedance measurements (section 4.1), a faradaic (photo)current is in phase with the light modulation. The Y component of the photocurrent corresponds to a capacitive or inductive photocurrent: a displacement current.

This implies a current due to a hindered (e.g. displacement current) movement of charge carriers. The charge carriers transport responsible for

this current can not sustain a stationary process and is characterized by a time reflecting the process limiting this transport. The experimental data (Figs.7.1 and 7.2) suggests this characteristic time to be in the millisecond range.

The signals measured at higher frequencies must be related to the reorganization kinetics of the excess charge carriers. The transition between the two stationary states (light and dark) lead to a displacement photocurrent with the absence of a real *electrode/electrolyte* charge transfer. In fact, the photocurrent and MWR signals measured are the harmonic response of the cell to the harmonic light perturbation. Capacitive currents will be measurable at higher light modulation frequencies and are not present at low modulation ones. It must be noted that the perturbation at this light intensities can not be considered as small and thus the system response may be non linear, making the interpretation of the Y and X components of the photocurrent more difficult. Small light perturbation measurements have not been done in the present electrochemical system but, in principle, it is a technique which can lead to information of the excess charge carriers kinetics under illumination and non stationary conditions [84],[37].

The MWR signal, however, shows no frequency dependency. This indicates that the stationary state of photo-conductance in the semiconductor is rapidly attained, even before the steady state of the photocurrent is reached. The MWR signal is not so high in depletion regime as in accumulation regime. With the excitation density equal in both regimes and the absence of a faradic current, the lower MWR signal may be due to an enhanced recombination or trapping of excess charge carriers in the depletion regime as it is frequently observed.

It can be concluded from the measurements shown above:

- No stationary photocurrent at potentials between $0V$ and $8V$ in Si/SiN_x based electrochemical cells in aqueous electrolytes can be observed. A $70nm - SiN_x$ insulator layer makes the *electrode/electrolyte* charge transfer unprovable in this potential range.

- The photocurrent measured is a displacement current, probably related to recombination or trapping at the Si/SiN_x interface.

- Field effect passivation characteristics can be observed under stationary

conditions. The MWR signal presents a relative maximum in accumulation and depletion and a minimum around flat band potential.

7.3.2 Steady-state photocurrent in aqueous electrolytes at negative (cathodic) potentials

A stationary faradaic photocurrent is measured for pSi based electrodes, in contact with an aqueous electrolyte, at negative potentials as shown in Fig.7.4. At negative potentials pSi is in strong inversion regime and the total charge of the electrode is negative due to the high concentration of electrons at the pSi/SiN_x interface. Thus, positive species present in the electrolyte are attracted by the electrode.

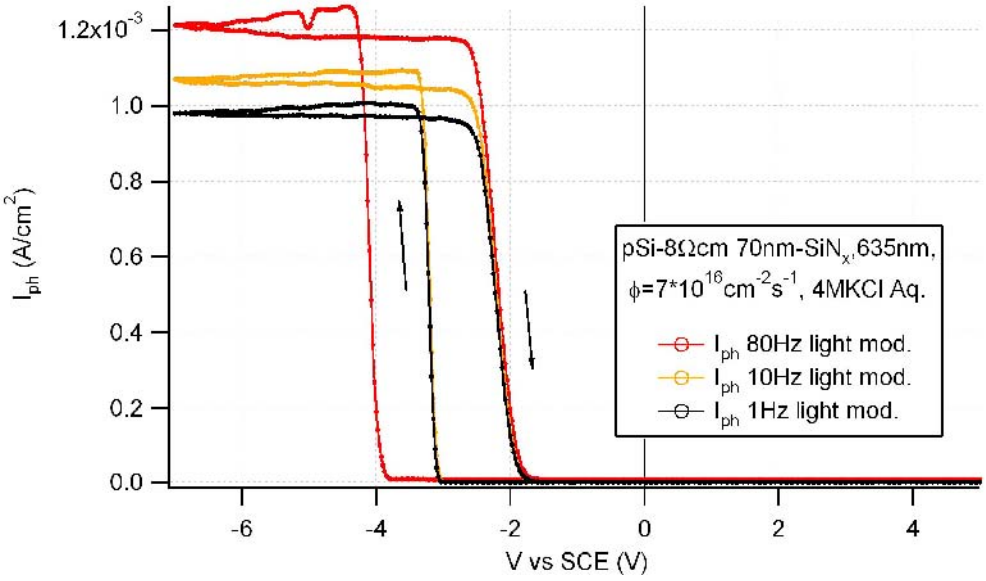

Figure 7.4: I_{ph} modulus in cathodic regimes for $pSi-8\Omega cm$ with $70nm-SiN_x$ electrode in $4MKCl$ aqueous electrolyte for different modulation frequencies. It is observed a I_{ph} in the mA/cm^2 range even for $1Hz$ frequency which indicates its stationarity.

In Fig.7.4 the photocurrent modulus for pSi covered by $70nm - SiN_x$ in $4MKCl$ aqueous electrolyte is shown for three different light modulation frequencies between $80Hz$ and $1Hz$. The photocurrent saturation value measured for potentials more negative than $-4V$ is around $1mA/cm^2$ even for the $1Hz$ modulation frequency, indicating that the photocurrent measured

is stationary.
A big hysteresis is observed between the forward and backward scan. The onset of the photocurrent when scanning from positive to negative potentials is $-3V$ ($-4V$ for the $80Hz$ measurement) and shifts to $-2V$ when scanning from negative to positive potentials.

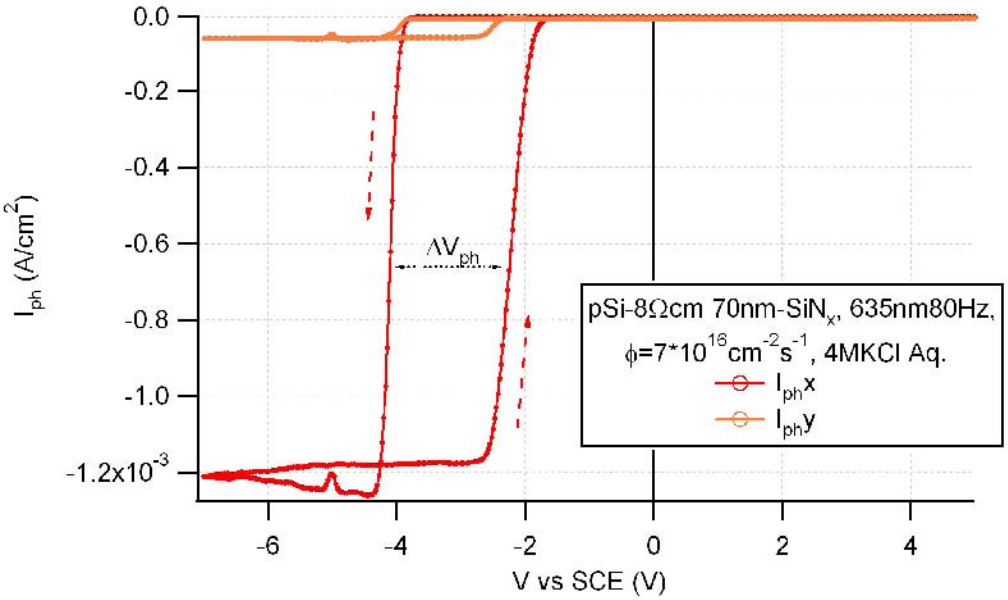

Figure 7.5: X and Y photocurrent components in cathodic regime for the $pSi - 8\Omega cm$ with $70nm - SiN_x$ electrode in $4MKCl$ aqueous electrolyte. $635nm$ light with $\phi = 7 \cdot 10^{16} cm^{-2} s^{-1}$ photon flux was modulated at $80Hz$. Photocurrent was accompanied by strong gas evolution at the electrode.

In Fig. 7.5 the X and Y components at $80Hz$ modulation in Fig.7.5 are shown. In contrast to the photocurrent measured at positive potentials (Fig.7.2), the main contribution to the photocurrent is the X component. This photocurrent is negative and would correspond to electrons flowing from working electrode to counter.

- The photocurrent measured for pSi/SiN_x electrode at negative potentials is a faradaic photocurrent. it is associated to the reduction of a chemical specie, most probable a proton reduction.

The photocurrent measured was accompanied by the observation of gas evolution at the electrode, the best chemical candidate in $4MKCl$ aqueous electrolyte is H_2. However, the potential of the onset of the photocurrent does not correspond to the electrochemical reduction potential $vs\ SCE$, expected at $-0.234V$ [41]. This mismatch in potentials can be explained by the presence of the SiN_x insulating layer. There is a potential decay in the isolator capacitor, thus, a greater potential is needed in order to give an electron from the Si wafer the energy to reduce a proton.

In order to observe the influence of the insulating layer thickness in the photocurrent potential onset, $pSi-8\Omega cm$ electrodes with $15nm-SiN_x$ (Fig. 7.6), $70nm-SiN_x$ (Fig. 7.4) and bare (Fig.7.7) electrodes have been measured in a KCl aqueous electrolyte solution.

Fig.7.6 shows the X and Y components of the photocurrent and MWR signals for the $15nm-SiN_x$ electrochemical cell. At potentials between $5V$ and $-7V$. It can be clearly distinguished between the capacitive and faradaic photocurrent regimes discussed above: the capacitive photo-effects between $-2V$ and $3V$ and the faradaic ones at potentials more negatives than $-2V$. In order to identify the regimes better, the logarithmic plot of the absolute values of X and Y photocurrent components (left axis) and MWR signal (right axis) are given.

It is observed that the Y component of the photocurrent dominates at voltages between $-2V$ and $3V$ and is accompanied by a high MWR signal. This corresponds to the depletion regime with very little charge transfer. At potentials more negative than $-2V$ the X component rises over the Y component, reaching values around $1mA/cm^2$. The MWR signal decreases around one order of magnitude, corroborating that the excess charge carriers are fast transfered out of the pSi. This corresponds to the cathodic regime (inversion) where faradaic photocurrent takes place by the reduction of protons.
Flatband potential can be identified around $3V$ by the onset of the (capacitive) photocurrent and by a minimum in the MWR signal (maximum of surface recombination).
Essentially the same results were obtained for the pSi with $50nm-SiN_x$ with a shift in the flat band potential to more positive potentials.

Photocurrent measurements on bare $pSi-8\Omega cm$ are shown in Fig.7.7.

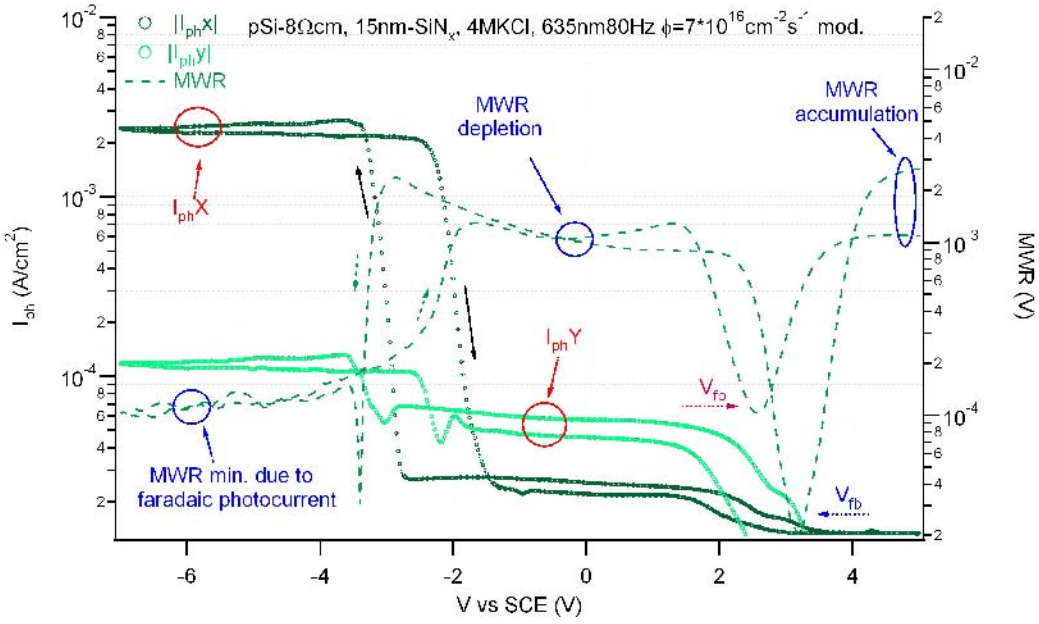

Figure 7.6: X and Y I_{ph} components for $pSi-8\Omega cm$ with $15nm-SiN_x$ electrode in $4MKCl$ aqueous electrolyte for $10Hz$ light modulation frequency, $\lambda = 635nm$ and $\phi = 7 \cdot 10^{16} cm^{-2} s^{-1}$.

The cell was measured in $1MKCl\ HF$ aqueous solution in order to avoid SiO_2 formation under positive polarization [85]. The experiment is done to compare the photocurrent magnitude and hysteresis for the case that no insulating layer covers the electrode. The photocurrent saturation value at negative potentials has the same magnitude as the values measured for aqueous electrolyte in the pSi/SiN_x electrodes. This time, for the bare Si electrode, the photocurrent onset is at $-0.5V$, different from the $-3V$ or $-2V$ found for the Si/SiN_x electrodes. The hysteresis observed is also smaller. The MWR signal in the bare Si electrode at positive potentials is small, it does not rise again as measured in the SiN_x covered electrodes. This shows the passivating effect of SiN_x on Si wafer: if a covered sample shows storage of excess charge carriers when illuminated under depletion and accumulation conditions, a bare sample shows surface recombination of these excess charge carriers.

The onset of the photocurrent does not depend strongly on the insulator thickness. The hysteresis, indicates that the Si/SiN_x cells suffer a modification. A possible reason may be the incorporation of hydrogen within the

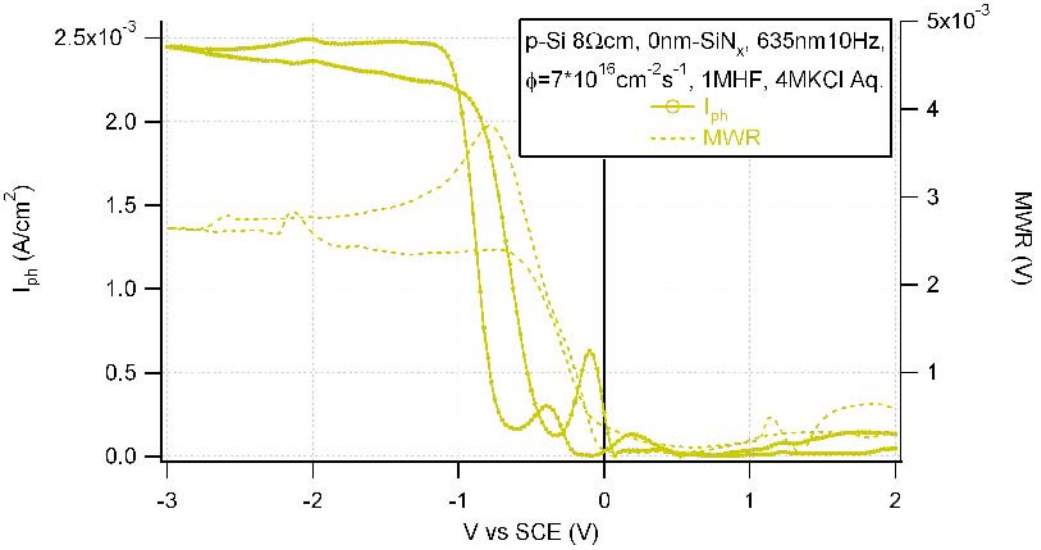

Figure 7.7: I_{ph} modulus and MWR signal measured for a bare $pSi - 8\Omega cm$ in $1MHF$ aqueous electrolyte with $4MKCl$ as function of the applied potential. Illumination wavelength $\lambda = 635nm$, $\phi = 7 \cdot 10^{16} cm^{-2} s^{-1}$ and $10Hz$ modulation frequency.

SiN_x, modifying its properties as the fixed charge Q_f or the interface states. As mentioned in section 6.3.1 hydrogen evolution probably takes place at the Si/SiN_x interface or the SiN_x volume, damaging the SiN_x layer. After being polarized at negative potentials, the photocurrent onset shifts $1V$ to more positive potentials, that is equivalent to an increase of the positive charge in the insulator. This hysteresis is not so large when measurements are done only at positive potentials, especially when no hydrogen evolution has taken place in the cycle. The hysteresis observed around flatband potentials in the MWR signal and the Y component of the photocurrent measured in Fig.7.2 are under $0.2V$. The hysteresis at positive potentials increases if cycling at negative potentials has involved hydrogen evolution as in Fig.7.6. The MWR minimum at flat band potential is greater in magnitude after cycling at negative potentials (indicated in Fig.7.6) suggesting a minor surface recombation. This can be explained by the hydrogen incorporation into the SiN_x layer passivating part of the dangling bonds responsible of the surface recombination.

With these results it can be concluded that the presence of hydrogen plays

a fundamental role in the hysteresis observed at positive potentials for the $Si/SiN_x/electrolyte$ system. The photocurrent process can lead to an exchange of electrons between the Si and SiN_x layer modifying its fixed charge Q_f and hydrogen can be incorporated in the SiN_x passivating (partially) the dangling bonds. This change in the fixed charge would be responsible for the (photo)hysteresis observed.

7.3.3 Steady-state photocurrent for aprotic electrolytes

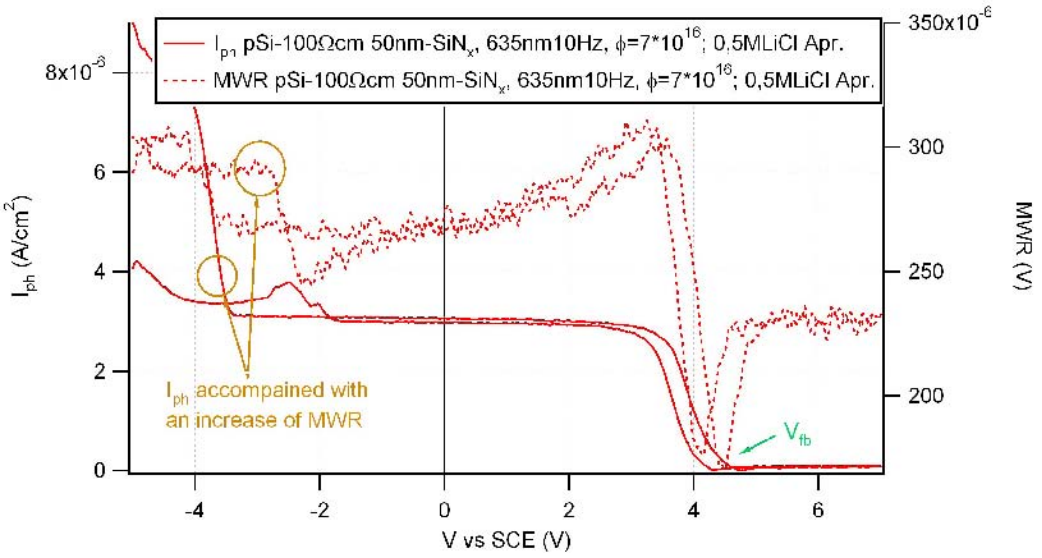

Figure 7.8: I_{ph} modulus and MWR signal for $pSi - 100\Omega cm$ with $50nm - SiN_x$ electrode in $0,5MLiCl$ aprotic electrolyte as function of the applied potential. $635nm$ light with a incident photon flux of $\phi = 7 \cdot 10^{16} cm^{-2} s^{-1}$ and modulated with $10Hz$.

In order to confirm that the photocurrent at negative potentials is due to proton reduction and that the hysteresis observed involves its presence, a $pSi{-}100\Omega cm$ with $50nm{-}SiN_x$ electrode has been contacted with $0.5MLiCl$ propylene carbonate; an aprotic electrolyte.
The photocurrent measured at negative potentials is three order of magnitude smaller than measured in aqueous electrolyte. Moreover, the MWR signal does not show a decrease indicating that the photocurrent measured is not due to a charge transfer. The MWR signal shows a minimum at flatband

potential where the onset of the photocurrent takes place. By analogy to the measurements around flatband, it suggests that the photocurrent has a capacitive nature, extended to further negative potentials.
The hysteresis observed around flatband has decreased as well.

7.4 Conclusions

- Displacement photocurrents are identified by the out of phase component of the photocurrent. Its magnitude depends strongly on the light modulation frequency.
- The combination of AC photocurrent and MWR spectroscopy has shown that in pSi/SiN_x and nSi/SiN_x at positive potentials show only capacitive photocurrents and the Faradaic photocurrents is negligible.
- Increasing the SiN_x insulating thickness does not appreciably change the onset of the photocurrent.
- Strong negative polarization of Si/SiN_x electrodes in aqueous electrolytes changes the charge within SiN_x. This fact has not been observed in bare silicon so it can be attributed to the interaction of the insulating layer with the electrolyte, probably proton intercalation into its volume.

Chapter 8

TRMC measurements on nSi/SiN_x based electrochemical cells

8.1 Introduction

SiN_x layers on nSi are used as antireflective and passivating layer in solar energy conversion applications. SiN_x has a volume positive charge which brings the nSi wafer into accumulation regime (sections 5.3.2 and 6.3.2).
In this section Time Resolve Microwave Conductance (TRMC) measurements (section 4.3.3) under voltage polarization in electrochemical cells based on nSi/SiN_x electrodes will be presented.

8.2 Experimental

Working electrodes are composed of nSi/SiN_x heterojunctions. $75nm$ and $50nm$ thick SiN_x layers were deposited on one side of the $nSi - 1.5\Omega cm$, $< 111 >$ oriented wafers by PECVD [28].
Description of the electrochemical cells measured is given in chapter 6 (Fig. 6.1). The electrolyte used to contact the nSi/SiN_x (working) electrodes was a $4MKCl$ aqueous solution. The cell was polarized by a voltage source connected to working and counter electrode.
Illumination was done by $532nm$ laser pulses (10ns FWHM) as described in section 4.3.6. MWR measurements were done in a Ka-band microwave

system.

8.3 Results

The laser pulse at $532nm$ generates a strongly non uniform minority charge carrier density and the time profile can not be considered as an ideal delta excitation function. Accurate treatment of charge carriers dynamics taking into account the initial boundary conditions can be done using deconvolution mathematics [14] which is of special interest if fast recombination processes or photoconductance onset are investigated. In the present section only a qualitative description of the excess charge carrier dynamics is given.

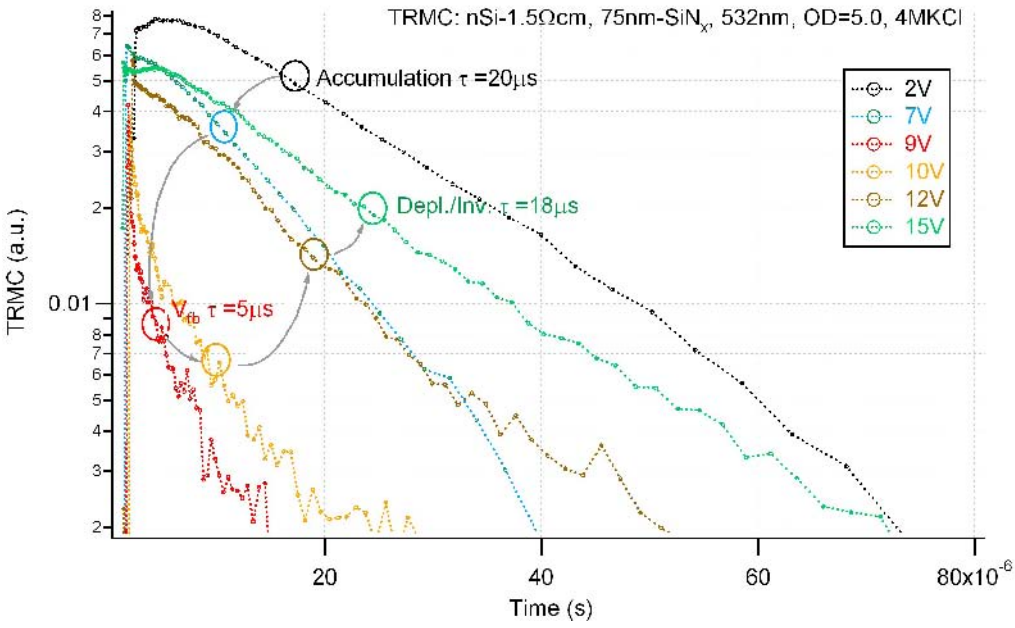

Figure 8.1: $TRMC$ transients for $nSi - 1.5\Omega cm$ with $70nm - SiN_x$ layer in $4MKCl$ for different applied potentials. Pulse wavelength was $532nm$ with $10ns$ FWHM and nominal intensity $I_0 = 50mJcm^{-2}$ and attenuated by $OD = 5.0$.

In Figs. 8.1 and 8.2 TRMC signals induced by light pulses are shown for different applied voltages in nSi/SiN_x electrochemical cells. Exciting the sample with $\lambda = 532nm$ generates charge carriers in the first $2\mu m$ of the illuminated Si surface. The absorption coefficient of intrinsic silicon for that

wavelength is $\alpha_{530} = 7850cm^{-1}$ [86] and the incident laser intensity on the cell is $I_0 = 50mJ/cm^2$, attenuated by $O.D. = 5.0$.
The TRMC signal induced by $532nm$ light is sensitive to the interface kinetics because nearly all charge carriers are generated in or very near to the space charge region. Up to $20\mu s$ the decay takes mainly place via the higher modes (section 2.5.3) and so the decay time in this time range is difficult to determine. Nevertheless the initial decay is representative for recombination at the illuminated surface and can be compared for different applied voltages.

At $0V$ ($75nm - SiN_x$) and $2V$ ($50nm - SiN_x$) polarization nSi is under strong accumulation conditions. Positive fixed charge in SiN_x drives electrons from the conduction band to the nSi/SiN_x interface (sections 5.3.2 and 6.3.2). In both samples ($50nm$ and $75nm$-SiN_x) the TRMC signal decays at longer times with a characteristic time of $\tau = 20\mu s$. This corresponds approximately to the fundamental mode decay time $\tau = 4L^2/D\pi^2$ (Eq. 2.77) for the case that the rear side is an ideal sink and the illuminated front side is ideal passivated. So in accumulation, the illuminated surface acts as a reflective mirror for photo-generated electron-hole pairs: nearly no recombination takes place on the accumulation surface and excess charge carriers diffuse together (section 2.5.1) to the rear surface where they recombine. The small increase of the TRMC signal for times shorter than $10\mu s$ may be due to a non stationary distribution of excess charge carriers in the sample and the non uniformity of the sensitivity factor S (section 4.3.1 and Fig. 4.4) because of the initially rather high excess charge carrier density (large perturbation) in an $1.5\Omega cm$ wafer.

Increasing the potential in reverse direction (more positive potentials) drives the semiconductor into the flat band regime: the fixed positive charge in the SiN_x is compensated by the negative ions in the electrolyte and the space charge region polarization in the nSi diminishes. The effective decay time at $9V$ for the $75nm - SiN_x$ cell and $4V$ for the $50nm - SiN_x$ cell is initially very small ($1\mu s$). These are the potentials, respectively for each cell, with the highest recombination rate.
Under flat band conditions, the nSi space charge region (SCR) is small and there is no bending of the bands. Excess charge carriers are not separated by a depletion field and so electron-hole pairs are present at the surface and available for recombination: the field induced passivation of the Si/SiN_x interface is suppressed.

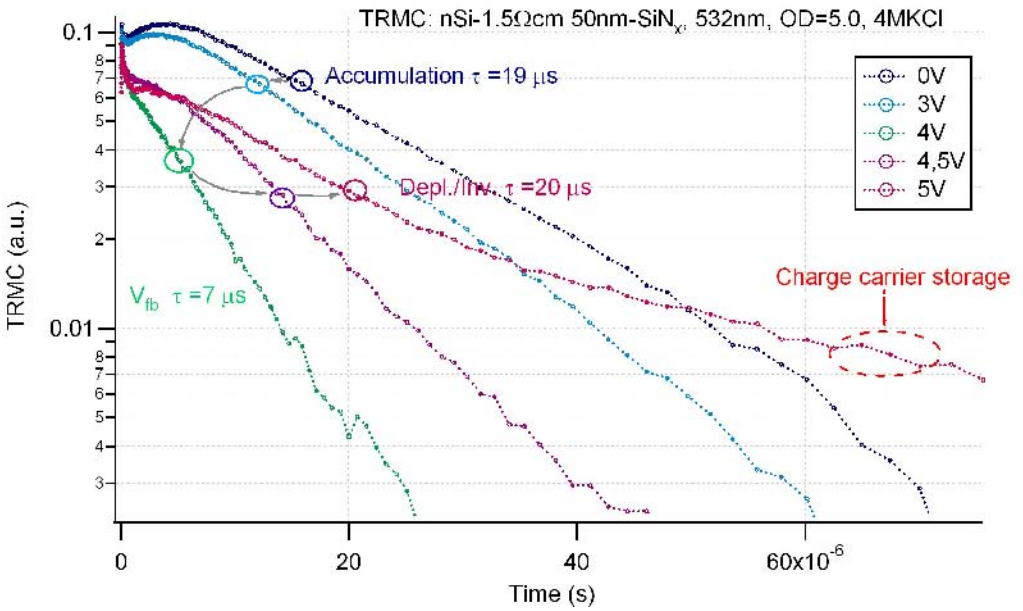

Figure 8.2: $TRMC$ transients for $nSi - 1.5\Omega cm$ with $50nm - SiN_x$ layer in $4MKCl$ for different applied potentials. Excitation was by $532nm$ pulses with $10ns$ FWHM and intensity $I_0 = 50mJcm^{-2}$ attenuated by $OD = 5.0$.

Further positive polarization brings the semiconductor into the depletion/inversion regime where photoinduced charge carriers are separated by the field in the depletion region and so holes accumulate at the nSi/SiN_x interface and electrons at the edge of the depletion zone. A fast decay is observed for times below $2\mu s$ and for times longer than $2\mu s$ the photoconductance is characterized by an extended decay with characteristic decay time increasing with time. This effect is due to the storage of charge carriers at the extremes of the depletion region. The excitation density is so high that the photo-generated electron-hole pairs accumulate on the extremes of the depletion region and shield the SCR field flattening the bands and allowing recombination at the surface. Thus, at shorter times a fast recombination takes place leading to a fast TRMC signal decay. At longer times the number of excess charge carriers has diminished and the SCR field cannot be totally shielded by them. Thus, the band bending is built up and electron-hole pairs have to overcome an energy barrier to recombine. This makes recombination less probable leading to a slower TRMC signal decay.

Fig.8.3 shows the effective life times plotted as function of the applied

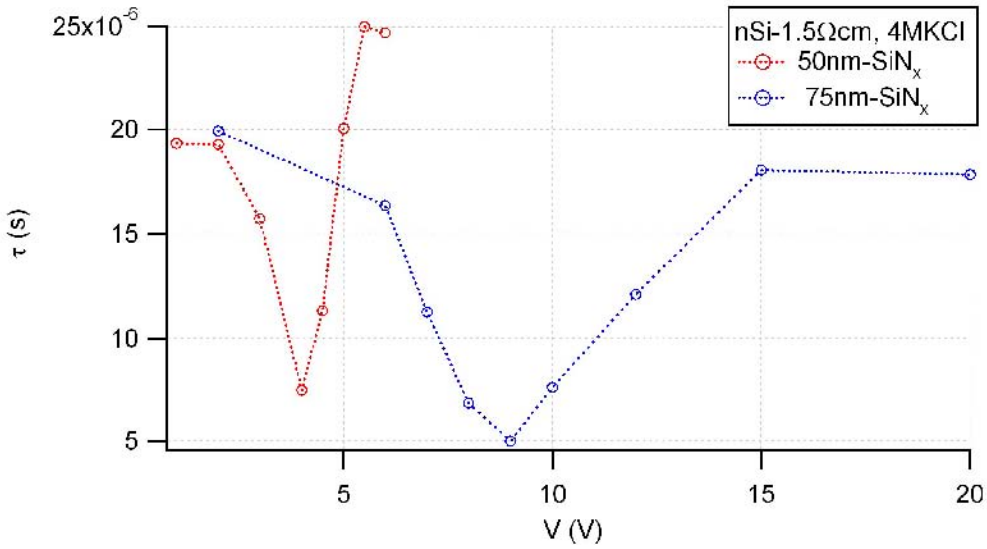

Figure 8.3: Effective lifetime as function of the applied voltage in $nSi-1\Omega cm$ with $70nm$ and $50nm$ SiN_x layers in $4MKCl$, $\lambda = 532nm$, $OD = 5$. The data are extracted from the measurements shown in Figs.8.1 and 8.2.

voltage for both samples. Decay times were estimated for the time range exceeding $20\mu s$ when possible. In this plot it is easier to compare the effective lifetime as function of potential polarization and distinguish the different regimes described.
Dauwe [87] analyzes experiments where the fixed SiN_x charge is compensated or increased by a corona discharge. The present experiment is comparable considering that the fixed charge is compensated or increased by charge in the electrolyte. Dauwe assumes that the surface recombination at the Si/SiN_x interface is limited by the availability of both kinds of charge carriers (field passivation). Adopting this assumption, the minimum effective lifetime is found around flat band and that is exactly what is found in these measurements too.
The fast decay found around flat band potential indicates that Si/SiN_x presents a high density of recombinative surface states.

In Fig.8.4 another interesting characteristic is observed: a clear hysteresis between forward and backward scanning. Flat band is found at $4V$ in the forward direction and shifts to $5.5V$ for the backward direction. The flat band potential shifts around $1.5V$ to more positive potentials after strong

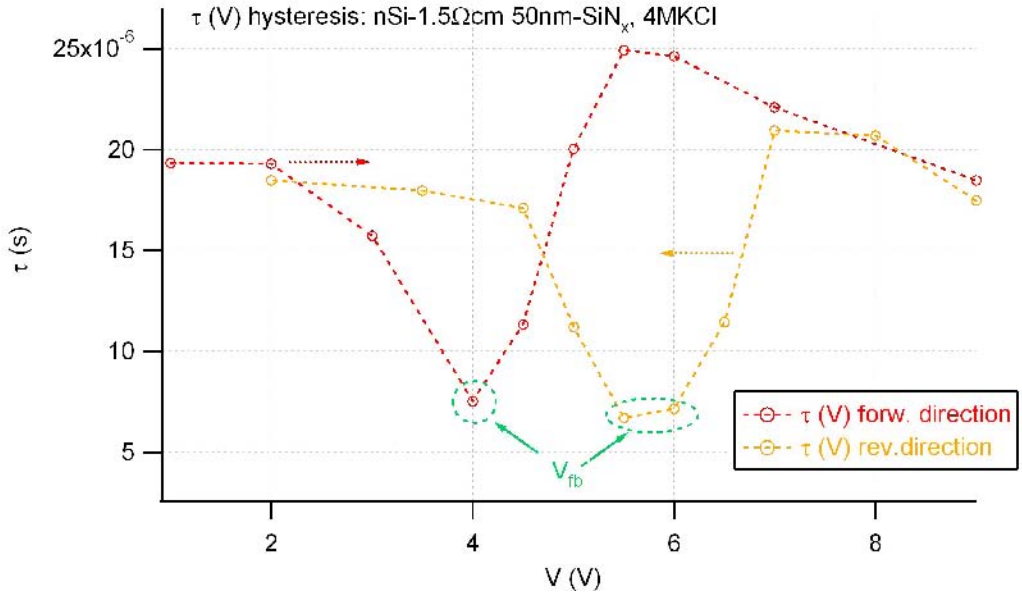

Figure 8.4: Effective life time as function of the applied voltage in $nSi - 1.5\Omega cm$ with $50nm - SiN_x$ layer in $4MKCl$ for forward direction (red markers) and backward direction (yellow markers).

polarization in inversion regime.
This change in flat band potential can be seen as a change in the SiN_x "fixed" charge. It has increased after the first scan. It may be that ions in the electrolyte intercalate within the SiN_x and change the total volume charge or alternatively it may be the case that holes from the Si are trapped in the SiN_x [88].

8.4 Conclusions

- TRMC transients in electrochemical cells as a function of the applied potential are promising for the determination of the flat band potential.
- The electric passivation in Si by SiN_x layer is mainly due to field passivation.
- In combination with standard electrochemical measurements, TRMC measurements may yield detailed information on hysteresis of Si/SiN_x devices.

- By comparison of the effective decay time at flat band potentials, information about the density of recombinative surface states can be estimated. Comparison between different system my lead information about the interface quality (good or bad chemical passivation).

Chapter 9

Dark conductivity and excess charge kinetics at the pSi/SiN_x and pSi/SiO_2 interfaces

9.1 Introduction

SiN_x films on Si (wafers) are characterized by a positive fixed charge within the insulator volume. This is an experimental fact deduced by analysis of the measured charge and conductivity characteristics of Si-wafers in contact with SiN_x films. The fixed charge density Q_f at the Si/SiN_x interface is estimated to be more than $10^{12}cm^{-2}$ and positive as determined in sections 5.3.2 and 6.3.2 [87]. This charge is screened by a negative charge from the Si space charge region (SCR): nSi with a strong accumulation region and pSi with an inversion/depletion region.
Previous TRMC measurements in the pSi/SiN_x system [51],[89] only with volume excitation (i.e.$1064nm$) show an initial decay assigned to diffusion of excess charge carriers to the SCR with a strong decreased mobility for electrons at the interface (in fact the latter fact is responsible for the TRMC signal decay according to [89]). The final slow decay is ascribed to excess charge carriers separated in the SCR. This suggests comparison of TRMC measurements with SPV measurements for the same samples.

In this work SPV and TRMC measurements are performed on the same samples. For comparative purposes also measurements on pSi/SiO_2 were performed. SiO_2 on Si presents also fixed positive charge in the insulator, although it is assumed to be lower than in pSi/SiN_x [87].

9.2 Experimental

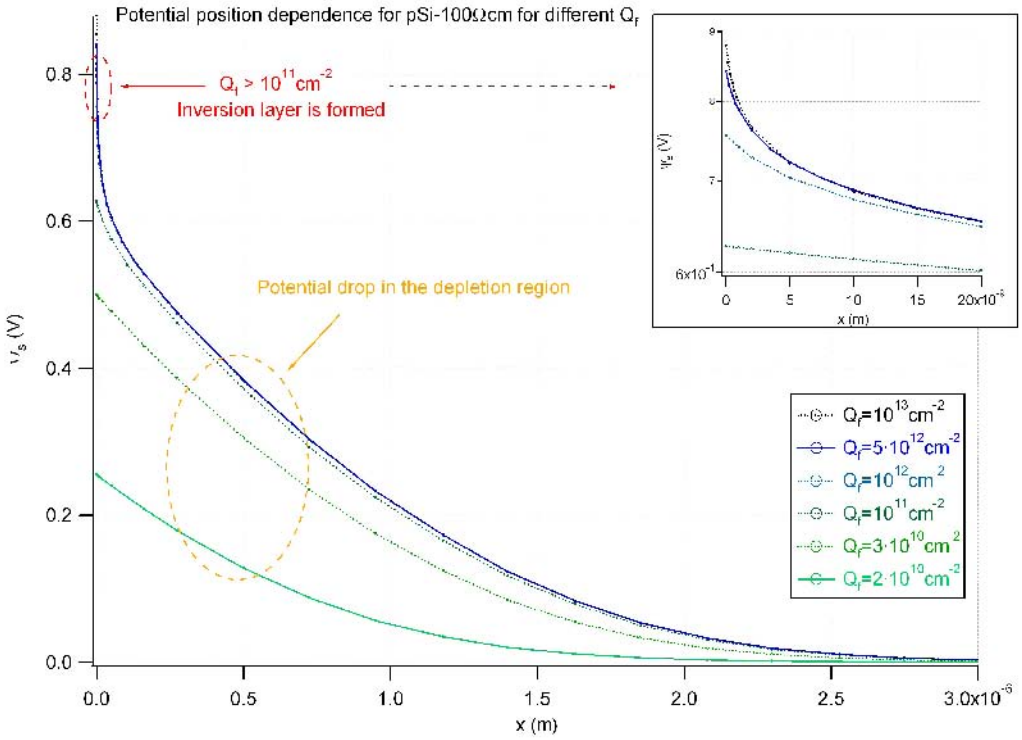

Figure 9.1: The dependence of the potential on the distance to the interface for different values of Q_f for a $pSi - 100\Omega cm$ wafer. Q_f is lying in the limit $x = 0^-$. The insert shows a magnification of the potential drop in the inversion layer which is restricted to the first $5nm$ length. The calculation was done with the program $PC - 1D$.

SiN_x and SiO_2 passivating layers were deposited and grown on crystalline pSi wafers, $100\Omega cm$ (as indicated by the producer) $504\mu m$-thick from Wacker.
SiN_x films were deposited by Plasma Enhanced Chemical Deposition (PECVD) from SiH_4/NH_3 gas mixture as described in [28] on one or both sides of the pSi wafer as indicated in Fig. 9.2. SiO_2 layers were thermally grown.
TRMC and SPV measurements are performed as described previously (sections 4.3.6 and 4.4.3 respectively).

The samples were excited by $10ns$ (FWHM) pulses at $532nm$ and $1064nm$

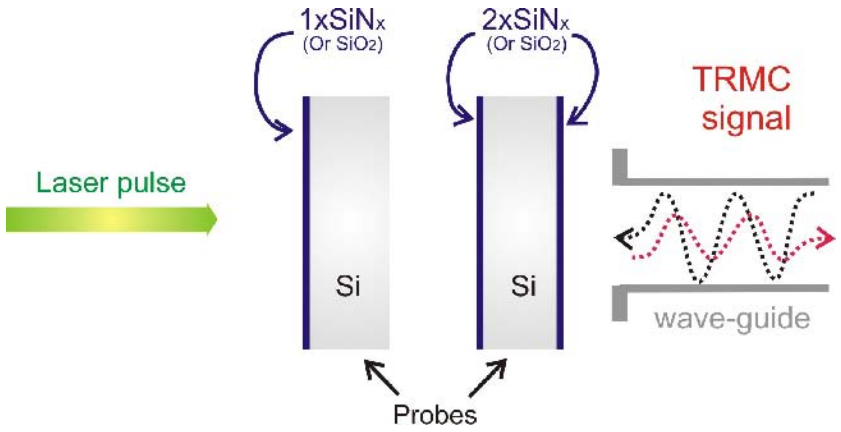

Figure 9.2: Illustration of the experimental configuration and the laser incidence with respect to one side and two sides silicon wafers covered by SiN_x layers (or SiO_2 layers).

for TRMC measurements and $545nm$ for SPV ones. Penetration depth for $532nm$ in Si is $1.5\mu m$ ($\alpha_{540} = 7050cm^{-1}$[86]) and so, generation of excess charge carriers occurs mainly in the SCR estimated with a length of about $2\mu m$ as shown in Fig.9.1 where the potential position dependence has been simulated by use of the program $PC-1D$. $1064nm$ excitation, with a penetration depth of about $1mm$ ($\alpha_{1060} = 11.1cm^{-1}$[86]), generates an approximately homogeneous profile of excess charge carriers over the whole wafer. Additional Q(uasi) S(teady) S(tate) P(hoto) C(onductance) measurements were performed to determine the steady state charge carrier lifetime [90].

9.3 Results

9.3.1 Dark conductivity measurements

A numerical simulation program using Eqs.4.41-4.44 has been used to fit the measurements of the microwave power reflection coefficient $R(\sigma, l)$ in a closed X-band (at $10GHz$) waveguide system as a function of the distance between sample and short circuit (section.4.3.2) for four different samples (Fig.9.3).

The experimental results (Fig. 9.3) show a periodicity of $2cm$. This $2cm$ corresponds to half a wavelength at $10GHz$ for the principal mode in a waveguide system and reflects the periodicity of the square of the microwave

field strength.
A difference between the pSi surface covered by SiO_2 and by SiN_x was observed: Where SiO_2 does not change the conductivity of the sample (the silicon wafer) as seen by comparing the bare wafer (red markers) with the measurement on the sample covered by both SiO_2 (blue markers).

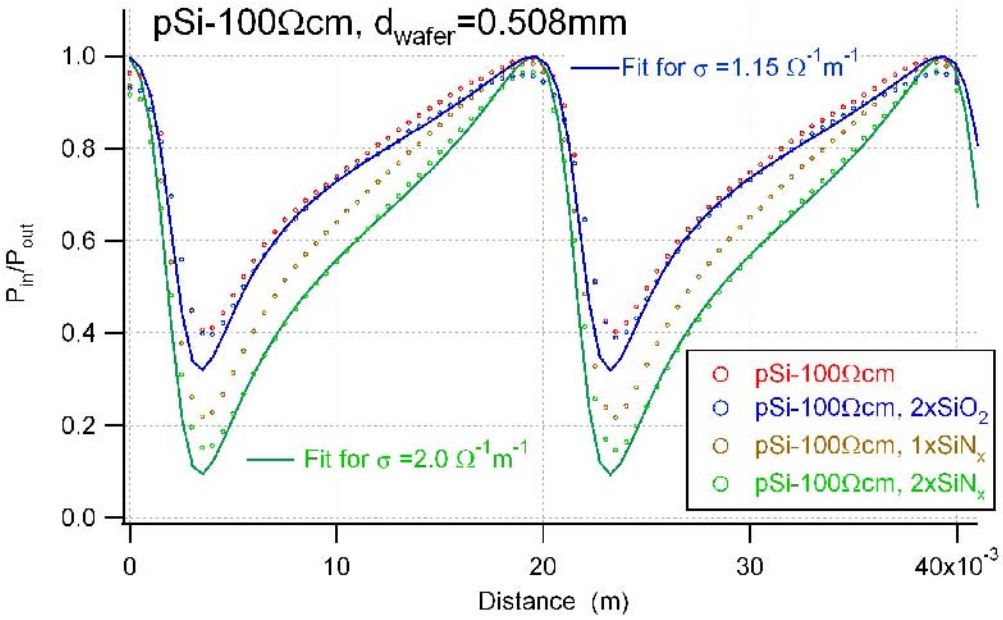

Figure 9.3: Reflection coefficient measurements as function of the distance between sample and short circuit for $pSi - 100\Omega cm$ bare (red markers), covered with both sides SiO_2 (blue markers), one side SiN_x (brown markers) and both sides with SiN_x (green markers). Fitting for $\rho = 87\Omega cm$ (blue solid line) and for $\rho = 50\Omega cm$ (green solid line) were done by use of numerical calculation.

But covering the wafer at one face with SiN_x (Fig.9.3 gold markers) already changes the conductivity of the sample. This change of the conductivity is enhanced by a factor 2 when covered at both surfaces by SiN_x (Fig.9.3 green markers). This change in conductivity is explained by the high density of fixed positive charge in SiN_x and the coupled increase of the number of electrons in silicon, due to injection from the SiN_x film. The equivalent SiN_x surface charge concentration has been estimated in the $Q_f = 10^{12} cm^{-2}$ range in a previous publication [91]. The fixed charge density was used for the numerical evaluation of the number of charge carriers present in the

Si wafer with the simulation program $PC-1D$ as shown in Fig.9.4 for a $pSi-100\Omega cm$ with $Q_f = 2 \cdot 10^{12}$. Comparison of the numerical simulation and the measured conductance suggests a strong reduced electron mobility (about $250 cm^2 V^{-1} s^{-1}$) in the inversion layer [62].

The results of the present samples (Fig.9.3) resemble within the accuracy of the measurements to those in Ref.[91], i.e. an increase of conductance of $2 \cdot 10^{-4} \Omega^{-1}$ per SiN_x layer. Also the fixed positive charge determined in sections 5.3.2 and 6.3.2 lies in the same order of magnitude ($Q_f \approx 2 \cdot 10^{12} cm^{-2}$) according to [91].

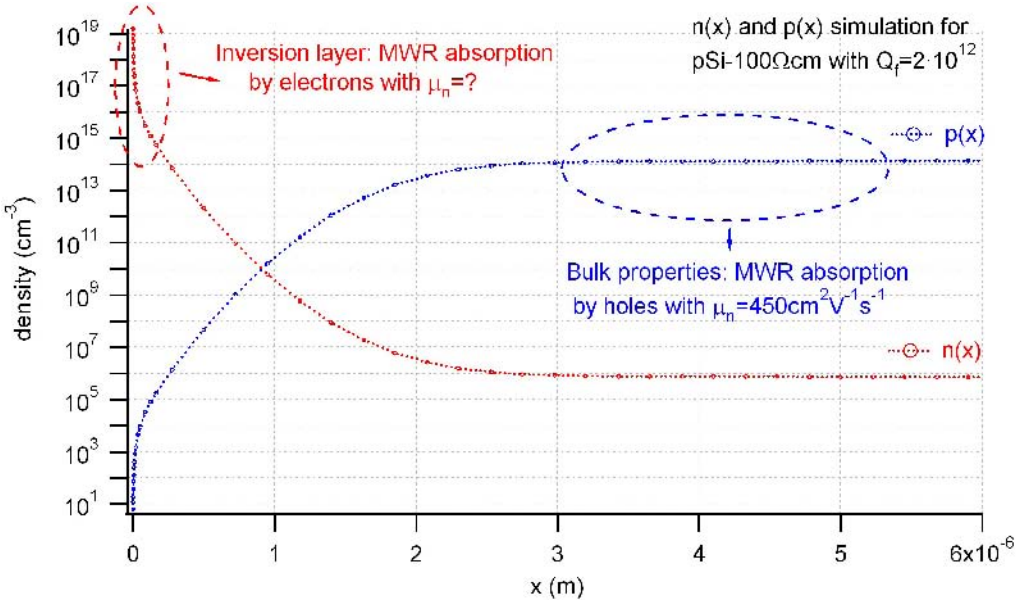

Figure 9.4: Simulation of the charge carrier density as function of the position for an $pSi-100\Omega cm$ wafer with a fixed surface charge of $Q_f = 2 \cdot 10^{12}$. Microwaves are mainly absorbed in the inversion layer by the electrons and in the bulk by the holes. The program $PC-1D$ was used for the simulation.

The change in the number of charge carriers for a $pSi-100\Omega cm$ wafer, with a thickness $d = 500\mu m$, induced by the presence of a fixed surface charge of $Q_f = 2 \cdot 10^{12} cm^{-2}$ is $\Delta n \cdot d \approx 1.73 \cdot 10^{12} cm^{-2}$ (for electrons) and $\Delta p \cdot d \approx -1.54 \cdot 10^{8} cm^{-2}$ (for holes). The values were calculated by the integration of $n(x)$ and $p(x)$ (Fig.9.4) over the position and subtracting from that value the one obtained for the same sample in the absence of a

fixed charge. The increase in conductance is mainly due to electrons located in the inversion/depletion region which compensate the fixed positive charge in the SiN_x.

$$\mu_n = \frac{\Delta\sigma d}{q\Delta n d} = \frac{2 \cdot 10^{-4}\Omega^{-1}}{1.6 \cdot 10^{-19} V\Omega^{-1} s 1.73 \cdot 10^{12} cm^{-2}} = 722 cm^2 V^{-1} s^{-1} \quad (9.1)$$

This calculation yields a decrease of the minority charge carrier mobility in the inversion regime. Effectively all electrons (minority charge carriers) are in the inversion layer. At the present calculation, $Q_f = 2 \cdot 10^{12} cm^{-2}$ has been taken. The determination of the Q_f value by use of impedance methods is not exempt from certain variability (sections 5.3.2 and 6.3.2). The fixed charge found in Si/SiN_x interfaces varies between $Q_f = 10^{12} cm^{-2}$ and $Q_f = 10^{13} cm^{-2}$, related to the SiN_x thickness. Q_f values are high enough to bring the pSi surface to the inversion regime. Under these conditions, it can be assumed that the charge is mainly compensated by electrons present in the inversion region with $\Delta n \cdot d \approx Q_f$:

$$\mu_n = \frac{\Delta\sigma d}{qQ_f} \quad (9.2)$$

Mobilities values around the one found for electrons in the inversion layer in the literature ($250 cm^2 V^{-1} s^{-1}$) [91],[62] are found for $Q_f = 5 \cdot 10^{12} cm^{-2}$.

9.3.2 TRMC measurements of pSi samples covered on one side and both sides by a SiN_x passivating layer

Fig. 9.5 shows a double logarithm plot comparing the signals induced in a piece of a pSi wafer covered at both faces with SiN_x with a piece of the same pSi wafer covered at one face with SiN_x and illuminated on this covered face. An identical decay behavior is observed for the lower excitation densities (Fig. 9.5 for $OD = 5.6$ and $OD = 4.6$). This implies that no influences of the rear (non-illuminated) surface are observed. All excess charge carriers are generated within the SCR at the illuminated surface or diffuse to the illuminated surface. Fig. 9.6 shows the half-logarithm representation for the same signals as in Fig.9.5. It is clearly seen that there is a difference at $OD = 3.6$ between one and two sides SiN_x passivation. One side SiN_x presents a faster decay due to a recombination of excess charge carriers at the rear surface: excess

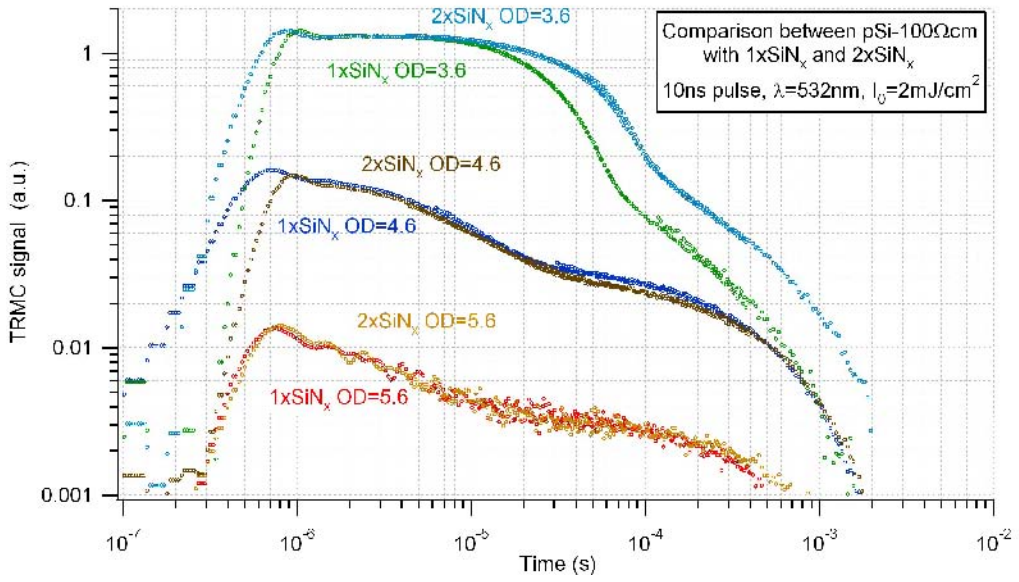

Figure 9.5: Double logarithmic plot comparing TRMC signals of $pSi - 100\Omega cm$ covered by SiN_x on one side and on both sides. Excitation by a $10ns$ pulse with $532nm$ wavelength and $I_0 = 2mJ/cm^2$ incident intensity. Attenuation of the excitation density was done by use of filters with OD between $OD = 3.6$ and $OD = 5.6$.

charge carriers which diffuse to the rear side recombine faster through surface defects at the bare surface while with a rear SiN_x layer they are separated in the SCR. The faster recombination at the uncovered surface diminishes the total number of charge carriers. For longer times, where only excess charge carriers separated in the SCR contribute to the signal, the recombination occurs only after the emission over the space charge barrier potential. The TRMC signal for the two sides SiN_x is higher because also storage of charge carriers at the rear surface occurs. The final decay observed at low intensity measurements ($OD = 5.6$ and $OD = 4.6$) is somewhat slower than that of the highest intensity one ($OD = 3.6$).

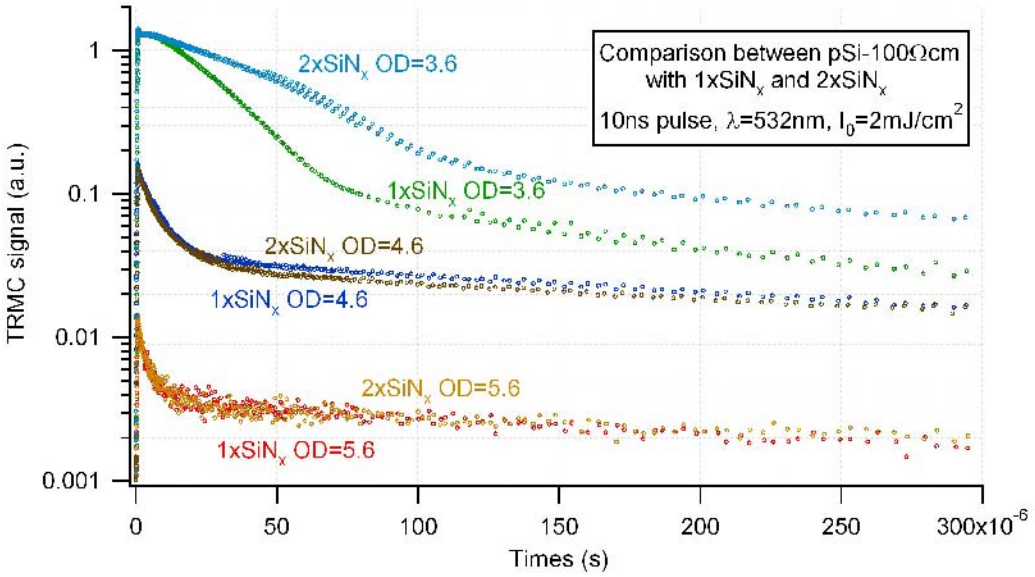

Figure 9.6: Semi-logarithmic plot comparing TRMC signals of $pSi-100\Omega cm$ covered by SiN_x on one side and on two sides. Excitation by a $10ns$ pulse with $532nm$ wavelength and $I_0 = 2mJ/cm^2$ incident intensity. Attenuation of the excitation density was done by use of filters with OD between $OD = 3.6$ and $OD = 5.6$.

9.3.3 TRMC measurements on two sides SiN_x and two sides SiO_2

Comparison between the same $pSi-100\Omega cm$ wafer covered at both faces with SiN_x and with SiO_2 is shown in Fig. 9.7 in a half-logarithmic representation. Excitation wavelength is $532nm$ with $3.2mJ/cm^2$ and optical attenuation densities between $OD = 4.6$ and $OD = 7$ were used. Most excess charge carriers are generated in the SCR on the illuminated surface as indicated in previous section (Fig. 9.5). They will be separated in the depletion layer by the effect of the electric field and stored on the extremes of the SCR reducing the band bending (by shielding the electric field). With increasing excitation intensity it is possible to reduce the band bending and enable excess charge carriers to escape from the SCR. Thus, with increasing excitation intensity, more excess charge carriers will diffuse to the other face.

The decay for the SiO_2 covered sample (blue lines in Fig. 9.7) is much slower than the one observed for the sample covered with SiN_x (red lines

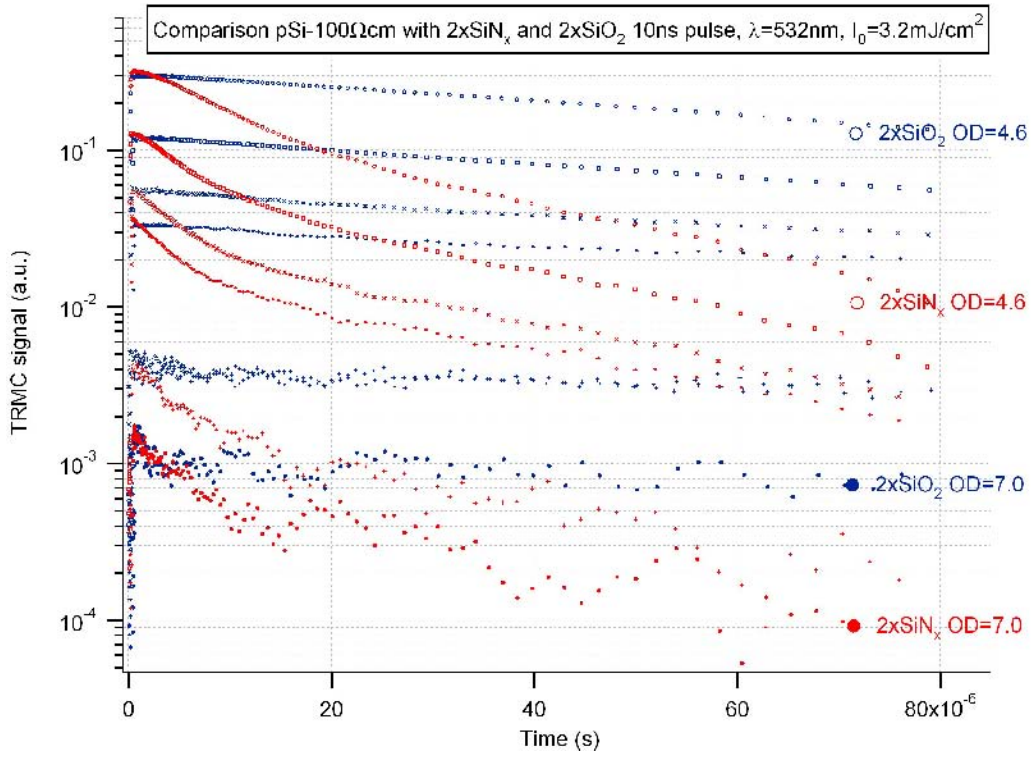

Figure 9.7: Semi-logarithmic plot comparing TRMC signals at low excitation densities of $pSi - 100\Omega cm$ covered by SiN_x and by SiO_2. Excitation by a $10ns$ pulse with $532nm$ wavelength and $I_0 = 3.2mJ/cm^2$ incident intensity. The excitation density was attenuated by use of filters with OD between $OD = 4.6$ and $OD = 7$.

Fig. 9.7). At low excitation intensities only recombination processes on the semiconductor surface and in the SCR take place, so it can be concluded that the pSi/SiN_x interface presents a faster decay of excess charge carriers.

For higher excitation densities with $1064nm$ wavelength illumination, shown in Fig. 9.8, it is observed that:

- At small excitation density (OD values larger than $OD = 4$) over the whole time range excess charge carriers decay slower in the pSi/SiO_2 system than in the pSi/SiN_x system.

- At higher excitation densities (OD smaller than $OD = 4$), in the μs range signal, the sample with pSi/SiN_x interface presents a slower

decay than the SiO_2 covered one while for longer times the pSi/SiO_2 sample presents a slower decay.

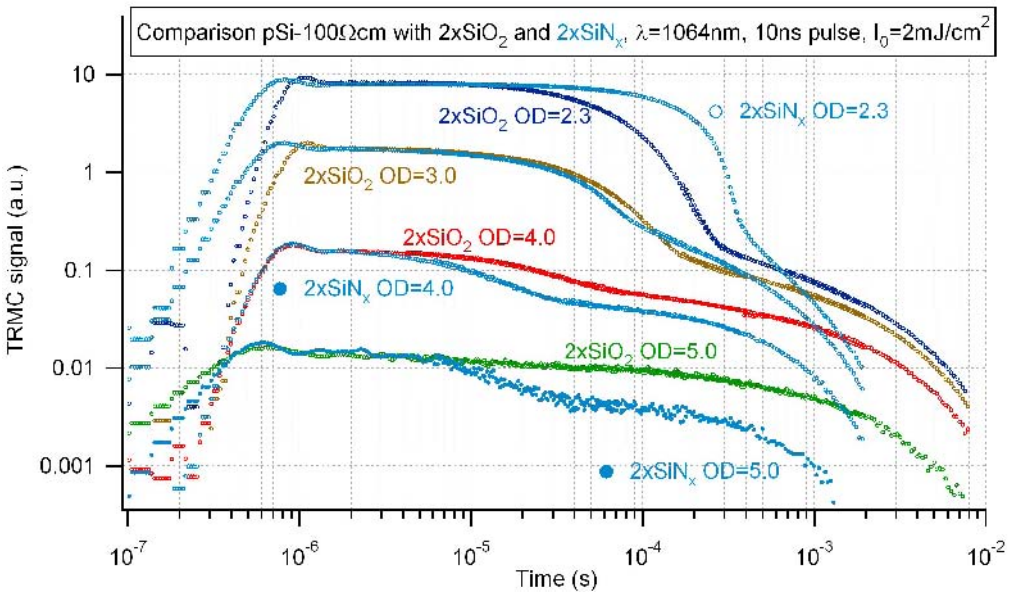

Figure 9.8: Double logarithmic plot comparing TRMC signal of $pSi{-}100\Omega cm$ covered by SiN_x and by SiO_2. Excitation by a $10ns$ pulse with $1064nm$ wavelength and $I_0 = 2mJ/cm^2$ incident intensity. Excitation density was attenuated by use of filters with OD between $OD = 2.3$ and $OD = 5$.

For $1064nm$ excitation, the generation profile of excess charge carriers is homogeneous. Electron-hole pairs are separated in the depletion region; at both faces electrons accumulate on the pSi/SiN_x interface (or directly after the inversion layer) and holes at the edge of the depletion region. Thus, a gradient of excess electrons is created and diffusion from the volume to the surfaces takes place.
At low excitation densities, the excess charge carriers stored in SCR do not dramatically change the band bending and recombination is expected to be limited by the probability that a hole reaches the semiconductor surface to recombine with an electron. The measurements (Fig.9.8) show that this process is more probable for SiN_x than for SiO_2.
For higher intensities the depletion region is flattened and the probability that electron and holes recombine via surface defects is higher. Thus, a faster decay is initially observed which slows down with time when the number of

excess charge carriers diminishes and the band bending is built up again making the recombination probability smaller and leading to the slower decay as the electron-hole recombination is hindered again by the depletion region barrier.
Thus, it is expected that increasing the excitation density leads to an initial faster decay of the TRMC signal until it reaches a certain TRMC value, related to the maximal number of excess charge carriers which can be stored in the depletion region, upon it the signal decays slower. The TRMC value of this final decay should not present a dependence on the excitation density at high enough laser intensities.
This is not exactly found for the SiN_x covered sample in Fig. 9.5, 9.6 and 9.8 neither for SiO_2 in Fig 9.8. The TRMC signal amplitude for the final decay increases with increasing excitation density as if the number of excess charge carriers which can be stored in the depletion region increases with increasing excitation density. This indicates complicated non-linear trapping and recombination processes.
The initial decrease of the TRMC signal in the pSi/SiN_x sample can be attributed to the decay of excess charge carriers in the space charge region or a decrease in the mobility of the electrons on the Si/SiN_x interface. This decay of the TRMC at low intensities has been attributed in previous work to a decrease of the electron mobility on the pSi/SiN_x interface [89] and related to the electron mobility decrease revealed by the dark conductivity microwave measurements (section 9.3.1).

However, the present measurements (Fig.9.8) provide a strong argument against this interpretation: Absolute evaluation of the data in Fig.9.8 yield that the maximum TRMC signal of the SiN_x covered samples corresponds to $(\mu_n + \mu_p) = 1800 cm^2 V^{-1} s^{-1}$ ($\pm 15\%$). This suggests that electrons and holes contribute with their band mobility [7] to the TRMC signal and so excludes that during the light excitation (about $10ns$) an appreciable number of electrons are characterized by a strongly decreased mobility.
It must be assumed that at the low excitation densities most of the excess charge carriers are generated in the SCR and the separation of electrons and holes is faster than $1ns$ and so can be considered that excess charge carriers are immediately stored in the SCR extremes. In section 9.3.1 electrons compensating the fixed charge Q_f in the SiN_x presented a reduced mobility and were mainly present in the inversion layer (Figs.9.1-9.4). The present TRMC measurements show that initially photoinduced electrons, stored in the SCR, present their bulk mobility (about $1400 cm^2 V^{-1} s^{-1}$) suggesting that

they might not be stored in the inversion layer (where mobility is decreased) but in the depletion region (characterized by the bulk mobility).

9.3.4 Low intensity SPV measurements on two sides SiN_x and two sides SiO_2

In Fig.9.9 an example of SPV transients at different excitation densities in a piece of the pSi wafer with SiO_2 at both faces are shown. At small intensities the SPV amplitude is proportional to the intensity (section 4.4). For the lower intensities the SPV signal refers to excess charge carriers stored and separated in the illuminated space charge (depletion/inversion) region of the Si/SiO_2 junction. At higher excitation densities the SPV amplitude saturates because of the flattening of the bands and the additional increase in the number of excess charge carriers is no more confined in the SCR and consequently does not contribute to the SPV signal (considering that the Dember potential due to excess charge carrier diffusing to the rear surface is negligible).

Fig. 9.9 suggests a decay time for excess charge carriers stored in the SCR in the millisecond time range. This agrees with the results of the TRMC measurements for the same sample in Fig. 9.8.

9.3.4.1 Comparison of SPV and TRMC signals

The TRMC signal and SPV signal (in the excitation density range where the SPV signal is proportional to the excitation density, up to $5nJcm^{-2}$) are characterized by the same decay time (Figs. 9.10 and 9.11).

This fact leads to the conclusion that the fast (microsecond decay) in the pSi/SiN_x sample can not be simply attributed to a decreased electron mobility at the interface as concluded previously [89] because this would not lead to a decay of the SPV signal in the most simple model for this process. However, this may be possible in more complicated models. Another explanation of this decay is recombination in the SCR [92].

In Fig. 9.10 it is seen that the SPV and TRMC magnitudes are proportional in the whole time domain in the wafer covered with SiO_2, whereas at the wafer covered with SiN_x this proportionality factor is not satisfied at times between $500ns$ and $5\mu s$. A true extinction of charge would lead to the

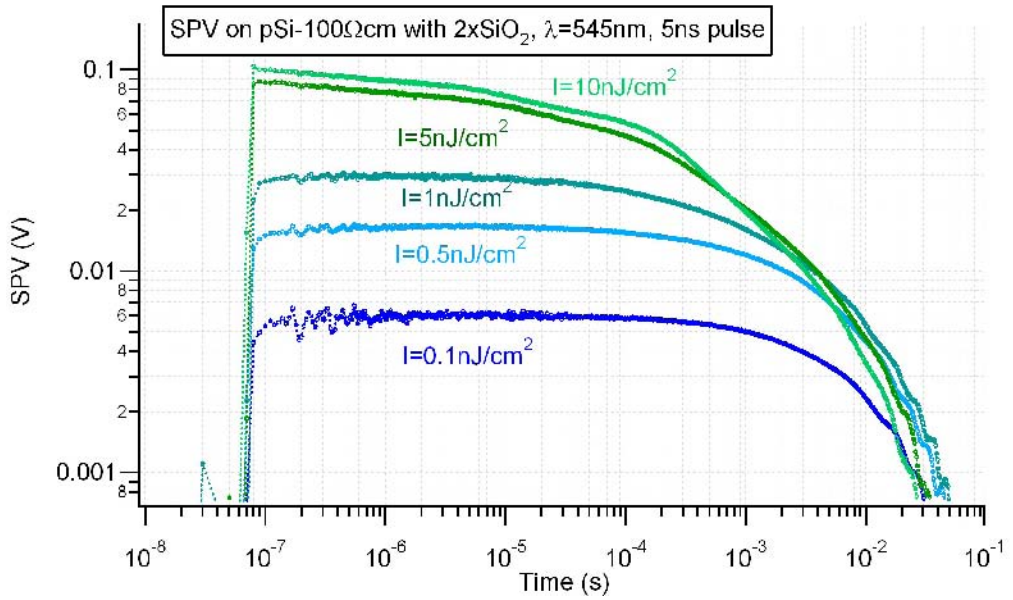

Figure 9.9: Double logarithmic plot of SPV transients on $pSi - 100\Omega cm$ covered by SiO_2 on the two faces. Laser pulse $5ns$ with $545nm$ wavelength and of excitation intensity between $10nJ/cm^2$ and $0.1nJ/cm^2$. The SPV signals are sign inverted.

same decay rate in both measurements.
This fact leads to two conclusions:

- the second decay in the microsecond-millisecond domain in the pSi/SiN_x sample is the final recombination of excess charge carriers previously separated in the SCR (giving rise the SPV signal).

- the first decay at times before $5\mu s$ in the pSi/SiN_x may be ascribed to a recombination process in the SCR or is related to charge carriers trapping or injection in the inversion region leading to a reduced mobility (not observed in the pSi/SiO_2sample).

Besides, the microsecond decay process is quenched at higher excitation densities (as it can be concluded from Figs. 9.8 and 9.5). Intermediates of this SCR recombination process may be defects induced under the interface

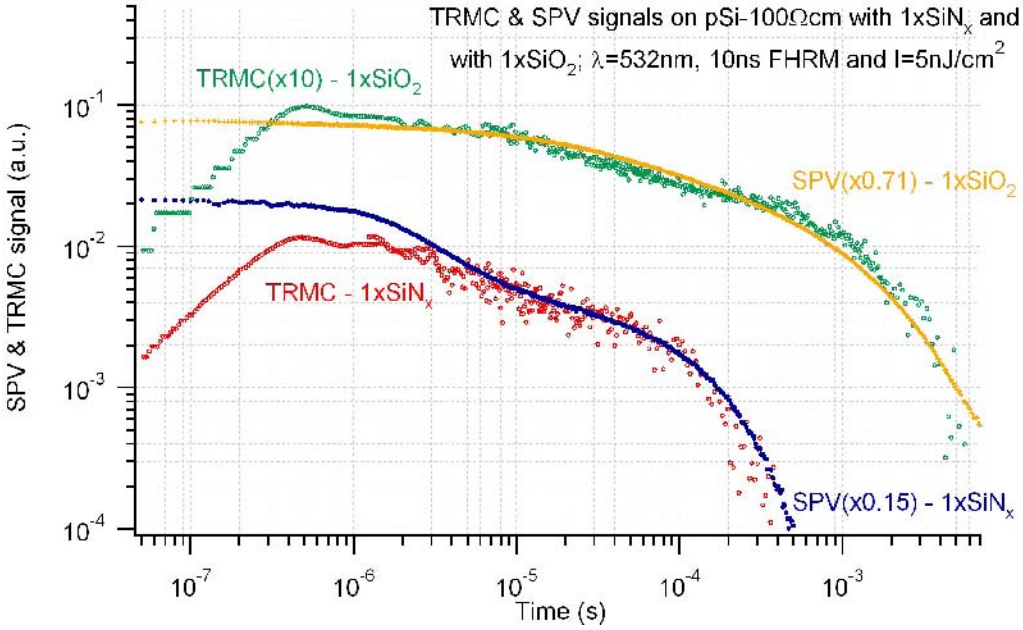

Figure 9.10: Double logarithmic plot for TRMC transients and SPV transients on $pSi - 100\Omega cm$ covered on one side by SiN_x and a second sample by SiO_2 for $5nJ/cm^2$ excitation intensity. The signals are arbitrarily displaced to better compare the decay behavior. The magnitude of the SPV signal is scaled by a proportionality factor until its height in the microsecond range is comparable to the TRMC signal.

by stress because of the presence of the SiN_x film as proposed by Dauwe [87].
This explanation has the problem that electrons injected from the SiN_x forming the inversion layer are characterized by a diminished mobility whereas electrons injected by light are characterized by the normal bulk mobility. The solution of this problem will be investigated in the future.

9.3.5 Comparative kinetics at the pSi/SiO_2 interface

In Fig.9.12 SPV signals at two intensities ($0.5nJ/cm^2$ and $1nJ/cm^2$) are shown for three samples on $pSi - 100\Omega cm$ covered at both faces by SiN_x (red markers), "good" quality SiO_2 (blue markers) and "bad" quality SiO_2 (green markers). "Good" quality SiO_2 corresponds to an effective lifetime

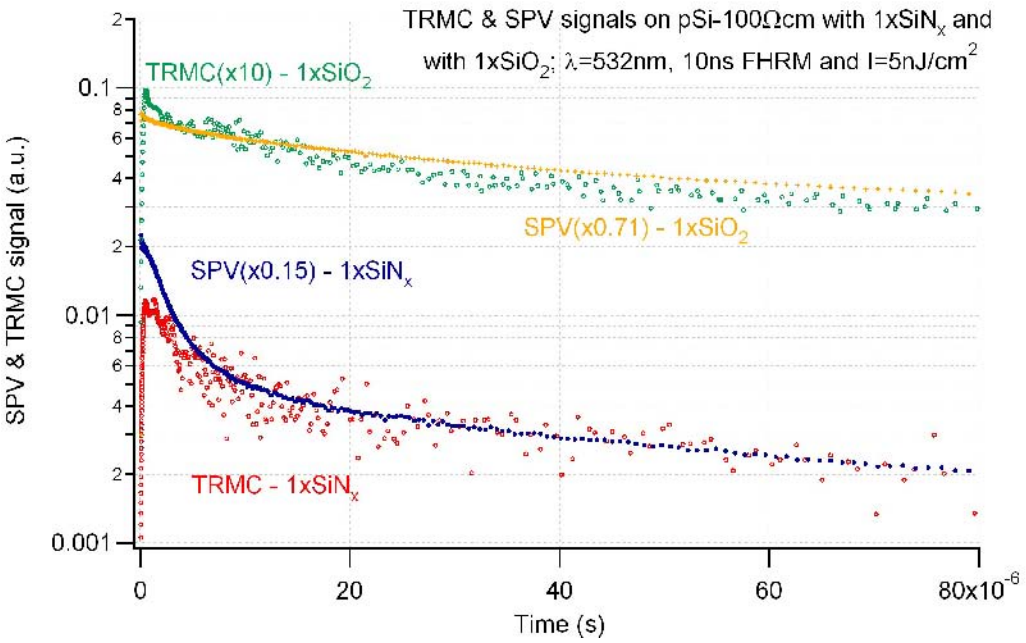

Figure 9.11: Semi logarithmic plot for TRMC transients and SPV transients on $pSi - 100\Omega cm$ covered on one sides by SiN_x and a second sample by SiO_2 for $1nJ/cm^2$ excitation intensity. The signals are arbitrarily displaced to better compare the decay behavior. The magnitude of the SPV signal is scaled by a proportionality factor until its height in the microsecond range is comparable to the TRMC signal.

of $200\mu s$ and "bad" quality of $15\mu s$ (both measured for an injection level between $10^{14}cm^{-3}$ and $10^{15}cm^{-3}$) as measured by QSSPC.
At low intensities the SPV signals in the SiO_2 covered samples decay much slower (in the millisecond time range) than in the SiN_x covered samples (in the microsecond time range).
The comparison between both SiO_2 samples is interesting:

- The signal amplitudes are approximately equal indicating that also in the bad sample a SCR is present.
- Both samples present time decays in the millisecond time range albeit the good sample somewhat slower.

It does not seem possible to decide on "good" or "bad" quality of the pSi/SiO_2 interface by SPV signals at low intensities.

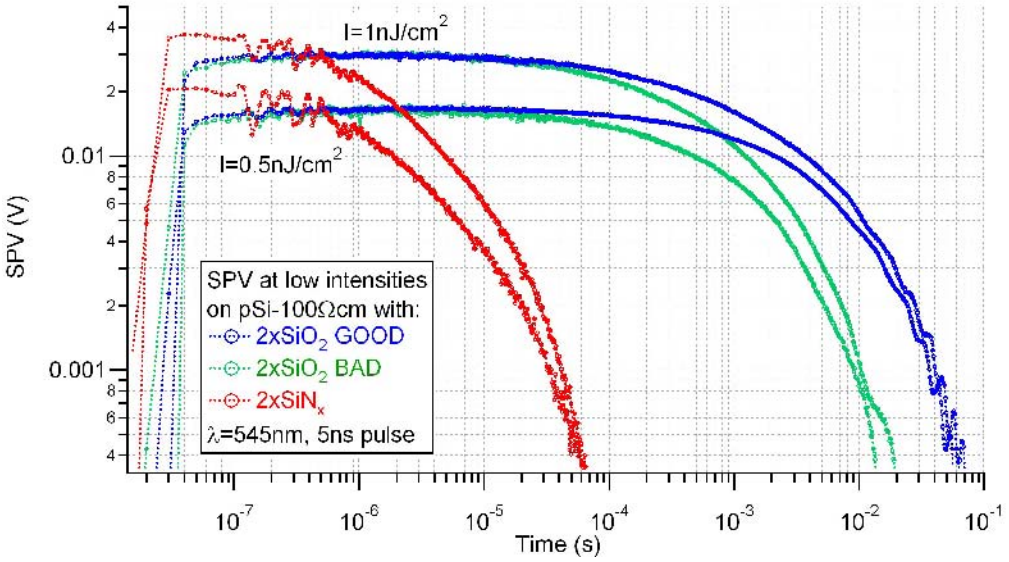

Figure 9.12: Comparison of SPV signals in a double logarithmic plot between $pSi - 100\Omega cm$ covered on both face by SiN_x (red), bad quality SiO_2 (green) and good quality SiO_2 (blue). Excitation by a laser pulse ($10ns$) with $545nm$ wavelength with $0.5nJ/cm^2$ and $1nJ/cm^2$ excitation intensities.

More information is obtained if the SPV data of Fig.9.12 are compared with the TRMC data in Fig.9.13 on the same SiO_2 covered samples:

- At the lowest intensity ($OD = 6.3$), the TRMC signals in both samples are approximately identical with a slightly faster final decay for the bad SiO_2.

- At higher excitation densities there is an initial decay in the bad sample (in the microsecond time range) whereas the initial decay in the good sample is about two orders of magnitude slower.

Consequently:

- The TRMC signal at the lowest intensity reflects excess charge carriers separated and stored in the SCR. The decay times of these signals (as of the SPV signals in Fig.9.13) do not have a direct relation to the electrical passivation of the interface for devices at working conditions (stationary illumination with high excitation densities).

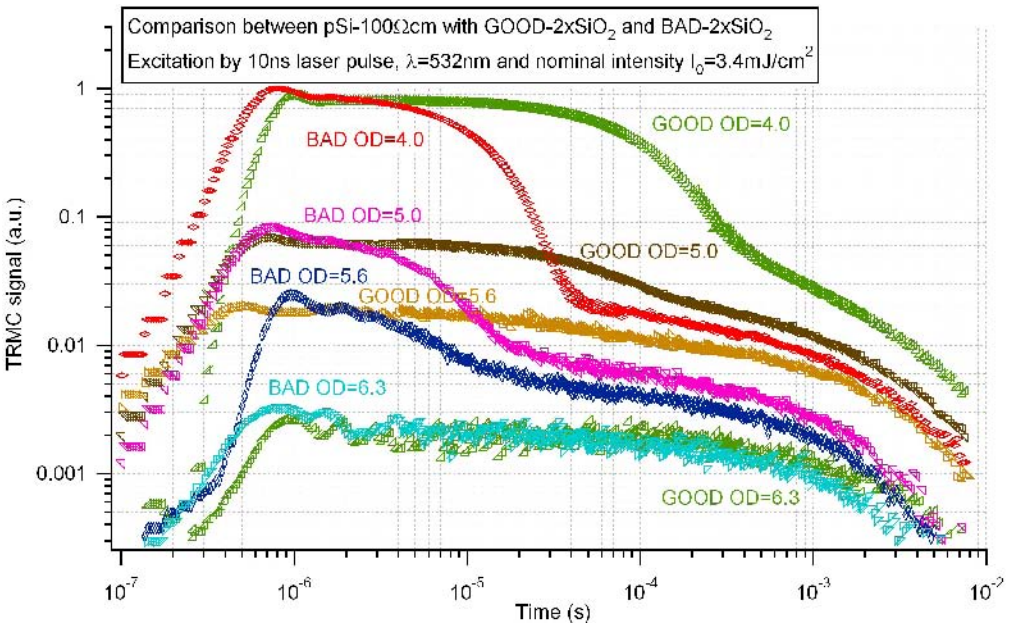

Figure 9.13: Comparison of TRMC signals in a double logarithmic plot between $pSi-100\Omega cm$ covered on both faces by $GOOD-SiO_2$ quality and by $BAD-SiO_2$ quality layer. Excitation by a laser pulse ($10ns$) with $532nm$ wavelength and $I_0 = 3.4mJ/cm^2$ nominal excitation intensity. Excitation density was attenuated by use of OD filters between $OD = 4$ and $OD = 6.3$.

- The decay of these charge carriers is mainly controlled by the probability of holes to attain the surface overcoming the SCR energy barrier.

- At higher excitation densities the interface with higher defect density leads to a much faster decay in the bad SiO_2 sample than in the good one.

The saturated photovoltage amplitude in the "good" sample is about $130mV$ and in the "bad" sample about $75mV$ (not shown in Fig.9.9).

At higher excitation densities, big differences between the two pSi/SiO_2 samples can be distinguished:
In both samples a faster decay sets in at higher excitation densities however, in the "bad" sample this faster decay sets in at lower excitation densities and is characterized by a much smaller decay time (Fig.9.13).
At the highest excitation density, the initial decay time in both samples

is approximately equal to the effective lifetime obtained by QSSPC measurements (for injection levels from $10^{14}cm^{-2}$ to $10^{15}cm^{-2}$). This confirms the attribution of this decay to recombination via surface defects where the bandbending can be neglected and both excess charge carriers can reach the Si/SiN_x interface. Consequently the "bad" Si/SiO_2 sample is characterized by a much more important surface recombination (a higher density of recombinative surface defects) than the "good" one. In fact, this process controls the efficiency of the junction in a photovoltaic cell as front or back surface passivation.

9.4 Conclusions

The present experiments lead to the following model for excess charge carriers kinetics in the SCR of pSi/SiO_2 and pSi/SiN_x:

- Recombination in the SCR can not be neglected a priori. In the pSi/SiN_x SCR this recombination is important if the band bending is still appreciable (low excitation densities) but is quenched under conditions approaching flatband by illumination at high excitation densities. In the pSi/SiO_2 samples recombination in the SCR is of no importance.
- Recombination via surface defects becomes important for transient measurements when the excess charge carriers density is sufficiently high to diminish largely the band bending. Comparison of the TRMC decay times with QSSPC effective lifetimes enable to identify the microsecond decay in the pSi/SiO_2 systems with the decay via surface defects.

Summarized it can be stated:

- At low excitation density the mobile charge carrier decay in $pSi - 100\Omega cm$ wafers covered by SiN_x is characterized by a decay time of a few microseconds, whereas the decay in the same $pSi - 100\Omega cm$ wafer covered by SiO_2 is characterized by a decay time of several hundreds microseconds.
- The initial decay in the pSi/SiN_x SCR is due to a SCR recombination becoming inactive at higher excitation densities.

- The decay of excess charge carriers stored in the SCR is faster in pSi/SiN_x than in pSi/SiO_2.
- The decay time of excess charge carriers stored in the SCR is not directly related to the quality of the interface as electrical passivation.

Chapter 10

Summary and overview

In the present work, excess charge carrier transport in crystalline silicon covered with SiN_x layers and also with SiO_2 layers have been investigated. These particular systems were chosen because of their enormous practical importance in photovoltaic and photocatalysis applications but also because they may serve as reference for the characterization of more unusual materials by the new experimental methods here used.

After the introduction, an overview of the relevant semiconductor theory is given (Chapter 2) followed by a description of Metal-Insulator-Semiconductor devices (Chapter 3) and the applied experimental techniques (Chapter 4). Here, we emphasized the new applied methods: microwave (photo) electrochemistry and microwave impedance spectroscopy.

The experimental chapters start with investigations of MIS devices (Chapter 5). The most significant results found are the importance of the back contact behavior for a proper functioning and characterization of MIS structures, in the particular case of the hardly considered inadequacy of the usual $In : Ga$ contact at high modulation frequencies. A more satisfactory ohmic contact was found by etching the rear Si surface with a HF solution previously to the $In : Ga$ application. It was found that the high leakage current existing in Si/SiN_x MIS structures (due to electrons or holes transport through the SiN_x) under the presence of an external electric field is responsible to bring the Si into the deep-depletion regime.

Moreover, the dark electrochemical experiments (Chapter 6) show the capacitive current expected for insulator/semiconductor structures but also

a faradaic current that leads to the damage of the SiN_x layer, specially when H_2 evolution is involved at negative potentials. This discards the Si/SiN_x system for (photo) catalytic applications in aqueous electrolytes.
The absence of leakage current brings the Si into inversion regime where charge carrier trapping into the SiN_x is observed.

The Si/SiN_x electrochemical cell configuration has permitted not only the characterization of the hetero-junction by capacitance methods but also by potential modulated conductance methods (the MWR-signal). The low frequency modulation MWR-signal is characterized by a change in sign in the transition from depletion to inversion. This change in MWR-signal sign is related to the contribution of the minority charge carriers to the conductance in inversion regime when they can follow the potential modulation. The high frequency MWR-signal is proportional to the high frequency capacity measurement (in depletion and inversion regime) where only the majority carriers follow the potential modulation.

The interface state density of the Si/SiN_x hetero-junction has been extracted by use of the high-low frequency capacitance method for six samples. By use of a simulation program, a realistic interface state density has been proposed for the Si/SiN_x interface. An acceptor-type Gaussian distribution centered in the midgap has been found as characteristic of this junction when compared to the Si/SiO_2 interface state density.

The SiN_x fixed positive charge has been determined but is characterized by a large range between $10^{12}cm^{-2}$ and $10^{13}cm^{-2}$ not clearly related to the thickness of the SiN_x layer. As the depositions conditions of the layers were identical, this implies an irreproducibility due to an uncontrolled deposition parameters or an inadequate Si surface handling previous to deposition.
The SiN_x fixed positive charge is more than one order of magnitude higher than the fixed charge in SiO_2 on Si wafers. This leads to a stronger accumulation regime in the nSi and a stronger inversion regime in the pSi in Si/SiN_x hetero-junctions.

Light modulated photo-current and photo-conductance measurements (Chapter 7) in pSi/SiN_x electrochemical cells lead to complementary charge carriers kinetic information: Faradaic photo-currents (as hydrogen evolution) are characterized with a small MWR signal and a high X-component of the photo-current. Displacement photo-currents are characterized by a

frequency dependent Y-component of the photo-current that decreases in magnitude whit decreasing modulation frequency and a high MWR signal not dependent on the modulation frequency. Flat band is characterized by a high surface recombination leading to a small photo-current and a minimum in the MWR signal.
Hydrogen evolution modifies the characteristics of the pSi/SiN_x heterojunction such as the SiN_x fixed charge and the recombination rate at flat band.

TRMC signals in nSi/SiN_x electrochemical cells as function of the applied potential (Chapter 8) show again that the highest surface recombination is observed around flat band regime and that the electrical passivation of crystalline Si by SiN_x is mainly due to field passivation.

Contactless microwave measurements (Chapter 9) show the increase of the conductance of a Si wafer after deposition of SiN_x layer (SiO_2 does not show an appreciable effect). Numerical evaluation of the result indicates a decreased mobility of the electrons in an inversion layer of these systems maybe related to the acceptor-like traps found by capacitance measurements. Storage of excess charge carriers in the space charge region of the pSi/SiN_x is observed. A comparison of the TRMC transients in pSi/SiN_x and pSi/SiO_2 reveals a decay process in the first system not present in the second one at low excitation densities. The comparison of the TRMC transient and the SPV transient at low excitation suggest that this decay is due to the recombination of excess charge carriers in the pSi/SiN_x depletion region. This initial decay in the depletion region becomes inactive at higher excitation densities.
This anomalous behavior of the excess charge carriers in pSi/SiN_x systems cannot be explained by the model ascribed to pSi/SiO_2 systems where excess charge carriers decay only through surface defects.
pSi/SiN_x junctions present different configuration than pSi/SiO_2: the pSi/SiN_x samples are in inversion regime unlike the pSi/SiO_2 ones which are in depletion regime. The kinetics of an inversion layer under illumination can be different from that of the classical depletion layer. Moreover, there is experimental evidence that holes and electrons can be easily trapped in the SiN_x volume changing its fixed charge. These are parameters that still are not correctly understood and modeled and might be of crucial importance in the future development of a satisfactory kinetic model for the excess charge carriers at Si/SiN_x interfaces.

In a future work a model including non linear recombination processes (such as trapping in the space-charge region) will be proposed to describe the kinetics in pSi/SiN_x heterojunctions at low injection levels. For this purpose, SPV measurements in combination with TRMC measurements will be used.
Charge transport in SiN_x and long-term instabilities are also a matter of interest in solar cell technology and memory devices. Different compositions of SiN_x layers will be studied in order to optimize the SiN_x layer for such purposes. Furthermore, electrochemical measurements will be done to identify chemical changes in SiN_x.

Zusamenfassung

In der vorliegenden Arbeit wurde der Ladungsträgertransport in kristallinem Silizium untersucht, dass mit SiN_x bzw. mit SiO_2 beschichtet war. Diese Materialsysteme wurden aufgrund ihrer hohen praktischen Relevanz für Anwendungen in der Fotovoltaik und der Fotokatalyse ausgewählt. Sie könnten jedoch auch als Referenzsysteme für alternative Materialen dienen, wenn die in der Arbeit vorgestellten neuartigen Methoden angewendet werden.

Im Anschluss an die Einleitung wird zunächst ein Überblick der für die Arbeit relevanten Theorie der Halbleiter gegeben (Kapitel 2). Es folgt die Beschreibung der Physik der Metall-Isolator-Halbleiter Kontakte und Bauelemente (Kapitel 3) und der experimentellen Techniken (Kapitel 4). Bei der Beschreibung der angewendeten Messtechniken liegt der Fokus auf der Mikrowellen-(Foto)elektrochemie und Mikrowellen-Impedanz-Spektroskopie.

Der experimentelle Teil der Arbeit beginnt mit den Untersuchungen der MIS-Strukturen (Kapitel 5). Als wichtigstes Ergebnis wurde hier der große Einfluss des Rückkontaktverhaltens für das Funktionieren und die Charakterisierung der MIS-Anordnung gefunden. Bei hohen Modulationsfrequenzen wurden bislang kaum betrachtete Unzulänglichkeiten bei den üblichen $In : Ga$-Kontakten festgestellt. Ein optimierter Ohmscher Kontakt konnte hergestellt werden, indem vor der In:Ga Kontaktierung die Si-Rückfläche mit HF-Lösung vorbehandelt (geätzt) wurde. Die Untersuchungen zeigten, dass der hohe Kriechstrom/Verluststrom (verursacht durch Transport von Elektronen bzw. Löchern), welcher in Si/SiN_x-MIS-Strukturen in Anwesenheit von externen elektrischen Feldern auftritt, das Silizium in den Zustand der tiefen Verarmung bringt.

Weiterhin zeigten elektrochemische Dunkelexperimente (Kapitel 6) neben dem erwarteten Strom für Isolator/Halbleiter Systeme auch einen Faradayschen Strom, der schädigend auf die SiN_x-Schicht wirkt, insbesondere wenn eine H_2-Entwicklung bei negativen Potentialen auftritt. Dies macht Si/SiN_x System ungeeignet für fotokatalytische Anwendungen in wässrigen Lösungen.

Durch die Abwesenheit von Verluststrom in elektrochemischen Experimenten kann das Silizium durch Anlegen eines Potentials in die Inversion gebracht werden, bei dem das Einfangen von Ladungsträgern durch Trapzustände beobachtet werden kann.

Die elektrochemische Si/SiN_x-Zellkonfiguration erlaubte die Charakterisierung des Heterokontaktes sowohl durch Messung der Kapazität als auch mittels potentialmodulierter Leitfähigkeitsmessungen (MWR-Signal). Das niederfrequente Modulations- MWR-Signal erfährt beim Übergang des Siliziums vom Zustand der Verarmung zur Inversion einen Vorzeichenwechsel. Dieser Wechsel hängt mit dem Beitrag der Minoritätsladungsträger zur Leitfähigkeit im Inversionszustand zusammen, sofern diese der Potentialmodulation folgen können. Das hochfrequente MRW-Signal ist proportional zur Hochfrequenz-Kapazitätsmessung (im Verarmungs- und Inversionszustand) bei der nur die Majoritätsladungsträger der Potentialmodulation folgen.

Die Grenzflächenzustandsdichte des Si/SiN_x-Heterokontaktes wurde durch die Bestimmunng und den Vergleich der Hoch-und Tieffrequenz-Kapazitäten an 6 Proben bestimmt. Mit Hilfe eines Simulationsprogramms konnte eine realistische Grenzflächenzustandsdichte für die Si/SiN_x Grenzfläche vorgeschlagen werden. Als charakteristische Eigenschaft dieser Grenzfläche wurde eine Gaußartige Verteilungsfunktion der Akzeptorzustände gefunden, deren Zentrum sich in der Mitte der Bandlücke befindet (verglichen mit der Si/SiO_2 Grenzflächenzustandsdichtefunktion).

Die Bestimmung der festen positiven Ladung in der SiN_x-Schicht ergab Werte im Bereich von $10^{12}cm^{-2}$ bis $10^{13}cm^{-2}$, welche nicht eindeutig mit der Dicke der SiN_x-Schicht korrelierten. Da die Abscheidungsbedingungen identisch waren, impliziert dies eine Nichtreproduzierbarkeit, die sich auf unkontrollierte Abscheidungsparameter oder ungeeignete Oberflächenbehandlung vor der Abscheidung zurückführen lässt.

Die feste positive Ladung der SiN_x-Schicht auf den Si-Wafern ist um mehr als eine Größenordnung höher als die der SiO_2-Schicht auf den Si-Wafern. Dies führt zu einer stärkeren Akkumulation im n-Si und zur stärkeren Inversion im p-Si bei der Si/SiN_x-Hetero-Grenzschicht.

Lichtmodulierte Foto-Strom und Foto-Leitfähigkeitsmessungen (Kapital 7) in elektrochemischen pSi/SiN_x Zellen lieferten komplementäre Informationen über die Kinetik der Ladungsträger: Die Faradayschen Fotoströme (H_2-Entwicklung) sind durch ein niedriges MWR-Signal und eine hohe X-Komponente des Fotostroms gekennzeichnet. Die Verschiebungsfotoströme weisen eine frequenzabhängige Y-Komponente auf, die mit abnehmender Modulationsfrequenz kleiner wird. Außerdem ist für diese Ströme ein von

der Modulationsfrequenz unabhängiges, hohes MWR-Signal charakteristisch. Das Flachband zeichnet sich durch eine hohe Oberflächen-Rekombinationsrate aus, die einen kleinen Fotostrom und ein Minimum des MRW-Signals bedingt.
Mit der Entwicklung von Wasserstoff verändert sich die Charakteristik der pSi/SiN_x-Heterokontaktes hinsichtlich der festen Ladung und der Rekombinationsrate bei Flachband.

Als Funktion des angelegten Potentials zeigten die TRMC-Signale der elektrochemischen nSi/SiN_x Zelle wiederum, dass die höchste Oberflächen-Rekombinationsrate im Bereich des Flachbands beobachtet werden kann und dass die elektrische Passivierung des kristallinen Si durch SiN_x hauptsächlich über eine Passivierung durch das elektrische Feld erreicht wird (Kapitel 8).

Kontaktlose Mikrowellenmessungen (Kapital 9) ergaben einen Anstieg der Leitfähigkeit von Si-Wafern nach der Abscheidung von SiN_x-Schichten (bei SiO_2 wurde kein nennenswerter Effekt registriert). Die numerische Auswertung der Ergebnisse deutet auf eine Verminderung der Mobilität der Elektronen in einer Inversionsschicht dieser Systeme hin. Die eingeschränkte Mobilität steht möglicherweise im Zusammenhang mit den akzeptorartigen Fehlstellen, die durch die Kapazitätsmessungen nachgewiesen wurden.

In der Raumladungszone wurde die Speicherung überschüssiger Ladungsträger beobachtet. Ein Vergleich der TRMC-Transienten von pSi/SiN_x und pSi/SiO_2 lässt im erstgenannten System einen Abklingprozess erkennen, der im zweiten System bei niedrigen Anregungsraten nicht auftritt. Der Vergleich der TRMC- und der SPV-Transienten bei niedriger Anregung legt nahe, dass dieses
Abklingverhalten auf die Rekombination der überschüssigen Ladungsträger in der Verarmungszone von pSi/SiN_x zurückzuführen ist. Für höhere Anregungsdichten ist dieses anfängliche Abklingverhalten nicht mehr zu beobachten.

Dieses ungewöhnliche Verhalten der Überschussladungsträger im pSi/SiN_x-System kann nicht durch das allgemeine Modell für pSi/SiN_x-Kontakte erklärt werden, welches für das Abklingen der Überschussladungsträger lediglich Oberflächendefekte verantwortlich macht.

Die pSi/SiN_x-Kontakte sind anders als die pSi/SiO_2 konfiguriert: die pSi/SiN_x-Proben befinden sich im Inversionszustand wohingegen im
pSi/SiO_2 ein Zustand der Verarmung herrscht. Die Kinetik einer beleuchteten

Inversionsschicht kann sich von der einer klassischen Verarmungsschicht unterscheiden. Außerdem gibt es experimentelle Belege dafür, dass Löcher und Elektronen leicht im SiN_x-Volumen gespeichert werden können, das daraufhin seine feste Ladung ändert. Diese Parameter sind bislang noch unzureichend verstanden und modelliert worden. Sie könnten eine entscheiden Rolle bei der zukünftigen Entwicklung von zufriedenstellenden kinetischen Modellen für die Überschussladungsträger an Si/SiN_x-Grenzflächen spielen.

In weiterführenden Arbeiten wird ein Modell vorgestellt, welches die Kinetik der pSi/SiN_x Heteroübergänge bei niedrigen Injektionsniveaus unter Einbezug der nicht-linearen Rekombinationsprozesse (wie z.B. Einfang von Ladungsträgern inder Raumladungszone) beschreibt. Dafür sollen weiterführende SPV Messungen in Kombination mit TRMC Messungen benutzt werden.

Der Ladungstransfer im SiN_x und Langzeituntersuchungen zur Instabilität sind desweiteren auch von großem Interesse für die Anwendung in der Fotovoltaik sowie in Speichermodulen. Verschiedene Zusammensetzungen der SiN_x Schichten sollen untersucht werden, um die Schichten für diese Anwendungen zu optimieren. Außerdem sollen elektrochemische Messungen durchgeführt werden, um Informationen über die mögliche Änderung der chemischen Eigenschaften der SiN_x Schichten zu erhalten.

Bibliography

[1] Sze, S. *Semiconductor Devices Physics and Technology.* John Wiley & Sons, Inc, 1985.

[2] Pearson, G. & Bardeen, J. *Electrical properties of pure silicon and silicon alloys containing boron and phosphorus.* Physical Review **75**(5), 865–883, 1949.

[3] Mathieu, H. *Physique des semiconducteur et des composants électroniques.* 2001.

[4] Drude, P. *Zur Elektronentheorie der Metalle* **306 (3):566**, 1900.

[5] Fick, A. *Ueber Diffusion.* Annalen der Physik und Chemie **170, Issue 1**, 59–86, 1855.

[6] Irene, E.A. *Electronic Materials Science.* Wiley Interscience, 2005.

[7] Nicollian EH., B.J. *MOS (Metal Oxide Semiconductor) Physics and Technology.* Wiley-Interscience, 1982.

[8] Shockley, W. & Read, W. *Statistics of the recombinations of holes and electrons.* Physical Review **87**(5), 835–842, 1952.

[9] Hall, R. *Electron-hole recombination in germanium.* Physical Review **87**(2), 387, 1952.

[10] Aberle, A., Glunz, S. & Warta, W. *Impact of illumination level and oxide parameters on shockley-read-hall recombination at the si-sio2 interface.* J. Appl. Phys. **71**(9), 4422–4431, 1992.

[11] Eades, W. & Swanson, R. *Calculation of surface generation and recombination velocities at the si-sio2 interface.* J. Appl. Phys. **58**(11), 4267–4276, 1985.

[12] Stubbe, L. & Gossick, B. *Measurements of the Dember Potential in Bulk Germanium.* J. Appl. Phys. **30**(4), 507–508, 1959.

[13] Lam, Y. *Surface-state density and surface potential in mis capacitors by surface photovoltage measurements .1.* Journal Of Physics D-Applied Physics **4**(9), 1370–1375, 1971.

[14] Luke, K. & Cheng, L. *Analysis of the interaction of a laser-pulse with a silicon-wafer-determination of bulk lifetime and surface recombination velocity.* J. Appl. Phys. **61**(6), 2282–2293, 1987.

[15] Kunst, M., Jaegermann, W. & Schmeisser, D. *Chemical etching of p-type si(100) by k2cr2o7 - a combined investigation by trmc and xps, ups, and leed.* Applied Physics A-Materials Science & Processing **42**(1), 57–64, 1987.

[16] Berz, F. *Surface physics of phosphors and semiconductors.* Academic Press, 1975.

[17] Terman, L. *An investigation of surface states at a silicon silicon oxide interface employing metal oxide silicon diodes.* Solid-State Electron. **5**(SEP-O), 285–299, 1962.

[18] Duwe, H. *Simultane optische und elecktrochemische Grendflächnanalyse beim Rückätzen von Siliziumdioxid.* Ph.D. thesis, Technischen Universität Berlin, 1993.

[19] Ligenza, J. & Spitzer, W. *The mechanisms for silicon oxidation in steam and oxygen.* J. Phys. Chem. Solids **14**, 131–136, 1960.

[20] Atalla, M., Tannenbaum, E. & Scheibner, E. *Stabilization of silicon surfaces by thermally grown oxides.* Bell System Technical Journal **38**(3), 749–783, 1959.

[21] Füssel, W., Schmidt, M., Angermann, H., Mende, G. & Flietner, H. *Defects at the Si/SiO2 interface: Their nature and behaviour in technological processes and stress.* Nuclear Instruments and Methods in Physics Research Section A: Accelerators, Spectrometers, Detectors and Associated Equipment **377**(2-3), 177 – 183, 1996.

[22] Füssel, W., schmidt, M. & flietner, H. *Radiation-induced degradation of si/sio2 structures and the nature of defects.* Nuclear Instruments &

Methods in Physics Research Section B-Beam Interactions with Materials and Atoms **65**(1-4), 238–242, 1992.

[23] Albohn, J., Fussel, W., Sinh, N., Kliefoth, K. & Fuhs, W. *Capture cross sections of defect states at the Si/SiO2 interface.* J. Appl. Phys. **88**(2), 842–849, 2000.

[24] Johnson, N., Biegelsen, D., Moyer, M., Chang, S., Poindexter, E. & Caplan, P. *Characteristic electronic defects at the si-sio2 interface.* Appl. Phys. Lett. **43**(6), 563–565, 1983.

[25] Robertson, J. *Defects and hydrogen in amorphous-silicon nitride.* Philosophical Magazine B-Physics Of Condensed Matter Statistical Mechanics Electronic Optical and Magnetic Properties **69**(2), 307–326, 1994.

[26] Robertson, J. *Electronic-structure of silicon-nitride.* Philosophical Magazine B-Physics Of Condensed Matter Statistical Mechanics Electronic Optical and Magnetic Properties **63**(1), 47–77, 1991.

[27] Schmidt, J. *Untersuchungen zur Ladungsträgerrekombination an den Oberflächen und im Volumen von kristallinen Silicium-Solarzelln.* Ph.D. thesis, Universität Hannover, 1998.

[28] Klein, D. *Characterization and improvement of silicon solar cells: Enhanced light acceptance and better separation and extraction of charge-carriers.* Ph.D. thesis, Paul Perlane Universite-metz, Frei Universität Berlin, 2009.

[29] Frohmanb.D & Lenzling.M. *Charge transport and storage in metal-nitride-oxide-silicon (mnos) structures.* J. Appl. Phys. **40**(8), 3307–3319, 1969.

[30] Lenahan, P., Krick, D. & Kanicki, J. *The Nature Of The Dominant Deep Trap In Amorphous-Silicon Nitride Films - Evidence For A Negative Correlation-Energy.* Appl. Surf. Sci. **39**(1-4), 392–405, 1989.

[31] Fujita, S. & Sasaki, A. *Dangling bonds in memory-quality silicon-nitride films.* J. Electrochem. Soc. **132**(2), 398–402, 1985.

[32] Krick, D., Lenahan, P. & Kanicki, J. *Stable photoinduced paramagnetic defects in hydrogenated amorphous-silicon nitride.* Appl. Phys. Lett. **51**(8), 608–610, 1987.

[33] Gritsenko, V., Petrenko, I., Svitasheva, S. & Wong, H. *Excess silicon at the Si(3)N4/SiO2 interface.* Appl. Phys. Lett. **72**(4), 462–464, 1998.

[34] Carr, E. & Buhrman, R. *Role of interfacial nitrogen in improving thin silicon-oxides grown in n2o.* Appl. Phys. Lett. **63**(1), 54–56, 1993.

[35] Gritsenko, V., Wong, H., Xu, J., Kwok, R., Petrenko, I., Zaitsev, B., Morokov, Y. & Novikov, Y. *Excess silicon at the silicon nitride/thermal oxide interface in oxide-nitride-oxide structures.* J. Appl. Phys. **86**(6), 3234–3240, 1999.

[36] Mark E. Orazem, B.T. *Electrochemical Impedance Spectroscopy.* Wiley, 2008.

[37] Peter, L. *Dynamic aspects of semiconductor photoelectrochemistry.* Chem. Rev. **90**(5), 753–769, 1990.

[38] Simon, P. & Gogotsi, Y. *Materials for electrochemical capacitors.* Nat. Mater. **7**(11), 845–854, 2008.

[39] Gratzel, M. *Photoelectrochemical cells.* Nature **414**(6861), 338–344, 2001.

[40] Lana-Villarreal, T., Straboni, A., Pichon, L. & Alonso-Vante, N. *Photoelectrochemical characterization of p-type silicon electrodes covered with tunnelling nitride dielectric films.* Thin Solid Films **515**(18), 7376–7381, 2007.

[41] Memming, R. *Semiconductor Electrochemistry.* Wiley-VHC, 2002.

[42] Zou, Z., Ye, J., Sayama, K. & Arakawa, H. *Direct splitting of water under visible light irradiation with an oxide semiconductor photocatalyst.* Nature **414**(6864), 625–627, 2001.

[43] Munoz, A., Moehring, A. & Lohrengel, M. *Anodic oxidation of chemically hydrogenated Si(100).* Electrochim. Acta **47**(17), 2751–2760, 2002.

[44] John R. Reitz, Frederick J. Milford, R.W.C. *Foundations of Electromagnetic Theory.*

[45] Jackson, J.D. *Classical Electrodynamics.* 1962.

[46] Johnk, C.T. *Engineering Electromagnetic Fields and Waves.* 1975.

[47] Kunst, M. & Beck, G. *The study of charge carrier kinetics in semiconductors by microwave conductivity measurements.* J. Appl. Phys. **60**(10), 3558–3566, 1986.

[48] Swiatkowski, C., Sanders, A., Buhre, K. & Kunst, M. *Charge-carrier kinetics in semiconductors by microwave conductivity measurements.* J. Appl. Phys. **78**(3), 1763–1775, 1995.

[49] Wunsch, F., Schlichthorl, G. & Tributsch, H. *Microwave photoelectric examination of photovoltaic devices.* Journal Of Physics D-Applied Physics **26**(11), 2041–2048, 1993.

[50] Lam, Y. & Rhoderic.EH. *Surface-state density and surface potential in mis capacitors by surface photovoltage measurements .2.* Journal Of Physics D-Applied Physics **4**(9), 1376–1389, 1971.

[51] Klein, D., Wuensch, F. & Kunst, M. *The determination of charge-carrier lifetime in silicon.* Physica Status Solidi B-Basic Solid State Physics **245**(9), 1865–1876, 2008.

[52] Stubbe, L. & Gossick, B. *Measurements of the Dember Potential in Bulk Germanium.* Journal of Applied Physics **30**(4), 507–508, 1959.

[53] Dittrich, T., Bonisch, S., Zabel, P. & Dube, S. *High precision differential measurement of surface photovoltage transients on ultrathin CdS layers.* Rev. Sci. Instrum. **79**(11), 113903, 2008.

[54] Endoh, T., Chiba, T., Sakuraba, H., Lenski, M. & Masuoka, F. *A quantitative analysis of stress-induced leakage currents and extraction of trap properties in 6.8 nm ultrathin silicon dioxide films.* J. Appl. Phys. **86**(4), 2095–2099, 1999.

[55] Sze, S. *Current transport and maximum dielectric strength of silicon nitride films.* J. Appl. Phys. **38**(7), 2951–2956, 1967.

[56] Bachhofer, H., Reisinger, H., Bertagnolli, E. & von Philipsborn, H. *Transient conduction in multidielectric silicon-oxide-nitride-oxide semiconductor structures.* J. Appl. Phys. **89**(5), 2791–2800, 2001.

[57] Frenkel, J. *On Pre-Breakdown Phenomena in Insulators and Electronic Semi-Conductors.* Phys. Rev. **54**, 647–648, 1938.

[58] Grieco, M., Worthing, F. & Schwartz, B. *Silicon nitride thin films from sicl4 plus nh3 - preparation and properties.* J. Electrochem. Soc. **115**(5), 525, 1968.

[59] Reizman, F. & Vangelde.W. *Optical thickness measurement of sio2-si3n4 films on silicon.* Solid-State Electron. **10**(7), 625, 1967.

[60] Vishnyakov, A., Novikov, Y., Gritsenko, V. & Nasyrov, K. *The charge transport mechanism in silicon nitride: Multi-phonon trap ionization.* Solid State Electronics **53**(3), 251 – 255, 2009.

[61] Enz, C., Krummenacher, F. & Vittoz, E. *An analytical mos-transistor model valid in all regions of operation and dedicated to low-voltage and low-current applications.* Analog Integrated Circuits and Signal Processing **8**(1), 83–114, 1995.

[62] Hezel, R. & Jager, K. *Properties of inversion-layers for mis/il solar-cells studied on low-temperature-processed mnos transistors.* Solid-State Electron. **26**(10), 993–997, 1983.

[63] Goetzber.A & Nicollia.FH. *Mos avalanche and tunneling effects in silicon surfaces.* J. Appl. Phys. **38**(12), 4582–4588, 1967.

[64] Greef, R., Peat, R., Peter, L., Pletcher, D. & Robinson, J. *Instrumental methods in electrochemistry.* Ellis Horwood Limited, 1985.

[65] Kwa, K., Chattopadhyay, S., Jankovic, N., Olsen, S., Driscoll, L. & O'Neill, A. *A model for capacitance reconstruction from measured lossy MOS capacitance-voltage characteristics.* Semicond. Sci. Technol. **18**(2), 82–87, 2003.

[66] Natarajan, A., Nellore, A. & Searson, P. *Theory of potential modulated microwave reflectivity at semiconductor surfaces.* J. Appl. Phys. **85**(3), 1631–1636, 1999.

[67] Peter, L. & Ushiroda, S. *Microwave reflectance studies of photoelectrochemical kinetics at semiconductor electrodes. 3. Photolectrochemical reduction of Ru(NH3)(6)(3+) at p-Si.* J. Phys. Chem. B **108**(8), 2660–2665, 2004.

[68] Schlichthorl, G. & Peter, L. *Impedance and microwave reflectivity measurements on n-si in 1m licl methanol .1. Depletion and inversion layer formation.* J. Electrochem. Soc. **142**(8), 2665–2669, 1995.

[69] Head, J. & Turner, J. *Silicon nitride for direct water-splitting and corrosion mitigation.* U.S. Department of Energy Journal of Undergraduate Research pp. 108–113, 2006.

[70] Natarajan, A., Oskam, G. & Searson, P. *Characterization of silicon surfaces in HF solution using microwave reflectivity.* J. Appl. Phys. **83**(4), 2112–2120, 1998.

[71] Munoz, A. & Lohrengel, M. *Kinetics of oxide growth and oxygen evolution on p-Si in neutral aqueous electrolytes.* J. Solid State Electrochem. **6**(8), 513–521, 2002.

[72] Seidel, H., Csepregi, L., Heuberger, A. & Baumgartel, H. *Anisotropic etching of crystalline silicon in alkaline-solutions .1. orientation dependence and behavior of passivation layers.* J. Electrochem. Soc. **137**(11), 3612–3626, 1990.

[73] Lu, X., Cheung, N., Strathman, M., Chu, P. & Doyle, B. *Hydrogen induced silicon surface layer cleavage.* Appl. Phys. Lett. **71**(13), 1804–1806, 1997.

[74] Bruel, M., Aspar, B. & Auberton-Hervé, A.J. *Smart-cut: a new silicon on insulator material technology based on hydrogen implantation and wafer bonding.* Japanese Journal of Applied Physics **36**, 1636–1641, 1997.

[75] Bruel, M. *Silicon-on-insulator material technology.* Electronics Letters **31**(14), 1201–1202, 1995.

[76] Homann, M. & Kliem, H. *Relaxational polarization and charge injection in thin-films of silicon-nitride.* Microelectronics Journal **25**(7), 559–566, 1994.

[77] Thorp, J., Ahmad, A., Kulesza, B. & Bushell, T. *The permittivity and dielectric loss of reaction-bonded silicon-nitride.* J. Mater. Sci. **19**(11), 3680–3686, 1984.

[78] Suzuki, E., Hayashi, Y. & Yanai, H. *Model of degradation mechanisms in metal-nitride-oxide-semiconductor structures.* Appl. Phys. Lett. **35**(10), 790–792, 1979.

[79] Kamigaki, Y., Minami, S. & Kato, H. *A new portrayal of electron and hole traps in amorphous-silicon nitride.* J. Appl. Phys. **68**(5), 2211–2215, 1990.

[80] Lewerenz, H. & Schlichthorl, G. *Separation of charge-transfer and surface recombination processes by simultaneous measurement of photocurrent and excess microwave conductivity profiles of si(111) in nh4f.* J. Appl. Phys. **75**(7), 3544–3547, 1994.

[81] Schlichthorl, G. & Tributsch, H. *Microwave photoelectrochemistry.* Electrochim. Acta **37**(5), 919–931, 1992.

[82] Cass, M., Duffy, N., Peter, L., Pennock, S., Ushiroda, S. & Walker, A. *Microwave reflectance studies of photoelectrochemical kinetics at semiconductor electrodes. 1. Steady-state, transient, and periodic responses.* J. Phys. Chem. B **107**(24), 5857–5863, 2003.

[83] Lewerenz J., J.H. *Photovoltaik.* Springer, 1995.

[84] Schieck, R. & Kunst, M. *Frequency modulated microwave photoconductivity measurements for characterization of silicon wafers.* Solid-State Electron. **41**(11), 1755–1760, 1997.

[85] Cass, M., Duffy, N., Peter, L., Pennock, S., Ushiroda, S. & Walker, A. *Microwave reflectance studies of photoelectrochemical kinetics at semiconductor electrodes. 2. Hydrogen evolution at p-Si in ammonium fluoride solution.* J. Phys. Chem. B **107**(24), 5864–5870, 2003.

[86] Green, M.A. *Self-consistent optical parameters of intrinsic silicon at 300 K including temperature coefficients.* Sol. Energy Mater. Sol. Cells **92**(11), 1305–1310, 2008.

[87] Dauwe, S. *Low-Temperature Surface Passivation of Crystalline Silicon and its Application to the Rear Side of Solar Cells.* Ph.D. thesis, Universität Hannover, 2004.

[88] Hu, S., Kerr, D. & Gregor, L. *Evidence Of Hole Injection And Trapping In Silicon Nitride Films Prepared By Reactive Sputtering.* Appl. Phys. Lett. **10**(3), 97–99, 1967.

[89] von Aichberger, S., Abdallah, O., Wunsch, F. & Kunst, M. *Influence of a space charge region on charge carrier kinetics in silicon wafers.* J. Appl. Phys. **91**(11), 9147–9150, 2002.

[90] Sinton, R. & Cuevas, A. *Contactless determination of current-voltage characteristics and minority-carrier lifetimes in semiconductors from quasi-steady-state photoconductance data.* Appl. Phys. Lett. **69**(17), 2510–2512, 1996.

[91] Elmiger, J. & Kunst, M. *Investigation of charge carrier injection in silicon nitride silicon junctions.* Appl. Phys. Lett. **69**(4), 517–519, 1996.

[92] Sah, C., Noyce, R. & Shockley, W. *Carrier generation and recombination in p-n junctions and p-n junction characteristics.* Proceedings of The Institute of Radio Engineers **45**(9), 1228–1243, 1957.

Statement

I hereby declare that this submission is my own work and that, to the best of my knowledge and belief, it contains no material previously published or written by another person, except where due acknowledgement is made in the text. I also declare that the intellectual content of this thesis is the product of my own work, even though I may have received assistance from others on style, presentation and language expression.

Erklärung

Ich erkläre hiermit, dass ich die vorliegende Arbeit selbstständig verfasst, andere als die angegebenen Quellen und Hilfsmittel nicht verwendet und die den benutzten Quellen wörtlich oder inhaltlich entnommenen Stellen als solche kenntlich gemacht habe. Die Arbeit wurde weder in gleicher noch ähnlicher Form einer anderen Prüfungsbehörde vorgelegt, noch veröffentlicht.

Elías Martínez Moreno

Berlin, 04.11.2009